



HAL
open science

Prediction of air nonequilibrium radiation with a collisional-radiative model: Application to shock-tube conditions relevant to Earth reentry

Adrien Lemal

► **To cite this version:**

Adrien Lemal. Prediction of air nonequilibrium radiation with a collisional-radiative model: Application to shock-tube conditions relevant to Earth reentry. Other. Ecole Centrale Paris, 2013. English. NNT: 2013ECAP0044 . tel-01175651

HAL Id: tel-01175651

<https://theses.hal.science/tel-01175651>

Submitted on 11 Jul 2015

HAL is a multi-disciplinary open access archive for the deposit and dissemination of scientific research documents, whether they are published or not. The documents may come from teaching and research institutions in France or abroad, or from public or private research centers.

L'archive ouverte pluridisciplinaire **HAL**, est destinée au dépôt et à la diffusion de documents scientifiques de niveau recherche, publiés ou non, émanant des établissements d'enseignement et de recherche français ou étrangers, des laboratoires publics ou privés.

Ph. D Thesis

Presented by

Adrien LEMAL

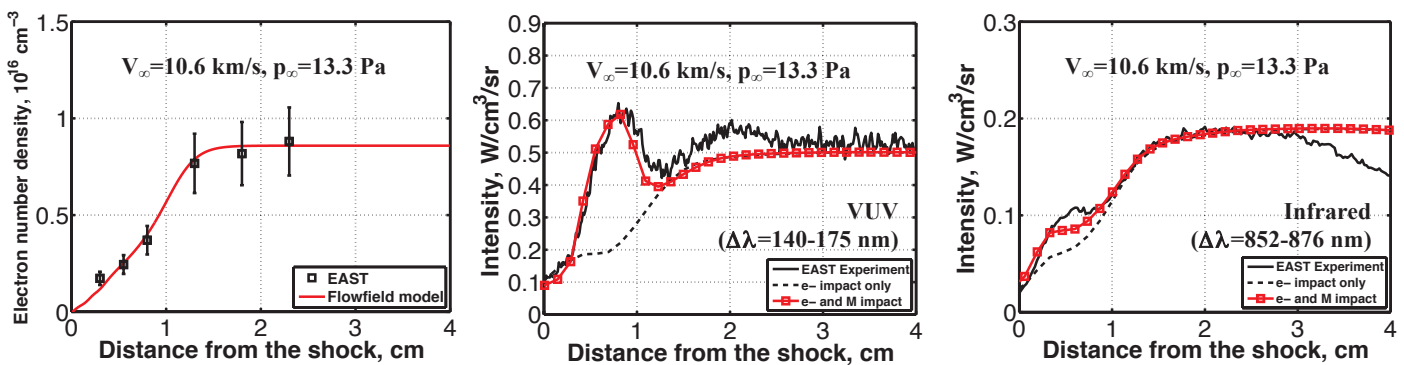
For the obtention of the grade of

DOCTOR IN AEROSPACE ENGINEERING

Doctoral School: ED 287 'Sciences pour l'Ingénieur, Energétique, Physique'

Laboratory: Laboratoire EM2C, UPR 288 of CNRS located at Ecole Centrale Paris

**PREDICTION OF NONEQUILIBRIUM AIR RADIATION WITH A COLLISIONAL-RADIATIVE MODEL
APPLICATION TO SHOCK-TUBE EXPERIMENTS RELEVANT TO EARTH ATMOSPHERIC REENTRY**



Prediction of the electron number density as well as the VUV and Infrared post-shock intensity profiles at peak heating conditions

Date: Wednesday, July 10th 2013

COMMITTEE

Dr. Gianpiero COLONNA	Consiglio Nazionale delle Ricerche, <i>Senior researcher</i>	Reviewer
Dr. Christopher JOHNSTON	NASA Langley Research Center, <i>Aerospace Engineer</i>	Reviewer
Pr. Christophe LAUX	Ecole Centrale Paris, <i>Professor</i>	Advisor
Dr. Lionel MARRAFFA	European Space Agency, ESTEC, <i>Aerothermodynamics Engineer</i>	Examiner
Pr. Richard MORGAN	The Centre for Hypersonics, the University of Queensland, <i>Professor</i>	Reviewer
Dr. Marie-Yvonne PERRIN	Centre National de la Recherche Scientifique, <i>Senior researcher</i>	Advisor
Dr. Elisabeth RAYNAUD	EADS Astrium Space Transportation, <i>Aerospace Engineer</i>	Examiner
Mr. Philippe TRAN	EADS Astrium Space Transportation, <i>Aerospace Engineer</i>	Examiner

Laboratoire d'Energétique Moléculaire et Macroscopique, Combustion (EM2C)
UPR 288, CNRS et Ecole Centrale Paris
Tél: +33 (0)1 41 13 10 31
Télécopie: +33 (0)1 47 02 80 35

Ecole Centrale des Arts et Manufactures
Grand Etablissement sous tutelle
du Ministère de l'Education Nationale
Grande Voie des Vignes
92295 CHATENAY-MALABRY Cedex
Tél: +33 (0)1 41 13 10 00
Télex: 634 991 F EC PARIS

European Aeronautics Defense and Space company
Astrium Space Transportation
51-61, Route de Verneuil
78133 Les Mureaux Cedex
Tél: +33 (0)1 39 06 12 34

Acknowledgments

I am thankful to Dr. Thierry Leveugle (EADS Astrium) for accepting funding the present work and for his constant interest in the present work.

I am indebted to my supervisors Pr. Christophe Laux and Dr. Marie-Yvonne Perrin for their constant support and enlightening guidance. I am also very appreciative of the freedom they gave to me so as to conduct my research within these three years. I am also very pleased of the direct and honest exchanges we shared during this time.

I am thankful to Dr. Elisabeth Raynaud (EADS Astrium) and Mr. Philippe Tran (EADS Astrium) for their constant interest in the present work and for the valuable discussions during our meetings. Thanks are due to Dr. Alexis Bourgoing (EADS Astrium), Mr. Jacques Soler (EADS Astrium) for providing their flowfield solution, to Mr. Laurent Visconti (EADS Astrium) for his remarks on radiation transport.

I am thankful to the members of the committee for their patience and time. Many thanks to Dr. Christopher Johnston (NASA Langley) and Pr. Richard Morgan (Centre of Hypersonics, University of Queensland) for reviewing this work. Their suggestions greatly improved this work and are greatly appreciated.

Thanks are due to Dr. Aaron Brandis (NASA Ames) and Dr. Brett Cruden (NASA Ames) for their support in analyzing the radiation measurements obtained in the EAST facility. Thanks are due to Dr. Daniel Potter (DLR) for his help in writing Poshax input files. Thanks are due to Dr. Daniel Kelley (University of Minnesota) for his support in collision theory

Thanks are due to Dr. Lionel Marraffa (ESA ESTEC) for having welcoming me at ESA during Summer 2010 and for his constant interest in this work.

Thanks are due to Anne-Cécile Aiach for her unparallel administrative support when dealing with travel cost refunding. Thanks are due to Jordan Marescaux, Matthieu Boileau and Sebastien Turgis for their help in Mac OS troubleshooting.

Many thanks to the other Ph.D students I shared great moments with. Thanks to my office mates Vincent, Florent, Da, Laurent and Jean, to the Plasma group Ph.D students and postdoctoral fellows Megan, Marien, Farah, Fabien, Umar, François, Diane and Aurélien. Thanks to the students Alexandre, Philippe and Charles, I was entrusted to supervise, for their help. Thanks to the other bright Ph.D students I shared great moments with. I enjoyed our discussions on key topics such as energy management and human rights. I also appreciated that some of you took part in activities such as Basket-Ball practise every Friday, swimming during summer and going to trendy Parisian places most of the week-ends.

Finally, I would like to acknowledge my family and my lovely girlfriend Carolyn for their constant support and love.

The research described in this dissertation has been supported by EADS under Astrium-09919 grant and RASTAS SPEAR project within the 7th European framework program.

Abstract

Upcoming exploration missions to the Moon and Mars continue to generate strong motivation in designing advanced thermal protection systems (TPS) with low design margins, which are conducive to:

- the reduction of the launching costs,
- the increase of the scientific value of the mission by embedding larger payloads and,
- the enhancement of the reliability and safety of the reentry systems

The sizing of the TPS significantly relies upon the prediction of the radiative heat flux, which can represent up to 50% of the total heat encountered by the spacecraft during reentry; thus requires an accurate and cost-effective description and modeling of the various physico-chemical processes occurring in front of the spacecraft.

Under nonequilibrium, the populations of the electronic states that strongly radiate in the shock layer are no longer governed by a Boltzmann distribution but rather by collisional and radiative processes. The key processes responsible for the depletion/population of the emitting states are electron-impact excitation, ionization, dissociation, heavy-particle impact excitation and dissociation, internal energy exchange processes such as vibration-vibration, vibration-translation, vibration-electron as well as bound-bound radiative mechanisms. In this work, a collisional-radiative (CR) model was developed to model these processes. A comprehensive review of the available experimental and theoretical reaction rates governing these processes was undertaken to produce a reliable set of rates. The bound-bound radiative mechanisms were treated using the escape factor concept, set to zero for VUV lines and set to one for visible and near-infrared lines, in accordance with literature results.

The CR model was interfaced with the flowfield solvers Poschax (Gollan, 2006; Potter, 2011) and the one provided by EADS and with the line-by-line spectral radiation code SPECAIR (Laux *et al.*, 2003) under the QSS assumption. This modeling strategy was used to predict the nonequilibrium radiation spectra very recently measured in the EAST facility at NASA Ames Research Center. These radiation measurements are of great interest, because they include the first ever published quantitative spectra in the VUV (102-180 nm), as well as the spectra in the near IR (856-882 nm) and visible (408-412 nm and 654-658 nm) for Earth reentry and thus they represent a unique opportunity to test the CR model developed in this work. Two shock-tube conditions representative of a Lunar return reentry trajectory were selected: $V_\infty=10.6$ and 11.17 km/s, both at $p_\infty=13.3$ Pa. The radiation measurements were investigated in the VUV, visible and infrared spectral ranges. A detailed analysis of these measurements was performed to extract the electron number density profiles (from the Stark-broadened H_α line at 656 nm and the N line at 411 nm), the vibrational and rotational temperatures (from the N_2 Second positive and N_2^+ First negative systems between 250 and 350 nm) and the spectral and intensity profiles in the post-shock region.

First, the electron number density profiles inferred from experiments were compared with the prediction of the flowfield model, showing excellent agreement in trend and absolute magnitude for both freestream conditions, and thus providing a way to accurately locate the shock front in the CCD images. The experimental post-shock intensity profiles were compared with the prediction of the CR model. The nonequilibrium intensities observed in the VUV and IR spectral ranges were underpredicted by the CR model when only electron-impact excitation and ionization processes were taken into account.

Then, the effect of heavy-particle impact processes was studied starting from the baseline Park non-preferential dissociation rate constant model (1985) and then applying various dissociation rate constants and dissociation-vibration coupling models. The nonequilibrium post-shock intensities observed in the VUV and in the IR predicted with the dissociation rate constant models of Park (1985) and Macheret and Rich (1993) were shown to be in good agreement with each other, but both underpredicted the experimental intensities. Moreover, the use of preferential dissociation-vibration coupling models increased the equilibrium distance and still underpredicted the experimental intensities. Subsequently, a sensitivity analysis on heavy-particle impact excitation processes was conducted. Excellent agreement between predicted and measured intensity profiles was obtained for both freestream conditions and for all spectral ranges, with heavy-particle rate constants of the order of 10^{-15} to 10^{-13} cm^3/s , which is consistent with Kelley (2012) analysis, suggesting that the nonequilibrium peak intensities observed in the VUV and IR spectral ranges are controlled by heavy-particle impact processes.

To test the often-used Boltzmann multi-temperature model, the CR model predictions and the experimental intensity profiles were compared with the predictions of a Boltzmann model at the electron temperature. For both conditions, the measured post-shock intensity profiles in the visible and IR spectral ranges were overpredicted by the Boltzmann model by a factor up to 5. In the VUV, the Boltzmann and CR predictions were shown to be very close to each other.

Finally, the measured spectra were also analyzed to infer the population distribution of the excited states responsible for the observed lines. In particular, the thin and self-observed lines were used to determine the populations of the metastable states, which do not radiate. For both freestream conditions, the populations of the low-lying excited states ($E < 11\text{eV}$) were shown to be well predicted by a Boltzmann distribution at the electron temperature, owing to strong collisions with electrons and heavy-particles. The higher excited states ($E > 11\text{eV}$) were shown to be strongly depleted from the Boltzmann distribution at the electron temperature, as a result of significant electron-impact ionization and radiative processes. For both conditions, the population distribution of the excited states were shown to be fairly well reproduced by the CR model.

This work represents the first quantitative comparison between VUV shock-tube radiation data and simulations at conditions representative of hypervelocity Earth reentry. The CR model developed in this work showed that the heavy-particle impact excitation processes have a strong influence on the atomic excited states with energy less than 11eV , whereas the states above 11eV are mostly controlled by electron-impact processes. Because the low lying states are responsible for the bulk of radiation in the VUV, which can represent up to 60% of the radiation emitted by the post-shock region during Earth hypervelocity reentry, heavy-particle impact excitation processes appear to be essential to correctly predict the radiative heat flux encountered by a spacecraft during its reentry into Earth's atmosphere.

Table of Contents

List of Symbols	10
List of Figures	12
List of Tables	16
Chapter I: Introduction	19
I.1. Motivation.....	20
I.1.1. Past and future reentry missions.....	20
I.1.2. Phenomenology of reentry flows.....	20
I.1.3. Ground-testing strategy	21
I.2. Background	22
I.2.1. Flight regimes.....	22
I.2.2. Thermochemical regimes.....	24
I.3. Computation of nonequilibrium radiation.....	26
I.3.1. Multi-temperature models	26
I.3.2. State-to-state models	26
I.3.3. Methodology	26
I.4. Scope and organization of the thesis.....	27
Chapter II: Air spectral model.....	31
II.1. Main radiators in high temperature air.....	32
II.2. Atomic spectra	32
II.2.1. Nomenclature for atomic states.....	32
II.2.2. Radiative transitions.....	33
II.3. Molecular spectra	33
II.3.1. Nomenclature for molecular electronic states	33
II.3.2. Radiative transitions.....	35
II.4. Emission and absorption coefficients.....	36
II.4.1. Bound-bound transitions.....	36
II.4.2. Broadening mechanisms.....	36
II.4.3. Bound-free and free-free transitions.....	39
II.5. The Radiative Transport Equation	40
II.6. Summary.....	41
Chapter III: Air collisional-radiative model	43
III.1. Literature review	44
III.2. Internal states	47
III.2.1. Atoms.....	47
III.2.2. Molecules.....	49
III.3. Elementary processes.....	50
III.3.1. Electron-impact excitation	50
III.3.2. Electron-impact ionization.....	51
III.3.3. Heavy-particle impact excitation.....	51
III.3.4. Electron-impact dissociation.....	52
III.3.5. Heavy-particle impact dissociation	53
III.3.6. V-T, V-V, V-e exchange energy processes	53
III.3.7. Predissociation	53
III.3.8. Radiative processes	54
III.4. Master equation.....	55
III.5. Selection of rate constants	56
III.5.1. Electron-impact excitation	57

III.5.1.1. Review of experimental data.....	57
III.5.1.2. Review of theoretical data.....	62
III.5.1.3. Selected rate constants	64
III.5.2. Electron-impact ionization.....	70
III.5.2.1. Review of theoretical data.....	70
III.5.2.2. Selected rate constants	71
III.5.3. Heavy-particle impact excitation.....	72
III.5.3.1. Review of theoretical data.....	72
III.5.3.2. Selected rate constants	74
III.5.4. Electron-impact dissociation.....	75
III.5.5. Heavy-particle impact dissociation	75
III.5.6. V-T, V-V, V-e exchange energy processes.....	76
III.5.7. Predissociation	76
III.5.8. Radiative processes	76
III.6. Summary	76
Chapter IV: EAST shock-tube experiments and flowfield model assessment.....	80
IV.1. Electric Arc Shock-tube (EAST) facility	80
IV.1.1. Facility description.....	81
IV.1.2. Radiation measurements.....	81
IV.1.2.1. Optical design	81
IV.1.2.2. Spectrometers and detectors	82
IV.1.2.3. Calibration	82
IV.1.3. Air conditions	83
IV.1.4. Spectral and spatial resolution	85
IV.2. Simulation strategy.....	87
IV.2.1. Assumptions.....	87
IV.2.2. Spectral and spatial resolution	88
IV.3. Analysis of the shock-tube measurements	88
IV.3.1. Spectral and total intensity profiles.....	88
IV.3.2. Emitting states	95
IV.4. Assessment of the flowfield thermochemistry model	95
IV.4.1. Measured temperature profiles.....	95
IV.4.2. Comparison with the flowfield model	97
IV.5. Assessment of the flowfield ionization model.....	97
IV.4.1. Measured electron number density profiles.....	97
IV.4.2. Comparison with the flowfield model and shock front location determination	100
IV.6. Summary	101
Chapter V: Assessment of the collisional-radiative model.....	102
V.1. Post-shock intensity profiles	103
V.1.1. Influence of electron-impact processes.....	103
V.1.1.1 Visible spectral range	103
V.1.1.2. Infrared spectral range	103
V.1.1.3. VUV spectral range	103
V.1.2. Influence of the dissociation model.....	106
V.1.3. Sensitivity to heavy-particle impact excitation processes	111
V.1.3.1. Visible spectral range	112
V.1.3.2. Infrared spectral range	112
V.1.3.3. VUV spectral range	112
V.1.4. Assessment of the Boltzmann multi-temperature model.....	115
V.1.4.1. Visible spectral range	115
V.1.4.2. Infrared spectral range	115
V.1.4.3. VUV spectral range	116
V.2. Spectral analysis.....	117
V.2.1. Visible spectral range	117

V.2.2. Infrared spectral range	118
V.2.3. VUV spectral range	118
V.3. Populations of the excited states	120
V.3.1. Experimental distribution of the grouped level populations.....	120
V.3.1.1. Methodology.....	120
V.3.1.2. Condition 117: $V_\infty=10.6$ km/s, $p_\infty=13.3$ Pa.....	126
V.3.1.3. Condition 119: $V_\infty=11.17$ km/s, $p_\infty=13.3$ Pa	127
V.3.2. Comparison with the CR and Boltzmann multi-temperature model predictions	129
V.3.2.1. Visible spectral range	129
V.3.2.2. Infrared spectral range	129
V.3.2.3. VUV spectral range	129
V.5. Summary	131
Chapter VI: Conclusions	132
VI.1. Contributions of this thesis	132
VI.2. Recommendations for future work.....	134
Appendix A: Poshax flowfield solver	137
A.1. Assumptions and governing equations	137
A.2. Nonequilibrium chemical kinetics.....	138
A.2.1. Forward and backward rate constants.....	138
A.2.2. Nonequilibrium dissociation rate constants	139
A.2.3. Energy exchanges between internal modes	140
A.2.3.1. V-T energy exchange source term S_{VT}	140
A.2.3.2. e-T energy exchange source term S_{eT}	141
A.2.3.3. Nonequilibrium dissociation-vibration coupling S_{VChm}	141
A.2.3.4. Nonequilibrium electron-chemistry coupling S_{eChm}	143
Appendix B: NIST and grouped levels	144
Appendix C: Strongest atomic lines.....	148
Appendix D: Spatial smearing.....	150
References	152

List of Symbols

Fundamental constants

a_0	: Bohr first radius	$a_0 = 5.292 \cdot 10^{-11} \text{ m}$
c	: Speed of light	$c = 2.998 \cdot 10^8 \text{ m/s}$
ϵ_0	: Permittivity of free space	$\epsilon_0 = 8.854 \cdot 10^{-12} \text{ F/m}$
f_s	: Fine structure constant	$f_s = 7.297 \cdot 10^{-3}$
h	: Planck constant	$h = 6.626 \cdot 10^{-34} \text{ J/s}$
k	: Boltzmann constant	$k = 1.381 \cdot 10^{-23} \text{ J/K}$
m_e	: Electron mass	$m_e = 9.109 \cdot 10^{-31} \text{ kg}$
q_e	: Electron charge	$q_e = 1.602 \cdot 10^{-19} \text{ C}$
R_y	: Hydrogen ionization potential	$R_y = 13.605 \text{ eV}$

Latin characters

A	: Einstein coefficients (s^{-1})
B	: Einstein coefficient ($\text{cm}^3/\text{J/s}$)
E	: Energy of a level (J)
f	: Absorption oscillator strength
g	: Degeneracy of a level
I	: Intensity ($\text{W}/\text{cm}^2/\text{sr}/\text{nm}$)
J	: Rotational quantum number
K	: Rate constant (cm^3/s or cm^6/s)
Kn	: Knudsen number (-)
L	: Length (m)
M	: Mach number (-)
m	: Mass (kg)
n	: Number density (cm^{-3})
Q	: Partition function (-)
q^{rad}	: Radiative heat flux (W/cm^2)
Re	: Reynolds number (-)
T	: Temperature (K)
V	: Velocity (km/s)
v	: Vibrational quantum number
W	: Molar mass (kg/mol)
x, z	: Distance from the shock (cm)

Subscripts

C	: Collisional
Chm	: Chemical
D	: Doppler
Dis	: Dissociation
Elec	: Electronic
Exc	: Excitation
h	: Hydrogen
Ion	: Ionization
L	: Lorentz
l	: Lower level of a transition
M	: Heavy-particle
N	: Natural
R	: Rotational
r	: Resonance

Rad	: Radiation
s	: Species
S	: Stark
T	: Translational
Thm	: Thermal
u	: Upper level of a transition
V	: Vibrational
V	: Voigt
VW	: Van der Waals
v',v''	: Upper and lower vibrational levels

Greek characters

α	: Absorption coefficient (cm^{-1})
ϵ	: Emission coefficient ($\text{W}/\text{cm}^3/\text{sr}/\text{nm}$)
ϵ	: Electron energy (eV)
Λ	: Escape factor (-)
λ	: Wavelength (nm)
μ	: Reduced mass (kg)
Φ	: Line shape function (nm^{-1})
σ	: Cross-section (cm^2)
τ	: Relaxation time (s)
ν	: Photon frequency (Hz)
$\Delta\lambda$: Line shape FWHM (nm)
Ω	: Collision strength (-)

Acronyms

ATV	: Automated Transfer Vehicle
CFD	: Computational Fluid Dynamics
ESA	: European Space Agency
EXPERT	: European eXPERimental Reentry Testbed
FCP	: Franck-Condon Principle
FLPP	: Future Launch Preparatory Program
FWHM	: Full Width at Half Maximum
IXV	: Intermediate eXperimental Vehicle
IR	: Infrared
JAXA	: Japan eXploration Agency
NASA	: National Aeronautics and Space Administration
QSS	: Quasi Steady State
RTE	: Radiative Transport Equation
SRF	: Spatial Resolution Function
TRL	: Technology Readiness Level
VUV	: Vacuum UltraViolet
WRC	: Weighted Rate Coefficient

List of Figures

Chapter 1

Figure 1.1: Physico-chemical processes in the shock layer	20
Figure 1.2: Energy fluxes at the surface of the TPS material	21
Figure 1.3: Ground-testing strategy for reentry phenomena characterisation.....	22
Figure 1.4: Flight regimes encountered by the Orion spacecraft during Earth reentry.....	23
Figure 1.5: Relaxation phenomena in a nonequilibrium gas.....	24
Figure 1.6: Chemical conditions encountered by Orion spacecraft Earth reentry at hypervelocity	25
Figure 1.7: Thermodynamic conditions encountered by Orion spacecraft during Earth reentry at hypervelocity	25
Figure 1.8: Flow chart for the computation of the radiative heat flux	27

Chapter 2

Figure 2.1: Potential energies of N_2 and N_2^+	34
Figure 2.2: FWHM in equilibrium air plasma at a temperature of 11000 K and a pressure of 17000 Pa	39
Figure 2.3: Geometrical parameters used to define the spectral radiative heat flux	40

Chapter 3

Figure 3.1: NIST and grouped levels of a) N and b) O	49
Figure 3.2: Electronic partition functions computed with NIST and grouped levels for a) N and b) O	49
Figure 3.3: Experimental electron-impact cross-sections of N: a) $N(1 \rightarrow 2)$, b) $N(1 \rightarrow 4)$, c) $N(1 \rightarrow 5)$	58
Figure 3.4: Experimental electron-impact cross-sections of O: a) $O(1 \rightarrow 2)$, b) $O(1 \rightarrow 5)$, c) $O(1 \rightarrow 9)$, d) $O(1 \rightarrow 11)$	59
Figure 3.5: Experimental electron-impact cross-sections in N_2 : a) $X^1\Sigma_g^+-A^3\Sigma_u^+$, b) $X^1\Sigma_g^+-B^3\Pi_g$, c) $X^1\Sigma_g^+-C^3\Pi_u$, d) $X^1\Sigma_g^+-W^3\Delta_u$, e) $X^1\Sigma_g^+-W^3\Delta_u$, f) $X^1\Sigma_g^+-b^1\Pi_u$, g) $X^1\Sigma_g^+-b'^1\Sigma_u^+$, h) $X^1\Sigma_g^+-c'^4_1\Sigma_u^+$	61
Figure 3.6: Experimental electron-impact cross-sections in N_2^+ ($X^2\Sigma_g^+-B^2\Sigma_u^+$)	62
Figure 3.7: Comparison between the electron-impact excitation rate constants from Spence and Burrow (1980), Stone and Zipf (1973) and Yang and Doering (1996) and the theoretical rate constants from Drawin (1966), Park (1985) and Frost <i>et al.</i> (1998) in N. a) $K_c(1 \rightarrow 2)$, b) $K_c(1 \rightarrow 4)$, c) $K_c(1 \rightarrow 5)$	65
Figure 3.8: Comparison between the electron-impact excitation rate constants from Doering (1992), Kanic <i>et al.</i> (2001) and Johnson <i>et al.</i> (2003) and the theoretical rate constants from Drawin (1966), Park (1985) and Zatsarinny and Tayal (2003) in O. a) $K_c(1 \rightarrow 2)$, b) $K_c(1 \rightarrow 4)$, c) $K_c(1 \rightarrow 9)$, d) $K_c(1 \rightarrow 11)$	66
Figure 3.9: Comparison between the experimental rate constants from Majeed and Strickland (1997), Itikawa (2005), Johnson <i>et al.</i> (2005), Khakoo <i>et al.</i> (2006), Malone <i>et al.</i> (2011) and the rate constants from Teulet <i>et al.</i> (1999) and Larichiutta (2011). a: $N_2(X^1\Sigma_g^+-A^3\Sigma_u^+)$, b: $N_2(X^1\Sigma_g^+-B^3\Pi_g)$, c: $N_2(X^1\Sigma_g^+-B'^3\Sigma_u^-)$, d: $N_2(X^1\Sigma_g^+-C^3\Pi_u)$, e: $N_2(X^1\Sigma_g^+-W^3\Delta_u)$, f: $N_2(X^1\Sigma_g^+-b^1\Pi_u)$, g: $N_2(X^1\Sigma_g^+-b'^1\Sigma_u^+)$, h: $N_2(X^1\Sigma_g^+-c'^4_1\Sigma_u^+)$	67
Figure 3.10: Assessment of the Franck-Condon principle for N_2 VUV systems. a: $N_2(X^1\Sigma_g^+-b^1\Pi_u)$, b: $N_2(X^1\Sigma_g^+-c'^4_1\Sigma_u^+)$, c: $N_2(X^1\Sigma_g^+-b'^1\Sigma_u^+)$,	68
Figure 3.11: Comparison between the experimental rate constant from Crandall <i>et al.</i> (1974)	69
Figure 3.12: Heavy-particle impact excitation rate constants in N	75

Chapter 4

Figure 4.1: EAST facility	81
Figure 4.2: EAST facility optical design.....	82
Figure 4.3: Spectral intensities from the two calibration sources	84
Figure 4.4: Reproduction of flight freestream thermodynamic conditions in EAST facility	84
Figure 4.5: Slit functions for the VUV, visible, IR spectral ranges for shot 117 ($V_\infty=10.6$ km/s, $p_\infty=13.3$ Pa)	85
Figure 4.6: Slit functions for the VUV, visible, IR spectral ranges for shot 119 ($V_\infty=11.17$ km/s, $p_\infty=13.3$ Pa) ..	85
Figure 4.7: Spatial smearing functions for the VUV, visible, IR spectral ranges for shot 116 ($V_\infty=10.54$ km/s, $p_\infty=13.3$ Pa)	86
Figure 4.8: Spatial smearing functions for the VUV, visible, IR spectral ranges for shot 119 ($V_\infty=11.17$ km/s, $p_\infty=13.3$ Pa).....	86
Figure 4.9: Spatial smearing of the intensity emitted by the shock-tube	86
Figure 4.10: Temperatures and species number density profiles predicted by Poshax for shot 117 ($V_\infty=10.6$ km/s, $p_\infty=13.3$ Pa).....	87
Figure 4.11: Temperatures and species number density profiles predicted by Poshax for shot 119 ($V_\infty=11.17$ km/s, $p_\infty=13.3$ Pa)	87

Figure 4.12: Analysis of the CCD image for shot 116 ($V_\infty=10.54$ km/s, $p_\infty=13.3$ Pa) in the VUV	89
Figure 4.13: Analysis of the CCD image for shot 117 ($V_\infty=10.6$ km/s, $p_\infty=13.3$ Pa) in the visible	90
Figure 4.14: Analysis of the CCD image for shot 117 ($V_\infty=10.6$ km/s, $p_\infty=13.3$ Pa) in the IR	91
Figure 4.15: Analysis of the CCD image for shot 119 ($V_\infty=11.17$ km/s, $p_\infty=13.3$ Pa) in the VUV	92
Figure 4.16: Analysis of the CCD image for shot 119 ($V_\infty=11.17$ km/s, $p_\infty=13.3$ Pa) in the visible	93
Figure 4.17: Analysis of the CCD image for shot 119 ($V_\infty=11.17$ km/s, $p_\infty=13.3$ Pa) in the IR	94
Figure 4.18: Spectra of N_2 and N_2^+ systems for shot 116 ($V_\infty=10.54$ km/s, $p_\infty=13.3$ Pa) at a) $x= 0.75$ cm and b) $x= 1$ cm	96
Figure 4.19: Experimental post-shock evolution of the vibrational and rotational temperatures for shot 116 ($V_\infty=10.54$ km/s, $p_\infty=13.3$ Pa)	96
Figure 4.20: Comparison between experimental and simulated temperature evolution for shot 116 ($V_\infty=10.54$ km/s, $p_\infty=13.3$ Pa)	97
Figure 4.21: FWHM post-shock evolution	98
Figure 4.22: H_α profile fits at several locations for shot 116 ($V_\infty=10.54$ km/s, $p_\infty=13.3$ Pa)	98
Figure 4.23: Electron number density profile inferred from Stark-broadened H_α line for shot 116 ($V_\infty=10.54$ km/s, $p_\infty=13.3$ Pa)	99
Figure 4.24: $N(410)$ profile fits at several locations for shot 119 ($V_\infty=11.17$ km/s, $p_\infty=13.3$ Pa)	99
Figure 4.25: Electron number density profile inferred from Stark-broadened $N(411)$ line for shot 119 ($V_\infty=11.17$ km/s, $p_\infty=13.3$ Pa)	100
Figure 4.26: Comparison between experimental and predicted electron number densities for shot 116 ($V_\infty=10.54$ km/s, $p_\infty=13.3$ Pa)	100
Figure 4.27: Comparison between experimental and predicted electron number densities for shot 119 ($V_\infty=11.17$ km/s, $p_\infty=13.3$ Pa)	101

Chapter 5

Figure 5.1: Comparison between experimental and simulated post-shock intensity profiles for shot 117 ($V_\infty=10.6$ km/s, $p_\infty=13.3$ Pa) in the visible ($\Delta\lambda=409-411$ nm), electron-impact processes only	104
Figure 5.2: Comparison between experimental and simulated post-shock intensity profiles for shot 119 ($V_\infty=11.17$ km/s, $p_\infty=13.3$ Pa) in the visible ($\Delta\lambda=409-411$ nm), electron-impact processes only	104
Figure 5.3: Comparison between experimental and simulated post-shock intensity profiles for shot 117 ($V_\infty=10.6$ km/s, $p_\infty=13.3$ Pa) in the IR ($\Delta\lambda=852-872$ nm), electron-impact processes only	104
Figure 5.4: Comparison between experimental and simulated post-shock intensity profiles for shot 119 ($V_\infty=11.17$ km/s, $p_\infty=13.3$ Pa) in the IR ($\Delta\lambda=852-872$ nm), electron-impact processes only	105
Figure 5.5: Comparison between experimental and simulated post-shock intensity profiles for shot 116 ($V_\infty=10.54$ km/s, $p_\infty=13.3$ Pa) in the VUV ($\Delta\lambda=140-176$ nm), electron-impact processes only	105
Figure 5.6: Comparison between experimental and simulated post-shock intensity profiles for shot 119 ($V_\infty=11.17$ km/s, $p_\infty=13.3$ Pa) in the VUV ($\Delta\lambda=175-176$ nm), electron-impact processes only	105
Figure 5.7: Sensitivity of the temperatures and species number density profiles to the dissociation rate constant model for shot 117 ($V_\infty=10.6$ km/s, $p_\infty=13.3$ Pa)	106
Figure 5.8: Sensitivity of of the temperatures and species number density profiles dissociation rate constant model for shot 119 ($V_\infty=11.17$ km/s, $p_\infty=13.3$ Pa)	106
Figure 5.9: Sensitivity of the post-shock intensity profile to the dissociation rate constant model for shot 116 ($V_\infty=10.54$ km/s, $p_\infty=13.3$ Pa) in the VUV ($\Delta\lambda=140-176$ nm)	107
Figure 5.10: Sensitivity of the post-shock intensity profile to the dissociation rate constant model for shot 119 ($V_\infty=11.17$ km/s, $p_\infty=13.3$ Pa) in the VUV ($\Delta\lambda=175-176$ nm)	107
Figure 5.11: Sensitivity of the post-shock intensity profile to the dissociation rate constant model for shot 117 ($V_\infty=10.6$ km/s, $p_\infty=13.3$ Pa) in the IR ($\Delta\lambda=852-872$ nm)	108
Figure 5.12: Sensitivity of the post-shock intensity profile to the dissociation rate constant model for shot 119 ($V_\infty=11.17$ km/s, $p_\infty=13.3$ Pa) in the IR ($\Delta\lambda=852-872$ nm)	108
Figure 5.13: Sensitivity of the temperatures and species number density profiles to the dissociation-vibration coupling model for shot 117 ($V_\infty=10.6$ km/s, $p_\infty=13.3$ Pa)	109
Figure 5.14: Sensitivity of the temperatures and species number density profiles to the dissociation-vibration coupling model for shot 119 ($V_\infty=11.17$ km/s, $p_\infty=13.3$ Pa)	109
Figure 5.15: Sensitivity of the post-shock intensity to the dissociation-vibration coupling model for shot 116 ($V_\infty=10.54$ km/s, $p_\infty=13.3$ Pa) in the VUV ($\Delta\lambda=140-176$ nm)	110
Figure 5.16: Sensitivity of the post-shock intensity to the dissociation-vibration coupling model for shot 119 ($V_\infty=11.17$ km/s, $p_\infty=13.3$ Pa) in the VUV ($\Delta\lambda=175-176$ nm)	110
Figure 5.17: Sensitivity of the post-shock intensity to the dissociation-vibration coupling model for shot 117 ($V_\infty=10.6$ km/s, $p_\infty=13.3$ Pa) in the IR ($\Delta\lambda=852-872$ nm)	110

Figure 5.18: Sensitivity of the post-shock intensity to the dissociation-vibration coupling model for shot 119 ($V_\infty=11.17$ km/s, $p_\infty=13.3$ Pa) in the IR ($\Delta\lambda=852-872$ nm).....	111
Figure 5.19: Prediction of the intensity profiles for shot 116 ($V_\infty=10.54$ km/s, $p_\infty=13.3$ Pa) with the baseline heavy-particle impact excitation rate constants of Park (1985)	112
Figure 5.20: Comparison between experimental and simulated post-shock intensity profiles for shot 117 ($V_\infty=10.6$ km/s, $p_\infty=13.3$ Pa) in the visible ($\Delta\lambda=409-411$ nm), electron and heavy-particle impact processes	113
Figure 5.21: Comparison between experimental and simulated post-shock intensity profiles for shot 119 ($V_\infty=11.17$ km/s, $p_\infty=13.3$ Pa) in the visible ($\Delta\lambda=409-411$ nm), electron and heavy-particle impact processes.....	113
Figure 5.22: Comparison between experimental and simulated post-shock intensity profiles for shot 117 ($V_\infty=10.6$ km/s, $p_\infty=13.3$ Pa) in the IR ($\Delta\lambda=852-872$ nm), electron and heavy-particle impact processes	113
Figure 5.23: Comparison between experimental and simulated post-shock intensity profiles for shot 119 ($V_\infty=11.17$ km/s, $p_\infty=13.3$ Pa) in the IR ($\Delta\lambda=852-872$ nm), electron and heavy-particle impact processes	114
Figure 5.24: Comparison between experimental and simulated post-shock intensity profiles for shot 116 ($V_\infty=10.54$ km/s, $p_\infty=13.3$ Pa) in the VUV ($\Delta\lambda=140-176$ nm), electron and heavy-particle impact processes	114
Figure 5.25: Comparison between experimental and simulated post-shock intensity profiles for shot 119 ($V_\infty=11.17$ km/s, $p_\infty=13.3$ Pa) in the VUV ($\Delta\lambda=175-176$ nm), electron and heavy-particle impact processes	114
Figure 5.26: Comparison between experimental and simulated post-shock intensity profiles with the CR and Boltzmann models for shot 117 ($V_\infty=10.6$ km/s, $p_\infty=13.3$ Pa) in the visible ($\Delta\lambda=409-411$ nm).....	115
Figure 5.27: Comparison between experimental and simulated post-shock intensity profiles with the CR and Boltzmann models for shot 119 ($V_\infty=11.17$ km/s, $p_\infty=13.3$ Pa) in the visible ($\Delta\lambda=409-411$ nm).....	115
Figure 5.28: Comparison between experimental and simulated post-shock intensity profiles with the CR and Boltzmann models for shot 117 ($V_\infty=10.6$ km/s, $p_\infty=13.3$ Pa) in the IR ($\Delta\lambda=852-872$ nm)	116
Figure 5.29: Comparison between experimental and simulated post-shock intensity profiles with the CR and Boltzmann models for shot 119 ($V_\infty=11.17$ km/s, $p_\infty=13.3$ Pa) in the IR ($\Delta\lambda=852-872$ nm)	116
Figure 5.30: Comparison between experimental and simulated post-shock intensity profiles with the CR and Boltzmann models for shot 116 ($V_\infty=10.54$ km/s, $p_\infty=13.3$ Pa) in the VUV ($\Delta\lambda=140-176$ nm).....	117
Figure 5.31: Comparison between experimental and simulated post-shock intensity profiles with the CR and Boltzmann models for shot 119 ($V_\infty=11.17$ km/s, $p_\infty=13.3$ Pa) in the VUV ($\Delta\lambda=175-176$ nm).....	117
Figure 5.32: Comparison between the experimental and simulated spectra in the visible for shot 117 ($V_\infty=10.6$ km/s, $p_\infty=13.3$ Pa) at a) $x= 1$ cm and b) $x =2.5$ cm.....	118
Figure 5.33: Comparison between the experimental and simulated spectra in the visible for shot 119 ($V_\infty=11.17$ km/s, $p_\infty=13.3$ Pa) at a) $x= 1$ cm and b) $x =2.5$ cm.....	118
Figure 5.34: Comparison between the experimental and simulated spectra in the IR for shot 117 ($V_\infty=10.6$ km/s, $p_\infty=13.3$ Pa).....	119
Figure 5.35: Comparison between the experimental and simulated spectra in the IR for shot 119 ($V_\infty=11.17$ km/s, $p_\infty=13.3$ Pa).....	119
Figure 5.36: Comparison between the experimental and simulated spectra in the VUV for shot 116 ($V_\infty=10.54$ km/s, $p_\infty=13.3$ Pa) at a) $x= 1$ cm and b) $x =2.5$ cm.....	119
Figure 5.37: Comparison between the experimental and simulated spectra in the VUV for shot 119 ($V_\infty=11.17$ km/s, $p_\infty=13.3$ Pa) at a) $x= 1$ cm and b) $x =2.5$ cm.....	120
Figure 5.38: Line center absorption coefficient in the VUV (a), visible (b) and IR (c) ranges computed at T_{Ve} for shot 117 ($V_\infty=10.6$ km/s, $p_\infty=13.3$ Pa).....	123
Figure 5.39: Line center absorption coefficient in the VUV (a), visible (b) and IR (c) ranges computed at T_{Ve} for shot 119 ($V_\infty=11.17$ km/s, $p_\infty=13.3$ Pa).....	123
Figure 5.40: Fit of the experimental spectra for shot 117 ($V_\infty=10.6$ km/s, $p_\infty=13.3$ Pa) at a) $x= 1$ cm and b) $x= 2.5$ cm in the visible.....	124
Figure 5.41: Fit of the experimental spectra for shot 119 ($V_\infty=11.17$ km/s, $p_\infty=13.3$ Pa) at a) $x= 1$ cm and b) $x= 2.5$ cm in the visible.....	124
Figure 5.42: Fit of the experimental spectra for shot 117 ($V_\infty=10.6$ km/s, $p_\infty=13.3$ Pa) at a) $x= 1$ cm and b) $x= 2.5$ cm in the IR	125
Figure 5.43: Fit of the experimental spectra for shot 119 ($V_\infty=11.17$ km/s, $p_\infty=13.3$ Pa) at a) $x= 1$ cm and b) $x= 2.5$ cm in the IR	125
Figure 5.44: Fit of the experimental spectra for shot 116 ($V_\infty=10.54$ km/s, $p_\infty=13.3$ Pa) at a) $x= 1$ cm and b) $x= 2.5$ cm in the VUV.....	125

Figure 5.45: Fit of the experimental spectra for shot 119 ($V_\infty=11.17$ km/s, $p_\infty=13.3$ Pa) at a) $x= 1$ cm and b) $x= 2.5$ cm in the VUV.....	126
Figure 5.46: Experimental distribution of the excited states in N for shot 117 ($V_\infty=10.6$ km/s, $p_\infty=13.3$ Pa)....	126
Figure 5.47: Post-shock experimental evolution of the 2 nd , 3 rd , 5 th , 7 th , 15 th grouped level of nitrogen for shot 117 ($V_\infty=10.6$ km/s, $p_\infty=13.3$ Pa).....	127
Figure 5.48: Experimental distribution of the excited states in N for shot 119 ($V_\infty=11.17$ km/s, $p_\infty=13.3$ Pa)...	128
Figure 5.49: Post-shock experimental evolution of the 3 rd , 5 th , 7 th , 15 th grouped level of nitrogen for shot 119 ($V_\infty=11.17$ km/s, $p_\infty=13.3$ Pa).....	128
Figure 5.50: Comparison of the post-shock evolution of the 15 th grouped level of N inferred from experiment with the predictions of the Boltzmann and CR models for shot 117 ($V_\infty=10.6$ km/s, $p_\infty=13.3$ Pa) and shot 119 ($V_\infty=11.17$ km/s, $p_\infty=13.3$ Pa).....	129
Figure 5.51: Comparison of the post-shock evolution of the 7 th grouped level of N inferred from experiment with the predictions of the Boltzmann and CR models for shot 117 ($V_\infty=10.6$ km/s, $p_\infty=13.3$ Pa) and shot 119 ($V_\infty=11.17$ km/s, $p_\infty=13.3$ Pa).....	130
Figure 5.52: Comparison of the post-shock evolution of the 5 th grouped level of N inferred from experiment with the predictions of the Boltzmann and CR models for shot 117 ($V_\infty=10.6$ km/s, $p_\infty=13.3$ Pa) and shot 119 ($V_\infty=11.17$ km/s, $p_\infty=13.3$ Pa).....	130
Figure 5.53: Comparison of the post-shock evolution of the 3 rd grouped level of N inferred from experiment with the predictions of the Boltzmann and CR models for shot 117 ($V_\infty=10.6$ km/s, $p_\infty=13.3$ Pa) and shot 119 ($V_\infty=11.17$ km/s, $p_\infty=13.3$ Pa).....	130

Appendix D

Figure D.1: Simulated post-shock intensity profile for shot 116 ($V_\infty=10.54$ km/s, $p_\infty=13.3$ Pa) in the VUV ($\Delta\lambda=140-176$ nm) with shock motion and total spatial smearing.....	150
Figure D.2: Simulated post-shock intensity profile for shot 117 ($V_\infty=10.6$ km/s, $p_\infty=13.3$ Pa) in the IR ($\Delta\lambda=852-872$ nm) with shock motion and total spatial smearing.....	150
Figure D.3: Simulated post-shock intensity profile for shot 119 ($V_\infty=11.17$ km/s, $p_\infty=13.3$ Pa) in the VUV ($\Delta\lambda=175-176$ nm) with shock motion and total spatial smearing.....	151
Figure D.4: Simulated post-shock intensity profile for shot 119 ($V_\infty=11.17$ km/s, $p_\infty=13.3$ Pa) in the IR ($\Delta\lambda=852-872$ nm), electron and heavy-particle impact processes.....	151

List of Tables

Chapter 2

Table 2.1: Stark width expression for nitrogen and hydrogen lines	38
---	----

Chapter 3

Table 3.1: Vibrational levels of N_2 and N_2^+ electronic states considered by Pierrot <i>et al.</i> (1999).....	47
Table 3.2: Grouped nitrogen and oxygen levels	48
Table 3.3: Vibrational levels of N_2 and N_2^+ electronic states considered in the present work	50
Table 3.4: Experimental cross-sections for electron-impact of N atom.....	58
Table 3.5: Experimental cross-sections for electron-impact of O atom.....	59
Table 3.6: Experimental cross-sections for electron-impact of N_2	60
Table 3.7: Experimental cross-sections for electron-impact of N_2^+	60
Table 3.8: Selected electron-impact excitation rate constants in N	65
Table 3.9: Selected electron-impact excitation rate constants in O	66
Table 3.10: Selected electron-impact excitation vibrational rate constants in N_2	70
Table 3.11: Selected electron-impact excitation vibrational rate constants in N_2^+	70
Table 3.12: Selected electron-impact ionization rate constants in N	71
Table 3.13: Selected electron-impact ionization rate constants in O	72
Table 3.14: Selected electron-impact ionization rate constants in N_2	72
Table 3.15: Selected heavy-particle impact excitation rate constants in N (M=N, O)	75
Table 3.16: Selected heavy-particle impact excitation rate constants in O (M=N, O)	75
Table 3.17: Comparison of the rate constants selected in the present CR model and in the CR models developed by Park (1985), Johnston (2006) and Panesi <i>et al.</i> (2011)	77

Chapter 4

Table 4.1: EAST spectrometers specifications	83
Table 4.2: Selected shock-tube freestream conditions and spectral ranges	84
Table 4.3: Spectral and spatial resolution	85
Table 4.4: Excited states inferred from selected shots.....	95
Table 4.5: Vibrational and rotational temperatures of $N_2(C)$ and $N_2^+(B)$	96
Table 4.6: Atomic lines considered for the determination of the electron number density	97

Chapter 5

Table 5.1: Observed nitrogen lines	121
Table 5.2: Optical thicknesses of the observed nitrogen lines	122

Appendix B

Table B.1: NIST and grouped levels of N.....	144
Table B.2: NIST and grouped levels of O.....	146

Appendix C

Table C.1: Strongest nitrogen lines in the VUV	148
Table C.2: Nitrogen lines in the visible	148
Table C.3: Strongest nitrogen lines in the IR.....	149
Table C.4: Strongest oxygen lines	149

Chapter I

Introduction

Overview

This chapter introduces the reader to the state-of-the art of the modeling of nonequilibrium radiating shock layers. In section 1, we review the past and future reentry missions on Earth. We briefly describe, at the macroscopic level, the physico-chemical phenomena occurring in the shock layer leading to the radiative heating encountered by the spacecraft. We present the ground-test strategy used to validate the physico-chemical models and to ensure a precise extrapolation to flight experiments. In section 2, we present the flight, chemical and thermodynamic regimes encountered by the spacecraft during a typical hypervelocity reentry. In section 3, we present the strategy retained to model the nonequilibrium radiation. Finally, in section 4, we present the objectives of the present work as well as the organization of the thesis.

Table of Contents

I.1. Motivation	20
I.1.1. Past and future reentry missions.....	20
I.1.2. Phenomenology of reentry flows.....	20
I.1.3. Ground-testing strategy.....	21
I.2. Background	22
I.2.1. Flight regimes.....	22
I.2.2. Thermochemical regimes.....	24
I.3. Computation of nonequilibrium radiation	26
I.3.1. Multi-temperature models.....	26
I.3.2. State-to-state models.....	26
I.3.3. Methodology.....	26
I.4. Scope and organization of the thesis	27

I.1. Motivation

I.1.1. Past and future reentry missions

Over the last decades, space missions for exploration and defense purposes have triggered intensive programs to design spacecraft entering into Earth's atmosphere at hypervelocity (Park, 1985; Smart *et al.*, 1990; Hirshel, 2004; Erbland, 2005; Wright *et al.*, 2006; Tran *et al.*, 2007). Recently, there have been successful reentry missions such as the small probe Hayabusa, which was designed by JAXA and landed in Australia in June 2011, or the Dragon probe, built by SpaceX, which landed in the USA in March 2012. The next decades will also witness reentry missions for exploration purposes. For instance, within its FLPP program, ESA proposes the flight experiments IXV (Tumino *et al.*, 2007) and EXPERT (Muylaert, 2007) to characterize the environment with embedded spectrometers. Within its Aurora program, ESA proposes as well the Mars sample return and Marco-Polo missions to bring back to Earth samples from Mars' ground and from an asteroid, respectively. ESA plans to upgrade the current ATV into a supplying cargo returning to Earth. Finally, NASA delegated the design and manufacturing of the crew transportation vehicle Orion to Lockheed Martin.

I.1.2. Phenomenology of reentry flows

Atmospheric reentry occurs at hypervelocity in the upper layers of the atmosphere. The mission success relies on the braking phase of the spacecraft. For cost and mass saving reasons, the braking phase is achieved by crossing the atmosphere layers (aerobraking). This phase is critical since the spacecraft encounters a severe environment, leading to a tremendous level of heating. To preserve the spacecraft payload and crew integrity, an adequate thermal protection system (TPS) must be designed. The design of this system relies on an accurate prediction of the thermal load experienced by the heat shield.

During hypersonic reentry, a strong bow shock is created in front of the spacecraft. The volume between the shock front and the spacecraft wall is called the shock layer. When crossing the shock, the flow is compressed and slowed down over a distance of the order of the mean free-path. Hence, its temperature drastically increases, leading to physico-chemical processes such as dissociation, ionization, excitation and radiation of the molecules and atoms (Zel'dovich and Raizer, 2002; Anderson, 2006), as depicted in figure 1.1.

As illustrated in figure 1.2 (Wright *et al.*, 2006), the shock layer flow transfers heat to the heatshield by convection, radiation and surface recombination processes. Part of this heat flux is sent back to the flow by surface radiation (labeled q_{rerad}) and ablative processes (labeled q_{mdot}), thus reducing the heat load on the TPS.

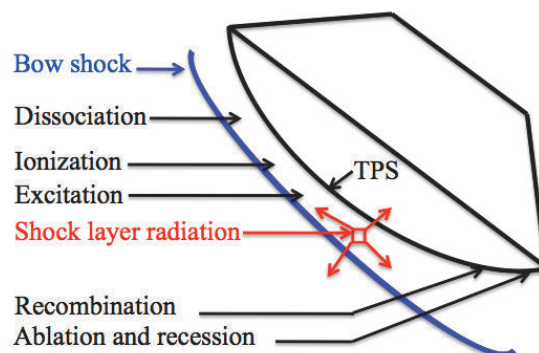


Figure 1.1: Physico-chemical processes in the shock layer (Zel'dovich and Raizer, 2002)

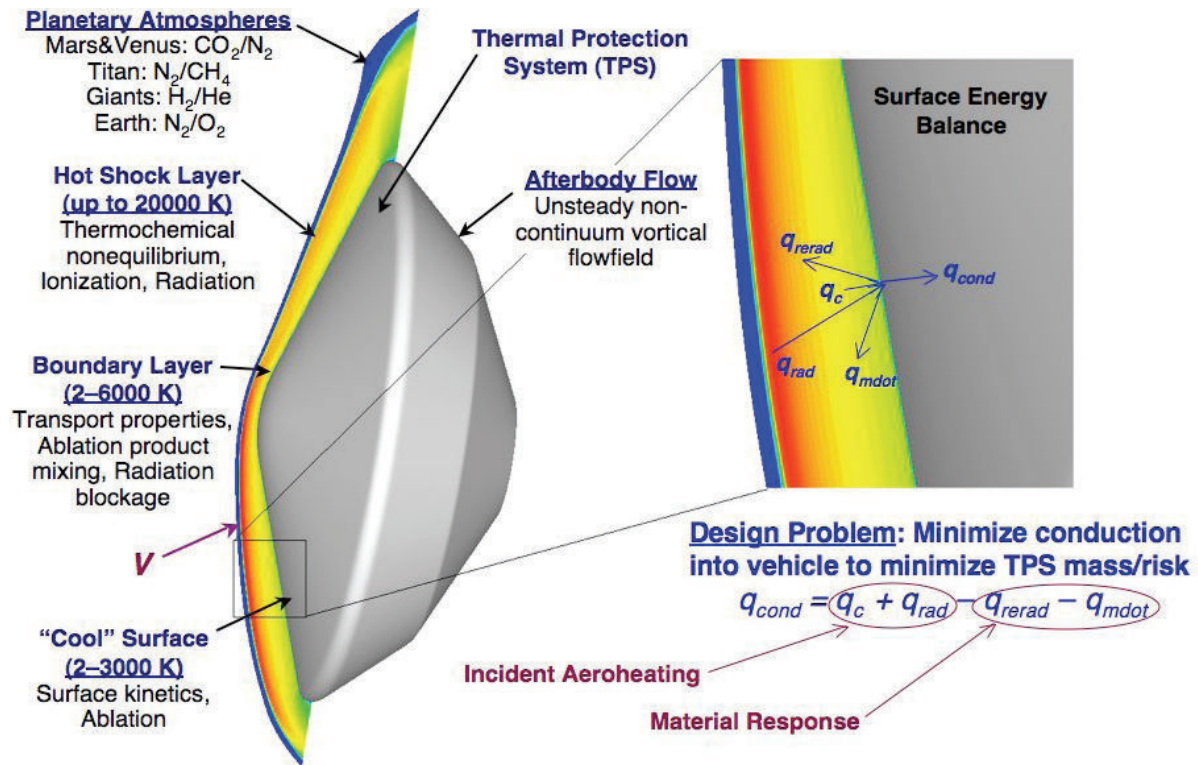


Figure 1.2: Energy fluxes at the surface of the TPS material (Wright *et al.*, 2006)

The “mission killers” that must be mastered for the success of the mission are the following:

- Shock layer radiation
- Surface phenomena such as recombination of species at the surface, surface catalicity and ablation
- Transition to turbulence

I.1.3. Ground-testing strategy

The determination of the radiation emitted by the shock layer during reentry relies on a combined approach based on ground experiments and numerical simulations. Ground-test facilities include shock-tubes or tunnels, plasma wind tunnels or arcjets and plasma torches. In shock-tubes or tunnels, a shock wave is created within a tube, and then heats up the test gas leading to the emission of radiation from which the degree of nonequilibrium in the plasma flow can be inferred and compared with numerical simulations. Within shock-tube facilities, various operating modes are available such as reflected and non-reflected modes. Unlike the reflected operating mode that induces pre-shock change to the gas, the non-reflected operating mode is the only one that can produce the real flow conditions immediately behind the shock in the same way as in flight and therefore is suitable for the present work. In plasma wind tunnels or arcjets, a sample of the thermal protection system is exposed to a plasma flow. The surface temperature is measured by thermocouples or pyrometers and can be compared to the prediction of the simulations. Finally, plasma torches provide hot and stationary plasma flows whose radiation analysis complements the measurements performed in the previous facilities. Figure 1.3 shows the physico-chemical processes occurring during flight that can be simulated in ground-test facilities. For instance, the bow shock created in front of the spacecraft can be reproduced in shock-tube or ballistic facilities, and thus these facilities enable the assessment of the nonequilibrium models used in the numerical simulations. As another example, the complex phenomena occurring at the surface of the vehicle can be

reproduced in plasma wind tunnels or arcjets, thus enabling the assessment of catalicity and ablation models. The reader is referred to the works of Fournier *et al.* (2011) and Louzet *et al.* (2011) for an extensive review of the ground-test facilities currently in operation worldwide and of the diagnostics associated with these facilities.

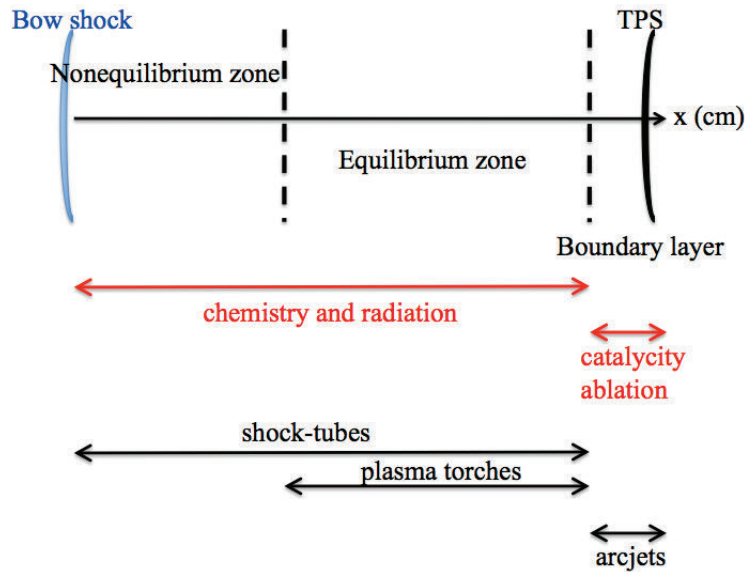


Figure 1.3: Ground-testing strategy for reentry phenomena characterisation

The work presented in this dissertation addresses the computation of shock layer radiation, which is a significant, if not dominant mechanism of heating as discussed by Anderson (2006) and Zel'dovich and Raizer (2002) in atmospheric reentry at hypervelocity (8-15 km/s). When the gas crosses the shock, its temperature and pressure drastically increase. Behind the shock, the flow relaxes towards equilibrium. As discussed in subsection I.2.2, if the time needed to reach equilibrium is greater than the residence time, the flow is in a nonequilibrium state. The length of the nonequilibrium zone increases with increasing speed and decreasing pressure and can represent up to 30% of the shock layer (Park, 1993; Johnston, 2006; Hash *et al.*, 2007)¹. Large uncertainties remain for radiative heating prediction under nonequilibrium conditions, because radiation is proportional to molecular and atomic emitting state populations, which are highly influenced by the thermodynamic state of the gas. These uncertainties drive engineers to apply significant design margins, which increase the launching costs and limit the technological value of the mission by reducing the payload weight. Therefore, the prediction of nonequilibrium radiation emitted behind the shock as well as its experimental validation remain state-of-the-art challenges for the aerospace community and led to the present work.

I.2. Background

I.2.1. Flight regimes

The flow regime surrounding a spacecraft depends on its speed, altitude, and geometry and on the atmosphere composition. Three dimensionless numbers are used to characterize the flow, namely the Knudsen, Mach and Reynolds numbers.

¹ Strong nonequilibrium processes such as atoms and ions recombination also occur in the boundary layer of the spacecraft (Armenise *et al.*, 1999; Armenise and Capitelli, 2005; Capitelli *et al.*, 2006).

The Mach number, M , characterizes the speed regime and is defined as the ratio between the local flow speed and the local speed of sound. Four regimes are distinguished:

- the subsonic regime ($M < 0.8$), for which the flow is weakly compressible
- the transonic regime ($0.8 < M < 1.2$), which is a transition zone
- the supersonic regime ($1.2 < M < 5$), in which a shock wave is created in front of the spacecraft
- the hypersonic regime ($M > 5$) where new physical phenomena become important. Of particular relevance to this study is the onset of thermo-chemical processes and the role of radiation.

The Knudsen number, Kn , characterizes the rarefaction of the flow regime and is defined by the ratio between the mean free path and a characteristic length of the flow (shock stand-off distance) or spacecraft (curvature radius, diameter). Three regimes can be distinguished:

- the continuum regime ($Kn < 10^{-2}$), for which pressure and density are high enough to define characteristic macroscopic flow quantities. The flow evolution is then governed by the Navier-Stokes equations
- the intermediate regime ($10^{-2} < Kn < 10^{-1}$), which requires slip conditions at the spacecraft's surface in addition to the Navier-Stokes equations.
- the transition regime ($10^{-1} < Kn < 10$)
- the free molecular flow regime ($Kn > 10$) where the pressure and the density are low. In this case, the Boltzmann equation is solved to obtain the flow solution. This regime is encountered in the upper layers of the atmosphere.

The Reynolds number, Re , characterizes the flow dynamics and is defined by the ratio of the inertia forces to the viscous forces.

Figure 1.4 illustrates the different regimes encountered by a spacecraft, such as the crew transportation vehicle Orion (Grinstead *et al.*, 2008) during its entry into Earth's atmosphere (Anderson, 2006). The maximum deceleration of the spacecraft, hence the peak heat flux, occurs in the hypersonic, continuum and laminar regime. The work presented in this thesis corresponds to these regimes.

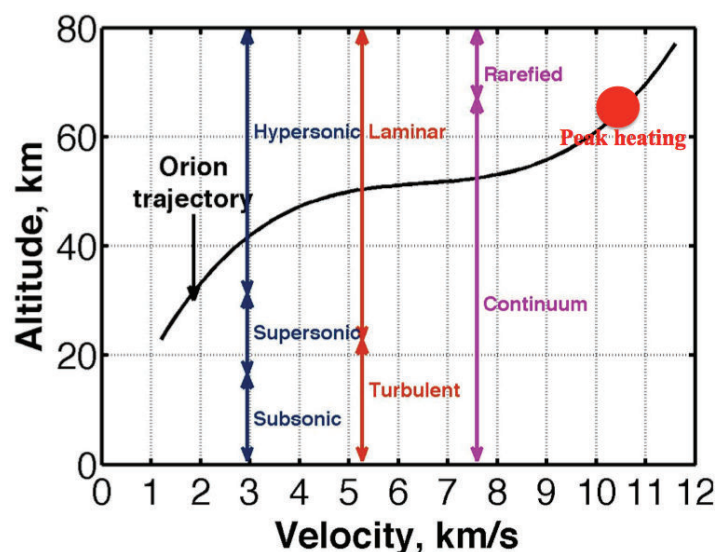


Figure 1.4: Flight regimes encountered by the Orion spacecraft during Earth reentry (Anderson, 2006)

I.2.2. Thermochemical regimes

Within the shock layer, collisions between particles lead to the excitation of internal degrees of freedom, which are the translational, rotational, vibrational and electronic. Three types of collisions can be distinguished (Zel'dovich and Raizer, 2002; Anderson, 2006):

- elastic collisions,
- inelastic non reactive collisions
- inelastic reactive collisions

Elastic collisions exchange translational energy. These collisions tend to bring the medium to translational equilibrium (T-T exchange). This phenomenon is called translational relaxation. In inelastic non-reactive collisions, species exchange energy between their internal energy modes. Many exchanges are possible, as sketched in Figure 1.5: vibration-translation (V-T), vibration-vibration (V-V), vibration-electronic (V-Elec), rotation-translation (R-T), etc. These phenomena tend to bring the medium to equilibrium via vibrational, rotational or electronic relaxation. Inelastic but reactive collisions lead to chemical reactions such as dissociation, ionization or charge exchange and are affected by the internal distribution of the gas.

The aforementioned processes are characterized by relaxation times such as τ_{VT} or τ_{VV} , for relaxation processes and τ_{Chm} for chemical reactions. Depending on these characteristic times relative to the time that a particle spends in the shock layer, referred to as τ_{flow} , several thermodynamic situations are encountered (Vincenti and Kruger, 1965; Mitchner and Kruger, 1972). First, let us consider chemical reactions.

- $\tau_{Chm} \ll \tau_{flow}$: chemical processes are faster than flow motion. Local chemical equilibrium is reached
- $\tau_{Chm} \gg \tau_{flow}$: chemical processes are slower than flow motion. The chemical state of the medium does not evolve. The medium is considered as chemically frozen
- $\tau_{Chm} \approx \tau_{flow}$: the medium is in chemical nonequilibrium.

Second, let us consider the thermal relaxation, denoted “Thm”:

- $\tau_{Thm} \ll \tau_{flow}$: relaxation processes are faster than flow motion. Local thermal equilibrium is reached
- $\tau_{Thm} \gg \tau_{flow}$: relaxation processes are slower than flow motion. The thermal state of the medium does not evolve. The medium is considered as thermally frozen
- $\tau_{Thm} \approx \tau_{flow}$: the medium is in thermal nonequilibrium.

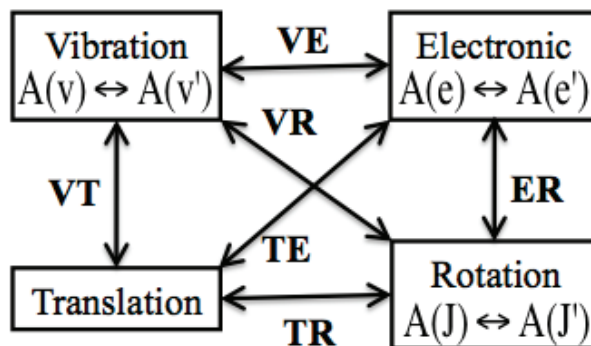


Figure 1.5: Relaxation phenomena in a nonequilibrium gas (adapted from Vincenti and Kruger, 1963)

Thermochemical nonequilibrium occurs in the shock layer region when the collision frequency is low. Thus, nonequilibrium conditions will prevail in the upper layers of the

atmosphere where the speed is high ($V > 10$ km/s) and the pressure low, and in a portion of the shock layer just behind the shock wave.

Figures 1.6 and 1.7 depict the various chemical and thermal conditions encountered by a spacecraft during its entry into Earth's atmosphere (Anderson, 2006). The Orion trajectory (Grinstead *et al.*, 2008) is again plotted. At peak heating ($h=60$ km, $V=10$ km/s), the shock layer is in chemical and thermal nonequilibrium. Therefore, accurate modeling of thermochemical nonequilibrium is required to optimize the TPS design.

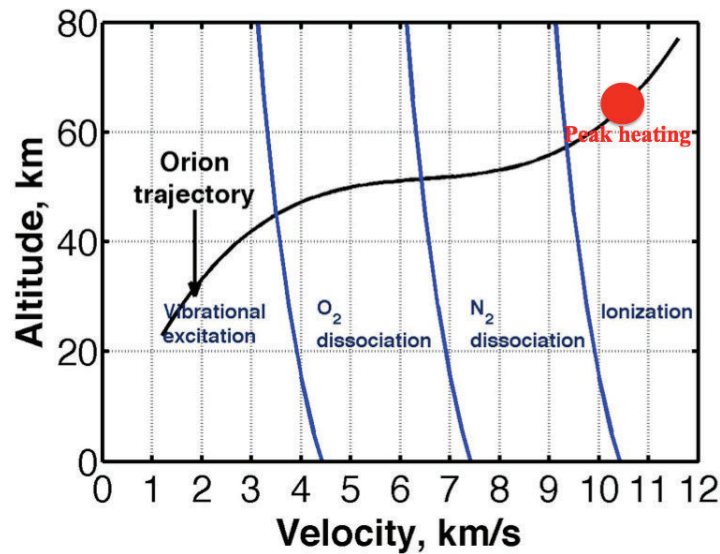


Figure 1.6: Chemical conditions encountered by Orion spacecraft during Earth reentry at hypervelocity (Anderson, 2006)

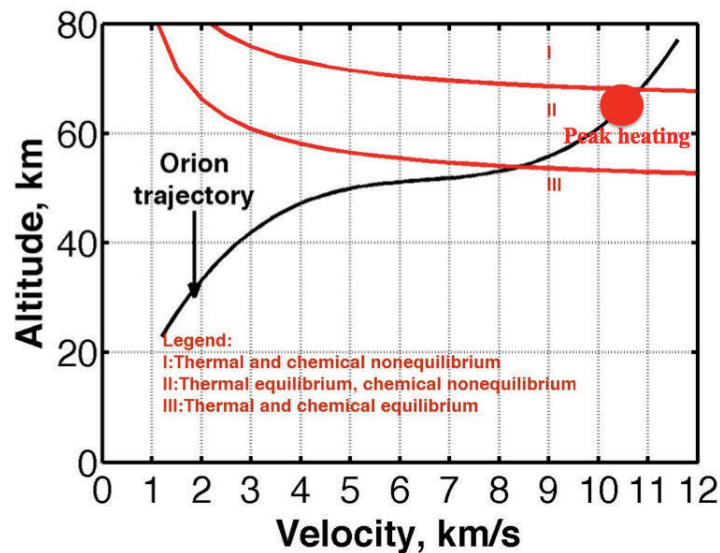


Figure 1.7: Thermodynamic conditions encountered by Orion spacecraft during Earth reentry at hypervelocity (Anderson, 2006)

I.3. Computation of nonequilibrium radiation

The estimation of the radiative heat flux on a spacecraft during its entry into Earth's atmosphere requires the determination of the populations of the excited atomic and molecular states, which are highly dependent of the thermodynamic conditions. The thermodynamic state of the gas, i.e., the concentrations of the species and the populations of the emitting states can be determined by various approaches: multi-temperature or state-to-state models.

I.3.1. Multi-temperature models

In these models, it is assumed that the population of each internal energy mode (translational, rotational, vibrational and electronic) follows a Boltzmann distribution at the characteristic temperature of the mode. To calculate these temperatures and the energy exchanged between energy modes, conservation equations for internal energy modes are added to the classical set of conservation equations for mass, momentum and total energy. Multi-temperature models are relatively easy to implement in multidimensional flow codes and have been used extensively in the literature. The reader is referred to the dissertations of Soubrié (2006) and William (2000) for a comprehensive review of multi-temperature models.

I.3.2. State-to-state models

When the gas strongly departs from equilibrium conditions, the multi-temperature approach may not be sufficient anymore because the internal energy state populations may depart from Boltzmann distributions. State-to-state models, also called collisional-radiative (CR) models, are then required. In this approach, the internal states are considered individually and their populations are determined by considering collisional and radiative processes. By increasing order of complexity and computational time, three kinds of CR models can be distinguished for air: electronic, vibronic and rovibronic state-to-state models. In electronic state-to-state models, transitions between the electronic states are considered and the vibrational and rotational levels of the molecules are assumed to be populated according to Boltzmann distributions at the vibrational and the rotational temperatures, respectively. In vibronic state-to-state models, transitions between the vibronic states of the molecules are considered and only a rotational temperature is defined. Because these models are much more computationally expensive than the multi-temperature models, their use today is still restricted to 1D computations.

I.3.3. Methodology

Due to current computer capabilities, a hybrid approach as illustrated in figure 1.8 was used in the present work. The species number densities as well as the heavy-particle and electron temperatures² are obtained with the flowfield code Poschax (Gollan, 2006; Potter, 2011). The heavy-particle and electron temperatures are assumed equal to the translational-rotational-gas and vibration-electronic temperatures, respectively. The populations of the excited states are determined by the CR model developed in this work. The radiation is computed with the SPECAIR line-by-line radiation code (Laux *et al.*, 2003). The various couplings between the models will be discussed throughout the dissertation.

² Recently, Li *et al.* (2011, 2013) showed that non-Maxwellian effects were significant up to 1 cm behind the shock for a reentry at 68 km ($p_\infty = 4.6$ Pa). Within our conditions, the pressure is twice as high thus restricting the non-Maxwellian effects to a narrower zone. Therefore, it is reasonable to define the heavy-particle and electron temperatures.

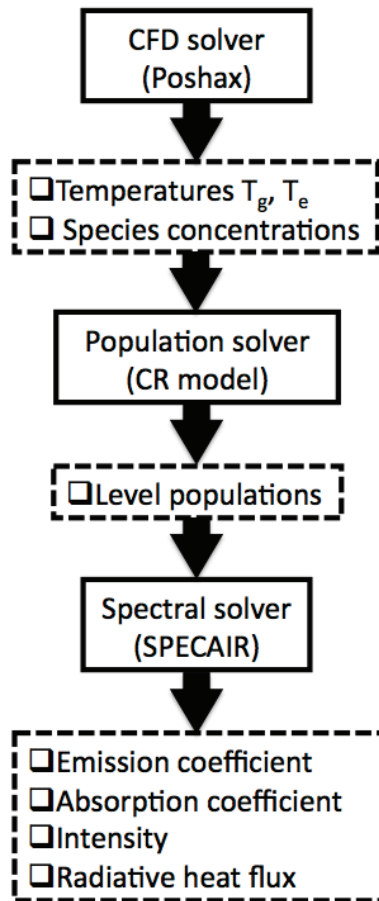


Figure 1.8: Flow chart for the computation of the radiative heat flux

I.4. Scope and organization of the thesis

This dissertation addresses the understanding and the modeling of high temperature nonequilibrium shock layer radiation in Earth reentry at hypervelocity between 8 and 15 km/s. The specific aims of the dissertation are fourfold:

1. Develop a nonequilibrium CR model accounting for electron- and heavy-particle-impact processes
2. Analyze the radiation measurements obtained in high enthalpy facilities to infer the thermodynamic properties of the flow
3. Compare the simulated spectra and the radiation intensity profiles with the selected experimental data
4. Implement the nonequilibrium CR model into EADS solvers so as to predict the radiative heat flux on a spacecraft reentering into Earth's atmosphere for future exploration missions.

The dissertation is organized in two parts:

Part 1 is devoted to the modeling of radiating shock layers. It comprises two chapters. In **chapter 2**, we briefly describe the air spectral model SPECAR (Laux *et al.*, 2003). We present the main radiators, the radiative transitions and the broadening mechanisms necessary to predict the emission and absorption of the shock layer and useful also for optical diagnostics. We derive the expression of the shock layer radiative heat flux under nonequilibrium conditions and present the approach enabling its calculation.

In **chapter 3**, we start by a literature review of existing CR models. We then introduce the CR model developed in this work. We describe the elementary processes governing the population/depletion of the molecular and atomic excited states, responsible for the bulk of radiation. We present the equation governing their population evolution, the Master Equation. We compute the rate constants of the elementary processes and validate them with available experimental data.

Part 2 is focused on the assessment of the model by comparing its predictions with experimental radiation measurements. It comprises two chapters. In **chapter 4**, we present and analyze the recent radiation measurements carried out in the EAST facility at NASA Ames Research Centre (Bogdanoff *et al.*, 2007; Cruden *et al.*, 2010; Brandis *et al.*, 2010, Grinstead *et al.*, 2010). The selected data are representative of the peak heating and high altitude conditions encountered by the spacecraft during its reentry into Earth's atmosphere. The spectral ranges encompass the VUV, the visible and the infrared. We infer from the radiation measurements the electron number density and the temperature profiles. We compare the electron number density and temperatures profiles predicted by the flowfield solver Poshax (Gollan, 2006; Potter, 2011) with the experimental data.

In **chapter 5**, we further assess the CR and spectral models. We extract from the radiation measurements the post-shock intensity profiles and spectra at various locations behind the shock front spanning from the nonequilibrium peak to the equilibrium zone. We compare the post-shock intensity profiles and spectra predicted by the CR model with the experimental data. We study the influence of electron-impact excitation, heavy-particle impact excitation processes, dissociation, dissociation-vibration coupling models as well as the Boltzmann distribution at electron temperature T_e on the post-shock intensity profiles. We infer from the radiation measurements the populations of the emitting states and further assess the predictions of the CR model.

Finally, **chapter 6** summarizes the contributions of the present work and give recommendations for future investigations.

Four appendices complement the dissertation. Appendix A gives a brief description of the flowfield model implemented in the Poshax solver (Gollan, 2006; Potter, 2011). Appendix B lists the atomic levels from the NIST database (2012). Appendix C lists the strongest atomic lines of nitrogen and oxygen in the VUV and IR spectral ranges. Appendix D presents the results obtained with a study of the spatial smearing on the computed post-shock intensity profiles.

Part I
Physico-chemical modeling

Chapter II

Air spectral model

Overview

The radiative heat flux on a spacecraft during its entry into Earth's atmosphere depends on the number density of the emitting and absorbing states and on the transition probabilities. In this chapter, we give a brief description of the spectral model SPECAIR (Laux et al., 2003) used to predict high temperature air radiation. In section 1, we list the atomic and molecular species responsible for the intense radiation emitted by the shock layer. In section 2, we present the key atomic electronic states and corresponding radiative transitions. In section 3, we present the molecular electronic and vibrational states and radiative transitions. In section 4, we discuss the expression of the emission and absorption coefficients. Finally, in section 5, we present the Radiation Transport Equation and the method to compute the intensity.

Table of contents

II.1. Main radiators in high temperature air	32
II.2. Atomic spectra	32
II.2.1. Nomenclature for atomic states.....	32
II.2.2. Radiative transitions.....	33
II.3. Molecular spectra	33
II.3.1. Nomenclature for molecular electronic states	33
II.3.2. Radiative transitions.....	35
II.4. Emission and absorption coefficients	36
II.4.1. Bound-bound transitions.....	36
II.4.2. Broadening mechanisms.....	36
II.4.3. Bound-free and free-free transitions.....	39
II.5. The Radiative Transport Equation	40
II.6. Summary	41

II.1. Main radiators in high temperature air

This section presents the key radiating systems for Earth entry. They include both the strongest radiators and the systems that can provide information on the chemistry and the thermodynamic state of the flow.

For the temperature conditions under investigation ($8000 < T < 12000$ K), the species that emit significant radiation are nitrogen and oxygen atoms, N_2 and N_2^+ molecules (Bose *et al.*, 2008). Nitric oxide NO and molecular oxygen O_2 do not contribute to radiative emission in the shock layer because they are totally dissociated. For instance, at peak heating conditions ($T=10500$ K, $p=17500$ Pa), around 90% of the radiation emitted is due to atomic lines of N and O in the VUV and IR ranges, the remaining 10% are due to the molecular systems of N_2 (First Negative, Second negative), N_2^+ (First negative) in the UV and visible range (Laux *et al.*, 2009). Also, the radiation from the resonant systems of N_2 in the VUV range (Birge Hopfield I, Birge-Hopfield II, Carroll-Yoshino, Worley, Worley-Jenkins) may be important at the lower end of the temperature range of interest (Laux *et al.*, 1993; Liebhart *et al.*, 2008). Finally, the continuum from N is thought to contribute in the VUV range (Huo, 2008-2009; Lamet, 2009). Therefore, an accurate computation of the populations of the emitting energy states and radiative signature from N, O, N_2 , N_2^+ is warranted.

II.2. Atomic spectra

II.2.1. Nomenclature for atomic states

The energy states of an atom are obtained from the time-independent Schrödinger equation. The Schrödinger equation admits only discrete solutions (eigenvalues), which are the quantized energy states.

Individual electrons are characterized by five quantum numbers:

- the principal quantum number n : 1, 2, ...
- the orbital quantum number l : 0, 1, ..., $n-1$
- the orbital magnetic quantum number m_l : 0, ± 1 , ..., $\pm l$ ($2l+1$ values)
- the spin quantum number s : 1/2
- the magnetic spin quantum number m_s : -1/2; 1/2

A wavefunction for a one-electron system is called an orbital. The set of orbitals having the same principal quantum number n is referred to as a shell, and the set of orbitals with the same n and l is called a subshell. The subshells are referred to as 1s, 2s, 2p, 3s, 3p, etc. According to the Pauli exclusion principle, a subshell nl may contain at most $2(2l+1)$ electrons. The number of electrons in each subshell is indicated with a superscript to the subshell designation.

For the majority of electronic transitions in common atoms, the orbital angular momenta of individual electrons are strongly coupled to one another, and similarly, the spins of individual electrons are also strongly coupled. The resultant angular momentum J is formed by vector addition of the resultant (i.e. summed over all electrons) spin, denoted by S , and the resultant orbital angular momentum denoted by L . This situation is called LS coupling. L takes the values 0, 1, 2, 3, etc and is denoted by the capital letters S, P, D, F, etc. For each configuration, there exist several possible energy levels called the terms. Each term, written as ^{2S+1}L , comprises a multiplet of electronic levels, each with a total angular momentum quantum number $J = L+S, \dots, |L-S|$. The multiplet terms are written as $^{2S+1}L_J$. The degeneracy

of each $^{2S+1}L_J$ level is equal to $2J+1$, which corresponds to the $2J+1$ Zeeman states (which degenerate in the absence of a magnetic field).

The SPECAIR (Laux *et al.*, 2003) model comprises 261 electronic states of N and 234 electronic states of O, which are listed in the NIST database (2012).

II.2.2. Radiative transitions

The line position centre is determined by the difference between the upper level energy E_u and the lower level energy E_l :

$$\lambda_{ul} = \frac{hc}{E_u - E_l} \quad (2.1)$$

The possible transitions between an upper electronic level $u=n'l' \ ^{2S'+1}L'_{J'}$ and a lower electronic level $l=n''l'' \ ^{2S''+1}L''_{J''}$ are given by selection rules issued from quantum mechanical calculations that stipulate which transitions are optically allowed and forbidden. These rules are:

- Δn : any value
- $\Delta l = \pm 1$
- parity must change

In case of LS coupling, additional rules are:

- $\Delta S = 0$
- $\Delta L = 0, \pm 1$ (except $L' = 0 \leftrightarrow L'' = 0$)
- $\Delta J = 0, \pm 1$ (except $J' = 0 \leftrightarrow J'' = 0$)

The Einstein coefficients can be expressed as:

$$A_{ul} = \frac{64\pi^4 \mu_{ul}^2}{3\epsilon_0 h \lambda_{ul}^3} \quad (2.2)$$

where μ_{ul} is the transition dipole moment.

SPECAIR (Laux *et al.*, 2003) comprises 1484 lines of N from 86.523 nm to 54.83 μm , 856 lines of O from 69.753 nm to 16.71 μm . In its most recent version, the Einstein coefficients were taken from the NIST database (2012).

II.3. Molecular spectra

II.3.1. Nomenclature for molecular electronic states

Figure 2.1 presents the energy level diagram as a function of internuclear distance of the electronic states of N_2 and N_2^+ .

The notations of electronic states parallel those for atoms. For N_2 , the levels are denoted $X^1\Sigma_u^+$, $A^3\Sigma_u^+$, $B^3\Pi_g$, etc. The general notation is $^{2S+1}\Lambda$ where S is the quantum number associated with the total electron spin, and Λ is the quantum number associated with the absolute value of the projection of the orbital angular momentum along the internuclear axis. The quantity $2S+1$ is called the spin multiplicity. The notation is preceded by a letter, which is generally X for the ground state, the sequence of letters A, B, C, etc for states of a given

II.3.2. Radiative transitions

Line positions as well as energy levels were determined by Laux *et al.* (2003) by diagonalizing the Hamiltonian of the electronic states involved in the various radiative transitions.

Electric dipole allowed transitions between electronic levels obey the following selection rules: $\Delta S=0$, $\Delta \Lambda=0, \pm 1$, $u \leftrightarrow g$, $\Sigma^+ \leftrightarrow \Sigma^+$ or $\Sigma^- \leftrightarrow \Sigma^-$.

The Einstein coefficient of a transition from upper rovibronic level $u=e'v'J'$ to lower rovibronic level $l=e''v''J''$ can be expressed as:

$$A_{ul} = \frac{64\pi^4 \mu_{ul}^2}{3\epsilon_0 h \lambda_{ul}^2} \quad (2.3.a)$$

The square of the transition dipole moment can be expressed as:

$$\mu_{ul}^2 = \frac{|R_e^{v'v''}|^2}{(2 - \delta_{0,\Lambda})(2S+1)} \frac{S_{J'J''}}{2J'+1} \quad (2.3.b)$$

where $S_{J'J''}$ is the rotational line strength and $|R_e^{v'v''}|^2$ is the square of the electronic-vibrational transition moment.

The square of the electronic-vibrational moment $|R_e^{v'v''}|^2$ measures the intrinsic strength of a transition from upper vibronic state (e',v') to lower vibronic state (e'',v'') . It is usually calculated from *ab initio* values of the electronic transition moment $R_e(r)$, where r is the internuclear distance and from the vibrational wavefunctions obtained from the RKR potentials of figure 2.1 (Laux and Kruger, 1992).

The square of the electron-vibrational moment $|R_e^{v'v''}|^2$ can be approximated by:

$$|R_e^{v'v''}|^2 \cong |R_e(\overline{r_{v'v''}})|^2 q_{v'v''} \quad (2.3.c)$$

where $\overline{r_{v'v''}}$ is the r-centroid and $q_{v'v''}$ is the Franck-Condon factor defined as:

$$q_{v'v''} = \left[\int_{-\infty}^{+\infty} \psi_{v'}(r) \psi_{v''}(r) dr \right]^2 \quad (2.3.d)$$

which measures how the intensity is distributed among the vibrational bands, and ψ is the wave function solution of the time-dependent Schrödinger equation.

The Franck-Condon factors for the systems N₂ Second Positive (C ³Π_u → B ³Π_g), N₂ First Positive (B ³Π_g → A ³Σ_u⁺) and N₂⁺ First Negative (B ²Π_u → X ²Σ_g⁺) were computed by Laux and Kruger (1992). The Franck-Condon factors for the six VUV systems are more difficult to obtain because of the strong perturbations due to strong homogeneous configuration interactions between emitting states with the same projected electronic orbital angular momentum L , either the states ¹Σ_u⁺ (b', c'₄, e') or the states ¹Π_u (b, c₃, and o₃). These

interactions cause near-resonant vibrational levels of the interacting states to borrow intensity from one another. In SPECAIR (Laux *et al.*, 2003), the vibronic interaction matrix of Stahel *et al.* (1983) is diagonalized to compute perturbed transition probabilities for all vibrational transitions from the six excited electronic states to $v=0-15$ of the ground state of N_2 (thus extending the work of Stahel *et al.* (1983) who had limited their study to transitions to the ground vibrational state of N_2). These data were recently presented in Laux and Lemal (2011).

II.4. Emission and absorption coefficients

The energy exchanges (emission and absorption) occurring during radiative processes can be classified in three categories:

- Bound-Bound transitions between two bound energy levels of atoms or molecules
- Bound-Free transitions between a bound energy level and a continuum. The most common processes are photoionization and photodissociation where a particle ionizes or dissociates when it absorbs a photon. The reverse process, radiative recombination, leads to the emission of a photon.
- Free-Free transitions, also called Bremsstrahlung, are due to the interaction between an electron and a heavy-particle, leading to the deceleration or acceleration of the electron. The energy lost or gained by the electron is converted into radiation.

II.4.1. Bound-bound transitions

The spectral emission coefficient ε_{ul} of a transition from an upper level u to a lower level l is given by:

$$\varepsilon_{ul}(\lambda) = n_u \frac{A_{ul}}{4\pi} \frac{hc}{\lambda_{ul}} \Phi_{ul}(\lambda - \lambda_{ul}) \quad (2.4)$$

The spectral absorption (including induced emission) coefficient α_{ul} due to a transition from a lower level l to an upper level u is expressed by:

$$\alpha_{ul}(\lambda) = (n_l B_{lu} - n_u B_{ul}) \frac{h}{\lambda_{ul}} \Phi_{ul}(\lambda - \lambda_{ul}) \quad (2.5)$$

where the Einstein coefficients A_{ul} , B_{ul} and B_{lu} satisfy the relations:

$$B_{ul} = \frac{A_{ul} \lambda_{ul}^5}{8\pi hc} \quad \text{and} \quad B_{lu} = \frac{g_u}{g_l} \frac{A_{ul} \lambda_{ul}^5}{8\pi hc} \quad (2.6)$$

The emission and absorption coefficients depend on the populations of the excited states, which depend on the thermodynamic conditions of the gas. Therefore, the physico-chemical processes governing these populations must be modelled carefully. This is the subject of **chapter 3**.

The line-shape function Φ is determined by various broadening mechanisms and is discussed in the next section.

II.4.2. Broadening mechanisms

Atomic transitions and rotational lines do not appear as Dirac lines in the spectrum, but rather are spread over a narrow range of wavelengths defined by the line shape function, $\Phi_{ul}(\lambda - \lambda_{ul})$ centered at λ_{ul} . The line shape is determined by a combination of mechanisms that include

natural, collisional and Doppler broadening. The line shape for natural and collisional broadening is given by a Lorentzian function:

$$\Phi_L(\lambda - \lambda_{ul}) = \frac{\frac{\Delta\lambda_L}{2}}{\left(\frac{\Delta\lambda_L}{2}\right)^2 + (\lambda - \lambda_{ul})^2} \quad (2.7)$$

and for Doppler broadening by a Gaussian function:

$$\Phi_G(\lambda - \lambda_{ul}) = \frac{1}{\Delta\lambda_G} \sqrt{\frac{4 \ln 2}{\pi}} \exp\left(-4 \ln 2 \left(\frac{\lambda - \lambda_{ul}}{\Delta\lambda_G}\right)^2\right) \quad (2.8)$$

The combination of Lorentzian and Gaussian line-shape functions is called the Voigt profile:

$$\Phi_V(\lambda - \lambda_{ul}) = \frac{a}{\pi \Delta\lambda_G} \sqrt{\frac{\ln 2}{\pi}} \int_{-\infty}^{+\infty} \frac{e^{-y^2} dy}{a^2 + (x - y)^2} \quad (2.9.a)$$

where:

$$a = \frac{\Delta\lambda_L}{\Delta\lambda_G} \sqrt{\ln 2} \quad x = \frac{\lambda - \lambda_{ul}}{\Delta\lambda_G} \sqrt{\ln 2} \quad (2.9.b)$$

The Voigt line shape function approximation proposed by Whiting (1968) is implemented into SPECAIR (Laux *et al.*, 2003):

$$\Phi_V(\lambda - \lambda_{ul}) = \frac{\xi(x, y)}{\Delta\lambda_V} \quad (2.10.a)$$

where:

$$x = \frac{\lambda - \lambda_{ul}}{\Delta\lambda_L}, \quad y = \frac{\Delta\lambda_L}{\Delta\lambda_V} \quad (2.10.b)$$

and:

$$\xi(x, y) = (1 - y) \frac{e^{-2.772x^2} + \frac{y}{1 + 4x^2} + 0.016y(1 - y)e^{-\frac{0.4x^{2.25} + 10}{10 + x^{2.25}}}}{1.065 + 0.047y + 0.058y^2} \quad (2.10.c)$$

In equations 2.10.a-e, $\Delta\lambda_V$ is the full width at half maximum (FWHM), which can be approximated according to Olivero and Longbothom (1977) by:

$$\Delta\lambda_V = (\Delta\lambda_L + \Delta\lambda_G) \left[1 - 0.18121(1 - d^2) - (0.023665e^{0.6d} + 0.00418e^{-1.9d}) \sin(\pi d) \right] \quad (2.10.d)$$

where:

$$d = \frac{\Delta\lambda_L - \Delta\lambda_G}{\Delta\lambda_L + \Delta\lambda_G} \quad (2.10.e)$$

The various broadening mechanisms were reviewed by Laux (1993) and are summarized as follows:

- Natural broadening: natural broadening is caused by the spreading of energy levels over their radiative lifetime due to the Heisenberg uncertainty principle. The FWHM $\Delta\lambda_N$ is given by:

$$\Delta\lambda_N = \frac{\lambda_{ul}^2}{4\pi c} \left(\sum_{k < u} A_{uk} + \sum_{k < l} A_{lk} \right) \quad (2.11)$$

- Collisional broadening: this type of broadening is caused by the different types of collisions that a radiating atom or molecule encounters. The main collisional broadening mechanisms are Stark broadening caused by collisions with charged particles, van der Waals broadening caused by collisions with neutral species, and resonance broadening caused by collisions with like species. The FWHM $\Delta\lambda_C$ is given by the sum of the Stark $\Delta\lambda_S$, Van der Waals $\Delta\lambda_{VW}$ and resonance $\Delta\lambda_R$ FWHM. The Stark FWHM $\Delta\lambda_S$ can be expressed as:

$$\Delta\lambda_S = n_e^p T_e^q \quad (2.12)$$

where n_e is the electron number density, T_e is the electron temperature and p and q are numerical parameters taken from various sources (Griem, 1964; Gigosos and Cardenoso, 1996) and used by Laux *et al.* (2003) and Cruden *et al.* (2011). Recently, Yiu *et al.* (2012) and Huo *et al.* (2012) provided more sophisticated expressions of the Stark broadening that could be used for future investigations.

For instance, table 2.1 gives the expression of the Stark FWHM $\Delta\lambda_S$ for atomic lines useful for the optical diagnostics carried out in **chapter 4**: N (410 nm), N (411 nm), H $_{\beta}$ (486 nm) and H $_{\alpha}$ (656 nm). These expressions were obtained by Cruden *et al.* (2011) and Laux *et al.* (2003). For the other lines, the coefficient q is set to 0.33.

Table 2.1: Stark width expression for nitrogen and hydrogen lines

Transition	Wavelength (nm)	$\Delta\lambda_S$ (nm)	Reference
N(88-9)	409.99	$7.19 \cdot 10^{-18} n_e [\text{cm}^{-3}]$	Cruden <i>et al.</i> (2011)
N(89-10)	410.99	$7.93 \cdot 10^{-18} n_e [\text{cm}^{-3}]$	Cruden <i>et al.</i> (2011)
H(4-2)	486.13 (H $_{\beta}$)	$2.00 \cdot 10^{-11} (n_e [\text{cm}^{-3}])^{0.668}$	Laux <i>et al.</i> (2003)
H(3-2)	656.30 (H $_{\alpha}$)	$1.82 \cdot 10^{-11} (n_e [\text{cm}^{-3}])^{0.671}$	Cruden <i>et al.</i> (2011)

- Doppler broadening: As the radiating atoms and molecules move away and toward an observer due to thermal motion, a Doppler spreading of the line intensity occurs causing a line broadening. The FWHM $\Delta\lambda_D$ is given by:

$$\Delta\lambda_D = 7.17 \times 10^{-17} \lambda_{ul} \sqrt{\frac{T_g}{W_s [\text{g/mol}]}} \quad (2.13)$$

where W_s is the mole mass of the radiator s and T_g is the gas temperature.

For a gas in equilibrium air at a temperature of 11000 K and a pressure of 17000 Pa, the FWHM of the various broadening mechanisms of N and O atoms are displayed in figures 2.2.a and 2.2.b, respectively (Bose *et al.*, 2008). It is shown that the Stark broadening mechanism is dominant under equilibrium conditions.

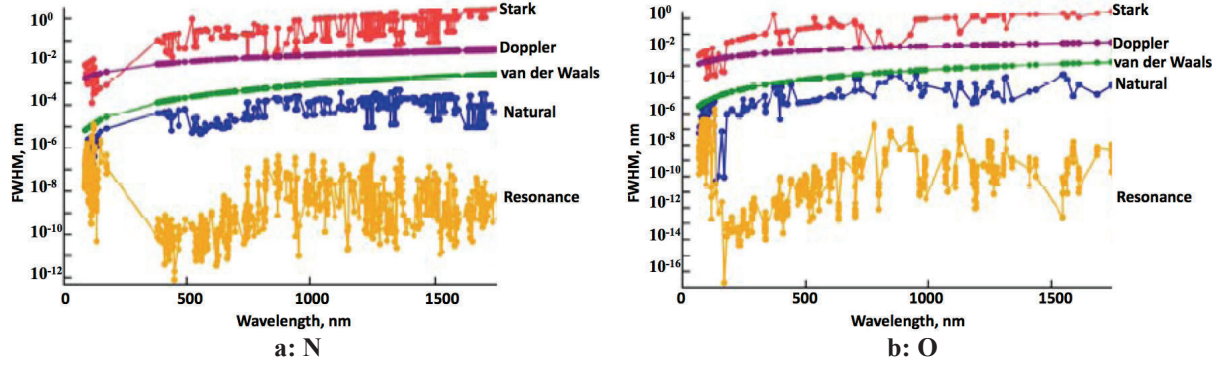


Figure 2.2: FWHM in equilibrium air plasma at a temperature of 11000 K and a pressure of 17000 Pa (Bose *et al.*, 2008)

II.4.3. Bound-free and free-free transitions

Bound-free continuum radiation is calculated from the absorption cross-sections of photo-ionization of neutral atoms. The absorption cross-sections σ_λ are defined for the process of ejecting an electron by the absorption of a photon. These data are approximated in SPECAIR by the product of the cross-section for the hydrogen atom $\sigma_{h\lambda}$ multiplied by the Gaunt factor \bar{g} , given by Peach (1970).

The hydrogenic cross-section $\sigma_{h\lambda}$ is given by:

$$\sigma_{h\lambda} = 7.9 \times 10^7 \frac{R_y}{u^5} \lambda [\text{nm}] \quad (2.14.a)$$

where u is the upper level index.

The absorption coefficient reads:

$$\alpha_\lambda = \sigma_{h\lambda} \bar{g} n_{SB} \quad (2.14.b)$$

where n_{SB} is the population of a fictitious level belonging to the ionization continuum, given by the Saha distribution:

$$n_{SB} = \frac{n^+ n_e}{2Q^+} \left(\frac{h^2}{2\pi m_e k T_e} \right)^{\frac{3}{2}} e^{-\frac{E_{ion}}{k T_e}} \quad (2.14.c)$$

The free-free radiation cross-section is also calculated from hydrogenic-like free-free cross-sections $\sigma_{h\lambda}$ multiplied by a correction factor d , given by Peach (1970). The absorption coefficient reads:

$$\alpha_\lambda = \sigma_{h\lambda} (1 + d) \frac{n^+ n_e}{n_{tot}} \quad (2.14.d)$$

For both bound-free and free-free transitions, SPECAIR (Laux *et al.*, 2003) assumes thermodynamic equilibrium. Thus, the emission coefficient is given by Kirchoff's law:

$$\varepsilon_\lambda = \alpha_\lambda B_\lambda \quad (2.15.a)$$

where B_λ is the Planck function:

$$B_\lambda = \frac{2hc^2}{\lambda^5 \left(e^{\frac{hc}{\lambda k T_e}} - 1 \right)} \quad (2.15.b)$$

II.5. The Radiative Transport Equation

At a macroscopic scale, the radiation field can be determined by the knowledge at every point of the medium \vec{r} , for each direction (Δ) directed by \vec{u} , for each wavelength λ of a quantity called the spectral intensity (or spectral radiance by the US researchers), defined by:

$$I(\lambda, \vec{r}, \vec{u}) = \frac{dq^{rad}(\lambda, \vec{r}, \vec{u})}{d\lambda dS \cos(\theta) d\Omega} \quad (2.16)$$

where dq^{rad} is the radiative heat flux reaching an elementary surface dS of normal \vec{n} in solid angle $d\Omega$, as sketched in figure 2.3.

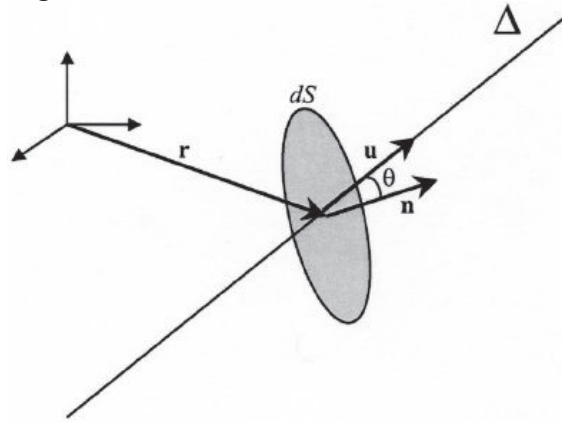


Figure 2.3: Geometrical parameters used to define the spectral radiative heat flux

The spectral intensity is determined by the Radiative Transfer Equation (RTE). Assuming the medium to be non diffusive, the RTE reads:

$$\frac{dI_\lambda}{dz}(z, \vec{u}) = \varepsilon_\lambda(z) - \alpha_\lambda(z) I_\lambda(z, \vec{u}) \quad (2.17)$$

where z is the abscissa along the optical path, and ε and α are the emission and absorption coefficients, respectively.

Solving the RTE requires an appropriate method, which is determined according to the nature of the thermodynamic state (equilibrium, nonequilibrium) and optical thickness (thin or self-absorbed) of the medium under consideration and by computer time and accuracy constraints as well. Five methods have been widely used in the aerospace community and have been reviewed by Lamet (2008):

- The methods of moments where the RTE is replaced by a system of differential equations governing the moments of the intensity and closure relations.
- The spherical harmonic method where the intensity is decomposed on spherical harmonics, which only depend on the direction.

- The Monte-Carlo methods or statistical methods where photons carrying a quantity of energy are considered throughout the domain. The emission point, the frequency and the propagation direction are chosen randomly.
- The ray tracing methods where the angular space surrounding a cell is partitioned in elementary solid angles.
- The tangent slab methods where it is assumed that the physical properties of the medium vary perpendicular to the spacecraft wall.

The heat load is governed by the physico-chemical processes occurring in the shock layer and is weakly dependent on the fashion by which the RTE is solved. The integration of the RTE over the stagnation streamline by the tangent slab method gives an upper limit of the radiative heat flux on the spacecraft surface, which is often sufficient for engineering design purposes.

II.6. Summary

During hypervelocity reentry of a spacecraft into Earth's atmosphere, a significant part of the heating suffered by the spacecraft is due to the surrounding shock layer radiation, which relies on an accurate prediction of the excited states of the strongest radiators, as well as on accurate computation of the radiative transitions. A literature review indicates that the strongest radiators during Earth reentry are the atomic species N and O and the molecular species N_2 and N_2^+ . The radiative transitions for atoms and molecules were presented. The line broadening mechanisms were discussed and the predominance of the Doppler and Stark broadening mechanisms was underscored. Finally, the various methods to estimate the radiative heat fluxes were presented.

Chapter III

Air collisional-radiative model

Overview

In this chapter, we describe the Collisional-Radiative (CR) model developed to predict the radiation emitted by air plasma under nonequilibrium conditions representative of reentry into Earth's atmosphere at hypervelocity. This chapter presents the calculation of the populations of the excited states of the key radiating species. In section 1, we review the CR models available in the literature. In section 2, we present the internal states of N and O atoms and the vibronic levels of the systems of N₂ and N₂⁺. In section 3, we discuss the collisional and radiative processes that govern the population evolution of the excited states considered. In section 4, we derived the Master equation with the processes described in section 3. Finally, in section 5, we present our compilation of rate constants obtained from theoretical and experimental cross-sections.

Table of contents

III.1. Literature review	44
III.2. Internal states	47
III.2.1. Atoms.....	47
III.2.2. Molecules.....	49
III.3. Elementary processes.....	50
III.3.1. Electron-impact excitation	50
III.3.2. Electron-impact ionization.....	51
III.3.3. Heavy-particle impact excitation.....	51
III.3.4. Electron-impact dissociation.....	52
III.3.5. Heavy-particle impact dissociation	53
III.3.6. V-T, V-V, V-e exchange energy processes.....	53
III.3.7. Predissociation	53
III.3.8. Radiative processes	54
III.4. Master equation.....	55
III.5. Selection of rate constants	56
III.5.1. Electron-impact excitation	57
III.5.1.1. Review of experimental data.....	57
III.5.1.2. Review of theoretical data.....	62
III.5.1.3. Selected rate constants	64
III.5.2. Electron-impact ionization.....	70
III.5.2.1. Review of theoretical data.....	70
III.5.2.2. Selected rate constants	71
III.5.3. Heavy-particle impact excitation.....	72
III.5.3.1. Review of theoretical data.....	72
III.5.3.2. Selected rate constants	74
III.5.4. Electron-impact dissociation.....	75
III.5.5. Heavy-particle impact dissociation	75
III.5.6. V-T, V-V, V-e exchange energy processes.....	76
III.5.7. Predissociation	76
III.5.8. Radiative processes	76
III.6. Summary	76

III.1. Literature review

In this section, the main CR models that have been developed for reentry air flows are reviewed. In most cases, the key rate constants governing the population evolution of the excited states of N, O, N₂ and N₂⁺, which strongly radiating in the VUV, UV and IR, were modeled using approximate theoretical formulations. For each of them, the species considered and the mechanisms taken into account are detailed.

Park CR models

Park (1985) proposed the first electronic QSS CR model for nonequilibrium air radiation: NEQAIR85. The internal structure of N and O was accounted for by considering 21 and 19 pseudo-levels, respectively. Collisional processes encompassed electron- and heavy-particle impact excitation and ionization, radiation of atoms and molecules. The radiation package was upgraded by Whiting *et al.* (1996). Recently, Park (2008) enhanced the rates of electron-impact excitation and dissociation of molecules and implemented them in SPRADIAN07 (Katsurayama *et al.*, 2007; Hyun, 2009) code. The QSS CR model was applied to various hypervelocity reentry missions. Departures from a Boltzmann distribution at the electron temperature T_e of the atomic and molecular electronic states were predicted.

Kunc and Soon CR model

Kunc and Soon (1989) and Soon and Kunc (1990) proposed the first time-dependent electronic specific CR model for temperature ranging from 11000 and 15000 K and electron number density ranging from 10¹⁰ to 10¹⁸ cm⁻³ for nitrogen and oxygen atom, respectively. The model comprises 43 levels for both nitrogen and oxygen. Depletion by radiation is included by with the concept of the escape factors that is not constant but dependent on plasma conditions. Collisional processes encompassed electron-impact excitation and ionization of atoms.

Cambier and Moreau CR model

Cambier and Moreau (1993) proposed an electronic CR model for the prediction of the populations of N₂ and N₂⁺ electronic states. The internal structure of N₂ and N₂⁺ was accounted for by considering seven and three electronic states, respectively. Collisional processes included electron and heavy-particle excitation and ionization, V-V, V-T, V-R energy exchange and dissociation. Preliminary results showed the influence of energy exchange processes on reaching chemical and/or thermal equilibrium.

Broc CR model

Broc *et al.* (1998) proposed an electronic CR model that included the first five levels of N. Collisional processes included electron and heavy-particle excitation. Departures from a Boltzmann distribution at the electron temperature T_e of the atomic states were predicted.

Teulet CR model

Starting from the works of Gomes *et al.* (1990), Sarette *et al.* (1995), Teulet *et al.* (2009, 2010) developed an electronic CR model for quasistationary atmospheric pressure air plasmas with electronic temperatures between 2000 and 13000 K. The model comprises 35 pseudo levels for N and 21 for O, as well as 4 electronic states of N₂ and N₂⁺. Collisional processes included electron-impact excitation, ionization, dissociation, charge exchange and dissociative recombination. For electronic temperatures below 4000K, it was shown that inelastic collisions between heavy-particles are the main population exchange processes and that the influence of radiative losses on the global densities of plasma components are weak: chemical equilibria (ionization, dissociation) were not appreciably shifted by radiative

emission. When considering a two-temperature air plasma with gas temperatures higher than the electron temperature, the influence of radiative losses on departures from an equilibrium distribution increases with increasing electronic temperature. For electronic temperatures above 4000 K, departures from a Boltzmann distribution were observed as a result of radiative losses. Teulet *et al.* (2009, 2010) improved the computation of the rate coefficients for the reactions considered by Sarette *et al.* (1995) and showed that departures from an equilibrium distribution due to radiative losses were limited to a temperature range between 8000 and 12000 K.

Bultel CR model

Bultel *et al.* (2006) proposed a time-dependent electronic CR model for high temperature air, for pressures ranging from 10^{-2} to 1 atm. The air mixture comprised 46 pseudo levels for N and 40 pseudo levels for O according to the previous works of Bourdon and Vervisch (1996) and Bourdon *et al.* (1998). Collisional processes include electron- and heavy-particle excitation, dissociation, charge exchange and associative ionization. It was shown that negative ions such as O^- and O_2^- played an important role in ionization processes. Furthermore, kinetic time scales were determined in order to implement a reduced CR model in CFD solvers. The predictions of the CR model with various kinetic mechanisms were compared and significant discrepancies were observed.

Johnston CR model

Johnston (2006) proposed an electronic QSS CR model for high temperature air radiation: HARA. The internal structure of N and O was accounted for by considering 35 and 30 pseudo-levels, respectively. The first three states (metastables) were assumed to follow a Boltzmann distribution at the electron temperature, whereas the higher states were governed by collisional and radiative processes. The internal structure of N_2 and N_2^+ was accounted for by considering 3 and 6 electronic states, respectively. Collisional processes included electron-impact excitation and ionization of atoms and molecules. A simplified atomic CR model (AACR) was also developed, based on the assumption that the populations of the atomic electronic pseudo-levels were governed by electron-impact excitation and ionization processes. The pseudo-levels of N and O were further lumped into 5 groups and the populations of the lumped levels were given by polynomial fits depending on the electron number density and temperature. Johnston *et al.* (2008) applied these two models to FIRE 2 flight conditions. The two models agreed with each other to within 5% and both predicted a depletion of the higher electronic states. Subsequently, Johnston *et al.* (2008) employed their model to predict the radiation emitted by shock heated air at freestream velocity $V_\infty=9$ km/s and at freestream pressure $p_\infty=0.1$ and 1.0 Torr, and compared the predictions with the radiation measurements carried out in the visible and IR spectral ranges at NASA Ames EAST facility³. The predictions of the model agreed with experimental data to within 35%.

Plastinin CR model

Plastinin *et al.* (2007) proposed an electronic specific CR model directly coupled to a CFD solver to predict the UV radiation on SOYOUZ spacecraft at low altitude ($h=60$ km). The study was mostly devoted to molecular excitation, thus the model comprised 4 electronic states for N_2 , 3 electronic states for N_2^+ , 6 electronic states for NO and 2 electronic states for O_2 . Species vibrational temperatures were assumed to be close to the translational gas temperature. Collisional processes include electron- and heavy-particle impact excitation,

³ These studies were performed before the upgrade of the EAST facility when radiation measurements in the VUV were not possible and when the level of impurities was not negligible.

dissociation and associative ionization. It was shown that the electronic states of N_2 and N_2^+ were strongly depleted with respect to the equilibrium distribution.

Surzhikov CR model

Surzhikov (2009) proposed an electronic CR model directly coupled to a CFD solver for application to FIRE 2 reentry conditions. The mixture was composed of N, O, N_2 , N_2^+ , NO, O_2 and electrons. Collisional processes include electron-impact excitation, ionization and dissociation of molecules, as well associative ionization. It was shown that increasing the associative ionization rates increased the electron temperature, thus the intensity. It was also shown that the intensity in the nonequilibrium region was due to associative ionization, electron-impact ionization and V-e transfer.

Panesi CR model

Panesi (2009) proposed an electronic time-dependent CR model fully coupled with a 1D shock-tube solver, based on the previous works of Bourdon and Vervisch (1996), Bourdon *et al.* (1998), Bultel *et al.* (2006) and Magin *et al.* (2006). No assumption was made on the first metastable states of N or O; unlike in the previous CR QSS models. Panesi *et al.* (2009) applied their model to FIRE 2 flight conditions and showed that the higher states were depleted by ionization processes. The model was also compared to the QSS predictions of Park (1985), and Johnston (2006). Good agreement was observed for the populations of high levels. Subsequently, Panesi *et al.* (2009) employed their model to predict the radiation emitted by shock heated air at freestream velocity $V_\infty = 9\text{km/s}$ and at freestream pressure $p_\infty = 0.1$ and 1.0 Torr and compared the predictions with the radiation measurements carried out in the visible and IR spectral ranges at NASA Ames EAST facility⁴. The predictions of the model agreed with experimental data within 50%. Panesi *et al.* (2011) also implemented electron-impact processes for molecular excitation and obtained good agreement with the predictions of SPRADIAN07 (Katsurayama *et al.*, 2007; Hyun, 2009). They also showed that the dissociation model had a weak influence on the species concentrations. Recently, Panesi and Huo (2011) improved the initial model by implementing more accurate rates for excitation and ionization processes and by coupling the flowfield and the radiation field. They found that the predictions of self-consistent radiation-flowfield CR model was comparable to the optically thick prediction.

Pierrot CR model

Pierrot *et al.* (1999) developed a vibrational QSS CR model for high temperature nitrogen. This model was the first effort to consider the vibrational levels of electronic states as individual reacting species. The internal structure of N was identical to the Park (1985) grouping. The internal structure of N_2 and N_2^+ was accounted by considering 6 and 4 electronic states, respectively, and the 356 vibrational levels listed in table 3.1. About 50,000 reactions were considered: electron-impact excitation, ionization and dissociation, V-T, V-e, V-V energy exchanges. A recent review of this vibrational specific model was presented in Laux *et al.* (2012). The CR model predictions were assessed by a comparison with the nitrogen recombining experiment carried out at Stanford University (Laux *et al.*, 1995; Gessman *et al.*, 1997; Gessman, 2000). The experimental vibrational distribution of $N_2(B)$ was very well predicted by the CR model and shown to be governed by the spontaneous process of predissociation.

⁴ The radiation measurements considered by Panesi *et al.* (2009) belonged to the test campaign previously analyzed by Johnston (2008). Again, these studies were performed before the upgrade of the EAST facility when radiation measurements in the VUV were not possible and when the level of impurities was not negligible.

Table 3.1: Vibrational levels of N₂ and N₂⁺ electronic states considered by Pierrot *et al.* (1999)

Species	Electronic state	Vibrational levels
N ₂	X ¹ Σ _g ⁺	0-47
N ₂	A ³ Σ _u ⁺	0-27
N ₂	B ³ Π _g	0-30
N ₂	W ³ Δ _u	0-37
N ₂	B' ³ Σ _u ⁻	0-41
N ₂	C ³ Π _u	0-4
N ₂ ⁺	X ² Σ _g ⁺	0-52
N ₂ ⁺	A ² Σ _u ⁺	0-24
N ₂ ⁺	B ² Π _u	0-63

Chauveau CR model

Starting from Pierrot *et al.*'s (1999) intensive research on vibrational processes in a nitrogen flow, Chauveau *et al.* (2003) proposed a vibrational specific QSS CR model for low temperature atmospheric pressure air plasma at gas temperature $T_g=2000$ K and electron temperature $T_e=12000$ K ($T_e>T_g$). The model extended the work of Pierrot *et al.* (1999) by adding vibrational specific rates for O and O₂ states and comprises about 10^3 pseudo-levels and 10^6 state-to-state processes.

Colonna CR model

Colonna and Capitelli (2001) developed a vibrational self-consistent CR model for nitrogen expansion flows. The CR model couple Euler equations with master equations as the well as the Boltzmann equation enabling them to determine the flow features, the populations of the excited states and the electron energy distribution function. The internal structure of N included the first five electronic states. The internal structure of N₂ and N₂⁺ was accounted by considering the first four electronic states and the ground state, respectively. In particular, 45 vibrational levels were considered for N₂ (X ¹Σ_g⁺). Collisional processes included dissociation, ionization and quenching processes. It was shown that strong nonequilibrium vibrational distributions were obtained during the recombination processes.

Potter CR model

Potter (2011) proposed an electronic QSS CR model for high temperature air radiation. The internal structure of N and O was accounted for by considering 37 and 32 pseudo-levels, respectively. Collisional processes encompassed electron-impact excitation and ionization of atoms and molecules. Then, Potter (2011) employed his model to predict the radiation emitted by shock heated air and compared the predictions with the radiation measurements carried out in the visible and IR spectral ranges at NASA Ames EAST facility and the Centre for Hypersonics X2 facilities. The model predictions agreed with experimental data within 45%.

III.2. Internal states**III.2.1. Atoms**

The NIST database includes 261 electronic states of N and 234 electronic states of O. To reduce the number of states and rate constants, the atomic electronic states close in energy can be grouped together. Following Park (1985), let us consider m energy levels with degeneracies g_m and energies E_m . A lumped level i can be constructed by grouping the levels close in energy. The degeneracy g_i and energy E_i in this lumped manifold I can be written as:

$$g_i = \sum_{m \in I} g_m \quad (3.1.a)$$

$$E_i = \frac{1}{g_i} \sum_{m \in I} g_m E_m \quad (3.1.b)$$

In this work, the same number of levels⁵ as in NEQAIR96 (Whiting *et al.*, 1996) was used. This grouping is also implemented in SPECAIR (Laux *et al.*, 2003). The grouped levels of N and O are displayed in figures 3.1.a and 3.1.b, respectively and listed in table 3.2, along with their degeneracies and energies. For clarity, the NIST levels are reminded in appendix B. The population of the NIST (2012) level n_m is related to the population of the grouped level n_i according to:

$$n_m = n_i \frac{g_m}{g_i} e^{-\frac{E_m - E_i}{kT_e}} \quad (3.1.c)$$

Under thermodynamic equilibrium, the statistical properties of the medium are described by the partition function, which should remain independent of the grouping. Figure 3.2 shows the electronic partition functions for N and O atoms based on the NIST database (2012) and the grouped levels and shows that the internal partition function is well described by the grouped levels.

Table 3.2: Grouped nitrogen and oxygen levels

N ($E_{\text{ion}}=117345 \text{ cm}^{-1}$)			O ($E_{\text{ion}}=109837 \text{ cm}^{-1}$)		
i	g_i	$E_i \text{ (cm}^{-1}\text{)}$	i	g_i	$E_i \text{ (cm}^{-1}\text{)}$
1	4	0	1	9	78
2	10	19228	2	5	15868
3	6	28840	3	1	33792
4	12	83337	4	5	73768
5	18	87488	5	3	76795
6	36	95276	6	15	86629
7	28	97818	7	9	88631
8	18	103862	8	8	95757
9	60	104857	9	40	97445
10	30	104902	10	49	100017
11	54	107082	11	8	102227
12	18	110021	12	101	102870
13	90	110315	13	24	103869
14	126	110486	14	168	105394
15	74	111140	15	288	106639
16	90	112851	16	392	107583
17	288	112929	17	512	108117
18	654	114280	18	648	108478
19	882	115107	19	800	108734
20	1152	115631	$O^+ (E_{\text{ion}}=283551 \text{ cm}^{-1})$		
21	1458	115991	i	g_i	$E_i \text{ (cm}^{-1}\text{)}$
22	1800	116248	1	4	0
N ⁺ ($E_{\text{ion}}=238847 \text{ cm}^{-1}$)					
i	g_i	$E_i \text{ (cm}^{-1}\text{)}$			
1	9	89.0			

⁵ In the initial grouping from NEQAIR96 (Whiting *et al.*, 1996), some levels from the NIST database were not included. They have been included in the present work, leading to small modifications of the degeneracies and the energies of the 5th, 7th, 15th, 18th level of N as well as of the 10th and 12th level of O.

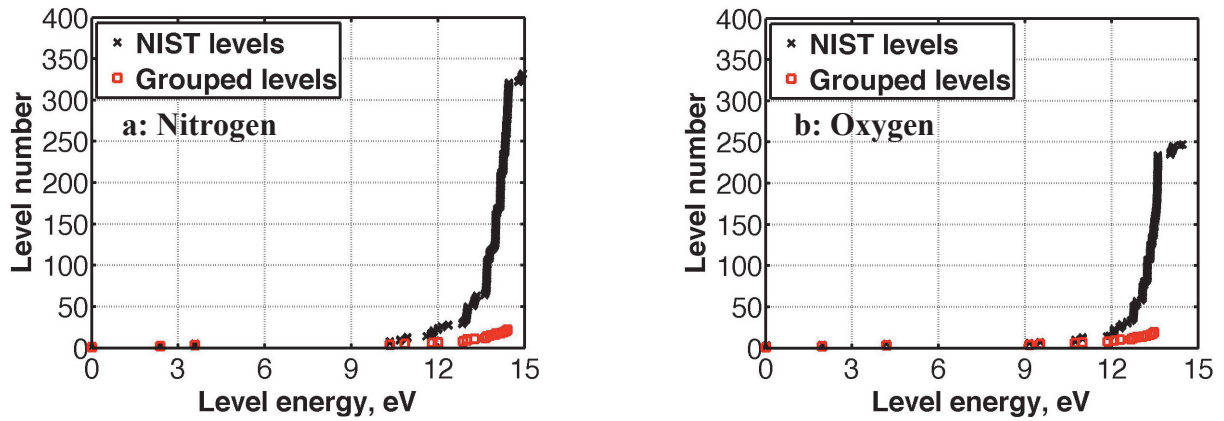


Figure 3.1: NIST and grouped levels of a) N and b) O

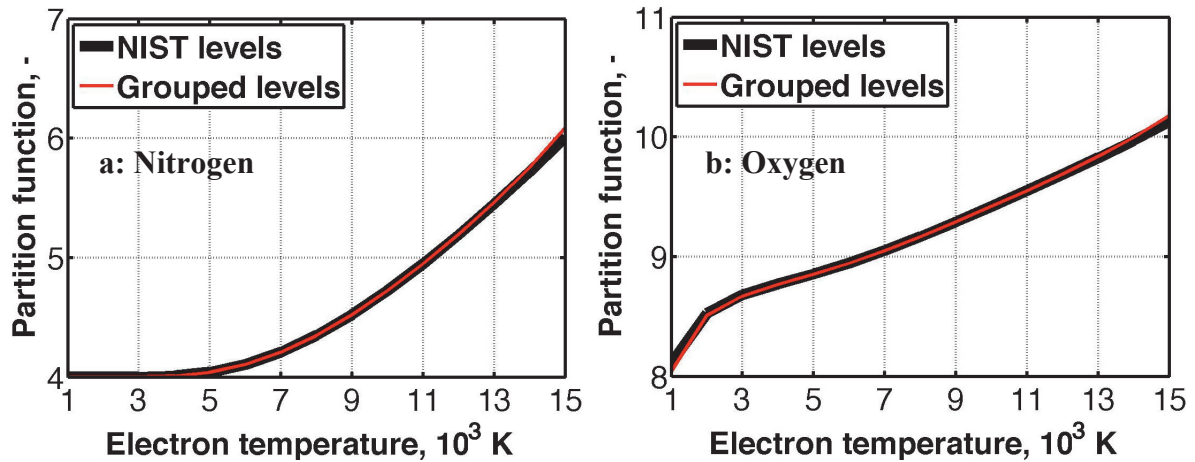


Figure 3.2: Electronic partition functions computed with NIST and grouped levels for a) N and b) O

III.2.2. Molecules

The dominant molecular transitions in reentry at $V > 8$ km/s are the following:

- N_2 Birge Hopfield I ($b^1\Pi_u \rightarrow X^1\Sigma_g^+$)
- N_2 Birge Hopfield II ($b'^1\Sigma_u^+ \rightarrow X^1\Sigma_g^+$)
- N_2 Carroll Yoshino ($c'_4^1\Sigma_u^+ \rightarrow X^1\Sigma_g^+$)
- N_2 Worley Jenkins ($c_3^1\Pi_u \rightarrow X^1\Sigma_g^+$)
- N_2 Worley ($o_3^1\Pi_u \rightarrow X^1\Sigma_g^+$)
- N_2 e' ($^1\Sigma_u^+ \rightarrow X^1\Sigma_g^+$)
- N_2 First Positive ($B^3\Pi_g \rightarrow A^3\Sigma_u^+$)
- N_2 Second Positive ($C^3\Pi_u \rightarrow B^3\Pi_g$)
- N_2^+ First Negative ($B^2\Pi_u \rightarrow X^2\Sigma_g^+$)

The vibrational levels of these electronic states have been computed by Pierrot *et al.* (1999) following the method of Liu *et al.* (1990) for N_2 First and Second Positive systems and for the N_2^+ First Negative system and are summarized in table 3.3, which complements the previous table 3.1 by adding the six electronic systems of N_2 in the VUV.

Table 3.3: Vibrational levels of N₂ and N₂⁺ electronic states considered in the present work

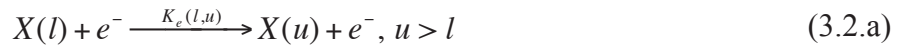
Specie	Electronic state	Vibrational levels	Spectral range of observed transitions
N ₂	X ¹ Σ _g ⁺	0-47	
N ₂	A ³ Σ _u ⁺	0-27	Visible-near IR
N ₂	B ³ Π _g	0-30	Visible-near IR
N ₂	W ³ Δ _u	0-37	
N ₂	B' ³ Σ _u ⁻	0-41	
N ₂	C ³ Π _u	0-4	UV
N ₂	b ¹ Π _u	0-43	VUV
N ₂	b' ¹ Σ _u ⁺	0-37	VUV
N ₂	c' ₄ ¹ Σ _u ⁺	0-10	VUV
N ₂	c ₃ ¹ Π _u	0-9	VUV
N ₂	o ₃ ¹ Π _u	0-11	VUV
N ₂	e' ¹ Σ _u ⁺	0-10	VUV
N ₂ ⁺	X ² Σ _g ⁺	0-52	
N ₂ ⁺	A ² Σ _u ⁺	0-24	Visible-near IR
N ₂ ⁺	B ² Π _u	0-63	UV

III.3. Elementary processes

This section introduces the considered collisional and radiative processes populating/depleting the excited states of the main radiators. The collisional mechanisms comprise electron-impact, heavy-particle impact processes. Radiative mechanisms comprise bound-bound processes. Throughout this section, the grouped upper energy level (electronic for atoms and vibrational for molecules) will be denoted u and the grouped lower energy level will be denoted l .

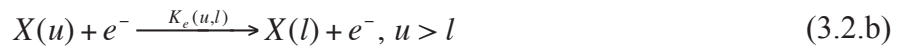
III.3.1. Electron-impact excitation

The process of electron-impact excitation is significant for both atoms and molecules, since the gas is partially ionized. For the excitation of an electronic lower level l to a higher level u , this process may be written as:



where X is the atom or molecule being excited and e^- represents the colliding electron. The rate of excitation of level u per unit volume for this process is written as $K_e(l,u)n_u n_e$, where $K_e(l,u)$ is the electron-impact rate constant, n_u is the population of level u , and n_e is the electron number density.

The reverse process of electron-impact de-excitation may be written similarly as:



The de-excitation rate constant $K_e(u,l)$ is related to the corresponding excitation rate constant $K_e(l,u)$ through detailed balance, which results in the following relation:

$$K_e(u,l) = K_e(l,u) \frac{g_l}{g_u} e^{-\frac{E_l - E_u}{kT_e}} \quad (3.2.c)$$

The net rate of excitation of level u due to electron-impact is obtained by summing over the populating and depopulating transitions from the m levels of the atom or molecule:

$$\left. \frac{\partial n_u}{\partial t} \right|_{Exc,e} = \sum_{k=1}^m K_e(k,u)n_k n_e - \sum_{k=1}^m K_e(u,k)n_u n_e \quad (3.2.d)$$

III.3.2. Electron-impact ionization

The process of electron-impact ionization is significant for both atoms and molecules, since the gas is partially ionized. The ionization of level u through this process may be written as:



where X^+ represents the ionized species and $K_e(u,c)n_u n_e$ represents the rate of ionization of level u .

The reverse process, or three-body recombination, is written as:



The recombination rate constant $K_e(c,u)$ is related to the corresponding ionization rate constant $K_e(u,c)$ through detailed balance, which results in the following relation:

$$K_e(c,u) = K_e(u,c) \frac{g_u}{2Q^+} \left(\frac{h^2}{2\pi m_e k T_e} \right)^{\frac{3}{2}} e^{-\frac{E_u - E'_{ion}}{k T_e}} \quad (3.3.c)$$

where E'_{ion} is the ionization energy E_{ion} of the atom lowered by the Debye shielding ΔE_{ion} given by:

$$\Delta E_{ion} = \frac{q_e^2}{4\pi\epsilon_0 L_D} \quad (3.3.d)$$

where L_D is the Debye length given by:

$$L_D = \sqrt{\frac{\epsilon_0 k T_e}{n_e q_e^2}} \quad (3.3.e)$$

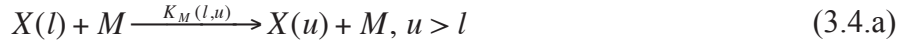
The net rate of ionization of level u due to electron-impact is given by:

$$\left. \frac{\partial n_u}{\partial t} \right|_{Ion,e} = K_e(c,u)n^+ n_e^2 - K_e(u,c)n_u n_e \quad (3.3.f)$$

where n^+ is the ion number density.

III.3.3. Heavy-particle impact excitation

The process of heavy-particle impact excitation is significant for both atoms and molecules in the portion of the shock layer where electrons are scarce. It may be written as:



where X is the atom or molecule being excited and M represents the colliding heavy-particle. The rate of excitation of level u for this process is written as $K_M(l,u)n_u n_M$, where $K_M(l,u)$ is the heavy-particle impact rate constant, n_u is the population of level u , and n_M is the heavy-particle number density.

The reverse process of heavy-particle impact de-excitation may be written similarly as:



The de-excitation rate constant $K_M(u,l)$ is related to the corresponding excitation rate constant $K_M(l,u)$ through detailed balance, which results in the following relation:

$$K_M(u,l) = K_M(l,u) \frac{g_l}{g_u} e^{-\frac{E_l - E_u}{kT_e}} \quad (3.4.c)$$

The net rate of excitation of level u due to heavy-particle impact excitation is obtained by summing over the populating and depopulating transitions from the m levels of the atom or molecule:

$$\left. \frac{\partial n_u}{\partial t} \right|_{Exc,M} = \sum_{k=1}^m K_M(k,u) n_k n_M - \sum_{k=1}^m K_M(u,k) n_u n_M \quad (3.4.d)$$

III.3.4. Electron-impact dissociation

The dissociation of level u of the molecule XY through electron-impact dissociation may be written as:



where X and Y represents the atomic species formed by dissociation and $K_e(u,d)n_u n_e$ represents the rate of dissociation of level u .

The reverse process, or three-body recombination, is written as:



The recombination rate constant $K_e(d,u)$ is related to the corresponding dissociation rate constant $K_e(u,d)$ through detailed balance, which results in the following relation:

$$K_e(d,u) = K_e(u,d) \frac{Q_u^{XY}}{Q_X Q_Y} \left(\frac{h^2}{2\pi m_e kT_e} \right)^{\frac{3}{2}} e^{-\frac{E_u^{Dis}}{kT_e}} \quad (3.5.c)$$

where Q_X , Q_Y are the total partition functions of atomic species, Q_{XY} is the rovibrational partition function of the molecule in its excited electronic state u and E_u^{dis} is the energy required to dissociate the molecule XY from state u .

The net rate of excitation of level u due to this process may be written as:

$$\left. \frac{\partial n_u}{\partial t} \right|_{Dis,e} = K_e(d,u)n_X n_Y n_e - K_e(u,d)n_u n_e \quad (3.5.d)$$

III.3.5. Heavy-particle impact dissociation

The process of heavy-particle impact dissociation may be written as:



where X and Y represents the atomic species formed by dissociation and $K_M(u,d)N_u N_M$ represents the rate of dissociation of level u .

The reverse process, or three-body recombination, is written as:



The recombination rate constant $K_M(d,u)$ is related to the corresponding dissociation rate constant $K_M(u,d)$ through detailed balance, which results in the following relation:

$$K_M(d,u) = K_M(u,d) \frac{Q_u^{XY}}{Q^X Q^Y} \left(\frac{h^2}{2\pi m k T_g} \right)^{\frac{3}{2}} e^{-\frac{E_u^{Dis}}{k T_g}} \quad (3.6.c)$$

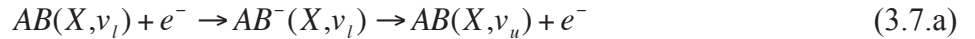
where Q_X , Q_Y are the total partition functions of atomic species, Q_{XY} is the rovibrational partition function of the molecule in its excited electronic state u and E_u^{dis} is the energy required to dissociate the molecule XY from state u .

The net rate of excitation of level u due to this process may be written as:

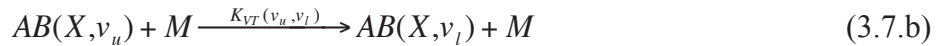
$$\left. \frac{\partial n_u}{\partial t} \right|_{Dis,M} = K_M(d,u)n_X n_Y n_M - K_M(u,d)n_u n_M \quad (3.6.d)$$

III.3.6. V-T, V-V, V-e exchange energy processes

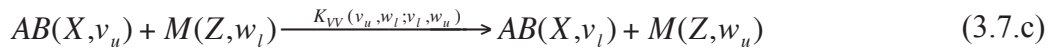
Vibrational excitation of a molecule AB by electron-impact (e-V) occurs via resonant transitions to the ground state of the unstable negative ion XY^- and is written as:



Vibrational excitation of a molecule AB by heavy-particle impact (V-T) may be written as:



Vibrational excitation of a molecule AB by heavy-particle impact (V-V) may be written as:



III.3.7. Predissociation

Predissociation is a mechanism by which some vibrational levels spontaneously decay into two atoms in their ground states:

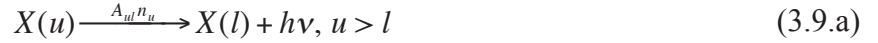


where V is the vibrational level manifold subject to predissociation.

This mechanism is caused by the crossing of the stable potential curve of the electronic state Y with unstable potential energy curves.

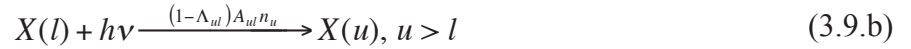
III.3.8. Radiative processes

The bound-bound radiative transitions are the results of the interaction between a photon and matter by emission or absorption. The spontaneous emission process can be written as:



The evolution of the excited states through radiative processes is complicated because the absorption at a point is a function of the radiative intensity at that point, which is a function of the radiation emitted throughout the flowfield. It requires a self-consistent resolution of the flowfield equations and the Radiative Transport Equation, which is beyond the scope of this work. Here, this process is treated using the escape factor concept, which assumes that the depletion of level u due to absorption is some fraction of the re-population of level l by emission. This fraction or escape factor, defined as A_{ul} , may be interpreted as the fraction of radiation that escapes from a point.

The radiation absorption process may therefore be written as:



If A_{ul} is set equal to unity, then all of the radiation escapes, meaning the gas is transparent and there is no re-population by absorption. Conversely, if A_{ul} is set equal to zero, then the repopulation and depletion of a level l due to absorption and emission cancel out, which may be interpreted as no net “escaping” radiation. The net rate of level u due to bound-bound radiative transitions is obtained by summing over the populating and depopulating transitions from the m levels of the atom or molecule:

$$\left. \frac{\partial n_u}{\partial t} \right|_{Rad.bb} = \sum_{k>u}^m \Lambda_{ku} A_{ku} n_k - \sum_{k<u}^m \Lambda_{uk} A_{uk} n_u \quad (3.9.c)$$

Sohn *et al.* (2012) conducted Monte-Carlo radiation computations for Stardust reentry. Stardust reentry occurs in the upper layers of Earth’s atmosphere, where the density of air is low, thus the excitation processes by collision are weak. They showed that the escape factors were close to zero for the optically thick (self-absorbed) VUV lines of nitrogen and oxygen. They also showed that, at the low density encountered, the emitting states of N and O were not significantly depleted by radiation escape. Recently, Lopez *et al.* (2013) conducted self-consistent flowfield-radiation computations for the first trajectory point of FIRE 2 flight experiment. They showed that the excited states of atoms emitting in the VUV were only depleted by radiation in a narrow zone (typically 0.1 cm) behind the shock. Therefore, in this thesis, the escape factors are assumed to be to zero for the VUV and to one for the visible and infrared lines

III.4. Master equation

The Master Equation is the governing equation for the electronic state populations of atoms and molecules. This differential equation, which must be solved for every state of a radiating molecule, equates the time-rate-of-change of a level's population with all of the populating and depopulating mechanisms discussed in the previous section:

$$\begin{aligned} \frac{\partial n_u}{\partial t} = & \left. \frac{\partial n_u}{\partial t} \right|_{Exc,e} + \left. \frac{\partial n_u}{\partial t} \right|_{Dis,e} + \left. \frac{\partial n_u}{\partial t} \right|_{Ion,e} + \left. \frac{\partial n_u}{\partial t} \right|_{V-e} \\ & + \left. \frac{\partial n_u}{\partial t} \right|_{Exc,M} + \left. \frac{\partial n_u}{\partial t} \right|_{Dis,M} + \left. \frac{\partial n_u}{\partial t} \right|_{V-V} + \left. \frac{\partial n_u}{\partial t} \right|_{V-T} \\ & + \left. \frac{\partial n_u}{\partial t} \right|_{Rad,bb} \end{aligned} \quad (3.10.a)$$

Therefore, from equations 3.1 to 3.6 and 3.9, equation 3.10.a reads for atoms:

$$\begin{aligned} \left. \frac{\partial n_u}{\partial t} \right| = & \sum_{k=1}^m K_e(k,u)n_k n_e - \sum_{k=1}^m K_e(u,k)n_u n_e \\ & + K_e(c,u)n^+ n_e^2 - K_e(u,c)n_u n_e \\ & + \sum_{k=1}^m K_M(k,u)n_k n_M - \sum_{k=1}^m K_e(u,k)n_u n_M \\ & + \sum_{k>u}^m \Lambda_{ku} A_{ku} n_k - \sum_{k=1}^m \Lambda_{uk} A_{uk} n_u \end{aligned} \quad (3.10.b)$$

Then, from equations 3.1 to 3.9, equation 3.10.a reads for molecules:

$$\begin{aligned} \left. \frac{\partial n_u}{\partial t} \right| = & \sum_{k=1}^m K_e(k,u)n_k n_e - \sum_{k=1}^m K_e(u,k)n_u n_e \\ & + K_e(d,u)n_X n_Y n_e - K_e(u,d)n_u n_e \\ & + K_e(c,u)n^+ n_e^2 - K_e(u,c)n_u n_e \\ & + K_{V_i-e} n_i n_e - K_{V_u-e} n_u n_e \\ & + \sum_{k=1}^m K_M(k,u)n_k n_M - \sum_{k=1}^m K_M(u,k)n_u n_M \\ & + K_M(d,u)n_X n_Y n_M - K_M(u,d)n_u n_M \\ & + K_{V_i-e} n_i n_{M_u} - K_{V_u-e} n_u n_{M_l} \\ & + K_{V_i-T} n_i n_M - K_{V_u-T} n_u n_M \\ & + \sum_{k>u}^m \Lambda_{ku} A_{ku} n_k - \sum_{k<u}^m \Lambda_{uk} A_{uk} n_u \end{aligned} \quad (3.10.c)$$

Equation 3.10.b and c represent a set of m differential equations for the m unknown n_u values.

There exist different ways to couple flowfield and CR models. The most widely used approach (Park, 1985; Pierrot *et al.*, 1999; Raynaud, 2005; Johnston, 2006; Hyun, 2009; Potter, 2011) is the Quasi Steady State (QSS) approach, which assumes that the excited state

concentrations adjust instantaneously to the flow changes. QSS CR models can be loosely coupled to flow codes. The profiles of the thermodynamic variables (pressure and temperatures) and species mass fractions are derived based on a flow calculation, then the populations of energy levels states are obtained at each desired location in the flow thanks to the state-to-state processes.

The second approach (Bultel *et al.*, 2006; Magin *et al.*, 2006; Panesi *et al.*, 2009) is called the time-dependent CR model where conservation equations for all species and energy levels are solved simultaneously without any assumption on characteristic relaxation times. Time-dependent CR models can be either loosely or fully coupled to CFD solvers. In the fully coupled approach, (Bultel *et al.*, 2006; Panesi *et al.*, 2009), state-to-state equations are solved simultaneously with mixture mass, momentum and energies equations. In the loosely coupled approach (Magin *et al.*, 2006), sometimes called Lagrangian approach, the populations of excited states are obtained by accurately following in time a cell of fluid.

Park (1985) claimed that the QSS assumption was not valid for the metastable states of atoms because their radiative life-time is significant. Panesi (2009) showed that the QSS assumption for the metastable states was only questionable in a narrow zone restricted to 3 mm behind the shock. Therefore, the QSS assumption was used in the present work and was solved thanks to a Newton algorithm (Pierrot *et al.*, 1999). Under this assumption, the Master equation reduces to system of linear equations:

$$\begin{aligned}
0 = & \sum_{k=1}^m K_e(k,u)n_k n_e - \sum_{k=1}^m K_e(u,k)n_u n_e \\
& + K_e(d,u)n_x n_y n_e - K_e(u,d)n_u n_e \\
& + K_e(c,u)n^+ n_e^2 - K_e(u,c)n_u n_e \\
& + K_{V_i-e} n_l n_e - K_{V_u-e} n_u n_e \\
& + \sum_{k=1}^m K_M(k,u)n_k n_M - \sum_{k=1}^m K_M(u,k)n_u n_M \\
& + K_M(d,u)n_x n_y n_M - K_M(u,d)n_u n_M \\
& + K_{V_i-e} n_l n_{M_u} - K_{V_u-e} n_u n_{M_l} \\
& + K_{V_i-T} n_l n_M - K_{V_u-T} n_u n_M \\
& + \sum_{k>u}^m \Lambda_{ku} A_{ku} n_k - \sum_{k<u}^m \Lambda_{uk} A_{uk} n_u
\end{aligned} \tag{3.10.d}$$

III.5. Selection of rate constants

This section presents the various models available in the literature for the rate constants corresponding to the collisional and radiative processes discussed in the previous section.

The rate constant K between two species A and B of mass m_A and m_B , characterized by Maxwellian translational energy distribution functions at temperatures T_A and T_B , respectively is given by (Vincenti and Kruger, 1965):

$$K(\theta_{AB}) = \frac{8\pi}{\sqrt{\mu_{AB}}} (2\pi k\theta_{AB})^{-\frac{3}{2}} \int_0^{+\infty} \sigma(\varepsilon) e^{-\frac{\varepsilon}{k\theta_{AB}}} \varepsilon d\varepsilon \tag{3.11}$$

where $\mu_{AB}=m_A m_B/(m_A+m_B)$ is the reduced mass of species A and B , $\theta_{AB}=(m_A T_A+m_B T_B)/(m_A+m_B)$ is the effective kinetic temperature and σ is the elementary cross-section of the reaction between species A and B .

Throughout this dissertation, the thermal state of the gas is described by a two-temperature model. A gas temperature, T_g , and an electron temperature, T_e , characterize heavy-particles and electrons, respectively, which leads to the following definition for the heavy-particle impact rate constant K_M and electron-impact rate constant K_e :

$$K_e(T_e) = \frac{8\pi}{\sqrt{m_e}} (2\pi k T_e)^{-\frac{3}{2}} \int_0^{+\infty} \sigma_e(\varepsilon) e^{-\frac{\varepsilon}{k T_e}} \varepsilon d\varepsilon$$

$$K_M(T_g) = \frac{8\pi}{\sqrt{\mu_{AM}}} (2\pi k T_g)^{-\frac{3}{2}} \int_0^{+\infty} \sigma_M(\varepsilon) e^{-\frac{\varepsilon}{k T_g}} \varepsilon d\varepsilon$$
(3.12)

In the following sections, the available experimental and theoretical sources are reviewed and compared, leading to the selection of the most appropriate formulations. For certain processes, no rates were available in the literature; thus, approximate formulas were used.

III.5.1. Electron-impact excitation

III.5.1.1. Review of experimental data

To the author's knowledge, there are very few experimental cross-section data for electron-impact excitation⁶. Some of the electron-impact cross-sections involving the states of nitrogen atom have been studied by Spence and Burrow (1980), Stone and Zipf (1973) and Yang and Doering (1996). The available transitions as well as the electron energy range are listed in table 3.4. These experimental cross-sections have been reviewed by Kato (1994) and recently quoted by Huo (2009) and are displayed in figure 3.3.

Oxygen electron-impact has been little investigated as well. Some of the electron-impact cross-sections involving oxygen states have been studied by Vaughan and Doering (1988), Doering (1992), Kanic *et al.* (2001) and Johnson *et al.* (2003). The available transitions as well as the electron energy range are listed in table 3.5. These experimental cross-sections are displayed in figure 3.4.

Unlike the electron-impact excitation in atoms, the electron-impact processes driving the electronic excitation in N_2 and N_2^+ have been widely investigated⁶. Cartwright *et al.* (1977), Zipf and Gorman (1980), Majeed and Strickland (1997), Itikawa (2005) and recently Johnson *et al.* (2005), Khakoo *et al.* (2006) and Malone *et al.* (2011) measured electron-impact cross-sections for the electronic states of N_2 .

The available transitions as well as the electron energy range are listed in table 3.6. The available experimental electron-impact cross-sections are presented in figure 3.5. The experimental cross-sections agree well with each other and thus can be considered as well established.

⁶ This subsection presents a comprehensive survey of the experimental cross-sections found in the literature.

Table 3.4: Experimental cross-sections for electron-impact of N atom

Transition	Corresponding lumped levels	Reference	Electron energy range (eV)	Note
$2s^2 2p^3 \ ^4S - 2s^2 2p^2 3s \ ^4P$	1-4	Spence and Burrow (1980) Stone and Zipf (1973)	10.3-12.0 12.0-100.0	Upper level emits at 120 nm
$2s^2 2p^3 \ ^4S - 2s 2p^4 \ ^4P$	1-5	Spence and Burrow (1980) Stone and Zipf (1973)	10.9-12.0 12.0-100.0	Upper level emits at 149 and 175 nm
$2s^2 2p^3 \ ^4S - 2s^2 2p^3 \ ^2D$	1-2	Yang and Doering (1996)	2.0-30.0	Upper level absorbs at 149 nm

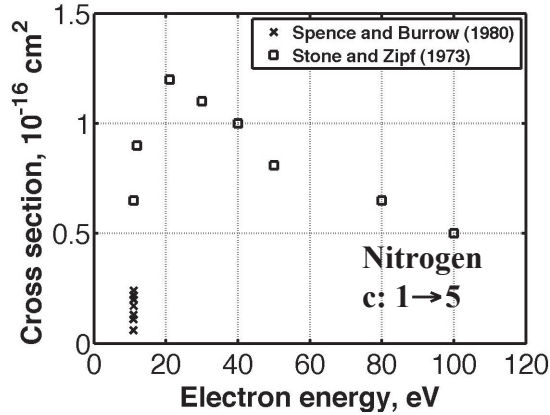
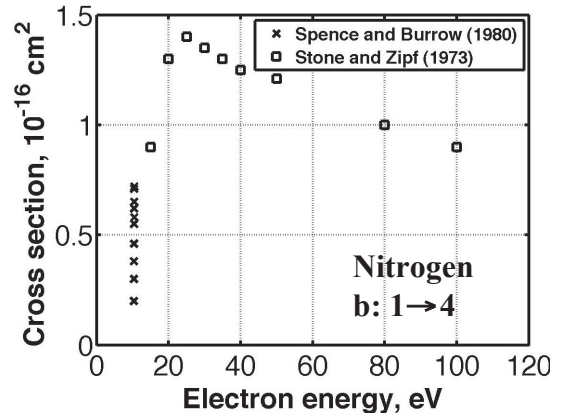
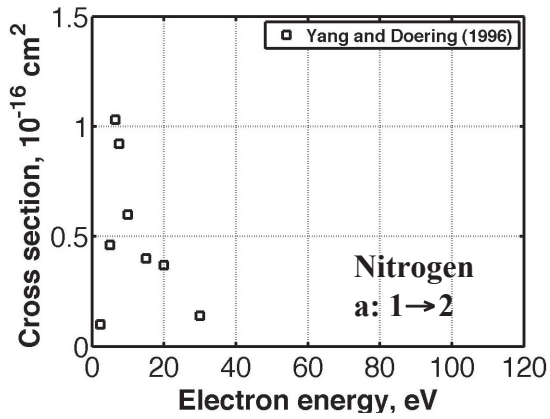


Figure 3.3: Experimental electron-impact cross-sections of N: a) N(1→2), b) N(1→4), c) N(1→5)

Table 3.5: Experimental cross-sections for electron-impact of O atom

Transition	Corresponding lumped levels	Reference	Electron energy range (eV)	Note
$2s^2 2p^4 \ ^3P - 2s^2 2p^4 3s \ ^3S$	1-5	Kanic <i>et al.</i> (2001) Johnson <i>et al.</i> (2003)	30-100 10-1000	Upper level emits at 130 nm
$2s^2 2p^4 \ ^3P - 2s^2 2p^4 \ ^1D$	1-2	Doering (1992)	3-30	
$2s^2 2p^4 \ ^3P - 2s^2 2p^4 \ ^1D$	1-9	Vaughan and Doering (1988) Kanic <i>et al.</i> (2001) Johnson <i>et al.</i> (2003)	30, 50, 70 50, 70 10-1000	Upper level emits at 102 nm
$2s^2 2p^4 \ ^3P - 2s^2 2p^3 5s \ ^3S$	1-11	Kanic <i>et al.</i> (2001) Johnson <i>et al.</i> (2003)	30, 50, 70 10-1000	Upper level emits at 98 nm

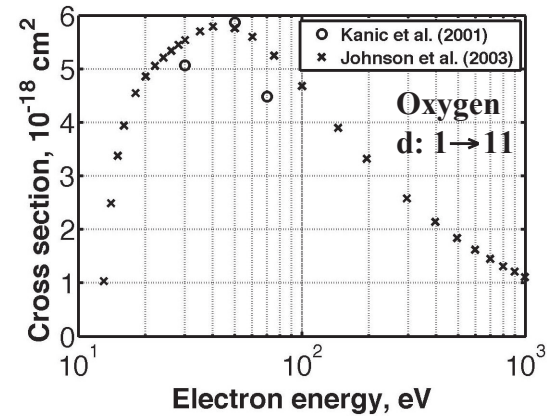
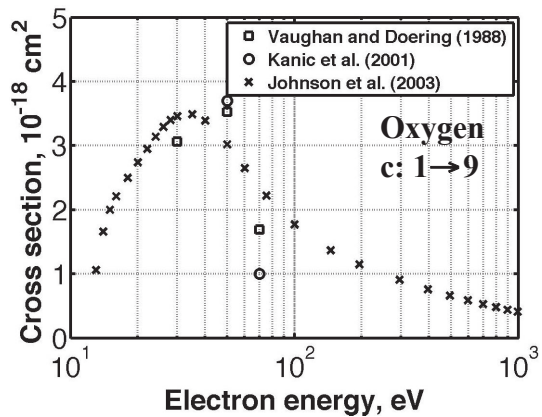
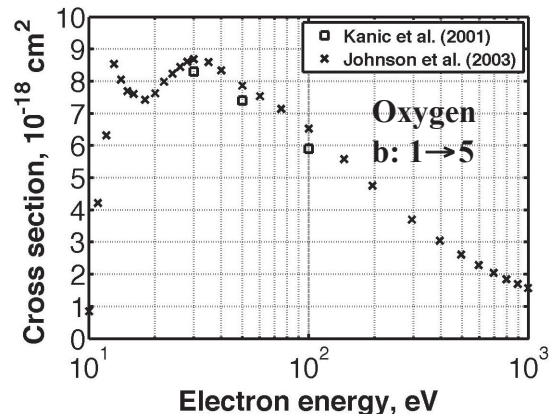
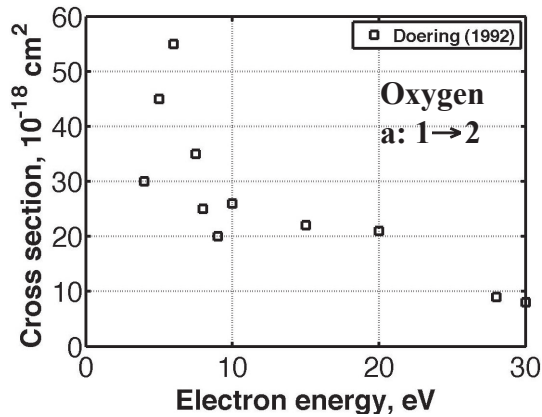


Figure 3.4: Experimental electron-impact cross-sections of O: a) O(1→2), b) O(1→5), c) O(1→9), d) O(1→11)

Table 3.6: Experimental cross-sections for electron-impact of N₂

Transition	Reference	Electron energy range (eV)	Note
$X^1\Sigma_g^+ \rightarrow A^3\Sigma_u^+$	Cartwright <i>et al.</i> (1977)	9-40	
	Majeed and Strickland (1997)	9-50	
	Itikawa (1997)	12-40	
	Johnson <i>et al.</i> (2005)	10-100	
$X^1\Sigma_g^+ \rightarrow B^3\Pi_g$	Cartwright <i>et al.</i> (1977)	9-40	Upper level emits in the visible
	Majeed and Strickland (1997)	9-50	
	Itikawa (1997)	12-40	
	Johnson <i>et al.</i> (2005)	10-100	
$X^1\Sigma_g^+ \rightarrow B',^3\Sigma_u$	Cartwright <i>et al.</i> (1977)	9-40	
	Majeed and Strickland (1997)	9-50	
	Itikawa (1997)	12-40	
	Johnson <i>et al.</i> (2005)	10-100	
$X^1\Sigma_g^+ \rightarrow C^3\Pi_u$	Cartwright <i>et al.</i> (1977)	9-40	Upper level emits in the UV
	Majeed and Strickland (1997)	9-50	
	Itikawa (1997)	12-40	
	Khakoo <i>et al.</i> (2006)	10-100	
$X^1\Sigma_g^+ \rightarrow W^3\Delta_u$	Cartwright <i>et al.</i> (1977)	9-40	
	Majeed and Strickland (1997)	9-50	
	Itikawa (1997)	12-40	
	Johnson <i>et al.</i> (2005)	10-100	
$X^1\Sigma_g^+ \rightarrow b^1\Pi_u$	Majeed and Strickland (1997)	9-50	Upper level emits in the VUV
	Itikawa (1997)	12-40	
	Malone <i>et al.</i> (2011)	10-100	
$X^1\Sigma_g^+ \rightarrow b',^1\Sigma_u^+$	Majeed and Strickland (1997)	9-50	Upper level emits in the VUV
	Itikawa (1997)	12-40	
	Malone <i>et al.</i> (2011)	10-100	
$X^1\Sigma_g^+ \rightarrow c',_4^1\Sigma_u^+$	Majeed and Strickland (1997)	9-50	Upper level emits in the VUV
	Itikawa (1997)	12-40	
	Malone <i>et al.</i> (2011)	10-100	

Table 3.7: Experimental cross-sections for electron-impact of N₂⁺

Transition	Reference	Electron energy range (eV)	Note
$X^2\Sigma_g^+ \rightarrow B^2\Sigma_u^+$	Crandall <i>et al.</i> (1974)	3-100	Upper level emits in the UV

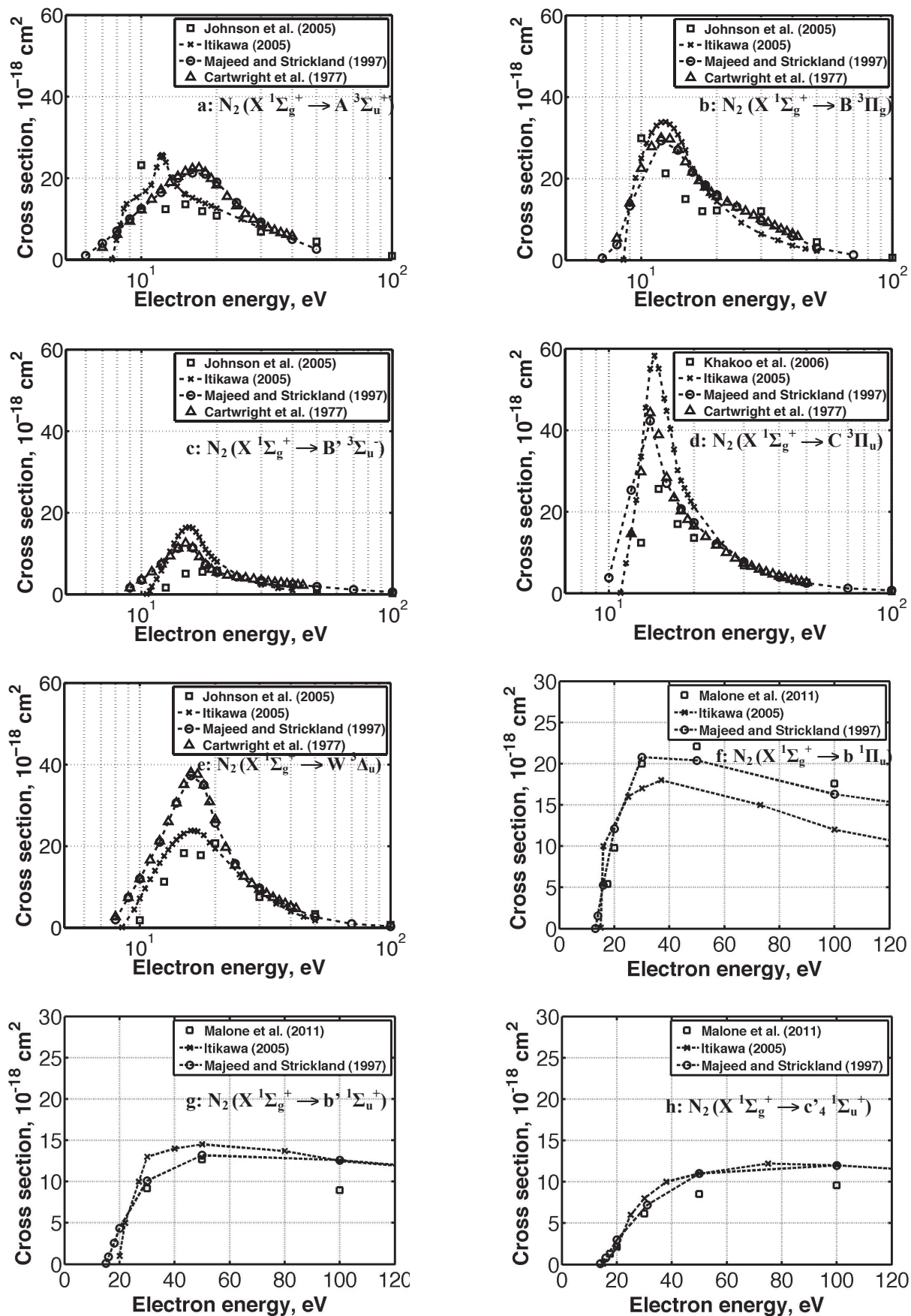


Figure 3.5: Experimental electron-impact cross-sections in N_2 : a) $X^1\Sigma_g^+ \rightarrow A^3\Sigma_u^+$, b) $X^1\Sigma_g^+ \rightarrow B^3\Pi_g$, c) $X^1\Sigma_g^+ \rightarrow C^3\Pi_u$, d) $X^1\Sigma_g^+ \rightarrow W^3\Delta_u$, e) $X^1\Sigma_g^+ \rightarrow W^3\Delta_u$, f) $X^1\Sigma_g^+ \rightarrow b^1\Pi_u$, g) $X^1\Sigma_g^+ \rightarrow b^1\Sigma_u^+$, h) $X^1\Sigma_g^+ \rightarrow c^4_1\Sigma_u^+$

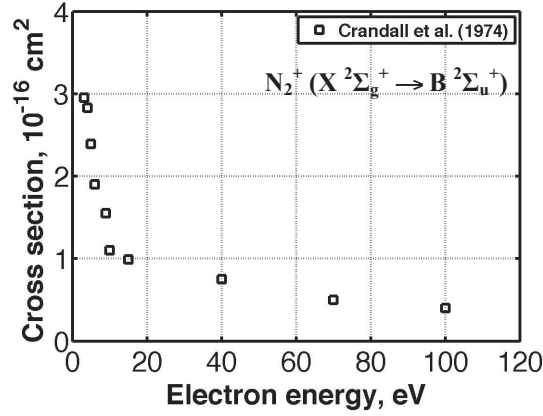


Figure 3.6: Experimental electron-impact cross-sections in N_2^+ ($X^2\Sigma_g^+ \rightarrow B^2\Sigma_u^+$)

III.5.1.2. Review of theoretical data

There is a lot of theoretical work on electron-impact excitation cross-sections in atoms. Two cases are considered: optically allowed and forbidden transitions.

a. Optically allowed transitions

Most models (Gryzinski, 1958; Seaton, 1962; Drawin, 1966) are semi-empirical or derived from quantum mechanical calculations, with adjustable parameters. Let us denote by l and u the grouped lower and upper electronic states of the optically allowed transition respectively, ε the electron-impact energy and by σ the cross-section. The expressions given by several authors are reviewed in the following.

Gryzinski (1958) cross-section reads:

$$\sigma_{lu} = 4\pi a_0^2 N_u \left[\left(\frac{R_y}{E_l - E_u} \right)^2 \zeta_1(u_{lu}, w_{lu}) - \left(\frac{R_y}{E_{u+1} - E_l} \right)^2 \zeta_1(u_{lu+1}, w_{lu+1}) \right] \quad (3.13.a)$$

where N_u is the number of equivalent electron in the outer shell and:

$$\begin{aligned} u_{lu} &= \frac{\varepsilon}{E_u - E_l} \\ w_{lu} &= \frac{E_{Ion} - E_l}{E_u - E_l} \\ u_{lu+1} &= \frac{\varepsilon}{E_{u+1} - E_l} \\ w_{lu+1} &= \frac{E_{Ion} - E_u}{E_{u+1} - E_l} \end{aligned} \quad (3.13.b)$$

and:

$$\zeta_1 = \frac{1}{x} \left(1 - \frac{1}{x} \right)^{1+\frac{y}{y+1}} \left(\frac{x}{x+y} \right)^{\frac{3}{2}} \left[1 + \frac{2y}{3} \left(1 - \frac{1}{2y} \right) \ln \left(e + \left(\frac{x-1}{y} \right)^{\frac{1}{2}} \right) \right] \quad (3.13.c)$$

Seaton (1962) cross-section reads:

$$\sigma_{lu} = \frac{8\pi a_0^2}{\sqrt{3}} \frac{R_y^2}{(E_l - E_u)\epsilon} f_{lu} \bar{g}(x) \quad (3.14.a)$$

where:

$$x_{lu} = \frac{1 + \sqrt{1 + \frac{1}{u_{lu}}}}{1 - \sqrt{1 - \frac{1}{u_{lu}}}} \quad (3.14.b)$$

where the effective Gaunt factor \bar{g} , given by Van Regmorter (1962), was fitted by Pierrot (1999):

$$\bar{g}(x) = \left(0.23603 - \frac{4.90398}{x + 23.271} \right) \ln(x) \quad (3.14.c)$$

Drawin (1966) cross-section reads:

$$\sigma_{lu} = 4\pi a_0^2 \left(\frac{R_y}{E_u - E_l} \right)^2 \alpha_{lu} \frac{u_{lu} - 1}{u_{lu}^2} f_{lu} \ln(\beta_{lu} u_{lu}) \quad (3.15.a)$$

where $\alpha=1.00$ and $\beta=1.25$. Drawin (1966) gives the following expression of the corresponding rate constant:

$$K_{lu} = 4\pi a_0^2 \sqrt{\frac{8kT_e}{\pi m_e}} \left(\frac{R_y}{kT_e} \right)^2 \alpha_{lu} f_{ul} \xi_2 \quad (3.15.b)$$

where:

$$\xi_2 = 0.63255 \left(\frac{E_u - E_l}{kT_e} \right)^{-1.6454} e^{-\frac{E_u - E_l}{kT_e}} \quad (3.15.c)$$

The cross-section from **Shemansky et al. (1985)** and **Avakyan et al. (1998)** reads:

$$\sigma_{lu} = \frac{\pi a_0^2}{g_l} \frac{R_y}{E_u - E_l} \frac{\Omega_{lu}(u_{lu})}{u_{lu}} \quad (3.16.a)$$

where Ω_{lu} is the collision strength given by:

$$\Omega_{lu}(x) = C_7 \left[\frac{C_0}{x^2} \left(1 - \frac{1}{x} \right) + \sum_{k=1}^4 C_k (x-1) e^{-kC_8 x} + C_5 + \frac{C_6}{x} + \ln(x) \right] \quad (3.16.b)$$

where $C_{k,k=0..8}$ are adjustable parameters from experimental data. Integrating analytically equation 3.12 yields the rate constant:

$$K_{lu} = \frac{8\pi^2 a_0^2}{g_l \sqrt{m_e}} (2\pi kT_e)^{-\frac{3}{2}} \frac{R_y}{E_u - E_l} \xi_3 \quad (3.16.c)$$

where:

$$\xi_3 = C_7 C_0 \left[\rho \left(\frac{\rho}{2} - 1 \right) E_1 + \frac{e^{-\rho}}{2} \left(1 - \frac{1}{\rho} \right) \right] + \sum_{k=1}^4 C_7 C_k \frac{e^{-\rho - kC_8}}{\rho + kC_8} + C_7 C_5 \frac{e^{-\rho}}{\rho} + C_7 \left(C_6 + \frac{1}{\rho} \right) E_1 \quad (3.16.d)$$

where $\rho = (E_u - E_l) / kT_e$ and E_l is the first order integral, which was expanded by Abramowitz and Stegun (1972) as:

$$E_1 = \frac{\rho^2 + 4.03640\rho + 1.15198 e^{-\rho}}{\rho^2 + 5.03637\rho + 4.19160} \quad (3.16.e)$$

b. Optically forbidden transitions

For optically forbidden transitions, Drawin (1966) proposed semi-empirical cross-sections for the following cases:

- transitions with no change in multiplicity

$$\text{Cross-section:} \quad \sigma_{lu} = 4\pi a_0^2 \left(\frac{R_y}{E_u - E_l} \right)^2 \alpha_{lu} \frac{u_{lu} - 1}{u_{lu}^2} \quad (3.17.a)$$

$$\text{Rate constant:} \quad K_{lu} = 4\pi a_0^2 \sqrt{\frac{8kT_e}{\pi m_e}} \left(\frac{E_u - E_l}{kT_e} \right)^2 \alpha_{lu} \xi_4 \quad (3.17.b)$$

where:

$$\xi_4 = 0.23293 \left(\frac{E_u - E_l}{kT_e} \right)^{-1.4933} e^{-\frac{E_u - E_l}{kT_e}} \quad (3.17.c)$$

- singlet-triplet forbidden transitions

$$\sigma_{lu} = 4\pi a_0^2 \left(\frac{R_y}{E_u - E_l} \right)^2 \alpha_{lu} \frac{u_{lu} - 1}{u_{lu}^5} \quad (3.17.d)$$

- triplet-singlet forbidden transitions

$$\sigma_{lu} = 4\pi a_0^2 \left(\frac{R_y}{E_u - E_l} \right)^2 \frac{\alpha_{lu}}{u_{lu}} \quad (3.17.e)$$

In addition to these semi-empirical cross-sections, there have been quantum mechanical calculations. Frost *et al.* (1998) and Zatsarinny and Tayal (2003) conducted *ab initio* quantum computations for nitrogen and oxygen atoms, respectively. They provided discrete values of the transition effective collision strength γ_{lu} as a function of the electron temperature T_e . The rate constant K_{lu} and the collision strength γ_{lu} are related as follows:

$$K_{lu} = 2cf_s a_0^2 \sqrt{\frac{\pi R_y}{kT_e}} \frac{\gamma_{lu}}{g_l} e^{-\frac{E_u - E_l}{kT_e}} \quad (3.18)$$

III.5.1.3. Selected rate constants

This subsection compares the various sources of electron-impact excitation rate constants. Atomic, then molecular processes are presented. The available electron-impact excitation cross-sections presented in subsection III.5.1.1 were integrated using equation 3.11, to obtain the experimental rate constants.

a. Selection of rate constants in N

Figure 3.7 compares the experimental rate constants with the rate constants of Drawin (1966), Park (1985), Frost *et al.* (1998) for N. The rate constant K_{l-3} from Park (1985) is in good agreement with the experimental rate constant derived from Yang and Doering (1996) cross-section measurement. The excitation rate constants K_{l-4} and K_{l-6} from Frost *et al.* (1998) are in good agreement with the experimental rate constant derived from Spence and Burrow (1980) and Stone and Zipf (1973) cross-section measurements. The selected rate constants are listed in table 3.8.

Table 3.8: Selected electron-impact excitation rate constants in N

Transitions	Rate constant	Equations
$l \leq 3 \rightarrow u \leq 3$	Park (1985)	
$l \leq 3 \rightarrow 4 \leq u \leq 5$	Frost <i>et al.</i> (1998)	(3.18)
all other transitions	Drawin (1966)	(3.15) or (3.17)

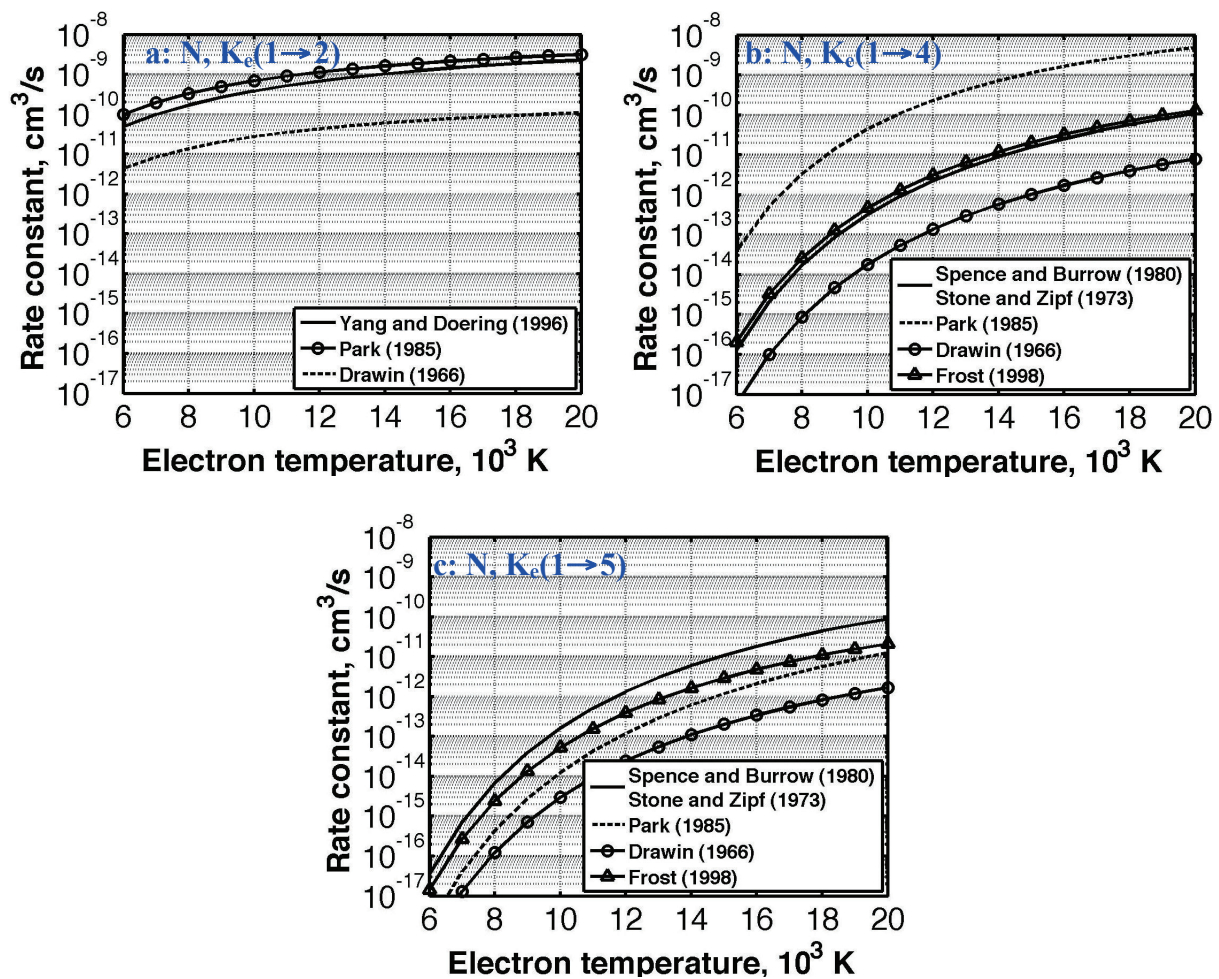


Figure 3.7: Comparison between the electron-impact excitation rate constants from Spence and Burrow (1980), Stone and Zipf (1973) and Yang and Doering (1996) and the theoretical rate constants from Drawin (1966), Park (1985) and Frost *et al.* (1998) in N. a) $K_e(1 \rightarrow 2)$, b) $K_e(1 \rightarrow 4)$, c) $K_e(1 \rightarrow 5)$

b. Selection of rate constants in O

Figure 3.8 compares the experimental rate constants with the rate constants of Drawin (1966), Park (1985), Zatsarinny and Tayal (2003) for O. The rate constant K_{l-2} from Park (1985) is in good agreement with the experimental rate constant derived from Doering (1992) cross-

section measurement. The rate constant K_{l-5} from Zatsarinny and Tayal (2003) is in good agreement with the experimental rate constant derived from Kanic *et al.* (2001) and Johnson *et al.* (2003) cross-section measurement. The rate constants K_{l-9} and K_{l-11} from Drawin (1966) are in good agreement with the experimental rate constant derived from Kanic *et al.* (2001) and Johnson *et al.* (2003) cross-section measurement. The selected rate constants are listed in table 3.9.

Table 3.9: Selected electron-impact excitation rate constants in O

Transitions	Rate constant	Equations
$l \leq 3 \rightarrow u \leq 3$	Park (1985)	
$l \leq 3 \rightarrow 4 \leq u \leq 5$	Zatsarinny and Tayal (2003)	(3.18)
all other transitions	Drawin (1966)	(3.15) or (3.17)

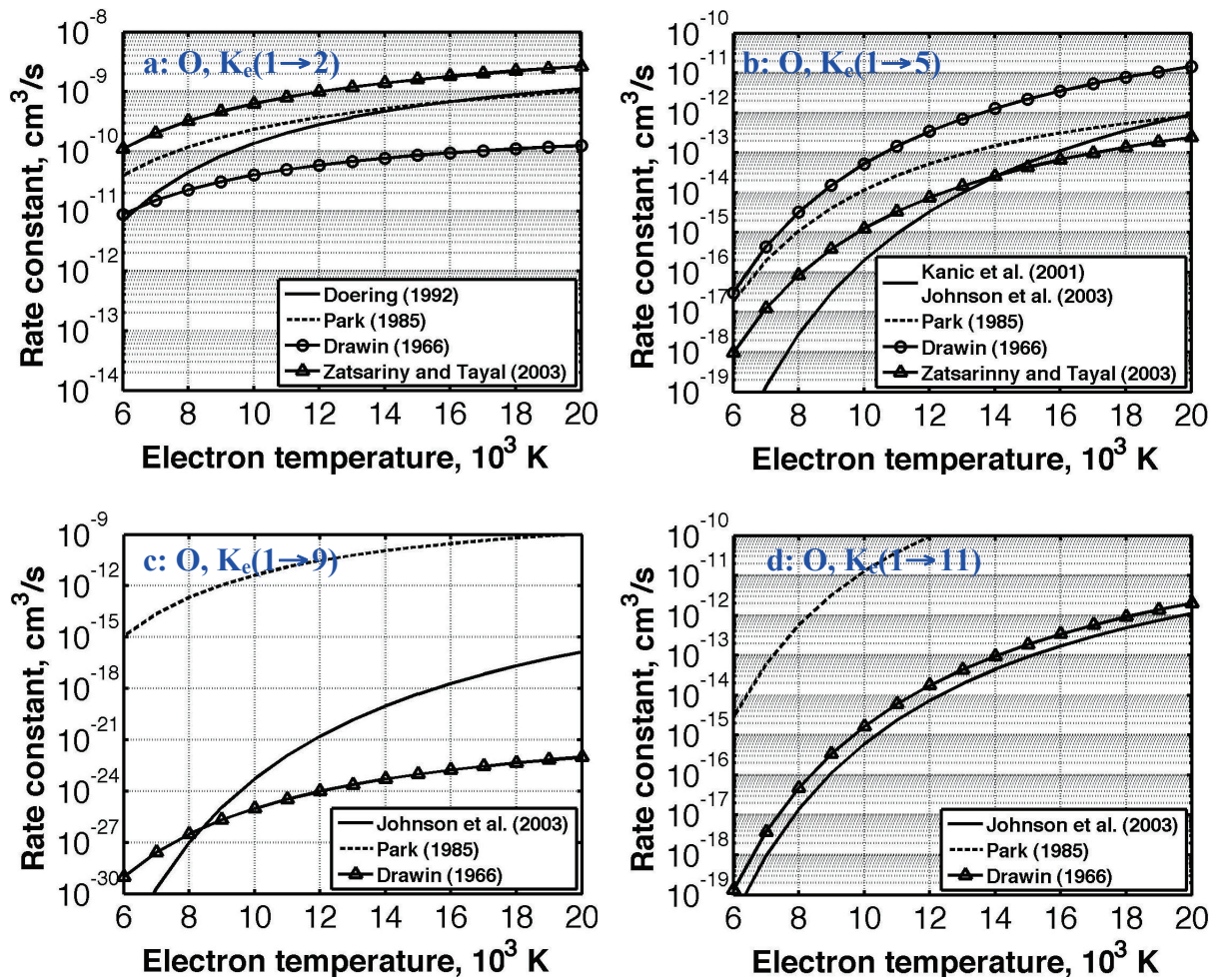


Figure 3.8: Comparison between the electron-impact excitation rate constants from Doering (1992), Kanic *et al.* (2001) and Johnson *et al.* (2003) and the theoretical rate constants from Drawin (1966), Park (1985) and Zatsarinny and Tayal (2003) in O. a) K_c(1→2), b) K_c(1→4), c) K_c(1→9), d) K_c(1→11)

c. Selection of rate constants in N₂

The electron-impact electronic excitation cross-sections from Cartwright *et al.* (1977), Zipf and Gorman (1980), Majeed and Strickland (1997), Itikawa (2005) Johnson *et al.* (2005) and recently Khakoo *et al.* (2006) and Malone *et al.* (2011) were integrated using equation 3.11, to obtain the experimental rate constants. Figure 3.9 compares the experimental constants with the rate constants from Teulet *et al.* (1999), and Larichiutta (2011).

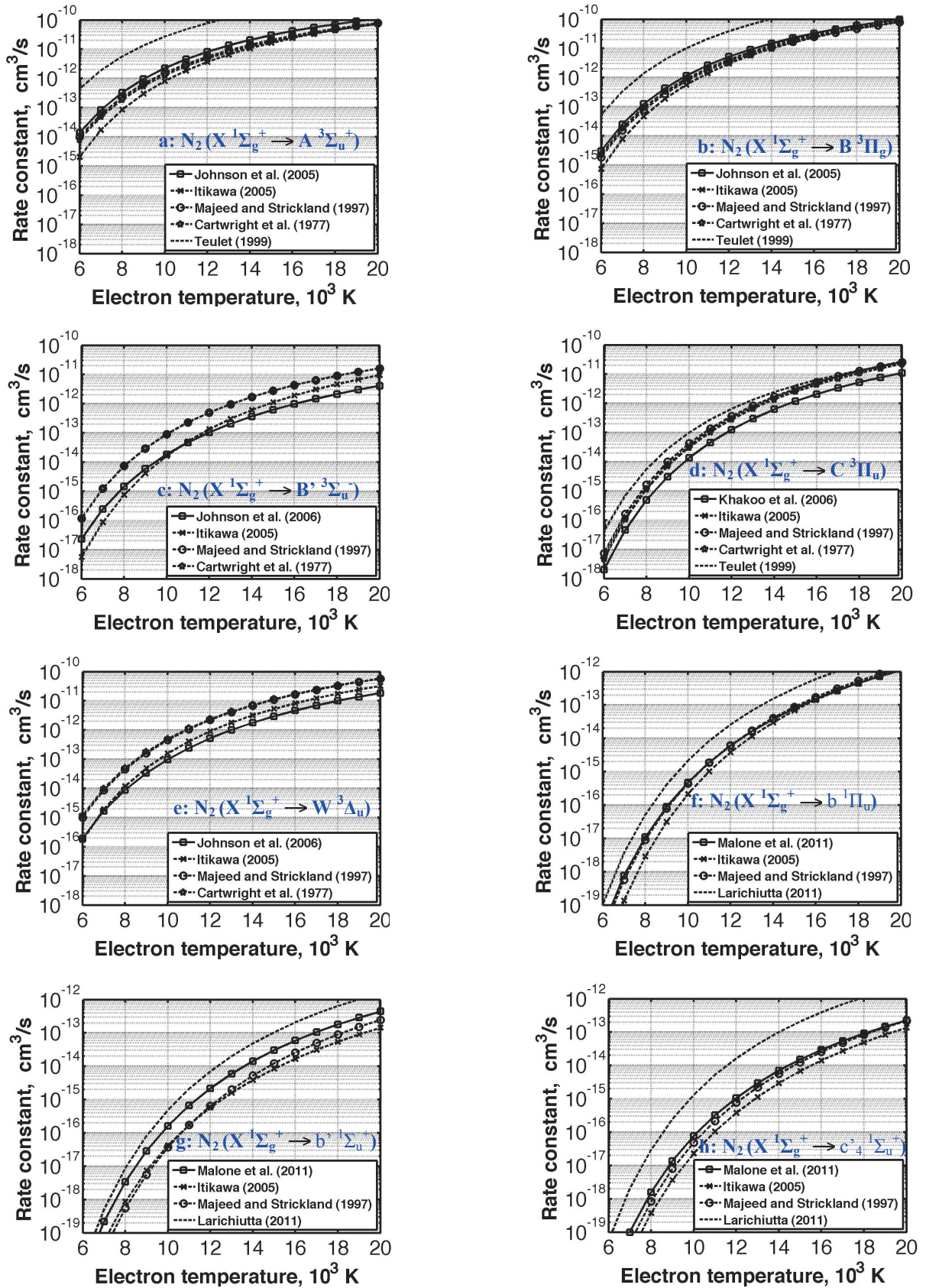


Figure 3.9: Comparison between the experimental rate constants from Majeed and Strickland (1997), Itikawa (2005), Johnson *et al.* (2005), Khakoo *et al.* (2006), Malone *et al.* (2011) and the rate constants from Teulet *et al.* (1999) and Larichiutta (2011). a: $N_2(X^1\Sigma_g^+ \rightarrow A^3\Sigma_u^+)$, b: $N_2(X^1\Sigma_g^+ \rightarrow B^3\Pi_g)$, c: $N_2(X^1\Sigma_g^+ \rightarrow B'^3\Sigma_u^-)$, d: $N_2(X^1\Sigma_g^+ \rightarrow C^3\Pi_u)$, e: $N_2(X^1\Sigma_g^+ \rightarrow W^3\Delta_u)$, f: $N_2(X^1\Sigma_g^+ \rightarrow b^1\Pi_u)$, g: $N_2(X^1\Sigma_g^+ \rightarrow b'^1\Sigma_u^+)$, h: $N_2(X^1\Sigma_g^+ \rightarrow c'_4{}^1\Sigma_u^+)$

It is shown that the semi-empirical rate constants from Teulet *et al.* (1999), and Larichiutta (2011) overestimate by one order of magnitude the rate constants obtained with the experimental cross-sections.

Ajello *et al.* (1989), James *et al.* (1990) measured electron-impact cross-sections from the ground vibrational level of $N_2(X^1\Sigma_g^+(v''=0))$ to several vibrational manifolds of the excited electronic states (b, b', c'_4). They fitted the measured vibronic cross-sections using equation 3.16.b. The electronic cross-sections were obtained by dividing the vibronic cross-sections by the perturbed Franck-Condon factors obtained in **chapter 2**. The results were compared with the measured experimental cross-sections from Majeed and Strickland (1997), Itikawa (2006) and Malone *et al.* (2011), as shown in figure 3.10.

Good agreement is obtained between the experimental and the theoretical electronic cross-sections, thus justifying the applicability of the Franck-Condon principle. Subsequently, the perturbed Franck-Condon factors were used to determine the vibrationally specific electron-impact cross-sections for the remaining transitions from all $v''>0$.

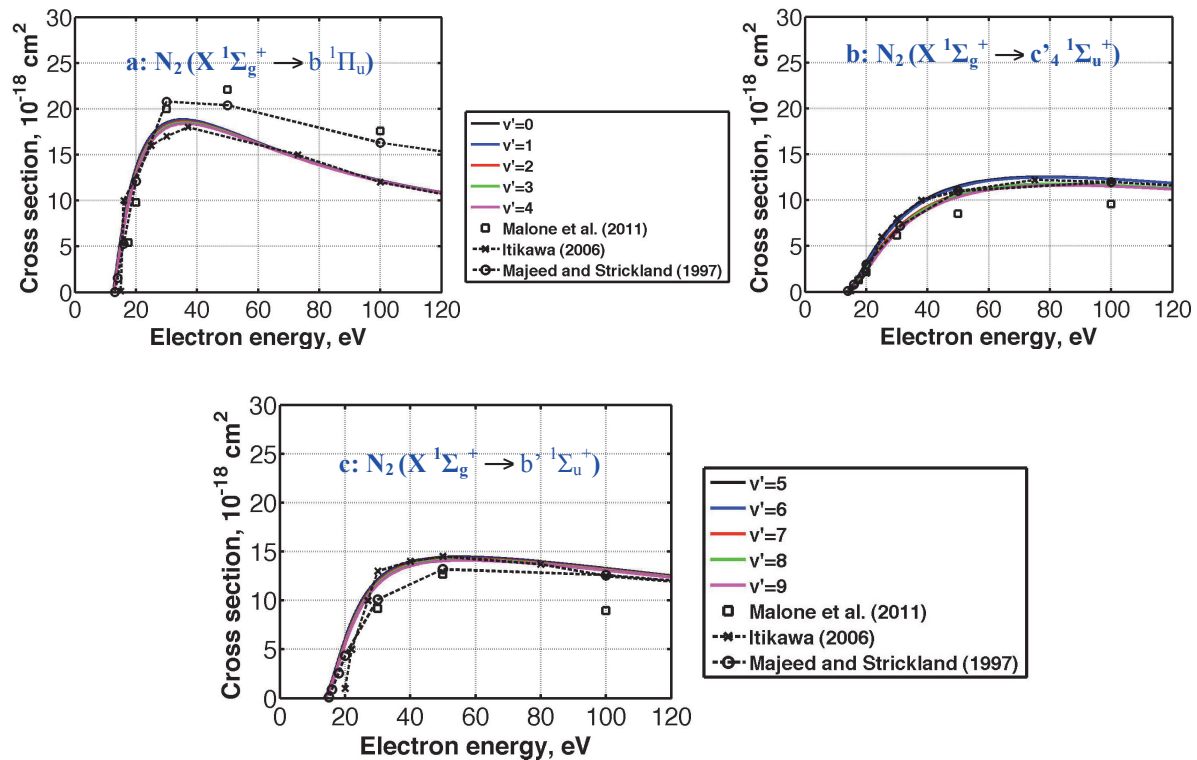


Figure 3.10: Assessment of the Franck-Condon principle for N_2 VUV systems⁷. a: $N_2(X^1\Sigma_g^+ \rightarrow b^1\Pi_u)$, b: $N_2(X^1\Sigma_g^+ \rightarrow c'_4^1\Sigma_u^+)$, c: $N_2(X^1\Sigma_g^+ \rightarrow b'^1\Sigma_u^+)$

The vibronic rate constants for which there exist no experimental data were determined by Pierrot *et al.* (1999) using the Weighted Rate Coefficient (WRC) approach. In this approach, the vibronic rate constants are obtained by averaging the rovibrational rates constants over the rotational levels. The rovibrational rate constants are obtained by integrating the elementary cross-sections given by:

⁷ For clarity, figure 3.10 presents the five first observed electron-impact vibrational cross-sections observed by Ajello *et al.* (1989) and James *et al.* (1990).

$$\chi_{Y''v''J''}^{Y'v'J'}(\varepsilon) = q_{Y''v''}^{Y'v'} \frac{S_{Y''J''}^{Y'J'}}{2J''+1} \sigma(\varepsilon, \Delta E_{Y''v''J''}^{Y'v'J'}) \quad (3.19)$$

where q is the Franck-Condon factor, S is the rotational line strength, both presented in **chapter 2**, ΔE is the energy threshold and σ is the cross-section given by Seaton (1962) and Drawin (1966) for optically forbidden and allowed transitions, respectively.

The energy E_{YvJ} of a rovibronic energy level YvJ is computed here in a simple manner by assuming that the total energy is the sum of the electronic, vibrational and rotational contributions:

$$E_{YvJ} = T_e + G_Y(v) + F_{Yv}(J) \quad (3.20.a)$$

where:

$$G_Y(v) = \omega_e \left(v + \frac{1}{2} \right) - \omega_e x_e \left(v + \frac{1}{2} \right)^2 + \omega_e y_e \left(v + \frac{1}{2} \right)^3 + \dots \quad (3.20.b)$$

$$F_{Yv}(J) = B_v J(J+1) - D_v J^2(J+1)^2 + \dots$$

with:

$$B_v = B_e - \alpha_e \left(v + \frac{1}{2} \right) + \dots \quad (3.20.c)$$

$$D_v = D_e + \beta_e \left(v + \frac{1}{2} \right) + \dots$$

The constants T_e , ω_e , $\omega_e x_e$, $\omega_e y_e$, B_e , α_e , D_e and β_e were taken from Pierrot *et al.* (1999)

d. Selection of rate constants in N_2^+

The electron-impact electronic excitation cross-section from Crandall *et al.* (1974) was integrated using equation 3.11, to obtain the experimental rate constant. Figure 3.11 compares the experimental constant with the rate constants from Teulet *et al.* (1999).

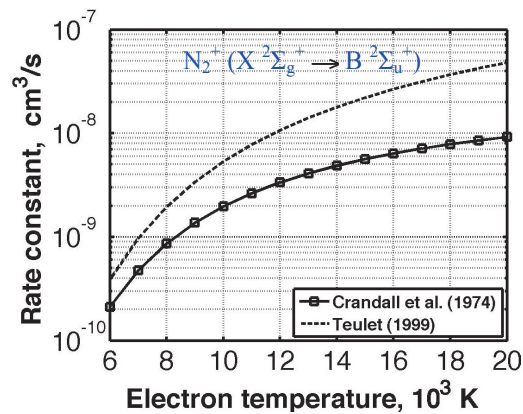


Figure 3.11: Comparison between the experimental rate constant from Crandall *et al.* (1974) and the rate constant from Teulet *et al.* (1999)

It is shown that the semi-empirical rate constants from Teulet *et al.* (1999) overestimate by one order of magnitude the rate constant obtained with the experimental cross-section.

The vibronic rate constants for the transition $N_2^+(X^2\Sigma_g^+ \rightarrow B^2\Sigma_u^+)$ was determined using the

Franck-Condon principle. The vibronic rate constants for which there exist no experimental data were determined by Pierrot *et al.* (1999) using the Weighted Rate Coefficient (WRC) approach.

Tables 3.10 and 3.11 list the sources to compute the rate constants of N_2 and N_2^+ , respectively.

Table 3.10: Selected electron-impact excitation vibrational rate constants in N_2

Transitions	Method	Cross-sections	Franck-Condon factors
$(X, v'') \rightarrow (A, v')$	FCP	Johnson <i>et al.</i> (2005)	a)
$(X, v'') \rightarrow (B, v')$	FCP	Johnson <i>et al.</i> (2005)	a)
$(X, v'') \rightarrow (W, v')$	FCP	Johnson <i>et al.</i> (2005)	a)
$(X, v'') \rightarrow (B', v')$	FCP	Johnson <i>et al.</i> (2005)	a)
$(X, v'') \rightarrow (C, v')$	FCP	Khakoo <i>et al.</i> (2006)	a)
$(A, v'') \rightarrow (B, v')$	WRC	Drawin (1966)	a)
$(A, v'') \rightarrow (W, v')$	WRC	Seaton(1962)	a)
$(A, v'') \rightarrow (B', v')$	WRC	Seaton(1962)	a)
$(A, v'') \rightarrow (C, v')$	WRC	Seaton(1962)	a)
$(B, v'') \rightarrow (W, v')$	WRC	Seaton(1962)	a)
$(B, v'') \rightarrow (B', v')$	WRC	Seaton(1962)	a)
$(B, v'') \rightarrow (C, v')$	WRC	Drawin (1966)	a)
$(W, v'') \rightarrow (B', v')$	WRC	Seaton(1962)	a)
$(W, v'') \rightarrow (C, v')$	WRC	Seaton(1962)	a)
$(B', v'') \rightarrow (C, v')$	WRC	Seaton(1962)	a)
$(X, v'') \rightarrow (b, v')$	FCP	Malone <i>et al.</i> (2011)	b)
$(X, v'') \rightarrow (b', v')$	FCP	Malone <i>et al.</i> (2011)	b)
$(X, v'') \rightarrow (c'_4, v')$	FCP	Malone <i>et al.</i> (2011)	b)
$(X, v'') \rightarrow (c_3, v')$	FCP	Larichiutta (2011)	b)
$(X, v'') \rightarrow (o_3, v')$	FCP	Larichiutta (2011)	b)
$(X, v'') \rightarrow (e', v')$	FCP	Larichiutta (2011)	b)

Table 3.11: Selected electron-impact excitation vibrational rate constants in N_2^+

Transitions	Method	Cross-section	Franck-Condon factor
$(X, v'') \rightarrow (A, v')$	WRC	Seaton(1962)	a)
$(X, v'') \rightarrow (B, v')$	FCP	Crandall <i>et al.</i> (1974)	a)
$(X, v'') \rightarrow (C, v')$	WRC	Seaton(1962)	a)
$(A, v'') \rightarrow (B, v')$	WRC	Drawin (1966)	a)
$(A, v'') \rightarrow (C, v')$	WRC	Seaton(1962)	a)
$(B, v'') \rightarrow (C, v')$	WRC	Seaton(1962)	a)

(a): Chauveau and Laux (2001), private communication

(b): Laux and Lemal (2012)

III.5.2. Electron-impact ionization

III.5.2.1. Review of theoretical data

Electron-impact ionization processes have been investigated by Drawin (1966), Kim and Rudd (1994), Kim (2001), Kim and Desclaux (2002) and Huo (2008).

Drawin (1966) proposed a semi-empirical model. Let us denote by u and c the excited state and the continuum, ε the electron-impact energy. Then, the cross-section σ_{uc} given by **Drawin's** formula (1966) reads:

$$\sigma_{uc} = 4\pi a_0^2 \left(\frac{R_y}{E_{ion} - E_u} \right)^2 f_u N_u \frac{w-1}{w^2} \ln(\beta w) \quad (3.21.a)$$

where

$$w = \frac{\varepsilon}{E_{ion} - E_u}, \beta = 1.25 \left(1 + \frac{z-1}{z+1} \right) \quad (3.21.b)$$

where z is the number of charge for atoms, f is the oscillator strength for ionization from state u attributed to one electron ($f_1=0.66, f_2=0.71, f_3=0.81, f_4=0.94, f_{n>4}=1.00$), N_u is the number of equivalent electron in the outer shell. The corresponding ionization rate constant is given by:

$$K_{uc} = 4\pi a_0^2 \left(\frac{R_y}{E_{ion} - E_u} \right)^2 f_u N_u \sqrt{\frac{8kT_e}{\pi m_e}} \zeta_5 \quad (3.21.c)$$

where $\rho = (E_{ion} - E_l)/kT_e$ and ζ_5 is given by:

$$\zeta_5 = \frac{\rho e^{-\rho}}{1 + \rho} \left[\frac{1}{20 + \rho} + \ln \left(\beta \left(1 + \frac{1}{\rho} \right) \right) \right] \quad (3.21.d)$$

Kim and Rudd (1994) developed the Binary-Encounter Bethe (BEB) model. Kim (2001), Kim and Desclaux (2002) and Huo (2008) subsequently upgraded the BEB model to take into account ionization by low energy impact electron and found very good agreement with available experimental data. The **BEB** cross-section reads:

$$\sigma_{uc}^s = 4\pi a_0^2 \left(\frac{R_y}{E_u^s} \right)^2 N_u^s \zeta_6 \quad (3.22.a)$$

where:

$$u = \frac{\varepsilon}{E_u^s}, w = \frac{W}{E_u^s} \quad (3.22.b)$$

and:

$$\zeta_6 = \frac{1}{1 + u + w} \left[\frac{\ln u}{2} \left(1 - \frac{1}{u} \right)^2 + 1 - \frac{1}{u} - \frac{\ln u}{u + 1} \right] \quad (3.22.c)$$

where N_u^s is the number of electron in shell s , E_u^s is the energy necessary to remove an electrons from shell s , W is the average kinetic energy of electron in shell s .

Recently, Huo (2009) provided the electron-impact ionization rate constants of the ten first electronic states of atomic nitrogen using quantum mechanical calculations.

III.5.2.2. Selected rate constants

a. Selection of rate constants in N and O

Table 3.12 and 3.13 list the selected electron-impact ionization rate constants for N and O, respectively.

Table 3.12: Selected electron-impact ionization rate constants in N

Transitions	Rate constant	Equation
$l \leq 10 \rightarrow c$	Huo (2009)	
all other transitions	Drawin (1966)	(3.19)

Table 3.13: Selected electron-impact ionization rate constants in O

Transitions	Rate constant	Equation
all transitions	Drawin (1966)	(3.19)

b. Selection of rate constants in N₂

The electron-impact ionization rate constants were computed with the WRC approach (Pierrot *et al.*, 1999), outlined in subsection III.5.2 and are listed in table 3.14. The elementary cross-sections were computed with the BEB model (equation 3.20) and the data from Hwang *et al.* (1996). The Franck-Condon factors were taken from Chauveau and Laux (2001).

Table 3.14: Selected electron-impact ionization rate constants in N₂

Transitions	Method
N ₂ (X, v'') → N ₂ ⁺ (X, v')	WRC
N ₂ (X, v'') → N ₂ ⁺ (A, v')	WRC
N ₂ (X, v'') → N ₂ ⁺ (B, v')	WRC
N ₂ (A, v'') → N ₂ ⁺ (X, v')	WRC
N ₂ (A, v'') → N ₂ ⁺ (A, v')	WRC
N ₂ (A, v'') → N ₂ ⁺ (B, v')	WRC
N ₂ (B, v'') → N ₂ ⁺ (X, v')	WRC
N ₂ (B, v'') → N ₂ ⁺ (A, v')	WRC
N ₂ (B, v'') → N ₂ ⁺ (B, v')	WRC
N ₂ (W, v'') → N ₂ ⁺ (X, v')	WRC
N ₂ (W, v'') → N ₂ ⁺ (A, v')	WRC
N ₂ (W, v'') → N ₂ ⁺ (B, v')	WRC
N ₂ (B', v'') → N ₂ ⁺ (X, v')	WRC
N ₂ (B', v'') → N ₂ ⁺ (A, v')	WRC
N ₂ (B', v'') → N ₂ ⁺ (B, v')	WRC
N ₂ (C, v'') → N ₂ ⁺ (X, v')	WRC
N ₂ (C, v'') → N ₂ ⁺ (A, v')	WRC
N ₂ (C, v'') → N ₂ ⁺ (B, v')	WRC

III.5.3. Heavy-particle impact excitation

Heavy-particle impact processes are important when electrons are scarce. There have been few studies on this process chief among them the works from Flannery (1970), Park (1986) Bultel *et al.* (2006) and Surzhikov (2009).

III.5.3.1. Review of theoretical data

Let us denote by l and u the lower and upper electronic states of the optically allowed transition respectively, ε the heavy-particle impact energy. Then, the cross-section σ_{lu} given by **Bultel's** formula (2006), which is taken from Capitelli *et al.* (2000) for atoms-atoms collisions reads:

$$\sigma_{lu} = \beta_{ul}(u - 1) \quad (3.23.a)$$

After integration, the rate constant reads:

$$K_{lu} = \frac{8\pi}{\sqrt{\mu}} (2\pi k T_g)^{-\frac{3}{2}} \beta_{ul} \zeta_7 \quad (3.23.b)$$

where $\rho = (E_u - E_l)/kT_g$ and ζ_7 is given by:

$$\zeta_7 = \frac{e^{-\rho}}{\rho^2} \left(1 + \frac{2}{\rho}\right) \quad (3.23.c)$$

For atom-molecule collisions, the cross-section reads:

$$\sigma_{lu} = 10^{-16} \frac{\ln u}{u} \quad (3.23.d)$$

After integration, the rate constant reads:

$$K_{lu} = \frac{8\pi}{\sqrt{\mu}} (2\pi k T_g)^{-\frac{3}{2}} \zeta_8 \quad (3.23.e)$$

where :

$$\zeta_8 = 10^{-16} \frac{E_l(\rho)}{\rho} \quad (3.23.f)$$

and $u = \varepsilon / (E_u - E_l)$, $\beta_{ul} = 3.4 \cdot 10^{-25} (E_u - E_l)$ for transitions between the metastable states, $\beta_{ul} = 3.4 \cdot 10^{-2.5} (E_u - E_l)^{-1.26}$ for transitions between higher states and E_l is given by equation 3.16.e.

The cross-section σ_{lu} given by **Park (1986)** reads:

$$\sigma_{lu} = 10^{-16} \frac{\ln u}{u} \quad (3.24.a)$$

The integration of the cross-section yields:

$$K_{lu} = \frac{8\pi}{\sqrt{\mu}} (2\pi k T_g)^{-\frac{3}{2}} \zeta_8 \quad (3.24.b)$$

where :

$$\zeta_8 = 10^{-16} \frac{E_l(\rho)}{\rho} \quad (3.24.c)$$

where E_l is given by equation 3.16.e.

The rate constant given by **Surzhikov (2009)** reads:

$$K_{lu} = 32\pi a_0^2 \left(\frac{R_y}{E_{ion} - E_u} \right)^2 f_{ul} \sqrt{\frac{k T_g}{\pi m_M}} \zeta_9 \quad (3.25.a)$$

where:

$$\zeta_9 = \frac{m_M m_e}{m_h (m_M + m_e)} \left(1 + \frac{1}{\rho}\right) \frac{e^{-\rho}}{1 + \left(\frac{2m_e}{(m_M + m_e)\rho} \right)^2} \quad (3.25.b)$$

Flannery (1970) computed the heavy-particle impact rates constants for excitation within hydrogenic levels ($E > 13$ eV, $\Delta E = 0.01$ eV). After correction of a few typos in the paper of Flannery (1970), the rate constant reads⁸:

$$K_{lu} = 16\pi a_0^2 k T_g (2\pi^3 E_{ion} \mu)^{-\frac{1}{2}} \eta^{\frac{5}{2}} \tau^{\frac{3}{2}} \left(a + 2 + \frac{1}{a} \right) \left(e^{\psi_1(\tau-\eta)} - \psi_2 \right) \quad (3.26.a)$$

where :

$$\psi_1 = \frac{\sqrt{\pi}}{6\eta^3} + \frac{1}{\sqrt{a}} \left[\frac{1}{8\tau^{\frac{5}{2}}} \left(\frac{\pi}{2} - \text{Arc tan} \left(\sqrt{\frac{\eta}{\tau} - 1} \right) \right) - \frac{\sqrt{\eta-\tau}}{\tau^2 \eta} \left(\frac{1}{8} + \frac{\tau}{12\eta} - \frac{\tau^2}{3\eta^2} \right) \right] \quad (3.26.b)$$

$$\psi_2 = \frac{\sqrt{\pi}}{6\eta^3} \text{erfc}(\sqrt{\eta-\tau}) + \frac{\sqrt{\eta-\tau} e^{\tau-\eta}}{6\eta^3} - \frac{1}{\sqrt{a}} \frac{\pi}{16\eta^{\frac{5}{2}}} e^{\tau-\eta} \quad (3.26.c)$$

where $a = \mu/m_e$, $\tau = E_l/kT_g$ and $\eta = E_u/kT_g$ and erfc is the complementary error function which was expanded by Abramowitch and Segun (1972):

$$\text{erfc}(x) = \frac{1}{(1 + 0.2784x + 0.2304x^2 + 0.001x^3 + 0.078x^4)^4} \quad (3.26.d)$$

III.5.3.2. Selected rate constants

To the author's knowledge, there are no experimental data on heavy-particle impact excitation processes between N and O atoms. Figure 3.12 compares the rate constants from Flannery (1970), Park (1986), Bultel *et al.* (2006) and Surzhikov (2009) with the upper limit given by kinetic rate constants for different transitions in N. As illustrated in figure 3.12, large discrepancies exist among the various sources. Also, the rate constants from Flannery (1970) between a lower level to a level close the ionization limit are surprisingly of the same order of magnitude than between two lower levels, as illustrated in figures 3.12.a and 3.12.c. For this reason, the rate constants of Flannery (1970) were not used in the present work. Also, the rate constants between two levels close to the ionization limit from Park (1985), Flannery (1970) and Bultel *et al.* (2006) are higher than the kinetic rate constants. Thus, the rate constants from Surzhikov (2009) will be used for the transitions between the lower excited states and the states close to the ionization limit.

Kelley (2013) performed an order of magnitude analysis of heavy-particle impact rate constants for N-N, N-O and O-O collisions and showed that their values should be of the order of 10^{-15} - 10^{-13} cm³/s. Given this order of magnitude, it appears that the rate constants from Park (1985), Bultel *et al.* (2006) or Surzhikov (2009) are the most appropriate and will be tested in the present work. Tables 3.15 and 3.16 list the various sources used to compute the heavy-particle impact excitation processes in N and O, respectively.

⁸ The heavy-particle impact excitation rate constants from the first level of N ($\tau = 0$) tend towards infinity. Therefore, they will be assumed to be equal to the heavy-particle impact excitation rate constants from the second level of N ($\tau = E_2/kT_g$).

Table 3.15: Selected heavy-particle impact excitation rate constants in N (M=N, O)

Transitions	Rate constant	Equations
$1 \leq l \leq 10 \rightarrow 2 \leq u \leq 11$	Park (1985)	(3.24)
$11 \leq l \leq 22 \rightarrow 12 \leq u \leq 22$	Surzhikov (1998)	(3.25)

Table 3.16: Selected heavy-particle impact excitation rate constants in O (M=N, O)

Transitions	Rate constant	Equations
$1 \leq l \leq 10 \rightarrow 2 \leq u \leq 11$	Park (1985)	(3.24)
$11 \leq l \leq 19 \rightarrow 12 \leq u \leq 19$	Surzhikov (1998)	(3.25)

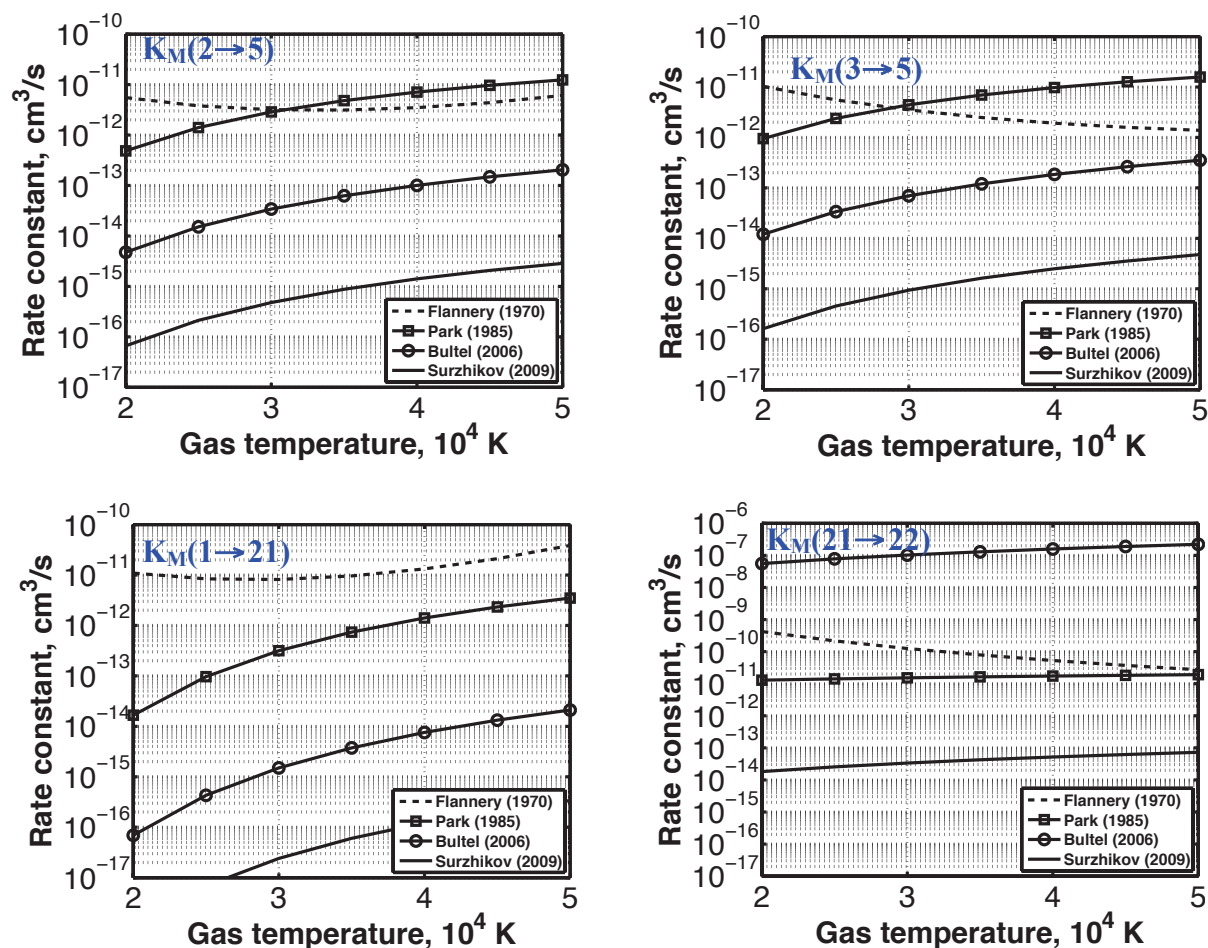


Figure 3.12: Heavy-particle impact excitation rate constants in N.

III.5.4. Electron-impact dissociation

The electron-impact dissociation vibrational rate constants were determined by Pierrot *et al.* (1999) using the experimental data from Majeed and Strickland (1997).

III.5.5. Heavy-particle impact dissociation

The heavy-particle impact dissociation rate constants governing the population of the vibrational manifold of the ground state of N₂ were determined by Pierrot *et al.* (1999) using Park (1985) analytical cross-sections. For the other vibrational manifolds, it was assumed that the last vibrational level below the dissociation limit is dissociated. Heavy-particle impact dissociation occurs then as a result of V-T and V-V transfer to this vibrational level.

III.5.6. V-T, V-V, V-e exchange energy processes

The V-e vibrational rate constants were determined by Pierrot *et al.* (1999) by using the method of Kazansky and Yelets (1984). The V-V, V-T vibrational rate constants were determined using the SSH theory (Billing and Fisher, 1979). The SSH theory, based on the harmonic oscillator, assumes monoquantum jumps, therefore needs to be improved for high energy heavy-particle impact.

III.5.7. Predissociation

The predissociation rate constants were computed by Pierrot *et al.* (1999) using the experimental data from Geisen *et al.* (1990).

III.5.8. Radiative processes

Johnston *et al.* (2008), Panesi *et al.* (2011) and Potter (2011) showed that the bound-free and free-free mechanisms were negligible for the reentry conditions ($V < 12$ km/s) considered in the present work. The atomic and molecular bound-bound radiative processes were modeled using the Einstein coefficients mentioned in **chapter 2**, with the use of the escape factor. The main atomic line positions as well as their transition probabilities were reviewed by Wiese *et al.* (1996) and are listed in appendix C. The molecular transitions probabilities were taken from Laux *et al.* (1992).

III.6. Summary

The radiative heat flux on a spacecraft during its entry into Earth's atmosphere strongly depends on the populations of the electronic states of N and O atoms and the vibrational levels of the electronic states of N_2 and N_2^+ , which are governed by collisional and radiative processes under nonequilibrium conditions.

In this work, a new CR model was developed. The collisional processes encompassed electron- and heavy-particle impact excitation and electron-impact ionization processes for the excited states of N and O as well as the vibrational levels of N_2 and N_2^+ electronic states. The rate constants governing these processes were selected from among the available experimental data and the most appropriate theoretical formulations. The present compilation is compared with the compilations of Park (1985), Johnston (2006) and Panesi *et al.* (2011) in table 3.17. The radiative processes taken into account were the bound-bound mechanisms. The flowfield and CR models were coupled through with the QSS assumption, in accordance with previous studies. The CR and spectral models were coupled with the use of the escape factor concept set to zero for VUV lines and to one for visible and infrared lines, in accordance with previous studies.

Table 3.17: Comparison of the rate constants selected in the present CR model and in the CR models developed by Park (1985), Johnston (2006) and Panesi *et al.* (2011)

a. Electron-impact excitation in N					
Transitions	Park (1985)	Johnston (2006)	Panesi <i>et al.</i> (2011)	Present	Note
$l \leq 3 \rightarrow u \leq 3$	a)	b)	f)	a)	The rate constant K_{1-3} inferred from the measurement of Ref. 1 was fairly well predicted by the formula a)
$l \leq 3 \rightarrow 4 \leq u \leq 6$	a)	b)	f)	b)	The rate constants K_{1-4} and K_{1-5} inferred from the measurement of Ref. 2-3 were fairly well predicted by the formula b)
Other transitions	a)	b), c), d), e)	f)	g)	

a) Park (1985); b) Frost *et al.* (2006); c) Van Regmorter (1962); d) Gryzinski (1958)
e) Allen (1962); f) Bultel *et al.* (2006); g) Drawin (1966)

1) Yang and Doering (1993); 2) Spence and Burrow (1980); 3) Stone and Zipf (1973)

b. Electron-impact excitation in O					
Transitions	Park (1985)	Johnston (2006)	Panesi <i>et al.</i> (2011)	Present	Note
$l \leq 3 \rightarrow u \leq 3$	a)	b)	g)	a)	The rate constant K_{1-2} inferred from the measurement of Ref. 1 was fairly well predicted by the formula a)
$l \leq 3 \rightarrow 4 \leq u \leq 6$	a)	b)	g)	b)	The rate constant K_{1-5} inferred from the measurement of Ref. 2-3 was fairly well predicted by the formula b)
Other transitions	a)	b), c), d), e), f)	g)	h)	The rate constants K_{1-9} and K_{1-11} inferred from the measurement of Ref. 2-3 were fairly well predicted by the formula h)

a) Park (1985); b) Zatsarinny and Tayal (2003); c) Gordillo and Kunc (1995); d) Van Regmorter (1962);
e) Allen (1962); f) Gryzinski (1958); g) Bultel *et al.* (2006); h) Drawin (1966)

1) Doering (1992); 2) Kanic *et al.* (2001); 3) Johnson *et al.* (2003)

c. Electron-impact ionization in N				
Transitions	Park (1985)	Johnston (2006)	Panesi <i>et al.</i> (2011)	Present
$u \leq 10 \rightarrow c$	a)	b), c)	d)	e)
Other transitions	a)	c)	d)	c)

a) Park (1985); b) Kunc and Soon (1989); c) Drawin (1966); d) Bultel *et al.* (2006); e) Huo (2009)

d. Electron-impact ionization in O				
Transitions	Park (1985)	Johnston (2006)	Panesi <i>et al.</i> (2011)	Present
All	a)	b), c)	d)	c)

a) Park (1985); b) Soon and Kunc (1990); c) Drawin (1966); d) Bultel *et al.* (2006)

e. Heavy-particle impact excitation in N

Transitions	Park (1985)	Johnston (2006)	Panesi <i>et al.</i> (2011)	Present	Note
$1 \leq l \leq 10 \rightarrow 2 \leq u \leq 11$	a)	-	b)	a)	As further seen in chapter 5, dividing the rate constants of Ref. a) by 8000 give excellent agreement with experimental intensities
Other transitions	a)	-	b)	c)	

a) Park (1985); b) Bultel *et al.* (2006); c) Surzhikov (2009)

f. Heavy-particle impact excitation in O

Transitions	Park (1985)	Johnston (2006)	Panesi <i>et al.</i> (2011)	Present
$1 \leq l \leq 10 \rightarrow 2 \leq u \leq 11$	a)	-	b)	a)
Other transitions	a)	-	b)	c)

a) Park (1985); b) Bultel *et al.* (2006); c) Surzhikov (2009)

g. Electron-impact excitation in N₂

Transitions	Park (1985)	Johnston (2006)	Panesi <i>et al.</i> (2011)	Present	Note
$X \rightarrow A$	a)	b)	d)	1)	Integration of the measured cross-sections from Refs 1-3 + WRC method
$X \rightarrow B$	a)	b)	d)	1)	
$X \rightarrow W$	a)	-	-	1)	
$X \rightarrow B'$	a)	-	-	1)	
$X \rightarrow C$	a)	c)	d)	2)	
$X \rightarrow b$	-	-	-	3)	
$X \rightarrow b'$	-	-	-	3)	
$X \rightarrow c'_4$	-	-	-	3)	
$X \rightarrow c_3$	-	-	-	e)	
$X \rightarrow o_3$	-	-	-	e)	
$X \rightarrow e'$	-	-	-	e)	
$A \rightarrow B$	-	b)	-	f)	
$A \rightarrow C$	-	d)	-	f)	
$B \rightarrow C$	-	d)	-	f)	

a) Cartwright *et al.* (1977); Chernyi and Losev (1993); c) Capitelli *et al.* (2000); d) Teulet *et al.* (1999)

e) Larichiutta (2011); f) Pierrot *et al.* (1999)

1) Johnson *et al.* (2006); 2) Khakoo *et al.* (2006); 3) Malone *et al.* (2011)

h. Electron-impact excitation in N₂⁺

Transitions	Park (1985)	Johnston (2006)	Panesi <i>et al.</i> (2011)	Present
$X \rightarrow A$	a)	b)	c)	d)
$X \rightarrow B$	a)	b)	c)	a)
$X \rightarrow C$	a)	c)	c)	d)
$A \rightarrow B$	-	b)	c)	d)
$A \rightarrow C$	-	b)	c)	d)
$B \rightarrow C$	-	b)	c)	d)

a) Crandall *et al.* (1974); Nagy (2003); c) Teulet *et al.* (1999); d) Pierrot *et al.* (1999)

Part II
**Validation of the physico-chemical
models**

Chapter IV

EAST shock-tube experiments and flowfield model assessment

Overview

In this chapter, we assess the predictions of the flowfield model against the experimental data obtained in the Electric Arc Shock-tube (EAST) facility at NASA Ames Research Center. In section 1, we briefly describe the EAST facility as well as the spectroscopic apparatus (spectrometers, CCD cameras) used to measure the radiation emitted by shocked air. The shock-tube conditions investigated in this work represent two flight conditions encountered by a spacecraft during a typical reentry into Earth's atmosphere:

- *Condition 50-117: $V_\infty=10.6$ km/s, $p_\infty=13.3$ Pa*
- *Condition 50-119: $V_\infty=11.17$ km/s, $p_\infty=13.3$ Pa*

In section 2, we describe our modeling strategy of the shock-tube experiments. In section 3, we present the experimental methodology used to extract the spectral and total intensity profiles from the CCD images. In section 4, we assess the capabilities of the thermochemistry model implemented in the flowfield solver by comparing the temperatures inferred from the N_2 Second Positive and N_2^+ First Negative systems with the predictions of the two-temperature model implemented in the flowfield solver. Finally, in section 5, we assess the capabilities of the ionization model implemented in the flowfield solver by comparing the experimental electron number density profile inferred from Stark-broadened atomic lines with the predictions of the flowfield model.

Table of contents

IV.1. Electric Arc Shock-tube (EAST) facility	80
IV.1.1. Facility description.....	81
IV.1.2. Radiation measurements.....	81
IV.1.2.1. Optical design	81
IV.1.2.2. Spectrometers and detectors	82
IV.1.2.3. Calibration	82
IV.1.3. Air conditions	83
IV.1.4. Spectral and spatial resolution	85
IV.2. Simulation strategy.....	87
IV.2.1. Assumptions.....	87
IV.2.2. Spectral and spatial resolution	88
IV.3. Analysis of the shock-tube measurements	88
IV.3.1. Spectral and total intensity profiles.....	88
IV.3.2. Emitting states	95
IV.4. Assessment of the flowfield thermochemistry model	95
IV.4.1. Measured temperature profiles.....	95
IV.4.2. Comparison with the flowfield model	97
IV.5. Assessment of the flowfield ionization model.....	97
IV.4.1. Measured electron number density profiles.....	97
IV.4.2. Comparison with the flowfield model and shock front location determination	100
IV.6. Summary	101

IV.1. Electric Arc Shock-tube (EAST) facility

IV.1.1. Facility description

The EAST facility is a 10.16 cm diameter shock-tube with an electric arc-heated driver. The arc in the driver is supported by a capacitor bank which can store up to 1.24 MJ of energy heated at 40 kV. A schematic of the EAST facility is given in figure 4.1. The driver gas in the experiments was helium, and the primary diaphragm was aluminium with a burst pressure of 1.1 MPa. The shock speed is measured by pressure transducers and photomultiplier tubes. For further details on the operating characteristics of the EAST facility, the reader is referred to the reports of Bogdanoff *et al.* (2007), Cruden *et al.* (2010), Brandis *et al.* (2010) and Grinstead *et al.* (2010).

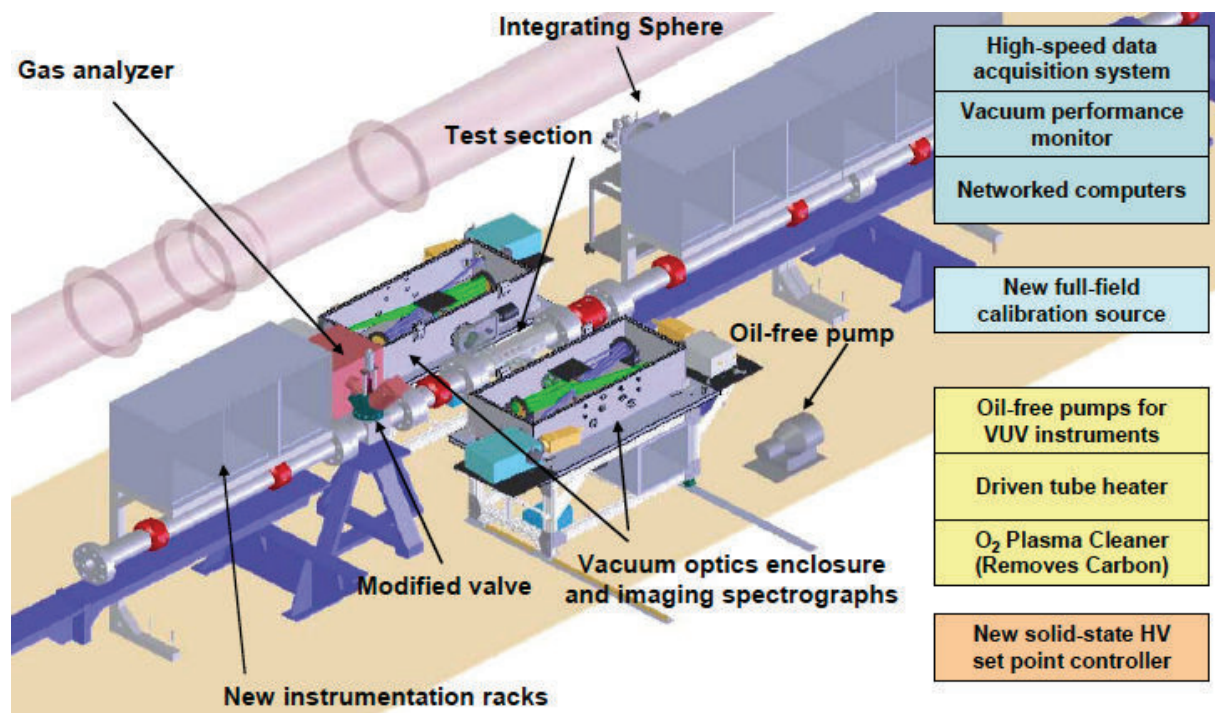


Figure 4.1: EAST facility (Grinstead *et al.*, 2010)

IV.1.2. Radiation measurements

IV.1.2.1. Optical design

Between 2003 and 2007, two imaging spectroscopy instruments were used, one on each side of the test section. The two instruments were dedicated to the UV/VIS and VIS/NIR/IR spectral regions, respectively. Shortcomings in the optical design, the lack of imaging capability in the VUV, cumbersome calibration procedures, and low duty cycle of the facility (typically two shots per week) motivated the upgrade of spectroscopy instrumentation and associated systems in 2007. The most significant improvement was the implementation of two additional spectrographs, one of which operates in the VUV. Doubling the number of instruments enabled the acquisition of shock intensity measurements from the VUV to the near IR in a single experiment.

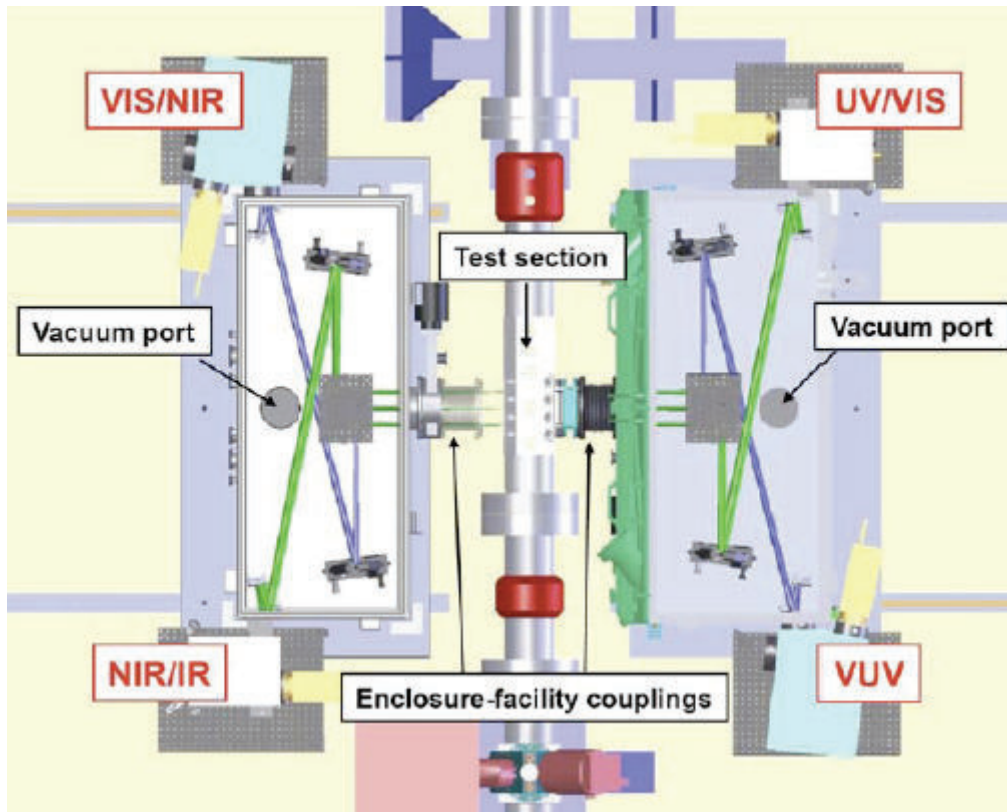


Figure 4.2: EAST facility optical design (Grinstead *et al.*, 2010)

IV.1.2.2. Spectrometers and detectors

The radiation measurements are obtained with four Princeton Instruments (PI)/Acton Imaging spectrometers. Array detectors are used to acquire the axially resolved spectra present at the exit planes of the spectrometers. Three CCD arrays, optimized for different regions of the spectrum, cover the VUV through NIR. An unintensified “InGaAs” array detector from FLIR Systems covers the NIR and IR out to 1700 nm. Figure 4.2 shows the arrangement of the two vacuum enclosures, the four imaging spectrographs, and labels identifying the spectral ranges each covers. Details of the spectrometers, their grating, and associated detectors are listed in table 4.1.

The spectrometer detectors are triggered simultaneously to capture the shock wave as it passes along the window. The short exposure time (0.1-1.0 μs for the CCD cameras, 1 μs for the NIR/IR InGaAs camera) reduces blur (spatial smearing) due to shock motion and allows for interpretation of the shock radiation image as spatiotemporal data. For further details on the spectroscopic apparatus of the EAST facility, the reader is referred to the reports of Bogdanoff *et al.* (2007), Cruden *et al.* (2010), Brandis *et al.* (2010) and Grinstead *et al.* (2010).

IV.1.2.3. Calibration

The spectrometer images are calibrated to enable comparison with simulations. The two pixel dimensions of the focal plane arrays are mapped to wavelength and distance. The pixel magnitude is mapped to absolute spectral intensity.

Wavelength calibration is accomplished using line source lamps such as Hg, Ne, and Ar. The spatial dimensions of the camera arrays were calibrated with a ruled scale for the spatial reference.

The emission magnitudes are calibrated in absolute intensity using two calibration sources: an integrating sphere for wavelengths above 300 nm manufactured by SphereOptics, Inc., and a deuterium lamp for wavelengths below 300 nm, which is a low-pressure arc source (model 632 from McPherson, Inc.). The spectral intensities of the two sources are shown in figure 4.3. The response functions of the spectrographs, measured for each grating and wavelength configuration, are determined using these reference sources. Each measured shock intensity spectrum is divided by a response function to convert the spectrum to absolute spectral intensity.

The uncertainty in absolute spectral intensity varies with instrument, configuration, spectral range, and emission magnitude. Typical values may range from approximately 15% to 40%, as outlined in the reports of Bogdanoff *et al.* (2007), Cruden *et al.* (2010), Brandis *et al.* (2010) and Grinstead *et al.* (2010).

Table 4.1: EAST spectrometers specifications (Grinstead *et al.*, 2010)

Channel	1	2	3	4
Mirror				
Spectral range (nm)	VUV 120-450	UV – Visible 185-800	Visible – near IR 300-1100	near IR – IR 535-1700
Demagnification	9.5	9.1	9.5	17.1
Camera				
Detector type	CCD	CCD	CCD	InGaAs
Array size (pixels)	1024 x 1024	256 x 1024	512 x 512	320 x 256
Spectral range (nm)	120-650	185-800	500-900	400-1700
Opening time (μ s)	0.1-1.0	0.1-1.0	0.1-1.0	1.0
Spectrometer				
Model	VM-504	SP2500i	SP2500i	SP2500i
Focal length (m)	0.39	0.50	0.50	0.50
Low resolution grating				
Blaze wavelength (nm)	300	300	675	800
Spectral range (nm)	190-450	200-450	480-900	535-1200
Ruling (g/mm)	150	150	50	150
Resolution (nm)	1.2	1.6	2.9	2.4
Medium resolution grating				
Blaze wavelength (nm)	150	Holographic Visible	750	1250
Spectral range (nm)	120-300	200-450	500-900	830-1900
Ruling (g/mm)	600	1200	1200	150
Resolution (nm)	0.13	0.3	0.7	2.4
High resolution grating				
Blaze wavelength (nm)	150	Holographic Visible	Holographic Visible	1250
Spectral range (nm)	120-300	185-375	300-800	830-1900
Ruling (g/mm)	2400	3600	2400	600
Resolution (nm)	0.10	0.14	0.2	0.6

IV.1.3. Air conditions

The experimental campaign conducted from November 2008 to November 2011 in the EAST facility was very fruitful. Various flight conditions in different planetary atmosphere (Venus, Mars, Jupiter, Earth, etc) were simulated. Specifically, figure 4.4 displays the shots undertaken in air together with Orion (Grinstead, 2008) lunar return trajectory. Among these numerous shots, which are available at <https://nsckn.nasa.gov> upon request, the shots whose thermodynamic freestream velocity and pressure conditions could represent the peculiar

conditions encountered by the spacecraft such as peak heating, ballistic entry, etc were selected. Moreover, shots with a high signal to noise ratio, with a large spectral range so as to identify several radiative features and further assess the predictions of the CR model were selected. Table 4.2 summarizes the selected freestream conditions as well as spectral ranges investigated in this work.

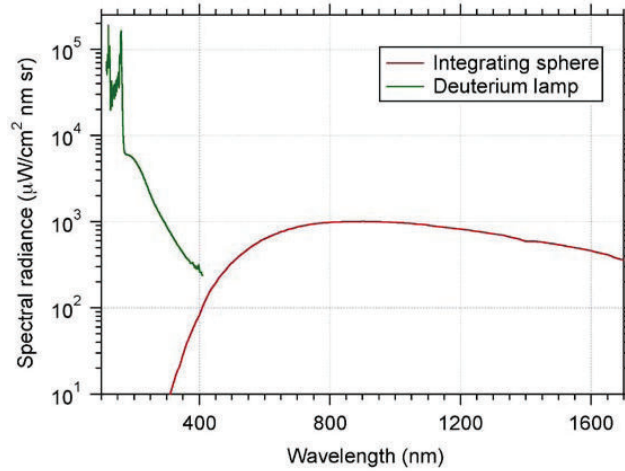


Figure 4.3: Spectral intensities from the two calibration sources (Grinstead *et al.*, 2010)

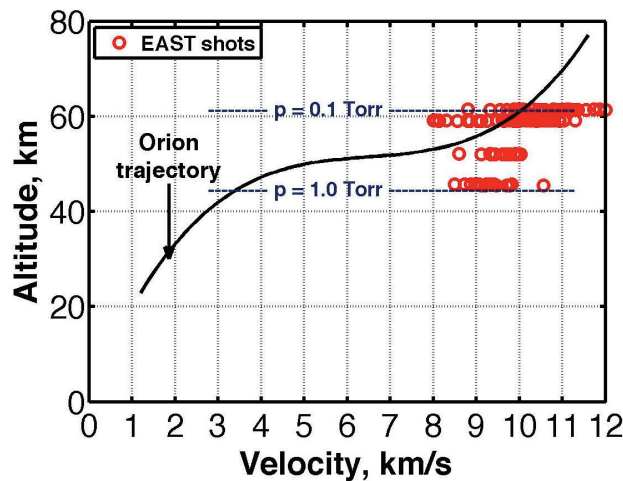


Figure 4.4: Reproduction of flight freestream thermodynamic conditions in EAST facility

Table 4.2: Selected shock-tube freestream conditions and spectral ranges⁹

Shot	Velocity (km/s)	Pressure (Pa)	Spectral range (nm)
50-116	10.54	13.3	140-176
			200-360
			653-659
50-117	10.6	13.3	406-414
			852-872
50-119	11.17	13.3	168-180
			406-414
			852-872

⁹ Throughout the dissertation, shot 50-117 will be referred as shot 50-116 unless specified, since the freestream conditions are similar.

IV.1.4. Spectral and spatial resolution

The intensity emitted from the shock-tube was measured with varying degrees of spatial and spectral resolution.

The spectral resolution is controlled by the spectrometer slit width, meaning that the intensity at a specified wavelength is the average value of the spectral intensity J_λ multiplied by the slit function (Cruden, 2011; Brandis, 2012), illustrated in figures 4.5 and 4.6 for the conditions investigated in this work. The slit functions were computed with the parameters provided by Brandis (2012) and Cruden (2012). The corresponding FWHM are listed in table 4.3.

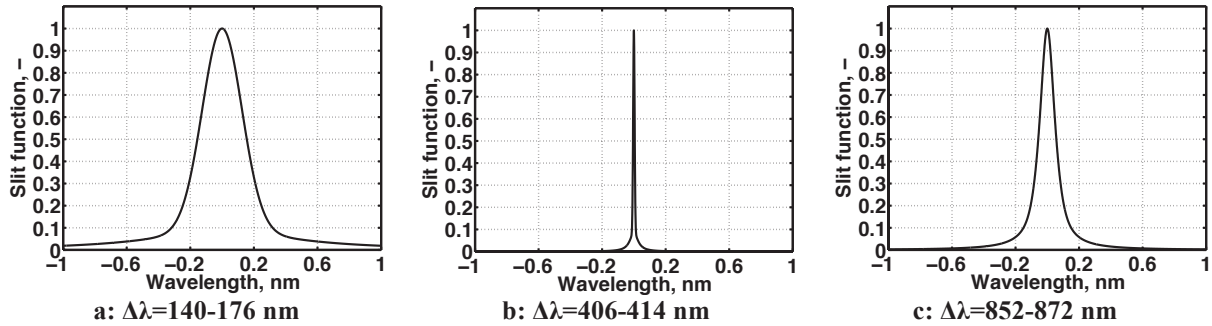


Figure 4.5: Slit functions for the VUV, visible, IR spectral ranges for shot 117 ($V_\infty=10.6$ km/s, $p_\infty=13.3$ Pa)

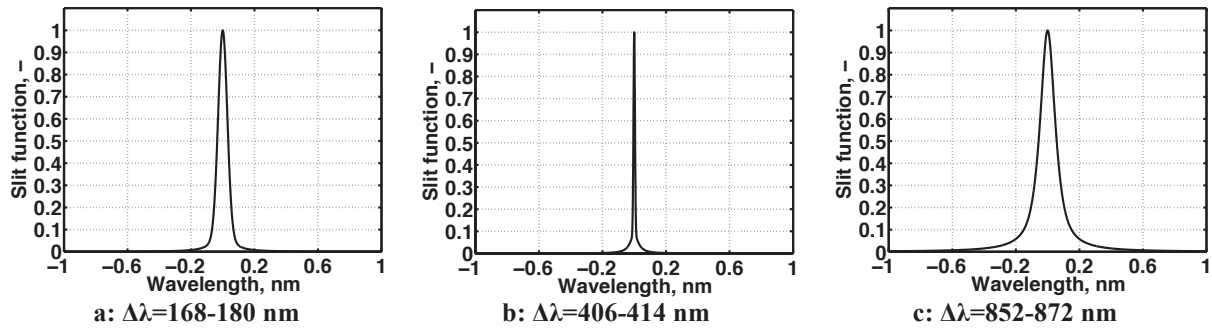


Figure 4.6: Slit functions for the VUV, visible, IR spectral ranges for shot 119 ($V_\infty=11.17$ km/s, $p_\infty=13.3$ Pa)

The spatial resolution comes from three sources (Cruden, 2011; Brandis 2012), namely the spectrometer and optics spatial resolution, the camera imaging function and the shock motion, as illustrated in figures 4.7 and 4.8 (see previous page). The spatial smearing functions were computed with the parameters provided by Brandis (2013). The corresponding FWHM are listed in table 4.3.

Table 4.3: Spectral and spatial resolution

Shot	Velocity (km/s)	Pressure (Pa)	Spectral range (nm)	FWHM slit function (nm)	FWHM SRF (cm)
50-116	10.54	13.3	140-176	0.29	0.55
50-117	10.6	13.3	406-414	0.008	1.10
			852-872	0.116	0.62
50-119	11.17	13.3	168-180	0.070	1.14
			406-414	0.008	1.14
			852-872	0.116	0.62

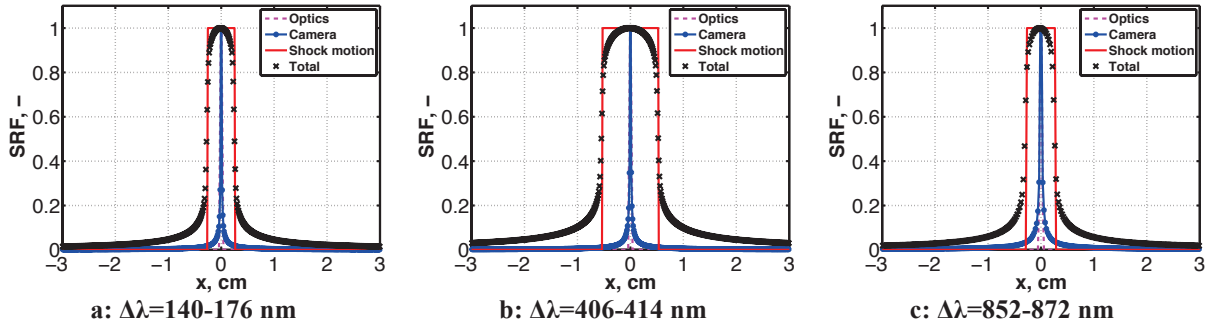


Figure 4.7: Spatial smearing functions for the VUV, visible, IR spectral ranges for shot 117 ($V_\infty=10.6$ km/s, $p_\infty=13.3$ Pa)

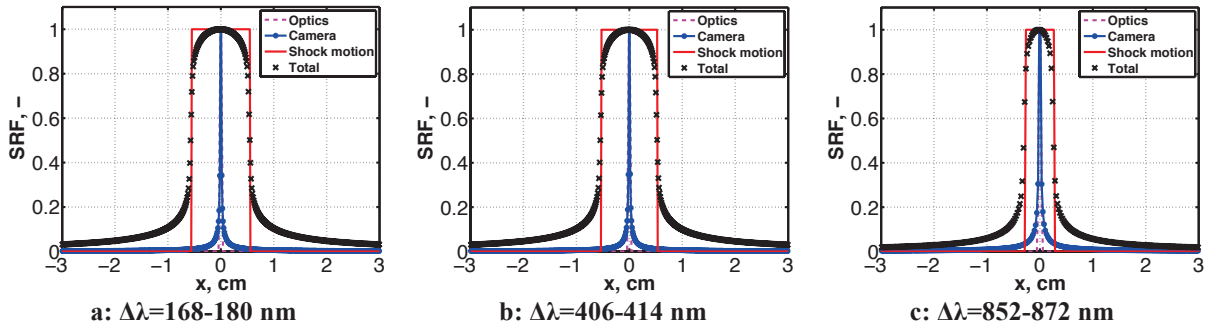


Figure 4.8: Spatial smearing functions for the VUV, visible, IR spectral ranges for shot 119 ($V_\infty=11.17$ km/s, $p_\infty=13.3$ Pa)

As can be seen the spatial smearing function width is dominated by the distance Δz_s that the shock traveled at velocity U_∞ during the spectrometer opening time Δt :

$$\Delta z_s = U_\infty \Delta t \quad (4.1)$$

Figure 4.9 shows the radiative intensity profile measured between the time t and $t-\Delta t$. The measured value is the sum of the profiles collected in this period of time. The methodology for simulating the spectral and spatial smearing in the predictions is discussed in the following.

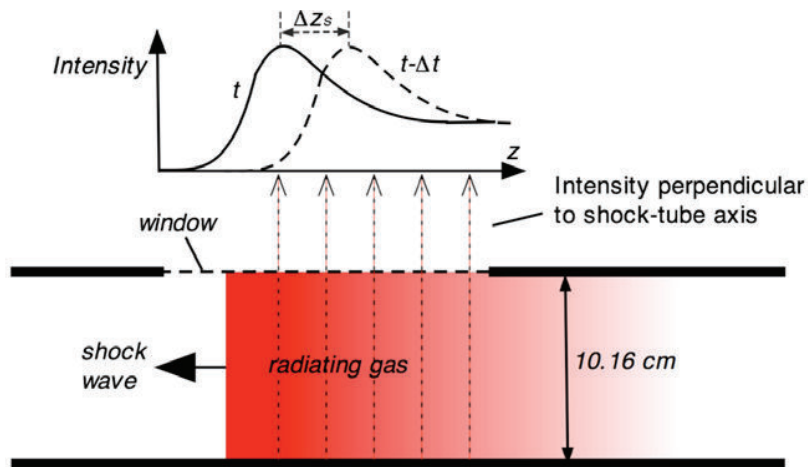


Figure 4.9: Spatial smearing of the intensity emitted by the shock-tube (Johnston, 2008)

IV.2. Simulation strategy

This section presents the strategy adopted to model the radiation emitted by the shock-tube perpendicularly to its axis.

IV.2.1. Assumptions

The flow inside the EAST facility is highly three dimensional and viscous. However, to make the computation tractable, the following assumptions are made in the flowfield solver:

- (H1): the flow is assumed stationary
- (H2): the flow is assumed inviscid
- (H3): the flow is assumed monodimensional
- (H4): no radiation is absorbed in the boundary layer.

The flowfield was computed with the Poshax two-temperature ($T_T=T_R=T_g$, $T_V=T_e$) solver (Gollan, 2006; Potter, 2011), which is described in appendix A. The temperatures and species densities are presented in figures 4.10 and 4.11, respectively. The radiation of the post-shock region was computed using the spectral and CR models described in **chapters 2** and **3** respectively, following the methodology described in **chapter 1**.

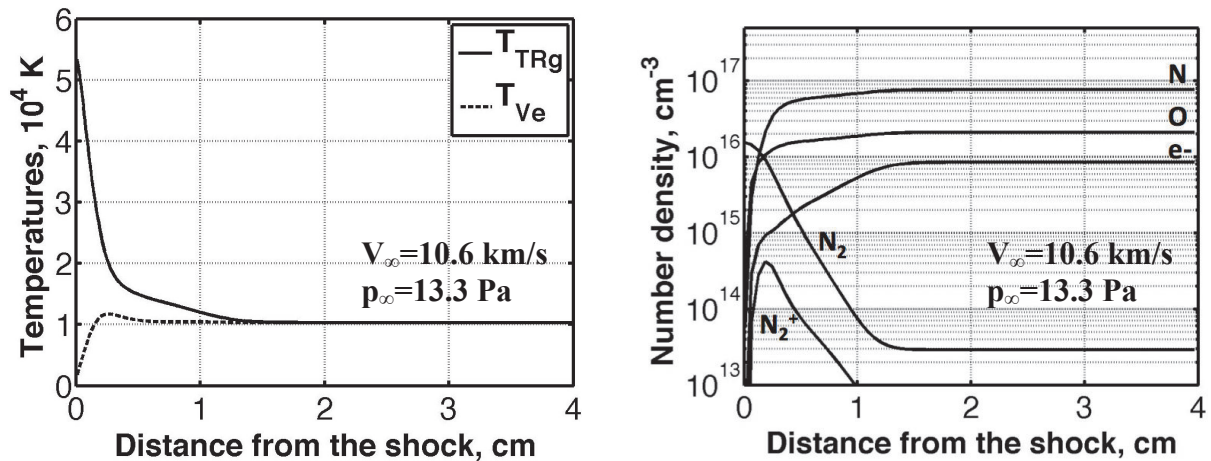


Figure 4.10: Temperatures and species number density profiles predicted by Poshax for shot 117 ($V_\infty=10.6$ km/s, $p_\infty=13.3$ Pa)

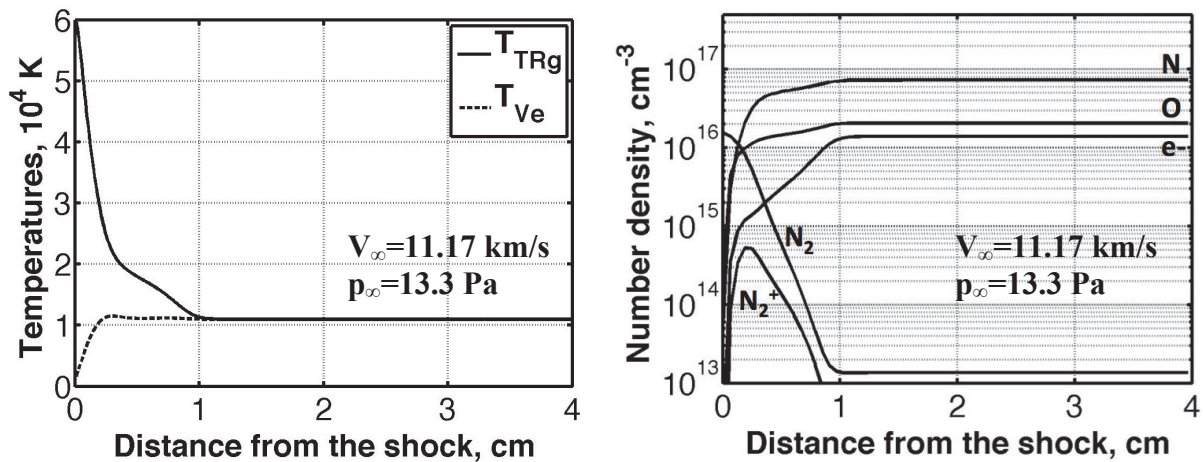


Figure 4.11: Temperatures and species number density profiles predicted by Poshax for shot 117 ($V_\infty=11.17$ km/s, $p_\infty=13.3$ Pa)

IV.2.2. Spectral and spatial resolution

The spectral intensity J was obtained by solving the RTE perpendicularly to the shock-tube axis at each axial location x :

$$J(x, \lambda) = \frac{\varepsilon(x, \lambda)}{\alpha(x, \lambda)} \left(1 - e^{-\alpha(x, \lambda)D}\right) \quad (4.2)$$

where $D=10.16$ cm is the EAST diameter. Subsequently, the predicted spectral intensity, I , accounting for the slit width, is obtained from the following convolution:

$$I(x, \lambda) = \int_{-\infty}^{+\infty} J(x, \lambda) S(\lambda - \lambda') d\lambda' \quad (4.3)$$

where S is the apparatus slit function. The spectral intensities I is directly compared to the spectra extracted at various locations, as shown in **chapter 5**. The integrated intensity is obtained by integrating the spectral intensity I over the spectral range $\Delta\lambda$ considered. A final convolution with the spatial smearing function is performed, yielding the smeared intensity profile \bar{I} :

$$\bar{I}(z) = \int_{-\infty}^{+\infty} \int_{-\infty}^{+\infty} I(x, \lambda) SRF(z - x) d\lambda dx \quad (4.4.a)$$

When the experimental spatial smearing function is not available, the smeared intensity profile, \bar{I} , is given by:

$$\bar{I}(z) = \frac{1}{\Delta z_s} \int_{z-\Delta z_s/2}^{z+\Delta z_s/2} \int_{-\infty}^{+\infty} I(x, \lambda) d\lambda dx \quad (4.4.b)$$

The smeared intensity profile \bar{I} is directly compared to the measured post-shock intensity profile, as shown in **chapter 5**.

IV.3. Analysis of the shock-tube measurements

This section describes the procedures used to analyze the radiation measurements and to infer the populations of the excited states responsible for the observed transitions. These data will be used to test the CR model developed in this thesis.

IV.3.1. Spectral and total intensity profiles

The calibrated CCD images obtained from the measurement campaign carried in the EAST facility have been made available to the scientific community. A specially developed MATLAB program (Jacobs, 2012) was used to extract the spectral intensities at ten locations from the nonequilibrium zone to the ‘plateau’ area.

The program sums each row of the CCD image and yields the post-shock intensity profile. To increase the signal-to-noise ratio, the data were averaged over 11 adjacent columns (typically over a distance of 2 mm), centered at the location of interest to obtain the experimental spectra. The shock front location, which is *a priori* unknown in the EAST CCD images, was determined as a first approximation by taking the tangent to the inflexion point of the rising front of the post-shock intensity profile. A refinement of this method is discussed in

subsection IV.4.4. Figures 4.12-4.17 present for the freestream and spectral ranges investigated the CCD images, the post-shock intensity profiles as well as the spectral intensity at $x=2.5$ cm, which corresponds to the plateau region.

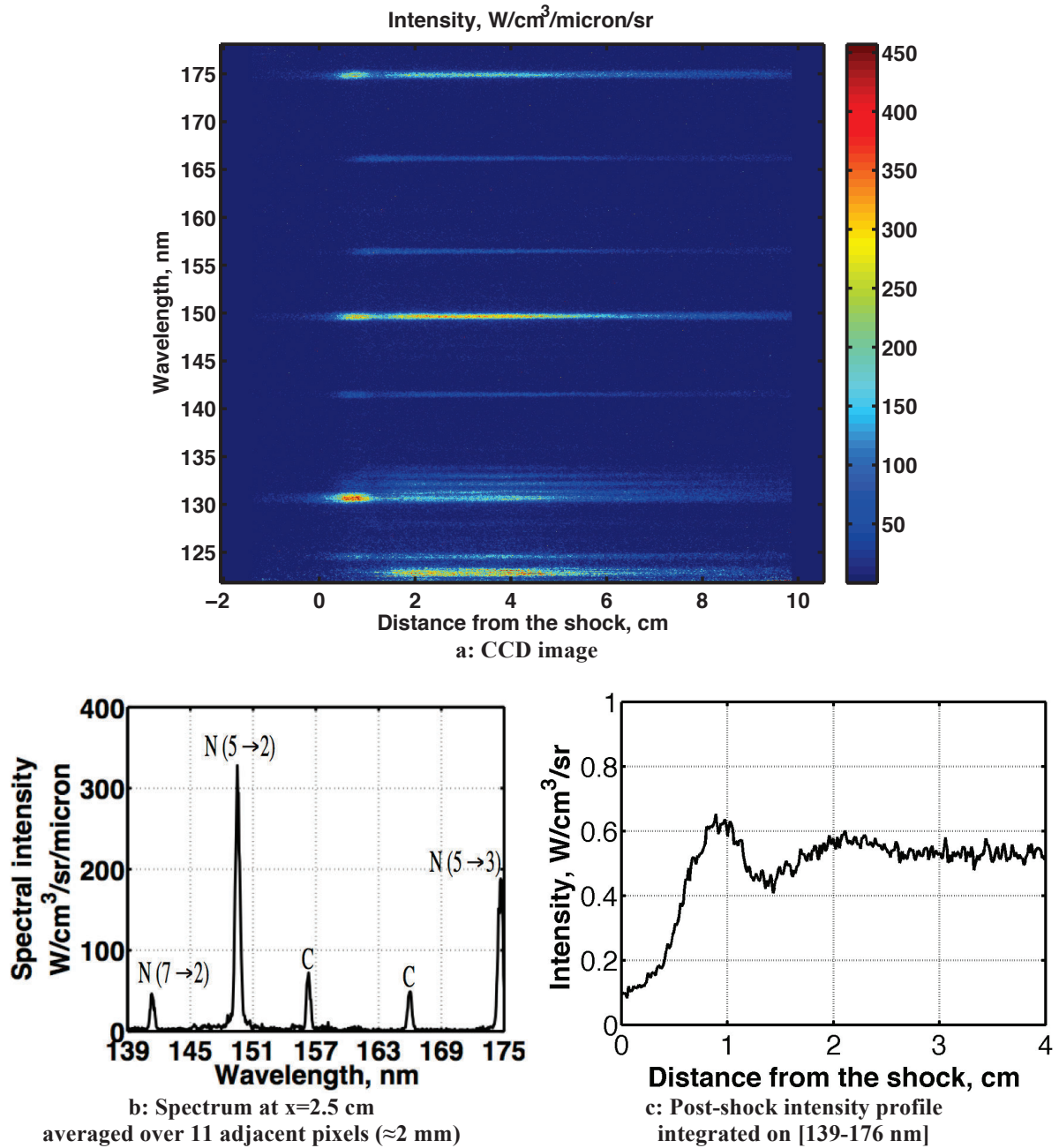
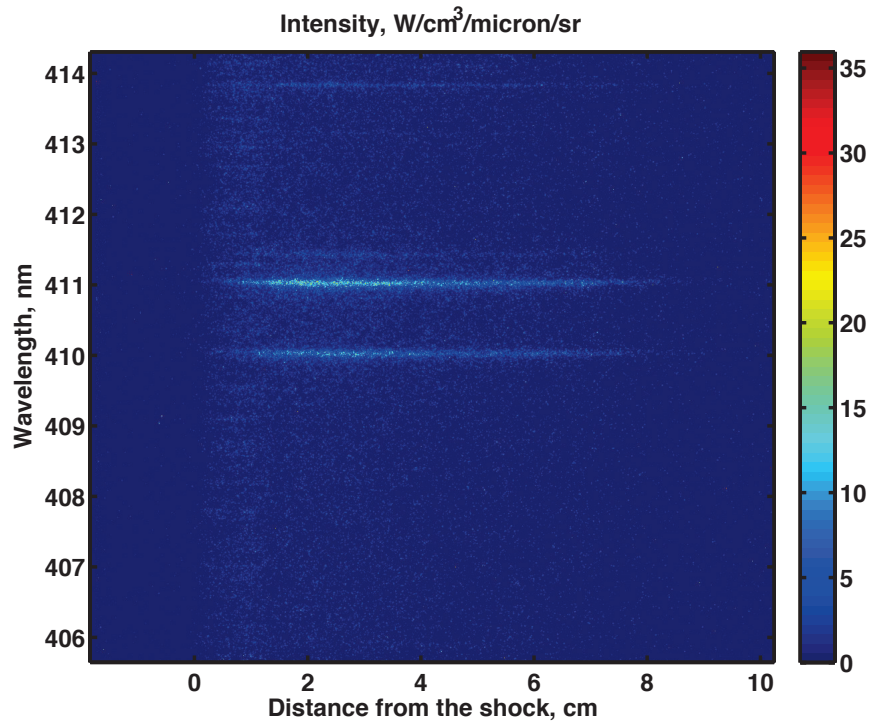
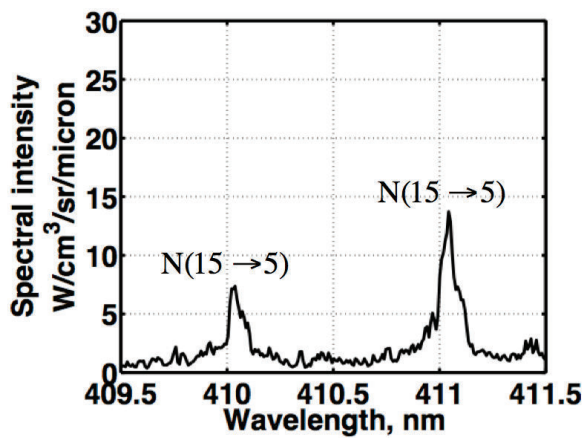


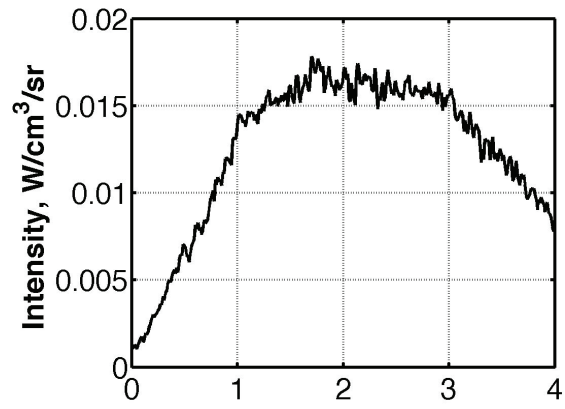
Figure 4.12: Analysis of the CCD image for shot 116 ($V_\infty=10.54$ km/s, $p_\infty=13.3$ Pa) in the VUV



a: CCD image



b: Spectrum at $x=2.5$ cm
averaged over 11 adjacent pixels (≈ 2 mm)



c: Post-shock intensity profile
integrated on [409.5-411.5 nm]

Figure 4.13: Analysis of the CCD image for shot 117 ($V_\infty=10.6$ km/s, $p_\infty=13.3$ Pa) in the visible

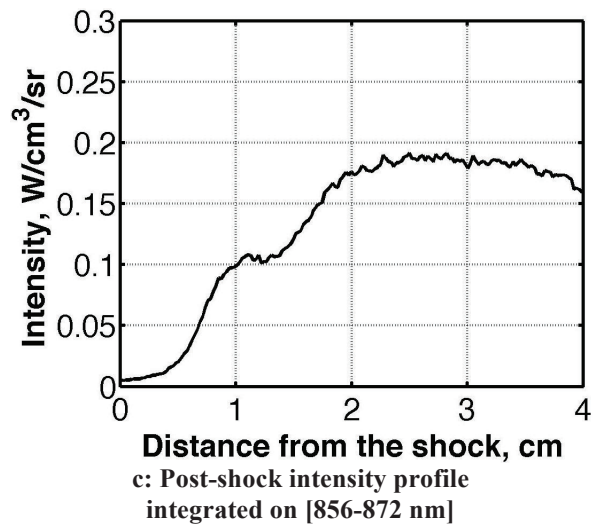
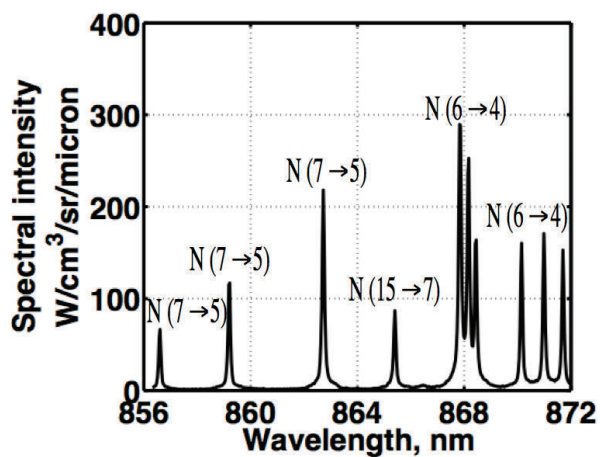
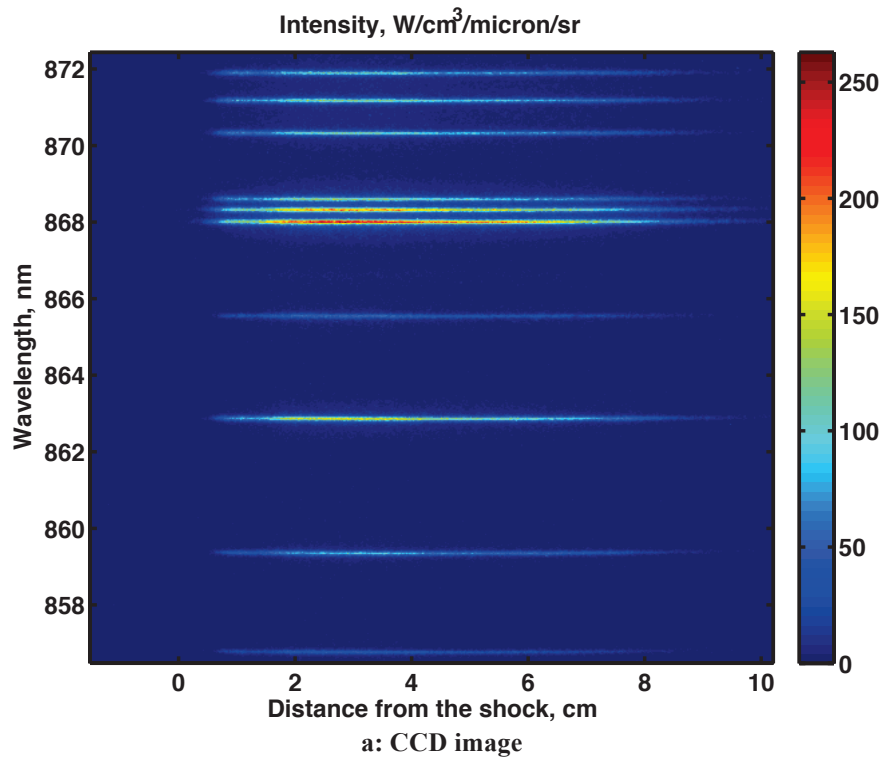


Figure 4.14: Analysis of the CCD image for shot 117 ($V_\infty=10.6$ km/s, $p_\infty=13.3$ Pa) in the IR

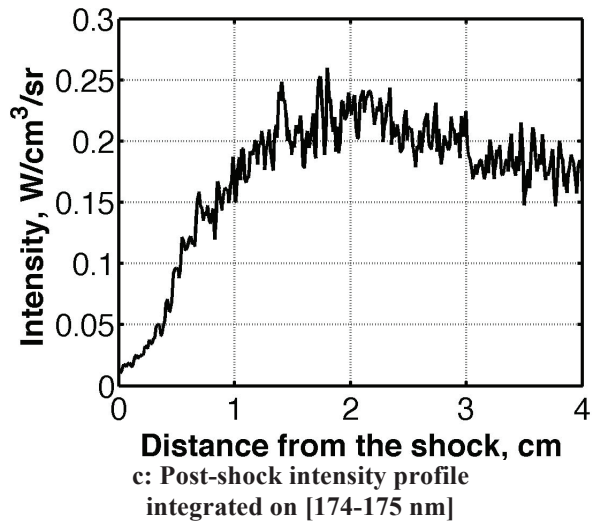
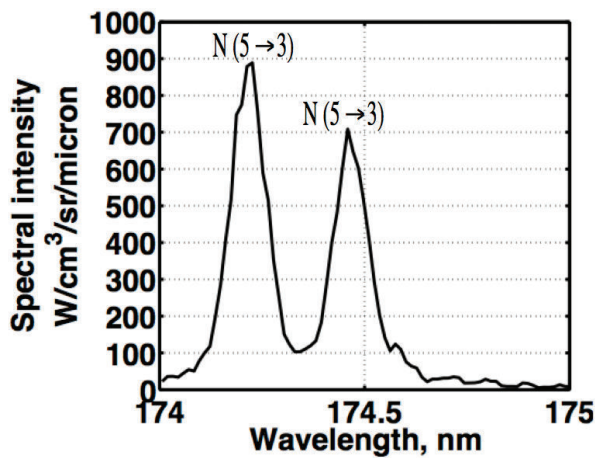
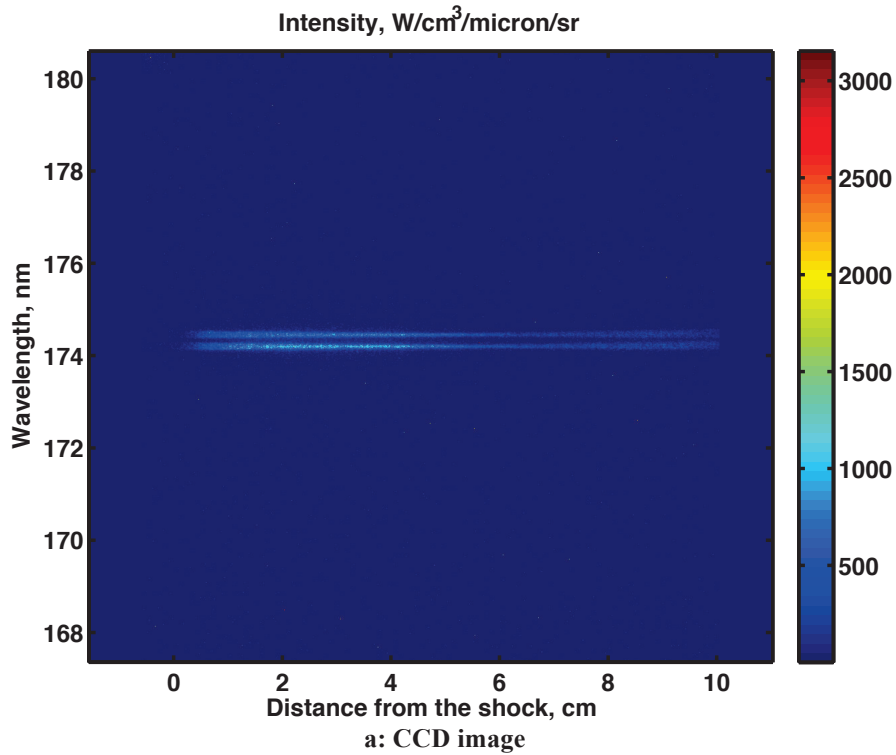
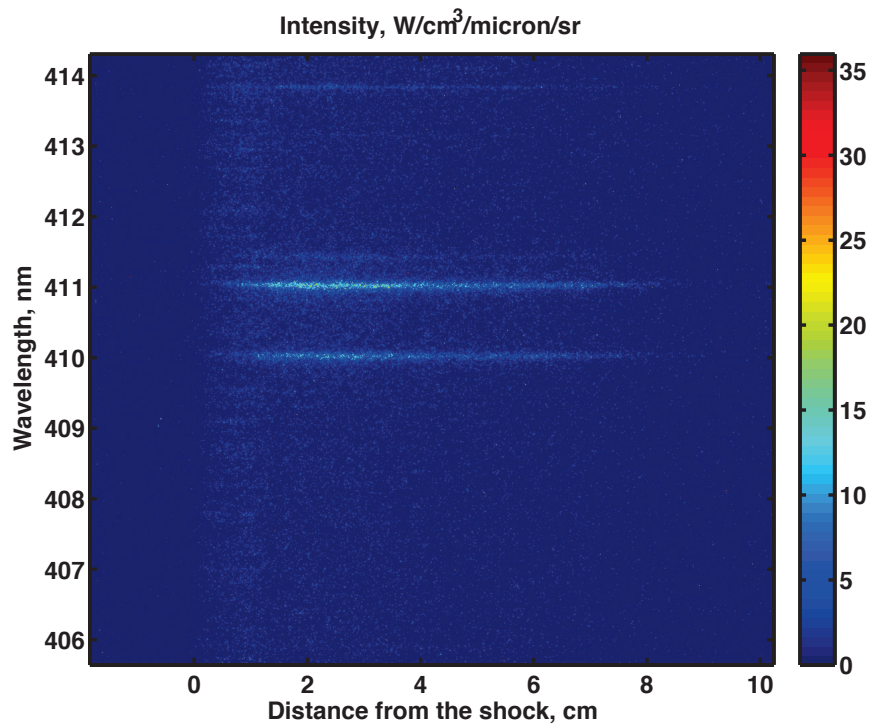
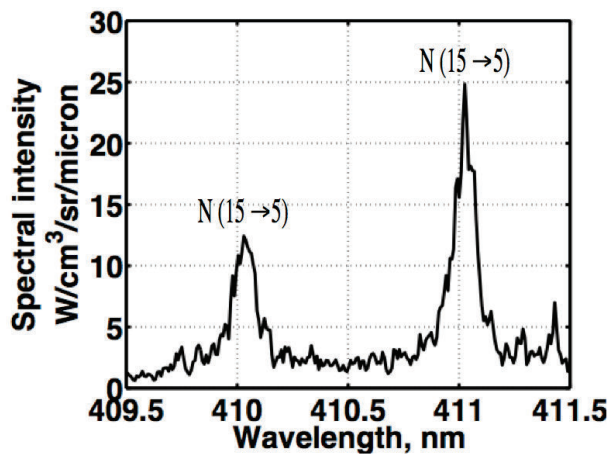


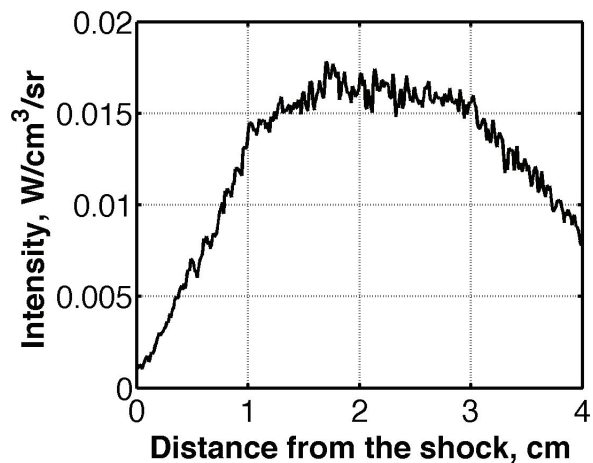
Figure 4.15: Analysis of the CCD image for shot 119 ($V_\infty=11.17$ km/s, $p_\infty=13.3$ Pa) in the VUV



a: CCD image



b: Spectrum at $x=2.5$ cm averaged over 11 adjacent pixels (≈ 2 mm)



c: Post-shock intensity profile integrated on [409.5-411.5 nm]

Figure 4.16: Analysis of the CCD image for shot 119 ($V_\infty=11.17$ km/s, $p_\infty=13.3$ Pa) in the visible

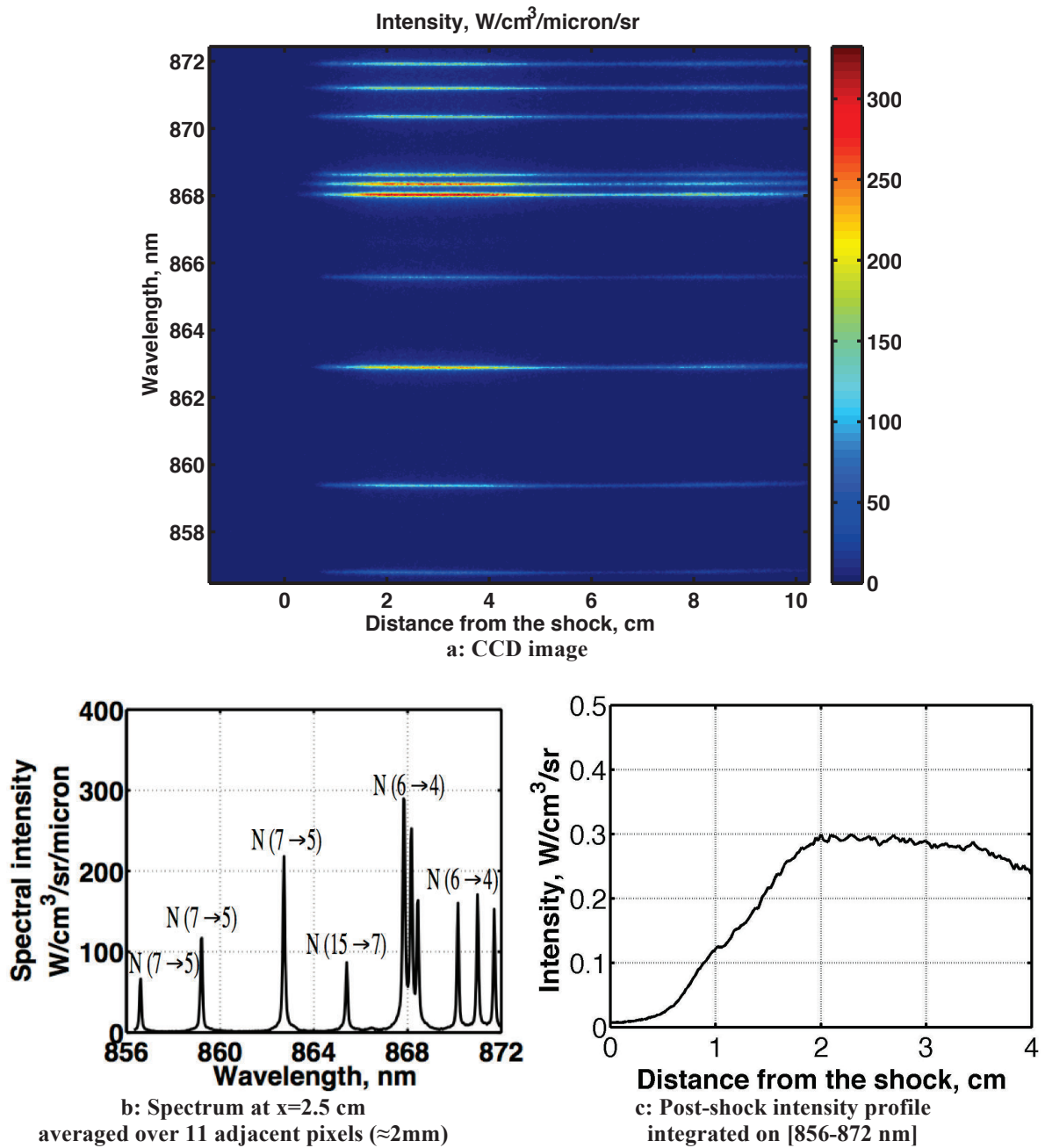


Figure 4.17: Analysis of the CCD image for shot 119 ($V_\infty=11.17$ km/s, $p_\infty=13.3$ Pa) in the IR

IV.3.2. Emitting states

Table 4.4 lists the observed lines as well the corresponding grouped excited states whose populations can be inferred from the selected shots. The selected spectra thus contain information on the populations of the 2nd, 3rd, 5th, 7th and 15th excited grouped level of N.

Table 4.4: Excited states inferred from selected shots

Species	Wavelength (nm)	Grouped level l	Grouped level u	Shot			Camera
				116	117	119	
N	141.1939	3	7	X			VUV
N	149.2625	2	5	X			VUV
N	149.2820	2	5	X			VUV
N	149.4675	2	5	X			VUV
N	174.2731	3	5	X	X	X	VUV
N	174.5249	3	5	X	X	X	VUV
N	409.9943	5	14		X	X	Vis.
N	410.9949	5	14		X	X	Vis.
N	856.7735	5	7		X	X	IR
N	859.4000	5	7		X	X	IR
N	862.9235	5	7		X	X	IR
N	865.5748	7	15		X	X	IR
N	865.5878	5	7		X	X	IR
N	868.0282	4	6		X	X	IR
N	868.3403	4	6		X	X	IR
N	868.6149	4	6		X	X	IR
N	870.3247	4	6		X	X	IR
N	871.1703	4	6		X	X	IR
N	871.8837	4	6		X	X	IR
H	656.3000	2	3	X			Vis.
N ₂	280-350	B ³ Π _g	C ³ Π _u	X			UV
N ₂ ⁺	280-350	X ² Σ _g ⁺	B ² Π _u	X			UV

IV.4. Assessment of the flowfield thermochemistry model

In the shocked air mixture, the molecules are excited in their vibrational and rotational modes. Therefore, the vibrational and rotational temperatures, provided they can be defined, give further insight of the thermodynamic state of the flow. The Poshax model (Gollan, 2006; Potter, 2011) is further tested by comparing the predicted temperatures with the experimental data.

IV.4.1. Measured temperature profiles

Vibrational and rotational temperatures of the molecular electronic states were determined from the spectra of the N₂ Second Positive (C ³Π_u → B ³Π_g) and N₂⁺ (B ²Π_u → X ²Σ_g⁺) First Negative systems, which are observed in the UV spectral range for the conditions of shot 50-116 (V_∞=10.54 km/s, p_∞=13.3 Pa). Under this freestream condition, these molecules are highly dissociated, thus limiting the observable and high quality radiation. The analysis of the molecular spectra was limited to two locations (at x=0.75 cm and x=1 cm). The vibrational and rotational temperatures of the N₂ and N₂⁺ systems were fitted with SPECAIR (Laux *et al.*, 2003) using the experimental slit function.

Figure 4.18 compares the experimental spectra with the simulated spectra at the nonequilibrium peak, i.e at x=0.75 cm and x=1 cm. Best agreement is obtained with the

vibrational and rotational temperatures listed in table 4.5. Figure 4.19 presents the post-shock evolution of the vibrational and rotational temperatures of N_2 ($C^3\Pi_u$) and N_2^+ ($B^2\Pi_u$). Interestingly, for each of these electronic states, the vibrational and rotational temperatures are similar, showing a strong coupling between the vibrational and rotational modes. Furthermore, the rotational temperature of N_2 ($C^3\Pi_u$) (3000 ± 1000 K) is much lower than the rotational temperature of N_2^+ ($B^2\Pi_u$) (15000 ± 2000 K). These observations are consistent with the earlier observations of Matsuda *et al.* (2002), Laux (2006) and Yamada *et al.* (2011).

Table 4.5: Vibrational and rotational temperatures of N_2 ($C^3\Pi_u$) and N_2^+ ($B^2\Pi_u$) electronic states

Species	Temperatures	Location (cm)	
		$x=0.75$	$x=1.00$
$N_2(C^3\Pi_u)$	T_V	5000 ± 2000 (K)	5000 ± 2000 (K)
$N_2(C^3\Pi_u)$	T_R	3000 ± 1000 (K)	3000 ± 1000 (K)
$N_2^+(B^2\Pi_u)$	T_V	13000 ± 2000 (K)	13000 ± 2000 (K)
$N_2^+(B^2\Pi_u)$	T_R	15000 ± 2000 (K)	15000 ± 2000 (K)

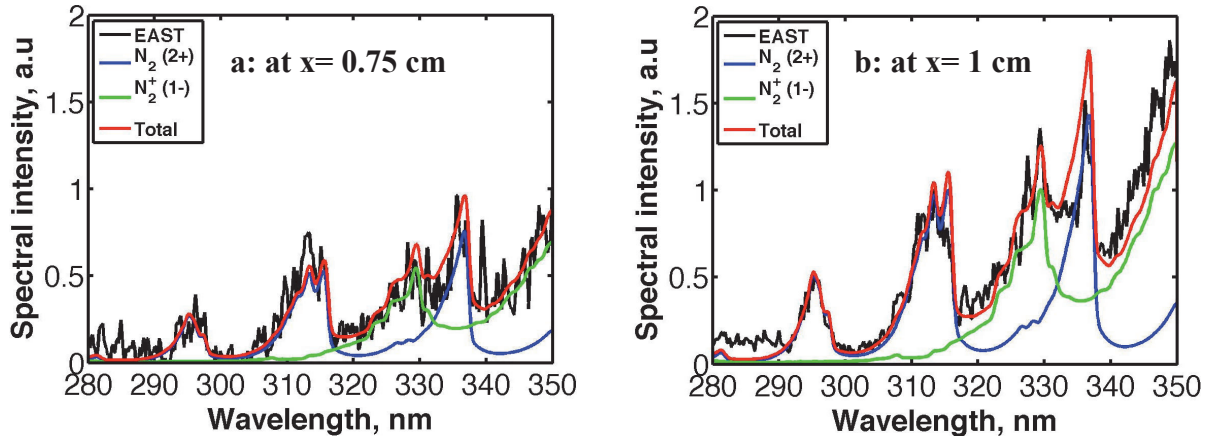


Figure 4.18: Spectra of N_2 and N_2^+ systems for shot 116 ($V_\infty=10.54$ km/s, $p_\infty=13.3$ Pa) at a) $x=0.75$ cm and b) $x=1$ cm. The experimental spectra are averaged over 10 adjacent pixels (≈ 2 mm)

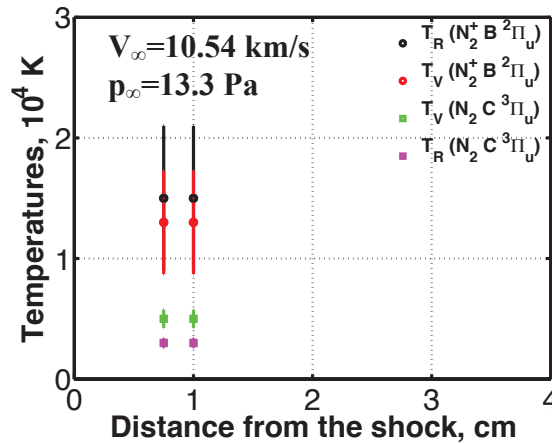


Figure 4.19: Experimental post-shock evolution of the vibrational and rotational temperatures of N_2 ($C^3\Pi_u$) and N_2^+ ($B^2\Pi_u$) electronic states for shot 116 ($V_\infty=10.54$ km/s, $p_\infty=13.3$ Pa)

IV.4.2. Comparison with the flowfield model

Figure 4.20 compares the post-shock temperature evolution given by Poshax (Gollan, 2006; Potter, 2011) with the vibrational and rotational temperatures of N_2 ($C^3\Pi_u$) and N_2^+ ($B^2\Pi_u$) electronic states inferred from the experimental data.

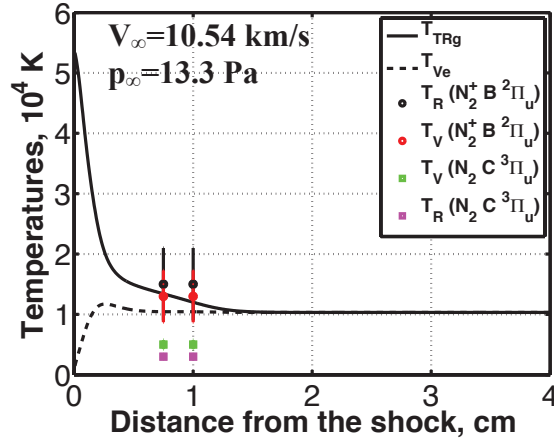


Figure 4.20: Comparison between experimental and simulated temperature evolution for shot 116 ($V_\infty=10.54$ km/s, $p_\infty=13.3$ Pa)

The vibrational temperatures of N_2 ($C^3\Pi_u$) and N_2^+ ($B^2\Pi_u$) differ from the vibrational-electron temperature T_{Ve} . The rotational temperature of N_2^+ ($B^2\Pi_u$), unlike the rotational temperature of N_2 ($C^3\Pi_u$), which is 10000 K lower, agrees with the translational-rotational temperature T_{TRg} . Given these comparisons, further work should be undertaken to model and understand the vibrational and rotational distributions of the levels in N_2 ($C^3\Pi_u$) and N_2^+ ($B^2\Pi_u$) electronic states.

IV.5. Assessment of the flowfield ionization model

In the shocked air mixture, one of the drivers of excitation and ionization are the electrons. It is therefore important to measure the electron number density profile behind the shock wave to determine the state of the plasma flow and locate the shock front. To this end, the electron number density profiles inferred from the radiation measurements are compared with the predictions of the flowfield model Poshax (Gollan, 2006; Potter, 2011).

IV.4.1. Measured electron number density profiles

As discussed in **chapter 2**, the electron number density is determined from Stark-broadened atomic lines. The lines used in this work are summarized in table 4.6.

Table 4.6: Atomic lines considered for the determination of the electron number density

Shot	Spectral range (nm)	Transition	Wavelength (nm)
50-116	653-659	H(3-2)	656.30 (H_α)
50-119	406-414	N(14-5)	410.99 (N)

The width of the H_α and N(411nm) lines were computed with the flowfield solution given in subsection IV.2.1, as illustrated in figure 4.18. It is shown that the Stark effect dominates the broadening of these lines at distance greater than 0.5 and 0.75 cm for shot 50-116 ($V_\infty=10.54$ km/s, $p_\infty=13.3$ Pa) and 50-119 ($V_\infty=11.17$ km/s, $p_\infty=13.3$ Pa), respectively.

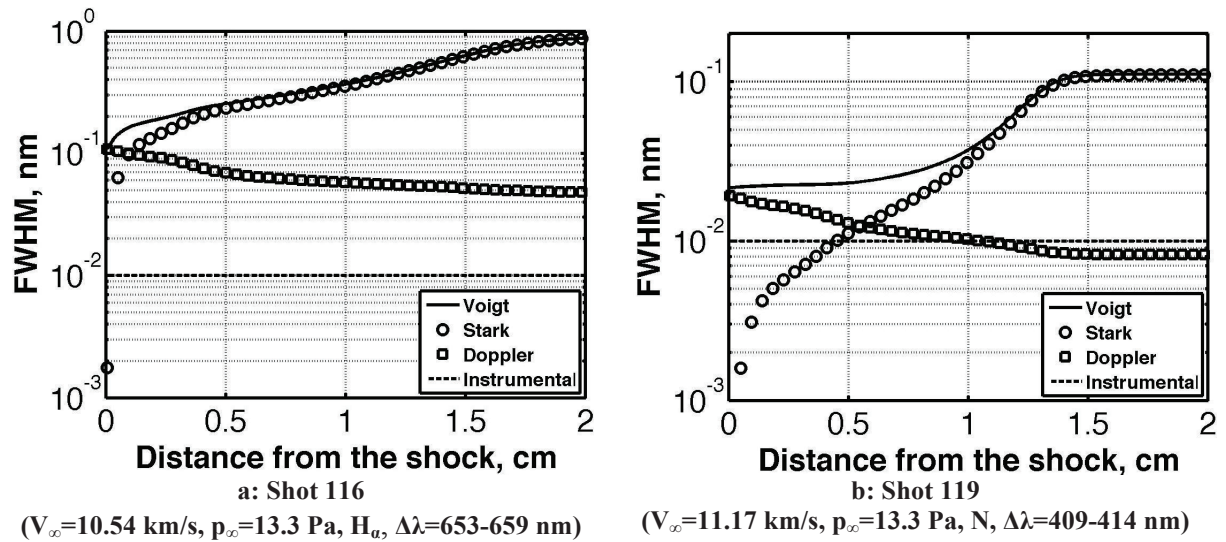


Figure 4.21: FWHM post-shock evolution

Figure 4.22 presents the fits of the H_α line at various locations behind the shock front where Stark broadening is dominant. These lines were fitted with a Lorentzian function. The Stark widths were then converted into electron number densities using the formula given in **chapter 2**.

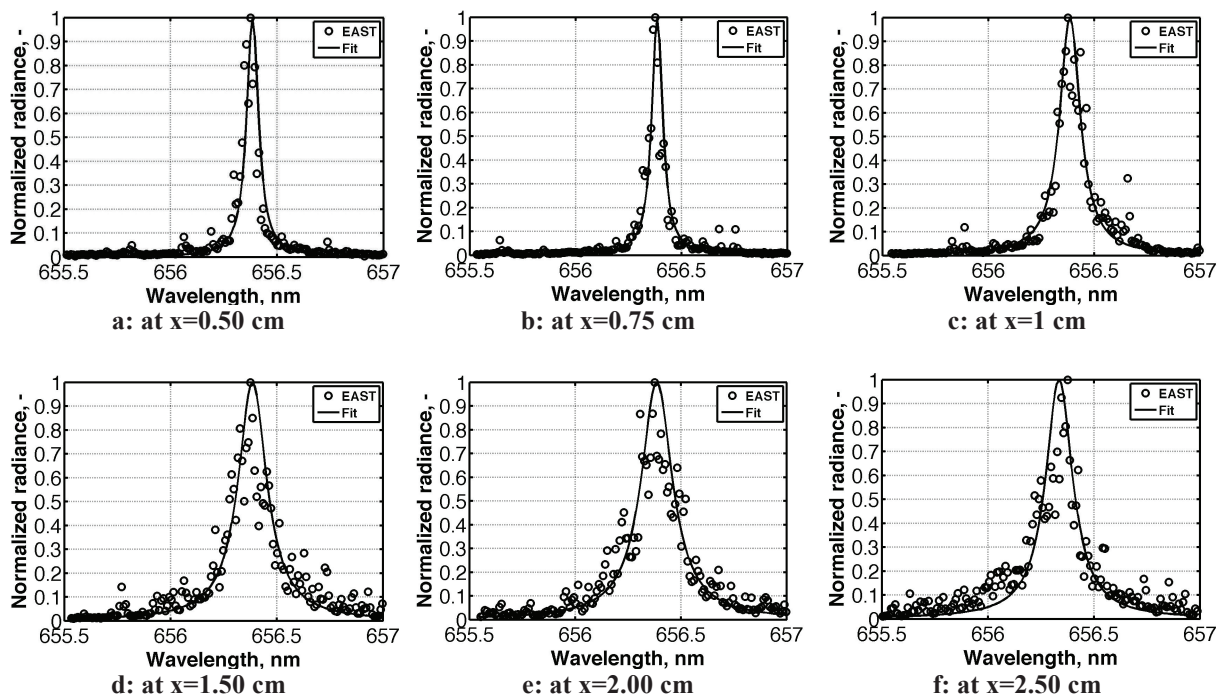


Figure 4.22: H_α profile fits at several locations for shot 116 ($V_\infty=10.54$ km/s, $p_\infty=13.3$ Pa)
The experimental spectra are averaged over 10 adjacent pixels (≈ 2 mm)

Figure 4.23 presents the electron number density profile determined from the measured line shapes. It is shown that the electron number density increases behind the shock as a result of ionization processes, before reaching a plateau.

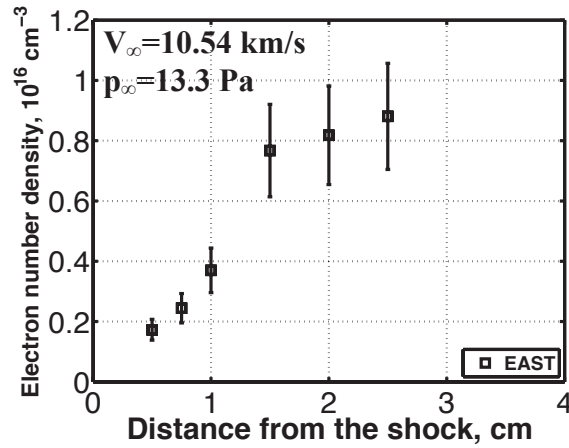


Figure 4.23: Electron number density profile inferred from Stark-broadened H_α line for shot 116 ($V_\infty=10.54$ km/s, $p_\infty=13.3$ Pa)

Figure 4.24 presents the fits of the N(411) line at various locations behind the shock front.

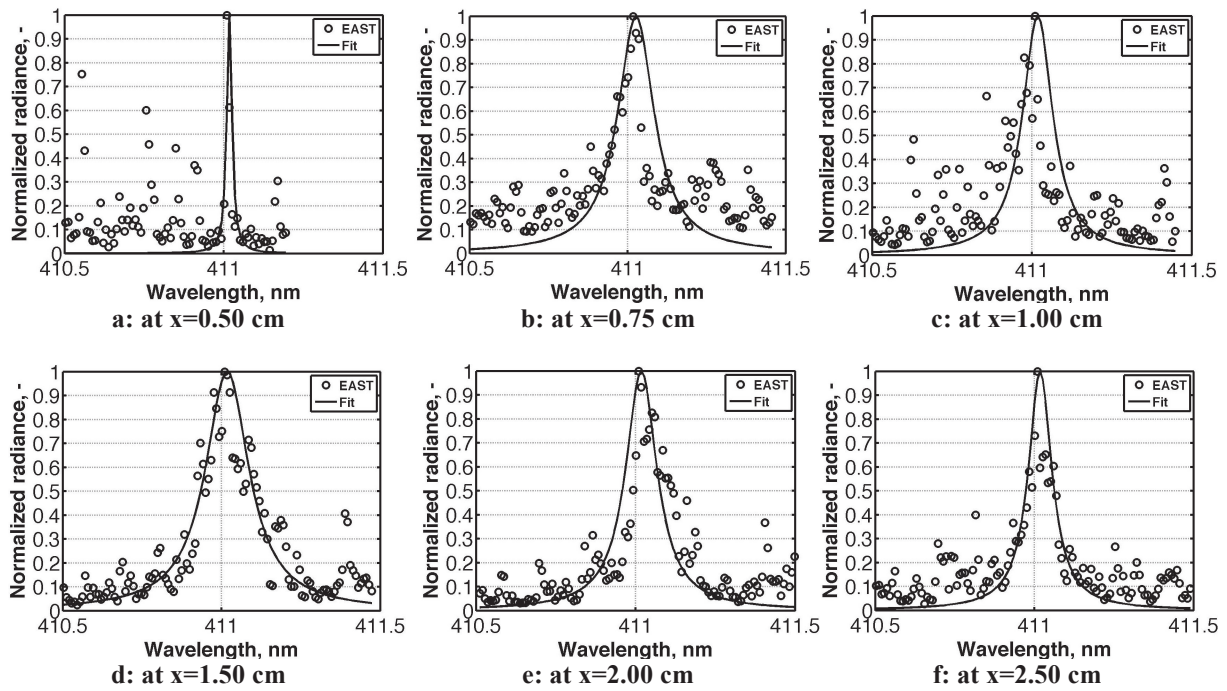


Figure 4.24: N(411) profile fits at several locations for shot 119 ($V_\infty=11.17$ km/s, $p_\infty=13.3$ Pa)
The experimental spectra are averaged over 10 adjacent pixels (≈ 2 mm)

Figure 4.25 presents the electron number density profile determined from the measured line shapes. The electron number density magnitude is higher than in the previous condition, since the freestream velocity is higher which leads to stronger ionization processes. It is shown that the electron number density reaches a peak. The observed decrease may reflect ion recombination due to the cooling of the flow, when the driver gas comes in contact with the test gas.

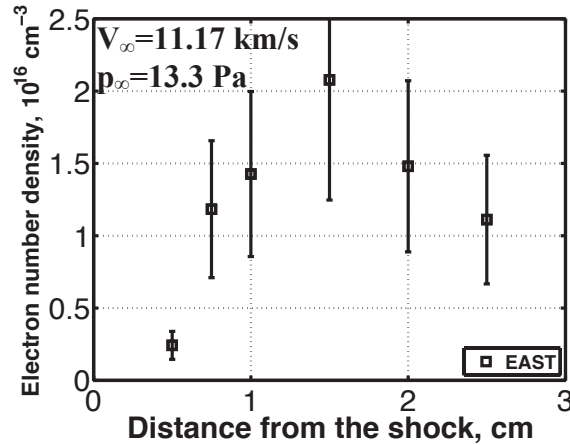


Figure 4.25: Electron number density profile inferred from Stark-broadened N(411) line for shot 119 ($V_\infty=11.17$ km/s, $p_\infty=13.3$ Pa)

IV.4.2. Comparison with the flowfield model and shock front location determination

Figures 4.25 and 4.26 compares the measured electron number density profiles with the profiles predicted by the flowfield model Poshax (Gollan, 2006; Potter, 2011) for shots 50-116 ($V_\infty=10.54$ km/s, $p_\infty=13.3$ Pa) and 50-119 ($V_\infty=11.17$ km/s, $p_\infty=13.3$ Pa), respectively. The experimental data were adjusted along the x-axis, so as to provide the best match with the predicted profile, enabling to locate the absolute position of the shock front in the experimental data, which will be very important for the subsequent spatial analyses.

The comparison of the experimental and simulated profiles for shot 50-116 clearly shows that the Poshax model (Gollan, 2006; Potter, 2011) accurately predicts the electron number density profile, both in shape and magnitude. The comparison for shot 50-119 is also reasonable and certainly within the experimental uncertainties.

Given the initial determination of the shock front location, the experimental electron number density profiles obtained for the shots 50-116 and 50-119 were slightly shifted of -0.2 cm and +0.1 cm along the x-axis, respectively. Thus, the experimental post-shock intensity profiles for shot 50-116, 117 and for shot 50-119 were shifted of -0.2 cm and +0.1 cm along the x-axis, respectively. Hereafter, the new shock front location is used as the reference for all comparisons between experimental and simulated intensities.

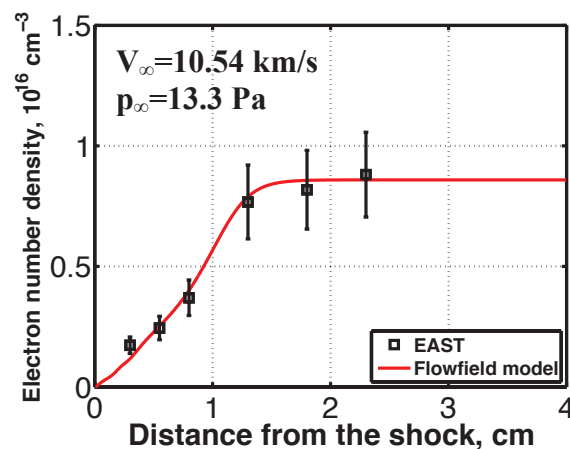


Figure 4.26: Comparison between experimental and predicted electron number densities for shot 116 ($V_\infty=10.54$ km/s, $p_\infty=13.3$ Pa)

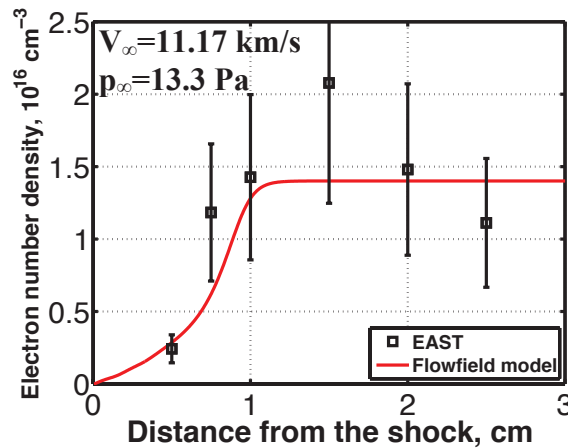


Figure 4.27: Comparison between experimental and predicted electron number densities for shot 119 ($V_{\infty}=11.17$ km/s, $p_{\infty}=13.3$ Pa)

IV.6. Summary

The characterization of the radiation on a spacecraft during its entry relies on a combination of numerical simulation and experimental validation. The absolute radiation measurements obtained in the EAST facility at NASA Ames Research Center were used and analyzed to test the CR model. Two conditions representative of the severe environment encountered by the spacecraft were investigated in the VUV, visible and IR spectral ranges.

For each of the conditions, the corresponding CCD images were analyzed. The vibrational and rotational temperatures of N_2 ($C^3\Pi_u$) and N_2^+ ($B^2\Pi_u$) electronic states were inferred from the nonequilibrium spectra of N_2 Second Positive and N_2^+ First Negative at two locations in the post-shock region. For both electronic states, strong coupling between the vibrational and rotational modes were shown. The discrepancy between the vibrational and rotational temperatures inferred from the experiments and the temperatures predicted by Poshax (Gollan, 2006; Potter, 2011) multi-temperature model warrant further effort in modeling the vibrational and rotational distribution of the levels in these states.

The electron number density was inferred from Stark-broadened nitrogen and H_{α} lines. Excellent agreement was obtained for the prediction of the electron number density profile, thus enabling us to validate the ionization rate constant model implemented in the flowfield solver and to accurately locate the shock front.

Chapter V

Assessment of the collisional- radiative model

Overview

In this chapter, we compare the predictions of the CR model with the radiation measurements obtained in the Electric Arc Shock-tube (EAST) facility at NASA Ames Research center. In section 1, we compare the predicted and experimental post-shock intensity profiles in the VUV, visible and IR spectral ranges and demonstrate the key role of heavy-particle impact excitation processes. In section 2, we carry out a sensitivity analysis on the dissociation, dissociation-vibration coupling and heavy-particle impact excitation rate constant models. In section 3, we further assess the CR and spectral models by comparing the simulated spectra with the spectra extracted from the CCD images. Finally, in section 4, we describe the methodology used to extract the populations of the corresponding emitting and absorbing states from the observed lines and we compare the populations inferred from the experiments with the predictions of the CR model.

Table of contents

V.1. Post-shock intensity profiles	103
V.1.1. Influence of electron-impact processes	103
V.1.1.1 Visible spectral range	103
V.1.1.2. Infrared spectral range	103
V.1.1.3. VUV spectral range	103
V.1.2. Influence of the dissociation model.....	106
V.1.3. Sensitivity to heavy-particle impact excitation processes	111
V.1.3.1. Visible spectral range	112
V.1.3.2. Infrared spectral range	112
V.1.3.3. VUV spectral range	112
V.1.4. Assessment of the Boltzmann multi-temperature model.....	115
V.1.4.1. Visible spectral range	115
V.1.4.2. Infrared spectral range	115
V.1.4.3. VUV spectral range	116
V.2. Spectral analysis.....	117
V.2.1. Visible spectral range	117
V.2.2. Infrared spectral range	118
V.2.3. VUV spectral range	118
V.3. Populations of the excited states	120
V.3.1. Experimental distribution of the grouped level populations.....	120
V.3.1.1. Methodology	120
V.3.1.2. Condition 117: $V_\infty=10.6$ km/s, $p_\infty=13.3$ Pa	126
V.3.1.3. Condition 119: $V_\infty=11.17$ km/s, $p_\infty=13.3$ Pa	127
V.3.2. Comparison with the CR and Boltzmann multi-temperature model predictions	129
V.3.2.1. Visible spectral range	129
V.3.2.2. Infrared spectral range	129
V.3.2.3. VUV spectral range	129
V.5. Summary	131

V.1. Post-shock intensity profiles

In this section, the simulated and experimental post-shock intensity profiles¹⁰ in the VUV, IR and visible spectral ranges are compared. The experimental post-shock intensity profiles were shifted by the same distance as the electron number density profile. The influence of electron-impact and heavy-particle impact processes are examined.

V.1.1. Influence of electron-impact processes

V.1.1.1 Visible spectral range

Figures 5.1 and 5.2 compare the post-shock intensity profiles in the visible spectral range for shots 50-117 ($V_\infty=10.6$ km/s, $p_\infty=13.3$ Pa) and shot 50-119 ($V_\infty=11.17$ km/s, $p_\infty=13.3$ Pa), respectively when only electron-impact excitation and ionization processes are taken into account. Given the uncertainty in this spectral range (30% on the Einstein coefficients (NIST, 2012) and 20% due to calibration) the trend and the magnitudes of the experimental post-shock intensity profiles are well predicted in this spectral range for both conditions, suggesting that the electron-impact excitation and ionization processes control the populations of the excited states emitting and absorbing in the visible. The experimental intensity magnitude decreases after 3.5 cm, which may be due to the cooling of the flow, when the driver gas comes in contact with the test gas.

V.1.1.2. Infrared spectral range

Figures 5.3 and 5.4 compare the post-shock intensity profiles in the IR spectral range when electron-impact excitation and ionization processes are taken into account for $V_\infty=10.6$ km/s and $V_\infty=11.17$ km/s, respectively. Given the uncertainty in this spectral range (10% on the Einstein coefficients (NIST, 2012) and 10% due to calibration) the trend and the magnitudes of the experimental post-shock intensity profiles are reasonably well predicted in this spectral range for both conditions. For both conditions, the nonequilibrium intensity ‘bump’ at $x=0.75$ cm is underpredicted when only electron-impact processes are considered. It will be shown in subsection V.1.3 that taking into account heavy-particle impact excitation processes improves the agreement with the experimental profile in the nonequilibrium zone. Again, the experimental intensity magnitude decreases after 3.5 cm, which may be due to the cooling of the flow, when the driver gas comes in contact with the test gas.

V.1.1.3. VUV spectral range

Figures 5.5 and 5.6 compare the post-shock intensity profiles in the VUV spectral range when electron-impact excitation and ionization processes are taken into account for $V_\infty=10.54$ km/s and $V_\infty=11.17$ km/s, respectively. For both conditions, the nonequilibrium peak intensity is strongly underpredicted when only electron-impact processes are taken into account. It will be shown in subsection V.1.3 that taking into account heavy-particle impact excitation processes significantly improves the agreement with the experimental profile in the nonequilibrium zone. Finally, it will be shown in section V.2 that the intensity ‘bump’ at 2 cm is due to carbon lines, which may be due to impurities traveling in the shock-tube

¹⁰ The post-shock intensity profile was computed as described in section IV.2 with the total spatial smearing function. The result was then divided by the EAST diameter ($D=10.16$ cm). Appendix D presents the post-shock intensity profile obtained when only the smearing due to shock motion is taken into account.

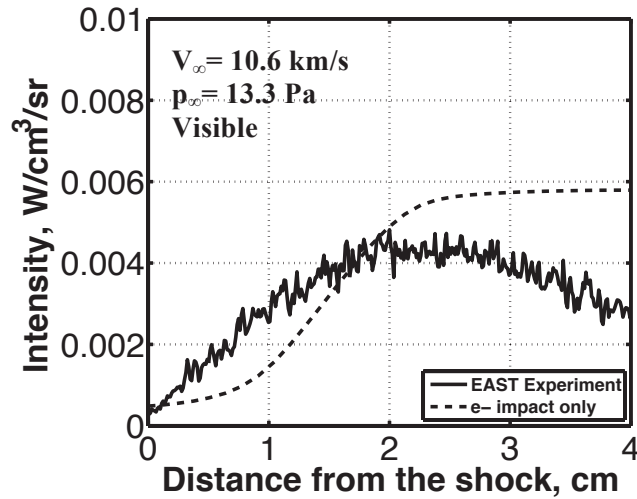


Figure 5.1: Comparison between experimental and simulated post-shock intensity profiles for shot 117 ($V_\infty=10.6 \text{ km/s}$, $p_\infty=13.3 \text{ Pa}$) in the visible ($\Delta\lambda=409\text{-}411 \text{ nm}$), electron-impact processes only

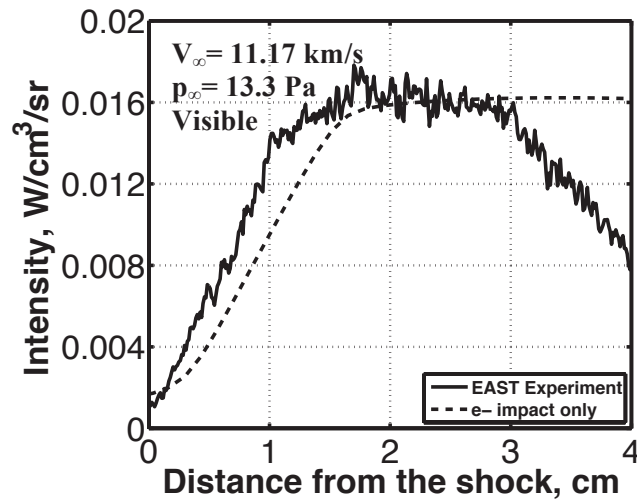


Figure 5.2: Comparison between experimental and simulated post-shock intensity profiles for shot 119 ($V_\infty=11.17 \text{ km/s}$, $p_\infty=13.3 \text{ Pa}$) in the visible ($\Delta\lambda=409\text{-}411 \text{ nm}$), electron-impact processes only

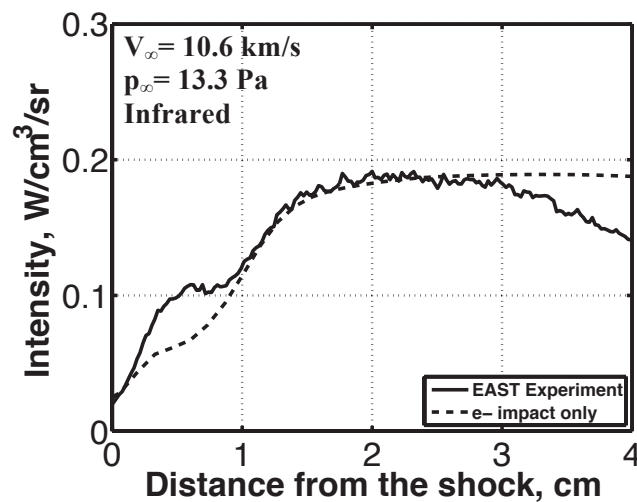


Figure 5.3: Comparison between experimental and simulated post-shock intensity profiles for shot 117 ($V_\infty=10.6 \text{ km/s}$, $p_\infty=13.3 \text{ Pa}$) in the IR ($\Delta\lambda=852\text{-}872 \text{ nm}$), electron-impact processes only

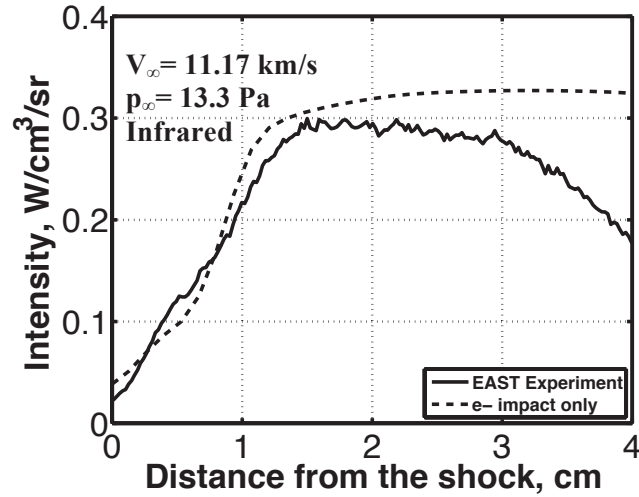


Figure 5.4: Comparison between experimental and simulated post-shock intensity profiles for shot 119 ($V_\infty=11.17 \text{ km/s}$, $p_\infty=13.3 \text{ Pa}$) in the IR ($\Delta\lambda=852\text{-}872 \text{ nm}$), electron-impact processes only

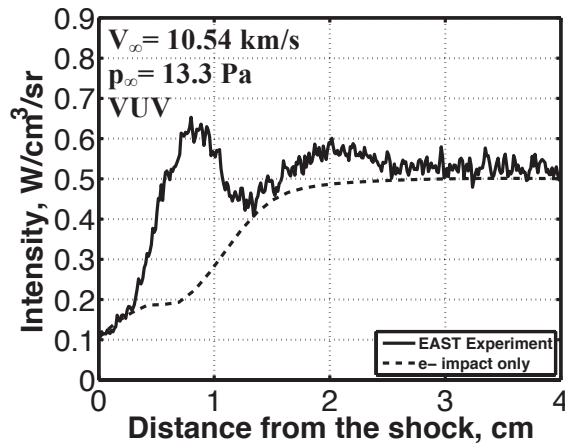


Figure 5.5: Comparison between experimental and simulated post-shock intensity profiles for shot 116 ($V_\infty=10.54 \text{ km/s}$, $p_\infty=13.3 \text{ Pa}$) in the VUV ($\Delta\lambda=140\text{-}176 \text{ nm}$), electron-impact processes only

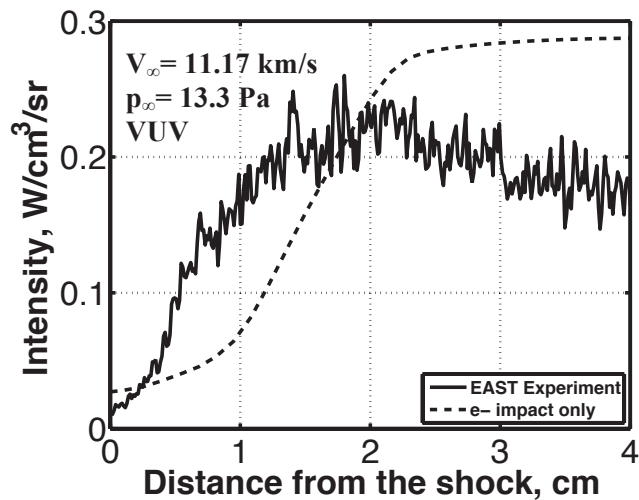


Figure 5.6: Comparison between experimental and simulated post-shock intensity profiles for shot 119 ($V_\infty=11.17 \text{ km/s}$, $p_\infty=13.3 \text{ Pa}$) in the VUV ($\Delta\lambda=174\text{-}175 \text{ nm}$), electron-impact processes only

This subsection showed that the electron-impact processes slightly and strongly underpredicting the nonequilibrium peak intensity observed in the IR and VUV spectral ranges. These discrepancies suggest that heavy-particle processes may play a significant role in the nonequilibrium region of the post-shock zone. Heavy-particle processes primarily depend on the number densities of the heavy particles, which result from the dissociation processes, and on the excitation rate constants. Both of these aspects will be discussed in the following subsections. In subsection V.1.2, the influence of the dissociation model is discussed. In subsection V.1.3, the influence of the excitation processes is outlined.

V.1.2. Influence of the dissociation model

The dissociation of nitrogen molecules is of great importance because atomic nitrogen lines dominate the post-shock intensity for the conditions considered in this work. The dissociation rate constant of N_2 has been the subject of extensive investigation over the last decades. Several dissociation rate constant models (Park¹¹, 1985-1986; Macheret and Rich, 1993) were implemented in Poshax by Potter (2011) and are recalled in appendix A. Figures 5.7 and 5.8 present the influence of the dissociation rate constant model on the flowfield variables for $V_\infty=10.6$ km/s and $V_\infty=11.17$ km/s, respectively.

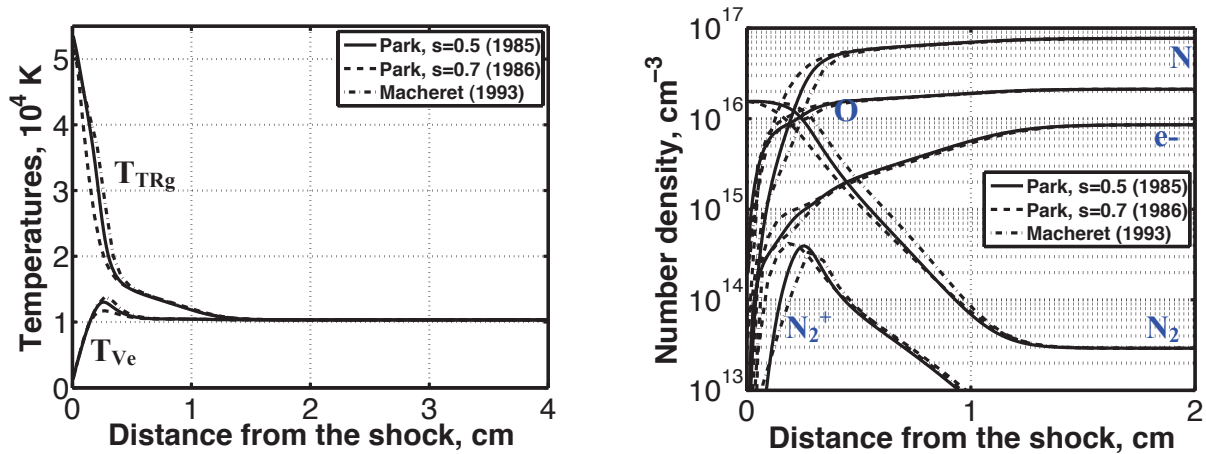


Figure 5.7: Sensitivity of the temperatures and species number density profiles to the dissociation rate constant model for shot 117 ($V_\infty=10.6$ km/s, $p_\infty=13.3$ Pa)

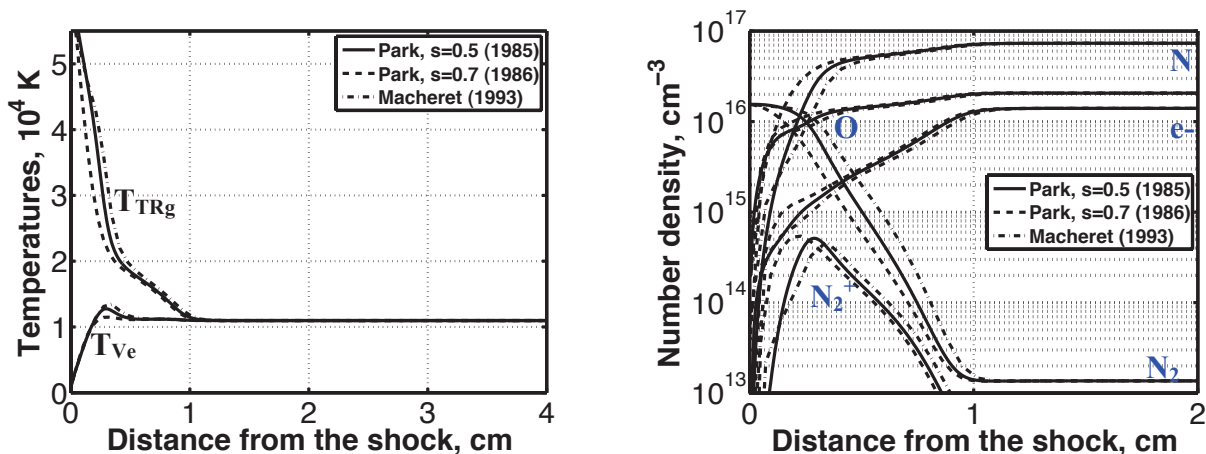


Figure 5.8: Sensitivity of the temperatures and species number density profiles to the dissociation rate constant model for shot 119 ($V_\infty=11.17$ km/s, $p_\infty=13.3$ Pa)

¹¹ The dissociation rate constant model from Park (1985-1986) is computed at temperature $T_a=T_{TRg}^s T_{Ve}^{1-s}$.

The influence of the dissociation rate constant model on post-shock intensity profiles in the VUV and IR spectral ranges for $V_\infty=10.6$ km/s and $V_\infty=11.17$ km/s, respectively is illustrated in figures 5.9-5.10 and figures 5.11-5.12, respectively. These figures show that the dissociation rate constant model is not influential on the post-shock intensity profile. Also, the various dissociation rate constant models still underpredict the nonequilibrium peak intensity observed in the VUV and in the IR spectral ranges for both conditions. Hereafter, the dissociation rate constant of Park (1985) with $s=0.5$ will be used in the remaining of the dissertation.

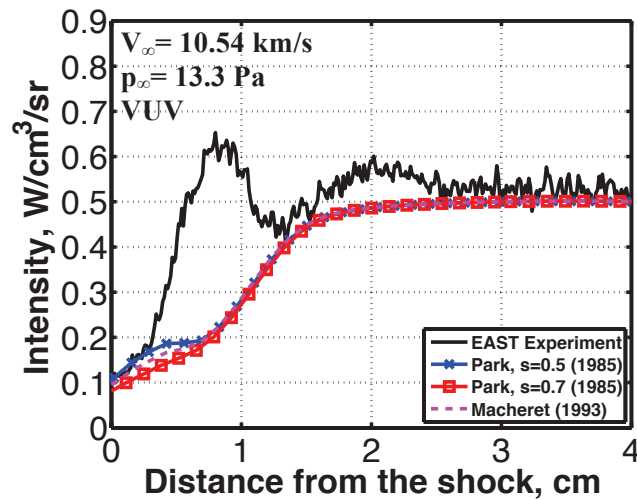


Figure 5.9: Sensitivity of the post-shock intensity profile to the dissociation rate constant model for shot 116 ($V_\infty=10.54$ km/s, $p_\infty=13.3$ Pa) in the VUV ($\Delta\lambda=140-176$ nm)

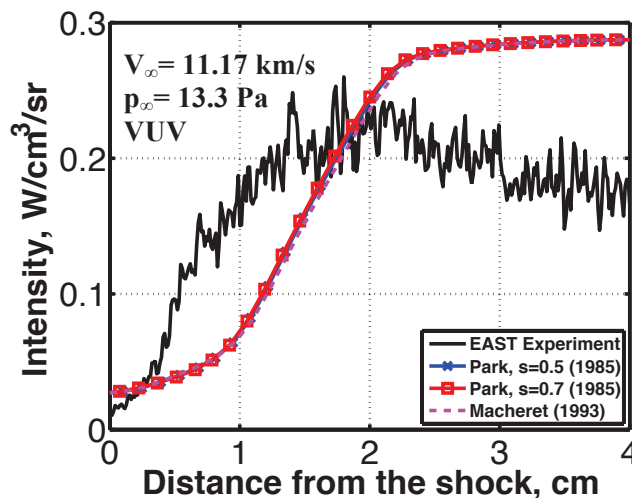


Figure 5.10: Sensitivity of the post-shock intensity profile to the dissociation rate constant model for shot 119 ($V_\infty=11.17$ km/s, $p_\infty=13.3$ Pa) in the VUV ($\Delta\lambda=174-175$ nm)

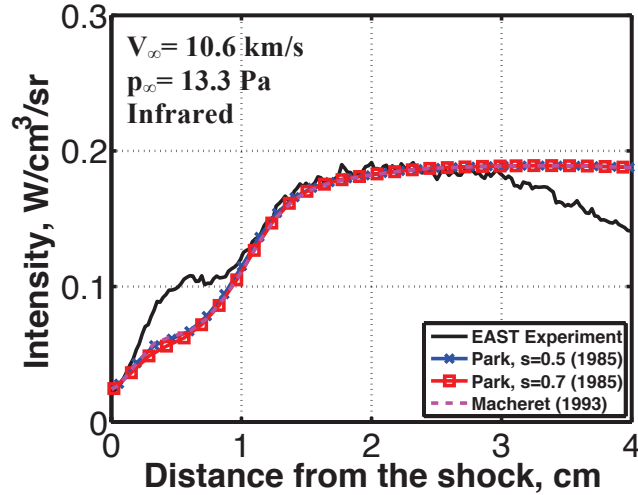


Figure 5.11: Sensitivity of the post-shock intensity profile to the dissociation rate constant model for shot 117 ($V_\infty=10.6$ km/s, $p_\infty=13.3$ Pa) in the IR ($\Delta\lambda=852-872$ nm)

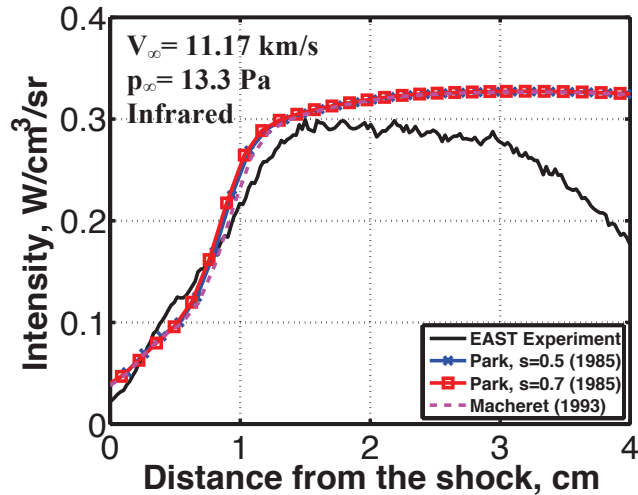


Figure 5.12: Sensitivity of the post-shock intensity profile to the dissociation rate constant model for shot 119 ($V_\infty=11.17$ km/s, $p_\infty=13.3$ Pa) in the IR ($\Delta\lambda=852-872$ nm)

The chemical reactions depleting or producing molecules affect the average vibrational energy in the gas, since they affect the distribution of the vibrational levels of the molecules. The vibration-dissociation coupling models have received substantial attention over the last decades. Among the various models, it is common to distinguish between preferential and non-preferential dissociation models. The non-preferential coupling (labeled n.p.c. in the following) models prescribe an equal probability of dissociation from all the vibrational levels of the molecules as opposed to the preferential coupling (labeled p.c. in the following) dissociation models which assume that dissociation takes place from the upper vibrationally excited states. The most commonly used models in the literature were implemented in Poshax by Potter (2011) and are briefly outlined in appendix A.

The influence of the vibration-dissociation model on the temperatures and species number densities for $V_\infty=10.6$ km/s and $V_\infty=11.17$ km/s, respectively, is illustrated in figures 5.13 and 5.14, respectively.

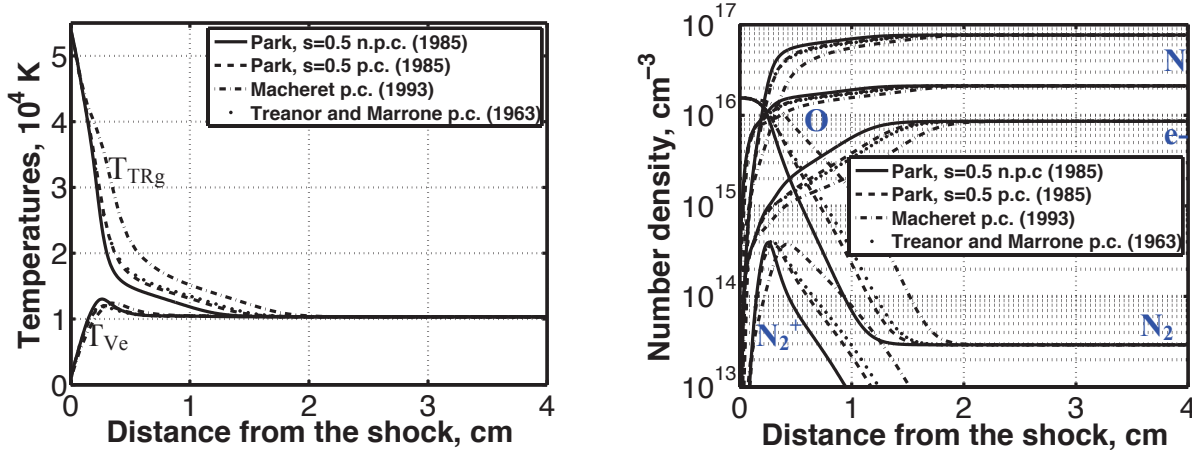


Figure 5.13: Sensitivity of the temperatures and species number density profiles to the dissociation-vibration coupling model for shot 117 ($V_\infty=10.6$ km/s, $p_\infty=13.3$ Pa)

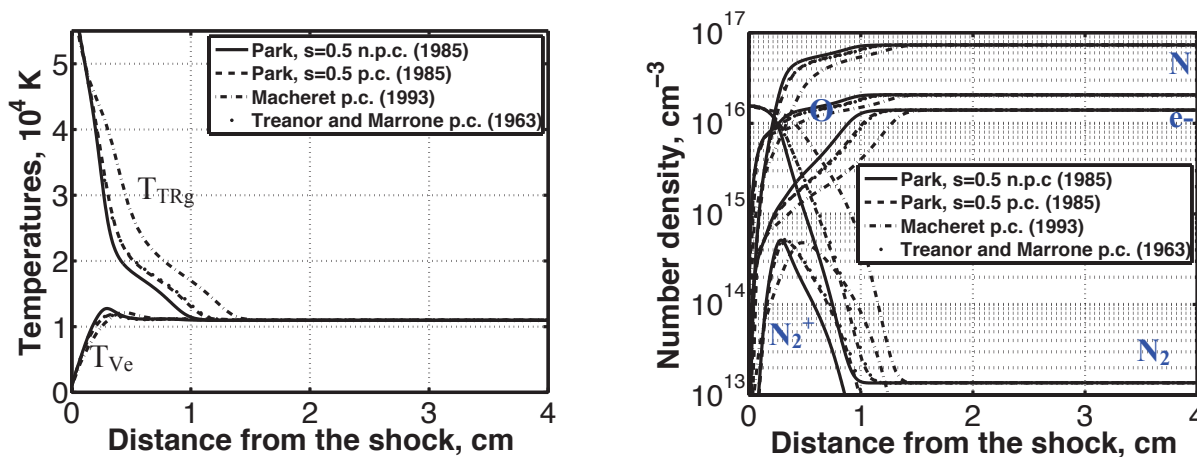


Figure 5.14: Sensitivity of the temperatures and species number density profiles to the dissociation-vibration coupling model for shot 119 ($V_\infty=11.17$ km/s, $p_\infty=13.3$ Pa)

The influence of the vibration-dissociation coupling model on the post-shock intensity profile for $V_\infty=10.6$ km/s and $V_\infty=11.17$ km/s in the VUV and IR spectral ranges is illustrated in figures 5.15-5.16 for the VUV spectral range and in figures 5.17-5.18 for the IR spectral range. The preferential vibration-dissociation models increase the equilibration distance but still underpredict the nonequilibrium peak intensity observed in the VUV and in the IR spectral ranges for both conditions. For practical purposes, the non-preferential dissociation-vibration rate constant model of Park (1985) with $s=0.5$ will be used in the remaining of the dissertation.

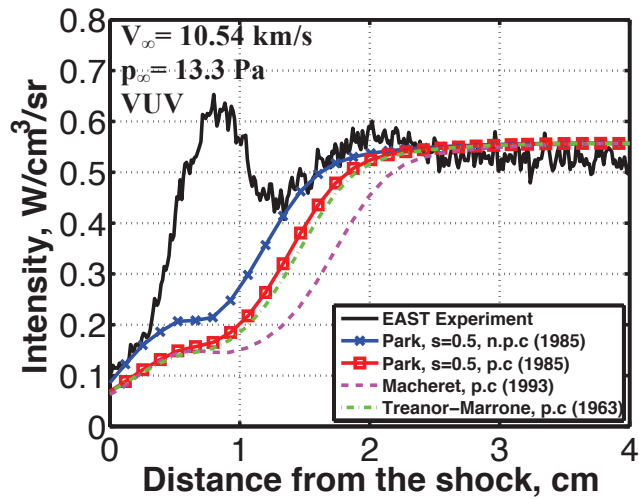


Figure 5.15: Sensitivity of the post-shock intensity to the dissociation-vibration coupling model for shot 116 ($V_\infty=10.54$ km/s, $p_\infty=13.3$ Pa) in the VUV ($\Delta\lambda=140-176$ nm)

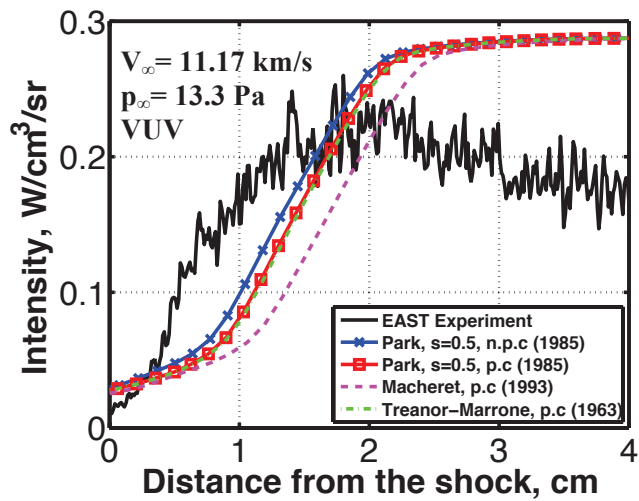


Figure 5.16: Sensitivity of the post-shock intensity to the dissociation-vibration coupling model for shot 119 ($V_\infty=11.17$ km/s, $p_\infty=13.3$ Pa) in the VUV ($\Delta\lambda=174-175$ nm)

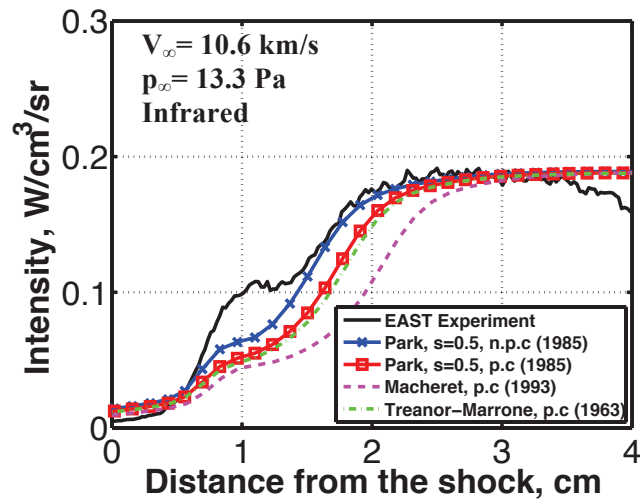


Figure 5.17: Sensitivity of the post-shock intensity to the dissociation-vibration coupling model for shot 117 ($V_\infty=10.6$ km/s, $p_\infty=13.3$ Pa) in the IR ($\Delta\lambda=852-872$ nm)]

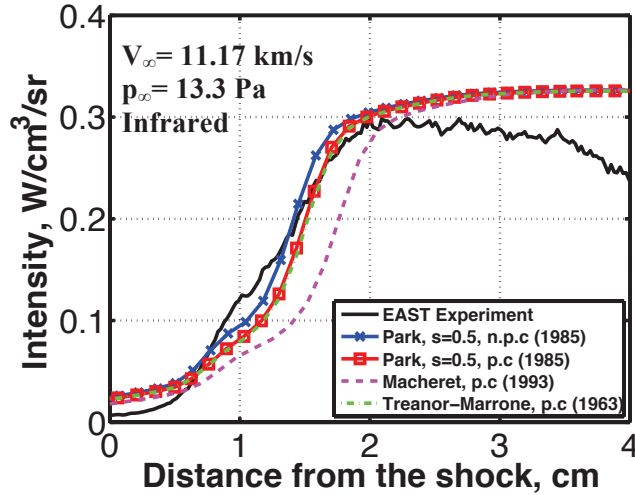


Figure 5.18: Sensitivity of the post-shock intensity to the dissociation-vibration coupling model for shot 119 ($V_\infty=11.17$ km/s, $p_\infty=13.3$ Pa) in the IR ($\Delta\lambda=852-872$ nm)

This subsection discussed the influence of N_2 dissociation rate constant and dissociation-vibration coupling models. It was shown that the various dissociation rate constant models of Park (1985) and Macheret and Rich (1993) were in good agreement with each other. Also, the preferential dissociation-vibration coupling models were shown to increase the equilibrium distance. Thus, the non-preferential dissociation rate constant model of Park (1985) with $s=0.5$ will be used in the remaining of the dissertation. Moreover, this subsection showed that the various dissociation rate constant models and dissociation-vibration coupling models still underpredict the intensity observed in the VUV and in the IR spectral ranges in the nonequilibrium post-shock zone, suggesting that the heavy-particle impact excitation processes may play a key role.

V.1.3. Sensitivity to heavy-particle impact excitation processes

As a starting point, the influence of the heavy-particle impact processes rate constants of Park (1985) are examined. As illustrated in figure 5.19, the CR model with the heavy-particle impact rate constants of Park (1985) overpredicts by a factor 3 the experimental post-shock intensity profile in the VUV spectral range.

As shown in **chapter 3**, the heavy-particle impact excitation rate constants suffer from large uncertainties. Given the order of magnitude discussed by Kelley (2013), the rate constants of Park (1985) are higher than the recommended value by Kelley (2013). Therefore, the rate constants of Park (1985) are used as a starting point and adjusted to obtain good agreement with the experimental data in the VUV, visible and IR spectral ranges for both conditions investigated. As shown in the following subsections, the experimental post-shock profiles measured in the visible, IR and VUV spectral ranges for both shot conditions are well predicted by dividing the rate constants of Park (1985) by a constant factor of 8000.

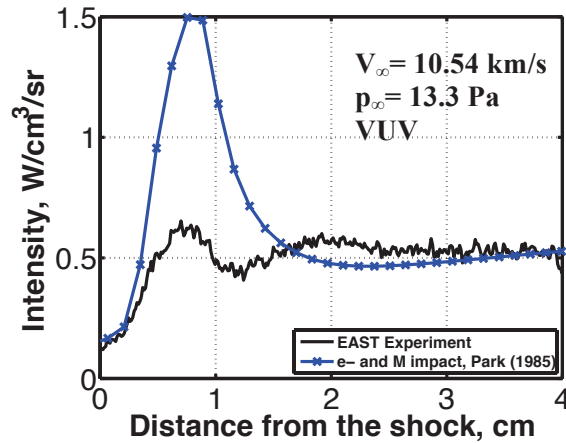


Figure 5.19: Prediction of the intensity profiles for shot 116 ($V_\infty=10.54$ km/s, $p_\infty=13.3$ Pa) with the baseline heavy-particle impact excitation rate constants of Park (1985)

V.1.3.1. Visible spectral range

Figures 5.20 and 5.21 compare the post-shock intensity profiles in the visible spectral range when electron-impact excitation and ionization processes as well as heavy-particle impact processes are taken into account for $V_\infty=10.6$ km/s and $V_\infty=11.17$ km/s, respectively. The trend and the magnitude of the experimental post-shock intensity profiles are well predicted in this spectral range for both conditions with electron-impact processes only, suggesting that the heavy-particle impact excitation processes have little influence on the population of N(15) in the nonequilibrium zone.

V.1.3.2. Infrared spectral range

Figures 5.22 and 5.23 compare the post-shock intensity profiles in the IR spectral range with both electron-impact and heavy-particle impact processes are taken into account for $V_\infty=10.6$ km/s and $V_\infty=11.17$ km/s, respectively. Again, the trend and the magnitude of the experimental post-shock intensity profiles are reasonably predicted in this spectral range for both conditions. In particular, for both conditions, the nonequilibrium intensity ‘bump’ at $x=0.75$ cm appears to be controlled by heavy-particle impact excitation processes.

V.1.3.3. VUV spectral range

Figures 5.24 and 5.25 compare the post-shock intensity profiles in the VUV spectral range when electron-impact excitation and ionization processes are taken into account for $V_\infty=10.54$ km/s and $V_\infty=11.17$ km/s, respectively. For both velocity conditions, the heavy-particle impact excitation processes significantly improve the comparisons with the experimental data. In particular, they appear to be responsible for the nonequilibrium peak intensity at 10.54 km/s and they induce an earlier increase of the intensity profile at 11.17 km/s.

In future work, it will interesting to examine whether the effect of heavy-particle impact processes becomes more important at lower speed, as suggested by the two shot conditions examined here.

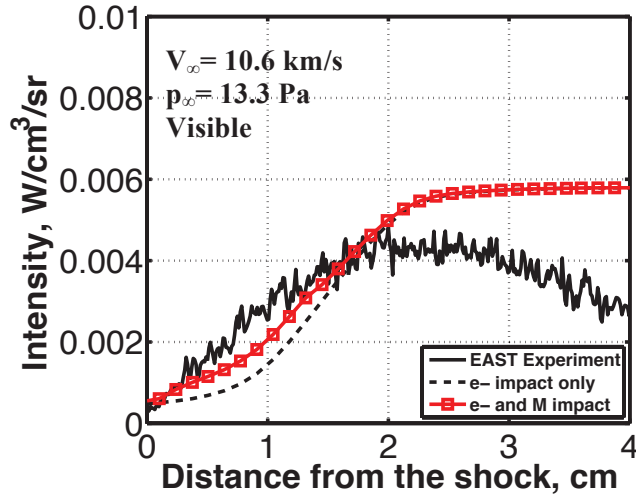


Figure 5.20: Comparison between experimental and simulated post-shock intensity profiles for shot 117 ($V_\infty=10.6$ km/s, $p_\infty=13.3$ Pa) in the visible ($\Delta\lambda=409-411$ nm), electron and heavy-particle impact processes

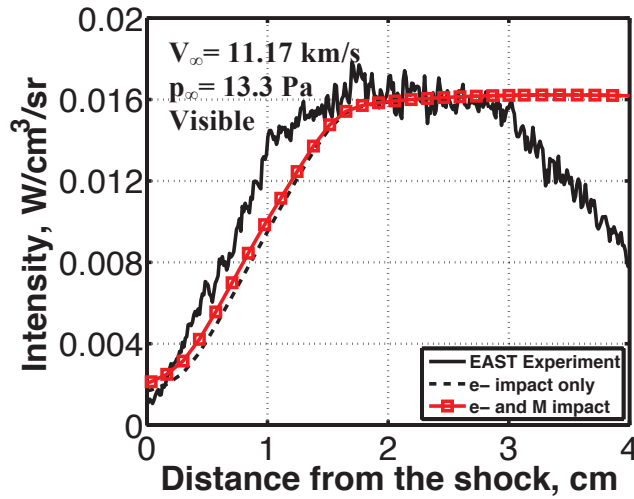


Figure 5.21: Comparison between experimental and simulated post-shock intensity profiles for shot 119 ($V_\infty=11.17$ km/s, $p_\infty=13.3$ Pa) in the visible ($\Delta\lambda=409-411$ nm), electron and heavy-particle impact processes

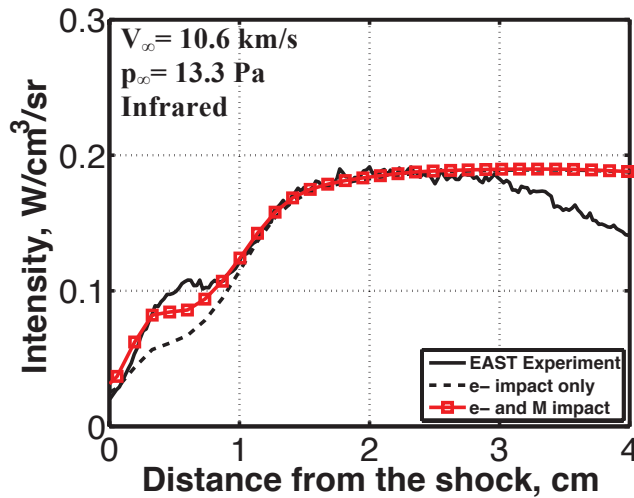


Figure 5.22: Comparison between experimental and simulated post-shock intensity profiles for shot 117 ($V_\infty=10.6$ km/s, $p_\infty=13.3$ Pa) in the IR ($\Delta\lambda=852-872$ nm), electron and heavy-particle impact processes

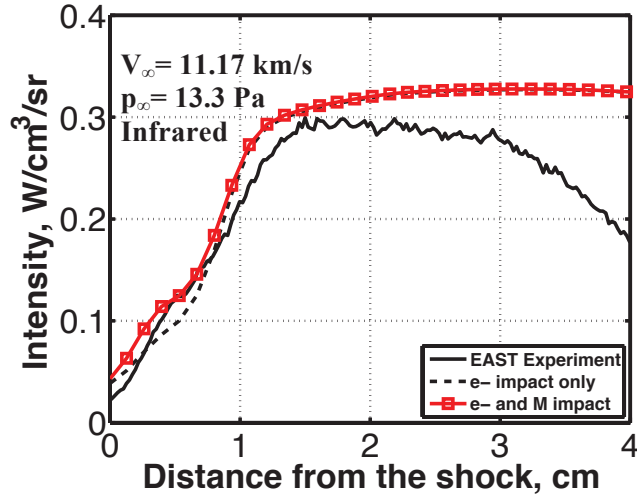


Figure 5.23: Comparison between experimental and simulated post-shock intensity profiles for shot 119 ($V_\infty=11.17$ km/s, $p_\infty=13.3$ Pa) in the IR ($\Delta\lambda=852-872$ nm), electron and heavy-particle impact processes

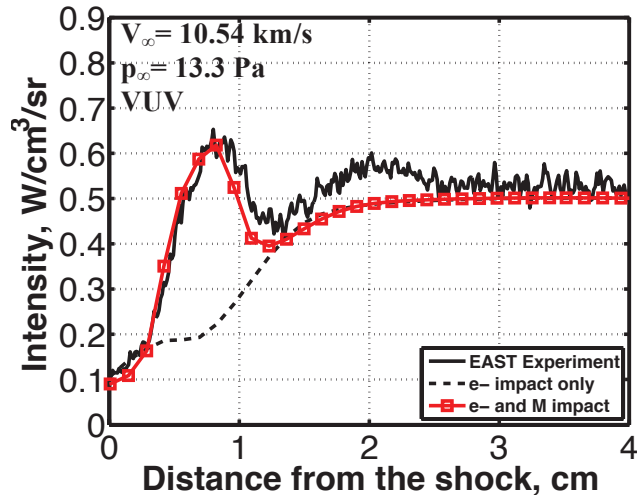


Figure 5.24: Comparison between experimental and simulated post-shock intensity profiles for shot 116 ($V_\infty=10.54$ km/s, $p_\infty=13.3$ Pa) in the VUV ($\Delta\lambda=140-176$ nm), electron and heavy-particle impact processes

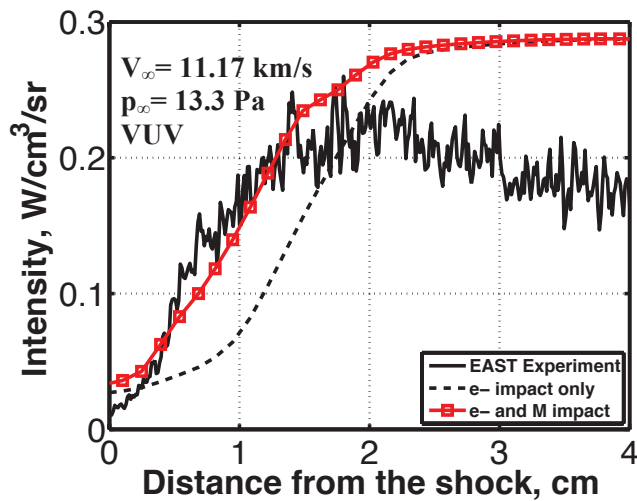


Figure 5.25: Comparison between experimental and simulated post-shock intensity profiles for shot 119 ($V_\infty=11.17$ km/s, $p_\infty=13.3$ Pa) in the VUV ($\Delta\lambda=174-175$ nm), electron and heavy-particle impact processes

V.1.4. Assessment of the Boltzmann multi-temperature model

In this subsection, the experimental post-shock profiles as well as the post-shock intensity profiles predicted with the CR model by adjusting heavy-particle impact processes of Park (1985) (i.e. divided by 8000) are compared with the widely used multi-temperature Boltzmann model.

V.1.4.1. Visible spectral range

Figures 5.26 and 5.27 compare the post-shock intensity profiles computed with the CR model and with the Boltzmann distribution of the excited states at T_{Ve} in the visible spectral range for $V_\infty=10.6$ km/s and $V_\infty=11.17$ km/s, respectively. For both conditions, the Boltzmann distribution overpredicts the post-shock intensity profile in the nonequilibrium zone.

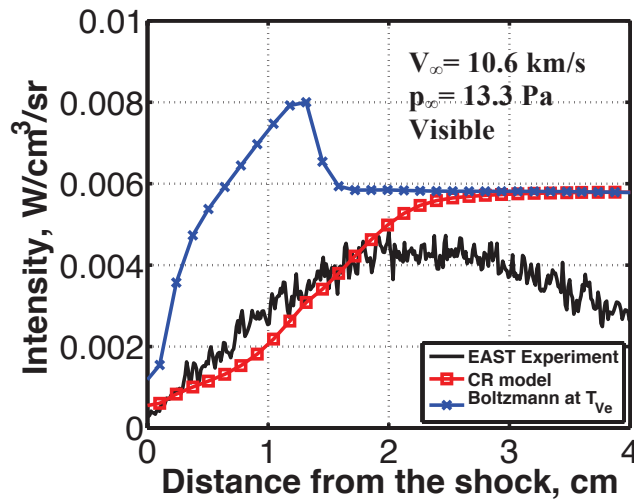


Figure 5.26: Comparison between experimental and simulated post-shock intensity profiles with the CR and Boltzmann models for shot 117 ($V_\infty=10.6$ km/s, $p_\infty=13.3$ Pa) in the visible ($\Delta\lambda=409-411$ nm)

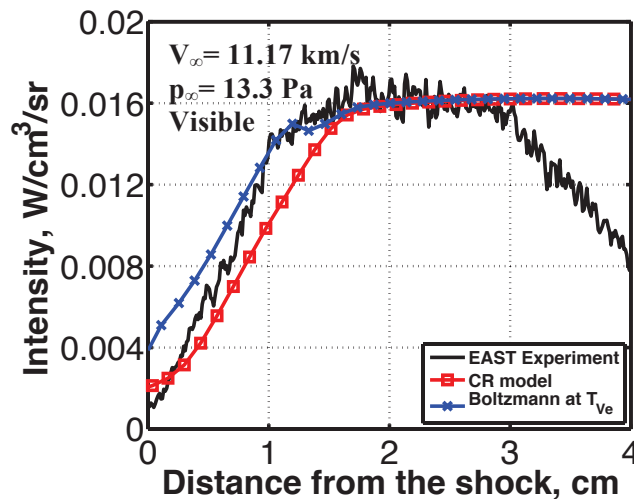


Figure 5.27: Comparison between experimental and simulated post-shock intensity profiles with the CR and Boltzmann models for shot 119 ($V_\infty=11.17$ km/s, $p_\infty=13.3$ Pa) in the visible ($\Delta\lambda=409-411$ nm)

V.1.4.2. Infrared spectral range

Figures 5.28 and 5.29 compare the post-shock intensity profiles computed with the CR model and with the Boltzmann distribution of the excited states at T_{Ve} in the IR spectral range for

$V_\infty=10.6$ km/s and $V_\infty=11.17$ km/s, respectively. Again, the Boltzmann distribution overpredicts the post-shock intensity profile in the nonequilibrium zone for both conditions.

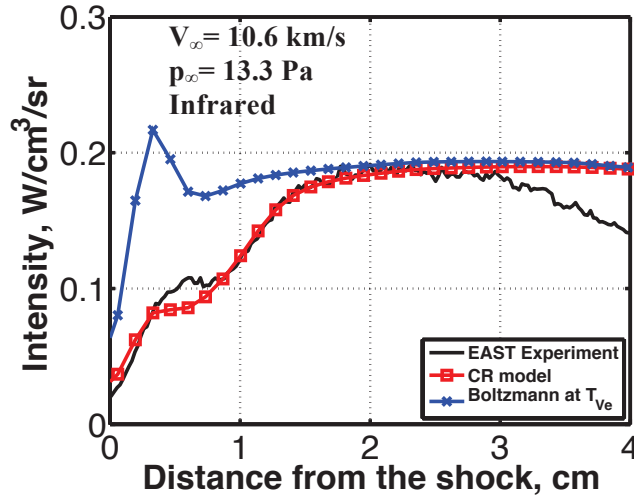


Figure 5.28: Comparison between experimental and simulated post-shock intensity profiles with the CR and Boltzmann models for shot 117 ($V_\infty=10.6$ km/s, $p_\infty=13.3$ Pa) in the IR ($\Delta\lambda=852-872$ nm)

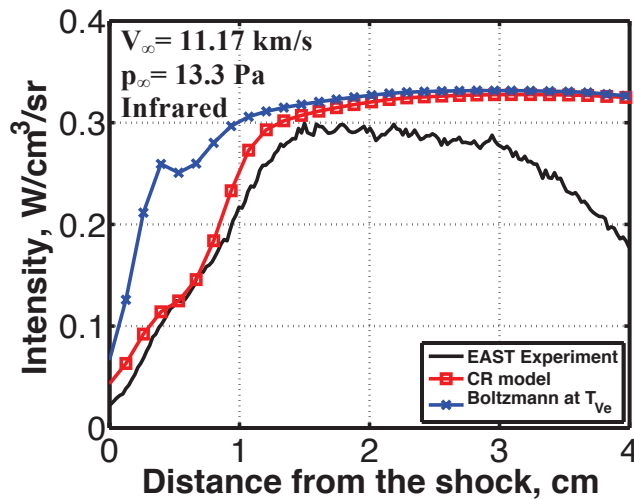


Figure 5.29: Comparison between experimental and simulated post-shock intensity profiles with the CR and Boltzmann models for shot 119 ($V_\infty=11.17$ km/s, $p_\infty=13.3$ Pa) in the IR ($\Delta\lambda=852-872$ nm)

V.1.4.3. VUV spectral range

Figures 5.30 and 5.31 compare the post-shock intensity profiles computed with the CR model and with the Boltzmann distribution of the excited states at T_{Ve} in the VUV spectral range for $V_\infty=10.6$ km/s and $V_\infty=11.17$ km/s, respectively. Surprisingly, the prediction with a Boltzmann distribution at T_{Ve} is in good agreement with the CR model in the VUV. This suggests that the emitting and absorbing excited states tend to follow a Boltzmann distribution at T_{Ve} due to strong electron- and heavy-particle impact processes.

In section V.3, the populations of the excited states responsible for the lines observed in the VUV, visible and IR spectral ranges will be inferred from the radiation measurements and compared with the predictions given by the Boltzmann and CR models, enabling us to further discuss the distribution of the excited states and to give further insight on the agreement

between the experimental profiles and the profiles predicted by the CR model and the Boltzmann multitemperature model.

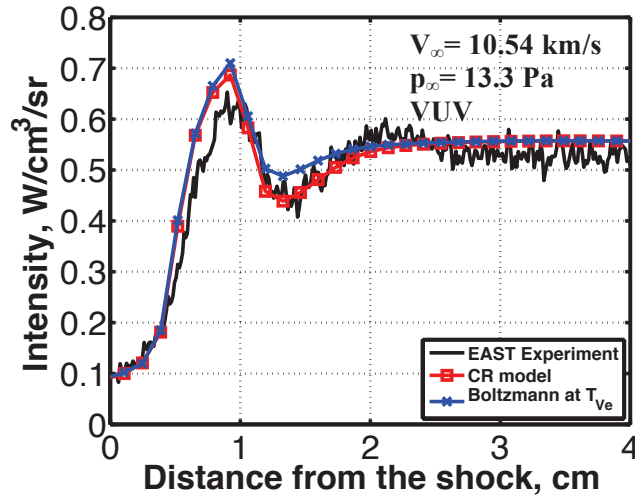


Figure 5.30: Comparison between experimental and simulated post-shock intensity profiles with the CR and Boltzmann models for shot 116 ($V_\infty=10.54$ km/s, $p_\infty=13.3$ Pa) in the VUV ($\Delta\lambda=140-176$ nm)

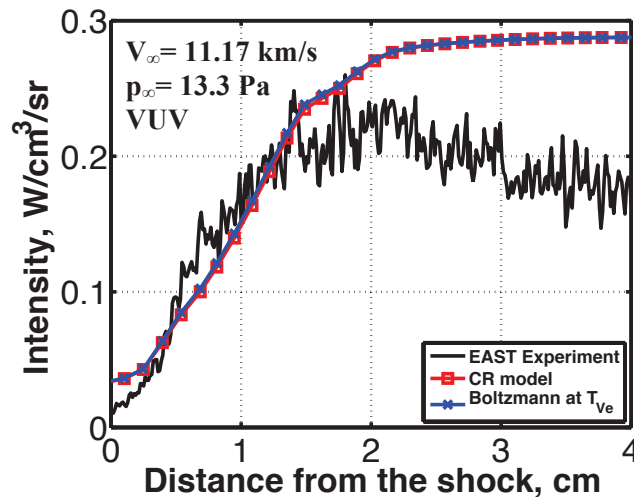


Figure 5.31: Comparison between experimental and simulated post-shock intensity profiles with the CR and Boltzmann models for shot 119 ($V_\infty=11.17$ km/s, $p_\infty=13.3$ Pa) in the VUV ($\Delta\lambda=174-175$ nm)

V.2. Spectral analysis

In this section, the predicted and experimental spectra extracted from the CCD images at various locations ($x=1$ and 2.5 cm), corresponding to the nonequilibrium zone and to the equilibrium zone are compared to further assess the CR model. The simulated spectra were smeared over the distance traveled by the shock wave (typically 0.5 cm). The experimental spectra were averaged over 10 adjacent pixels (typically $2-3$ mm) to improve the signal/noise ratio.

V.2.1. Visible spectral range

The simulated and experimental spectra are compared in figure 5.32 for shot 50-117 ($V_\infty=10.6$ km/s, $p_\infty=13.3$ Pa) and in figure 5.33 for shot 50-119 ($V_\infty=11.17$ km/s, $p_\infty=13.3$ Pa). At 10.6 km/s, the CR model tends to overpredict the measured lines by a factor 2 in the

nonequilibrium zone and by a factor 3 in the equilibrium region. The latter discrepancy is surprising, given the good agreement in the equilibrium region observed in the other spectral ranges. The quoted NIST uncertainty for this line is 18%, which lead to suspect a possible issue with the calibration in this spectral range.

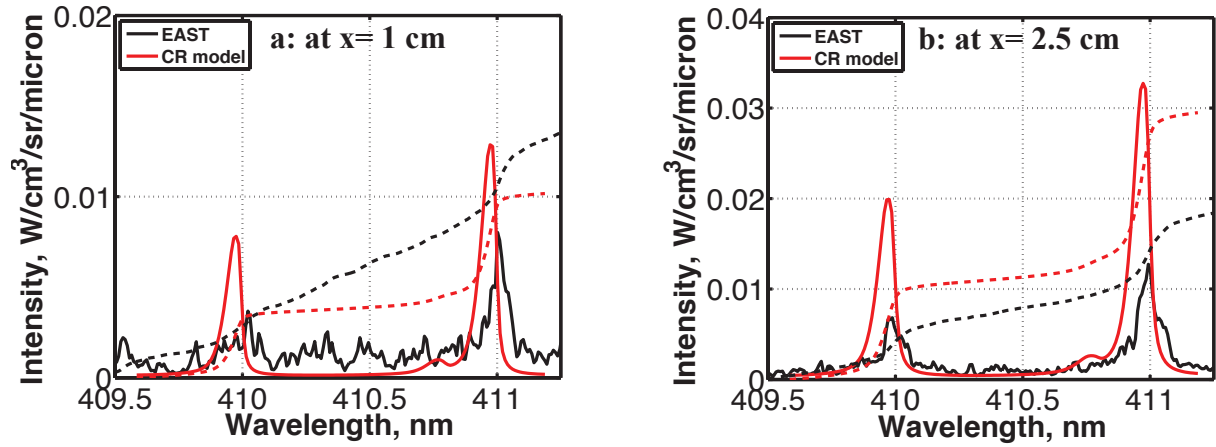


Figure 5.32: Comparison between the experimental and simulated spectra in the visible for shot 117 ($V_\infty=10.6$ km/s, $p_\infty=13.3$ Pa) at a) $x=1$ cm and b) $x=2.5$ cm. The experimental spectra were shifted by -0.08 nm. The cumulated intensities were multiplied by 5 for clarity.

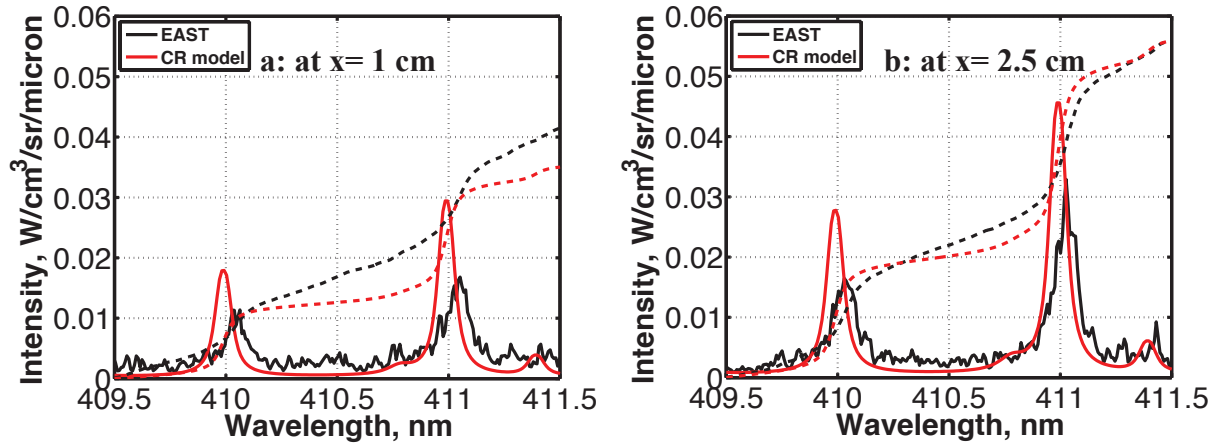


Figure 5.33: Comparison between the experimental and simulated spectra in the visible for shot 119 ($V_\infty=11.17$ km/s, $p_\infty=13.3$ Pa) at a) $x=1$ cm and b) $x=2.5$ cm. The experimental spectra were shifted by -0.05 nm. The cumulated intensities were multiplied by 5 for clarity.

V.2.2. Infrared spectral range

The simulated and experimental spectra are compared in figure 5.34 for shot 50-117 ($V_\infty=10.6$ km/s, $p_\infty=13.3$ Pa) and in figure 5.35 for shot 50-119 ($V_\infty=11.17$ km/s, $p_\infty=13.3$ Pa). For both conditions and locations, the experimental spectra are fairly well reproduced by the simulations, enabling an accurate determination of the populations of $N(7)$ excited state at $x=1$ cm and $x=2.5$ cm.

V.2.3. VUV spectral range

The simulated and experimental spectra are compared in figure 5.36 for shot 50-116 ($V_\infty=10.54$ km/s, $p_\infty=13.3$ Pa) and in figure 5.37 for shot 50-119 ($V_\infty=11.17$ km/s, $p_\infty=13.3$ Pa). At 10.54 km/s, the experimental spectra present carbon lines, which are from the shock tube wall, that represent up to 20% of the integrated intensity and account for the

nonequilibrium radiation overshoot observed at $x=2.5$ cm. Over all, the experimental spectra are fairly well reproduced by the simulations, enabling an accurate determination of the populations of $N(5)$ excited state at $x=1$ cm and $x=2.5$ cm.

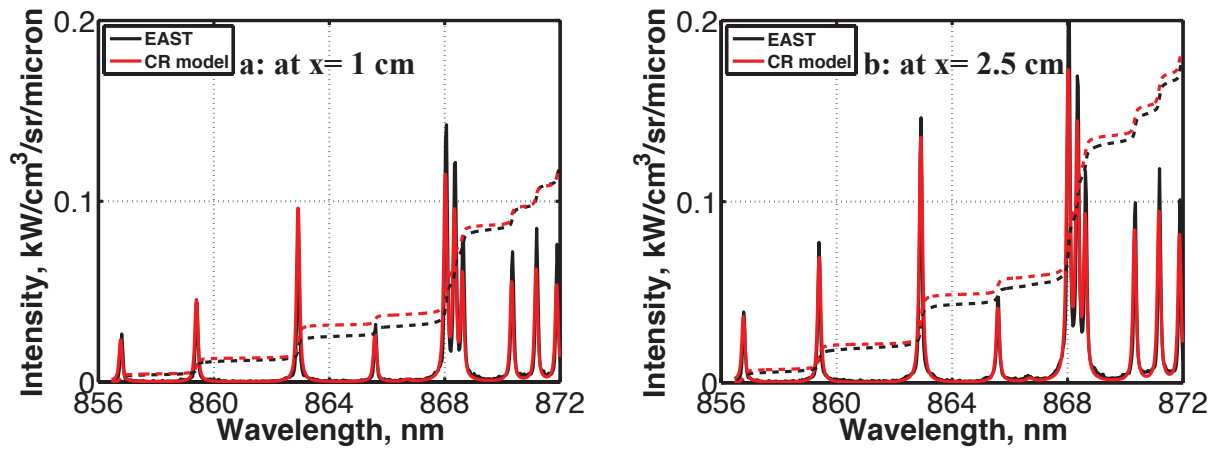


Figure 5.34: Comparison between the experimental and simulated spectra in the IR for shot 117 ($V_\infty=10.6$ km/s, $p_\infty=13.3$ Pa) at a) $x=1$ cm and b) $x=2.5$ cm

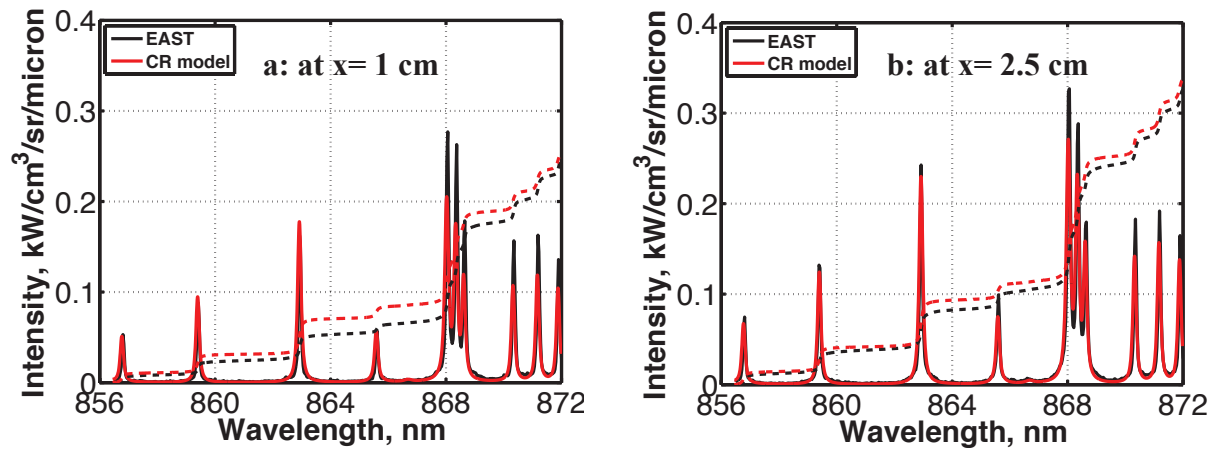


Figure 5.35: Comparison between the experimental and simulated spectra in the IR for shot 119 ($V_\infty=11.17$ km/s, $p_\infty=13.3$ Pa) at a) $x=1$ cm and b) $x=2.5$ cm

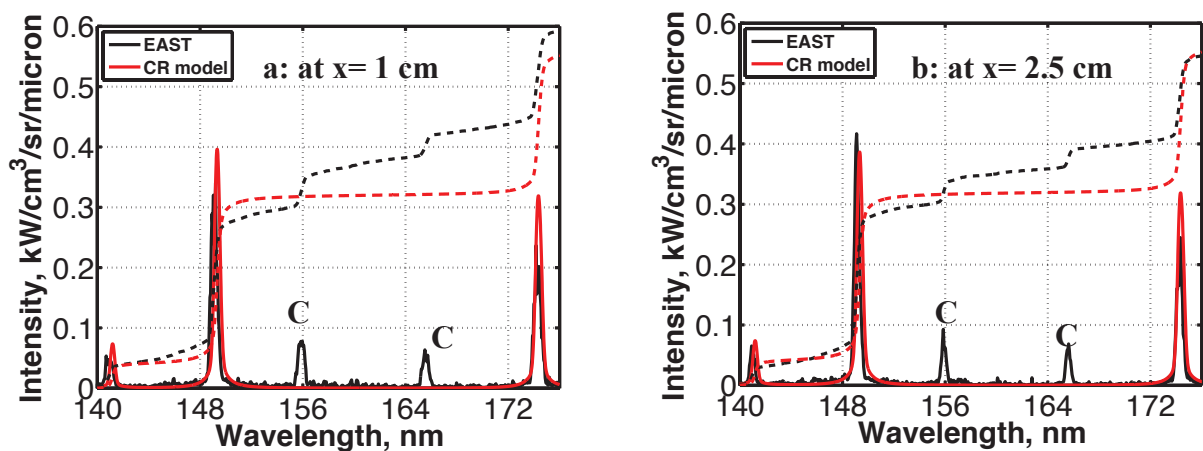


Figure 5.36: Comparison between the experimental and simulated spectra in the VUV for shot 116 ($V_\infty=10.54$ km/s, $p_\infty=13.3$ Pa) at a) $x=1$ cm and b) $x=2.5$ cm. The experimental spectra were shifted by -0.60 nm.

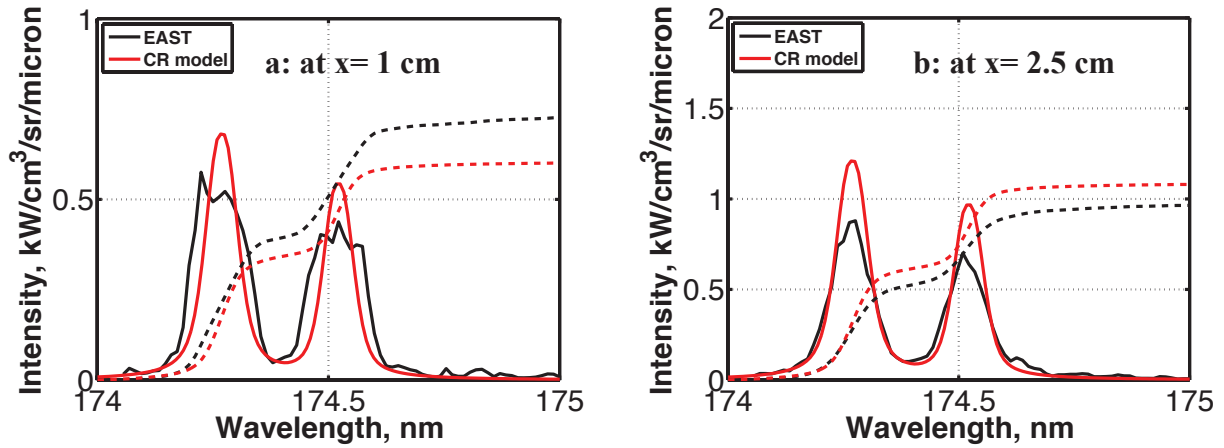


Figure 5.37: Comparison between the experimental and simulated spectra in the VUV for shot 119 ($V_{\infty}=11.17$ km/s, $p_{\infty}=13.3$ Pa) at a) $x= 1$ cm and b) $x=2.5$ cm. The experimental spectra were shifted by - 0.05 nm. The cumulated intensities were multiplied by 5 for clarity.

V.3. Populations of the excited states

To go one step further in testing the CR model, it is interesting to compare the predicted population distribution of the nitrogen levels with experimental values. As seen in this section, the spectra extracted in the CCD images turn out to contain a wealth of atomic lines that can provide information about the absorbing and emitting excited states. In subsection V.3.1, the methodology used to extract the populations of the excited states from the spectra is presented. In subsection V.3.2, the predicted and experimental population distributions are compared.

V.3.1. Experimental distribution of the grouped level populations

V.3.1.1. Methodology

Table 5.1 summarizes the atomic lines observed in the EAST spectra for shots 50-117 ($V_{\infty}=10.6$ km/s, $p_{\infty}=13.3$ Pa) and shot 50-119 ($V_{\infty}=11.17$ km/s, $p_{\infty}=13.3$ Pa), as well as the grouped upper and lower levels of the transitions. The analysis of the observed lines enables us to infer the populations of N(5), N(7) and N(15) excited states, which emit in the VUV, IR and visible, respectively, as well as the populations of N(2), N(3) which are the metastable states and do not radiate.

The general idea is to exploit the optical thickness of these lines. The nitrogen lines at 410 and 411 nm are optically thin and will be used to extract the population of N(15). With the knowledge of the population of N(15), the population of N(7) will be obtained from the slightly self-absorbed line at 865.57 nm. In turn, the population of N(5) can be inferred from the lines at 856.80, 859.44 and 862.92 nm, given the population of N(7). Finally, the strongly self-absorbed lines at 149.75 and 174.93 nm will be used to determine the populations of the metastable states N(2) and N(3), respectively.

In the following, the relation between the intensity of a thin and self-absorbed line and the population of the lower and upper levels is presented.

Table 5.1: Observed nitrogen lines

Wavelength (nm)	Grouped lower level	Grouped upper level	Camera
149.75	2	5	VUV
174.93	3	5	VUV
409.99	5	15	Vis.
410.99	5	15	Vis.
856.80	5	7	IR
859.44	5	7	IR
862.92	5	7	IR
865.57	7	15	IR
868.03	4	6	IR
868.34	4	6	IR
868.61	4	6	IR
870.32	4	6	IR
871.17	4	6	IR
871.88	4	6	IR

The spectral intensity $J_{ul}(\lambda)$ of a transition between the upper level u and lower level l of the transition is given by:

$$J_{ul}(\lambda) = \frac{\varepsilon_{ul}(\lambda)}{\alpha_{ul}(\lambda)} (1 - e^{-\alpha_{ul}(\lambda)D}) \quad (5.1)$$

where D is the EAST diameter ($D= 10.16$ cm). With the definitions of the spectral emission and absorption coefficients (given in **chapter 2**), equation 5.1 reads:

$$J_{ul}(\lambda) = \frac{8\pi hc^2}{\lambda_{ul}^5} \left(\frac{n_l / g_l}{n_u / g_u} - 1 \right)^{-1} (1 - e^{-\alpha_{ul}(\lambda)D}) \quad (5.2)$$

Assuming $n_l g_u / n_u g_l \gg 1$ yields¹²:

$$J_{ul}(\lambda) = \frac{8\pi hc^2}{\lambda_{ul}^5} \frac{n_u / g_u}{n_l / g_l} (1 - e^{-\alpha_{ul}(\lambda)D}) \quad (5.3)$$

When the line is optically thin ($\alpha D \ll 1$), the expression of spectral intensity $J_{ul}(\lambda)$ simplifies to:

$$J_{ul}(\lambda) = \varepsilon_{ul}(\lambda)D \quad (5.4)$$

or:

$$J_{ul}(\lambda) = \frac{n_u A_{ul} \Delta E_{ul}}{4\pi} D \phi_{ul}(\lambda - \lambda_{ul}) \quad (5.5)$$

Convolving the spectral intensity J_{ul} with the slit function S gives the predicted spectral intensity I_{ul} , which is compared with the experimental spectral intensity I_{Exp} :

¹² The populations of the excited states inferred from the observed lines in VUV, visible and infrared spectral ranges confirm this assumption, as will be shown in subsection V.3.2.

$$I_{ul}(\lambda) = \frac{n_u A_{ul} \Delta E_{ul}}{4\pi} D \Sigma_{ul}(\lambda) \quad (5.6)$$

where:

$$\Sigma_{ul}(\lambda) = \int_{-\infty}^{+\infty} \phi_{ul}(\lambda' - \lambda_{ul}) S(\lambda - \lambda') d\lambda' \quad (5.7)$$

Therefore, the intensity of an optically thin transition is directly proportional to the population of the upper level of the transition and to the convolution of the lineshape function.

When the line is self-absorbed, the predicted spectral intensity I_{ul} , which is compared with the experimental spectral intensity I_{Exp} reads:

$$I_{ul}(\lambda) = \frac{8\pi hc^2}{\lambda_{ul}^5} \frac{n_u/g_u}{n_l/g_l} \Xi_{ul}(\lambda) \quad (5.8)$$

where:

$$\Xi_{ul}(\lambda) = \int_{-\infty}^{+\infty} (1 - e^{-\alpha_{ul}(\lambda')D}) S(\lambda - \lambda') d\lambda' \quad (5.9)$$

Therefore, the intensity of a self-absorbed transition is proportional to the population of the upper level of the transition and to the convolution of the lineshape function and inversely proportional to the population of the lower upper level of the transition.

Figures 5.38 and 5.39 display the optical thicknesses $A = \tau_{ul}(\lambda_{ul}) = \alpha_{ul}(\lambda_{ul})D$ at the center of the considered nitrogen lines computed at Boltzmann temperature T_{Ve} at several locations in the post-shock region for the shots 50-117 ($V_\infty = 10.6$ km/s, $p_\infty = 13.3$ Pa) and 50-119 ($V_\infty = 11.17$ km/s, $p_\infty = 13.3$ Pa), respectively. It is shown that the lines in the visible spectral range are thin, whereas the lines in the VUV and in the IR are strongly and slightly self-absorbed, respectively.

Table 5.2 complements table 5.1 by indicating the range of the optical thickness of the observed transitions at line center in the post-shock zone.

Table 5.2: Optical thicknesses of the observed nitrogen lines

Wavelength (nm)	Grouped lower level	Grouped upper level	Camera	Optical thickness at line center	Note
409.99	5	15	Vis.	10^{-3} - 10^{-2}	Thin
410.99	5	15	Vis.	10^{-3} - 10^{-2}	Thin
865.57	7	15	IR	0.4	Slightly self-absorbed
856.80	5	7	IR	0.8	Slightly self-absorbed
859.44	5	7	IR	2	Slightly self-absorbed
862.92	5	7	IR	0.8	Slightly self-absorbed
174.93	3	5	VUV	10^2 - 10^3	Strongly self-absorbed
149.75	2	5	VUV	10^2 - 10^3	Strongly self-absorbed

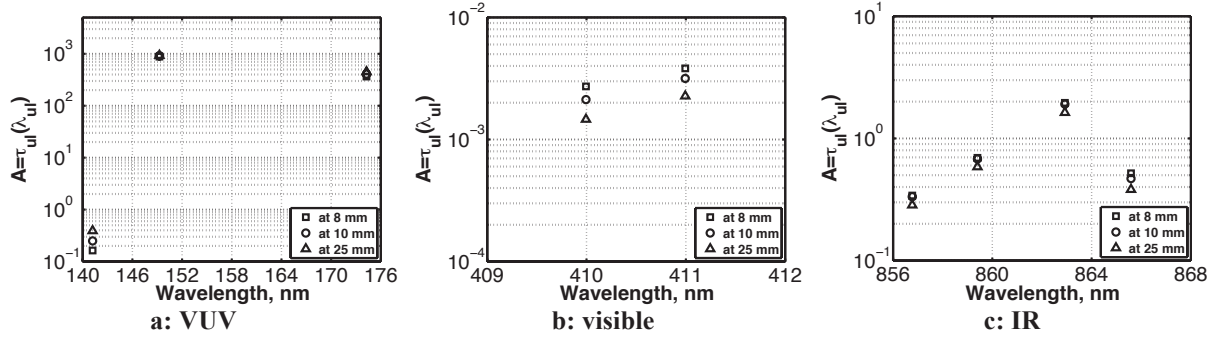


Figure 5.38: Line center absorption coefficient in the VUV (a), visible (b) and IR (c) ranges computed at T_{Ve} for shot 117 ($V_{\infty}=10.6$ km/s, $p_{\infty}=13.3$ Pa)

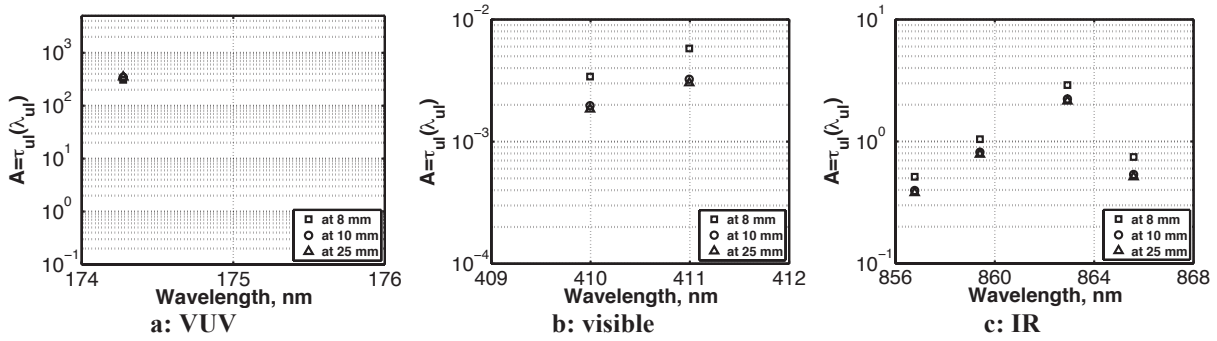


Figure 5.39: Line center absorption coefficient in the VUV (a), visible (b) and IR (c) ranges computed at T_{Ve} for shot 119 ($V_{\infty}=11.17$ km/s, $p_{\infty}=13.3$ Pa)

The populations of the excited states are determined by the following three-step method:

- 1) Start by a reference distribution of the excited states, for instance the Boltzmann distribution at T_{Ve} .
- 2) Compute the spectra and compare the latter until agreement with the experimental spectra is obtained.
- 3) Compare the populations inferred from experiments with the populations predicted by the CR model.

This method is applied for the different lines by following the order of table 5.2.

- The N lines at 409.99 and 410.99 nm ($15 \rightarrow 5$) are optically thin. Thus, the population of N(15) is directly determined by matching the experimental line profile at 410 and 411 nm, as illustrated in figures 5.40 and 5.41 for shots 50-117 ($V_{\infty}=10.6$ km/s, $p_{\infty}=13.3$ Pa) and shot 50-119 ($V_{\infty}=11.17$ km/s, $p_{\infty}=13.3$ Pa), respectively. As previously discussed, possible calibration issues make difficult the analysis of these spectra. Thus, the population of N(15) will be determined in the following by using the lines in the IR spectral range.

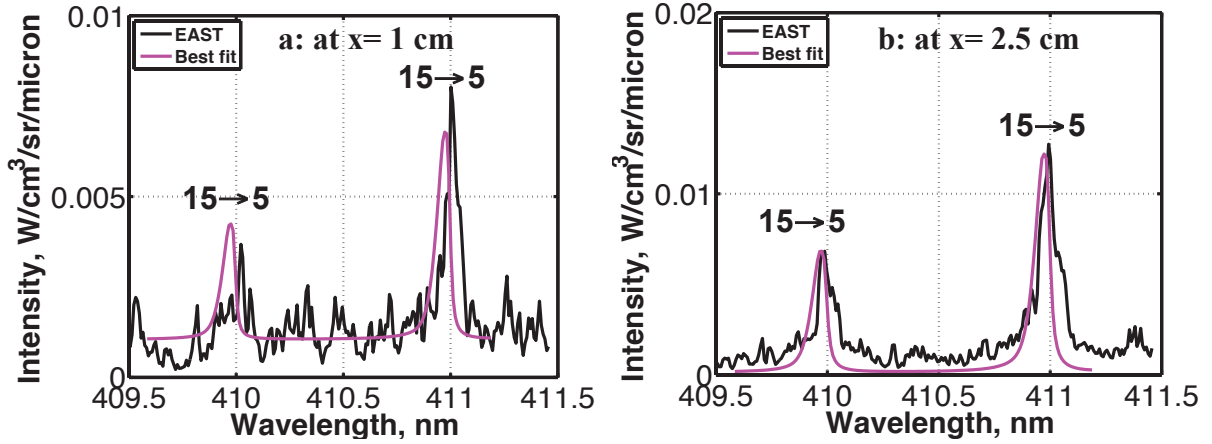


Figure 5.40: Fit of the experimental spectra for shot 117 ($V_\infty=10.6$ km/s, $p_\infty=13.3$ Pa) at a) $x=1$ cm and b) $x=2.5$ cm in the visible. Constant offsets of $1 \text{ mW/cm}^3/\text{sr/micron}$ were added to the spectra at a) $x=1$ cm and b) $x=2.5$ cm.

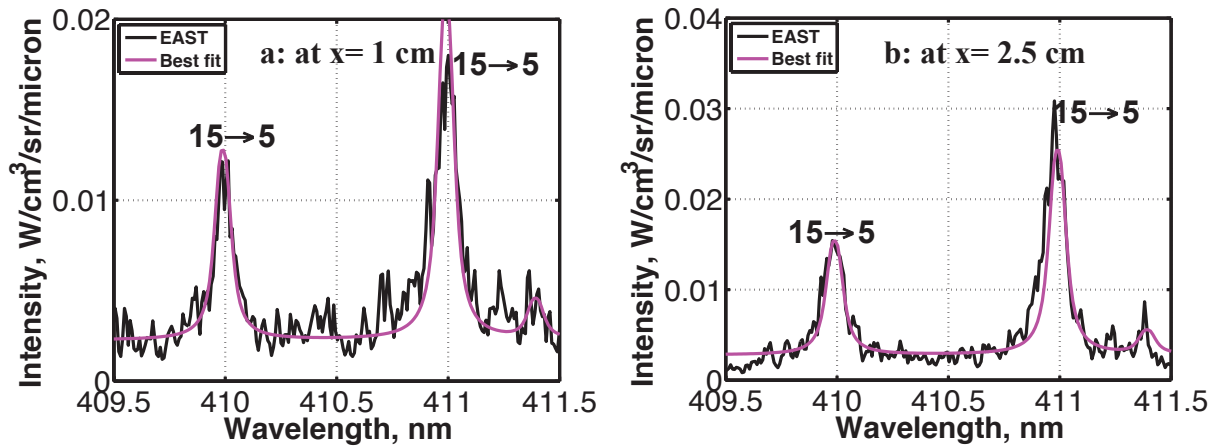


Figure 5.41: Fit of the experimental spectra for shot 119 ($V_\infty=11.17$ km/s, $p_\infty=13.3$ Pa) at a) $x=1$ cm and b) $x=2.5$ cm in the visible. Constant offsets of 2 and $3 \text{ mW/cm}^3/\text{sr/micron}$ were added to the spectra at a) $x=1$ cm and b) $x=2.5$ cm, respectively.

- The N line at 865.57 nm ($15 \rightarrow 7$) and the N lines at 856.77 , 859.40 , 862.92 ($7 \rightarrow 5$) are slightly self-absorbed. Thus the intensity $I_{865.57}$ is proportional to the population ratio n_{15}/n_7 , while the intensities $I_{856.77}$, $I_{859.40}$ and $I_{862.92}$ are proportional to the population ratio n_7/n_5 . The population of N(15) determined previously was not straightforward due possible calibration issues; thus, it is determined by matching the experimental line profile at 865.57 nm. The population of N(7) is determined by matching the experimental line profile at 856.77 , 859.40 , 862.92 nm. The adjusted spectra $V_\infty=10.6$ km/s and $V_\infty=11.17$ km/s are displayed in figures 5.42 and 5.43, respectively.
- The N lines at 174.93 nm ($5 \rightarrow 3$) and at 149.75 nm ($5 \rightarrow 2$) are strongly self-absorbed. Thus the intensity $I_{174.93}$ is proportional to the population ratio n_5/n_3 . Given n_5 determined previously, the population of N(3) is determined by matching the experimental line profile at 174.93 nm. In turn, the population of N(2) is determined by matching the experimental line profile at 149.75 nm. The adjusted spectra for $V_\infty=10.54$ km/s and $V_\infty=11.17$ km/s are displayed in figures 5.44 and 5.45, respectively.

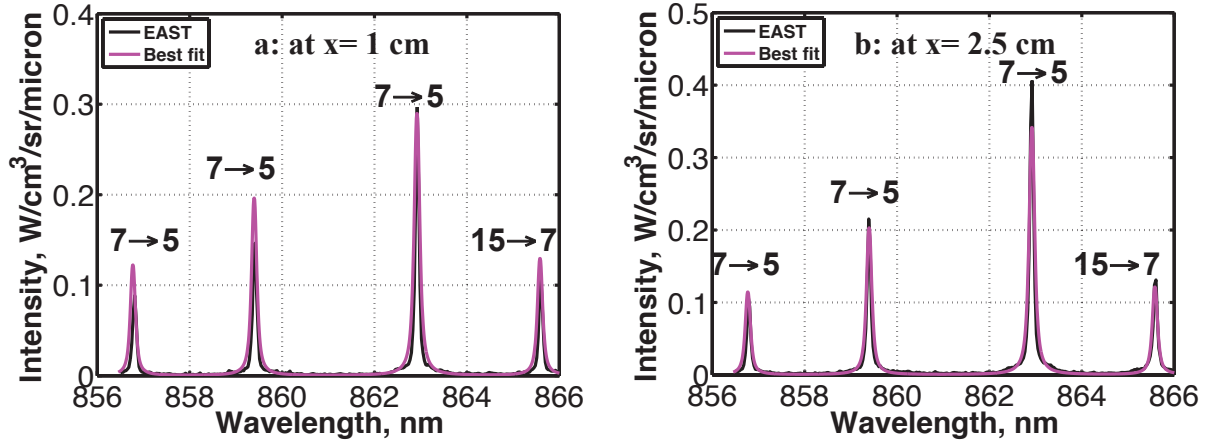


Figure 5.42: Fit of the experimental spectra for shot 117 ($V_\infty=10.6$ km/s, $p_\infty=13.3$ Pa) at a) $x=1$ cm and b) $x=2.5$ cm in the IR

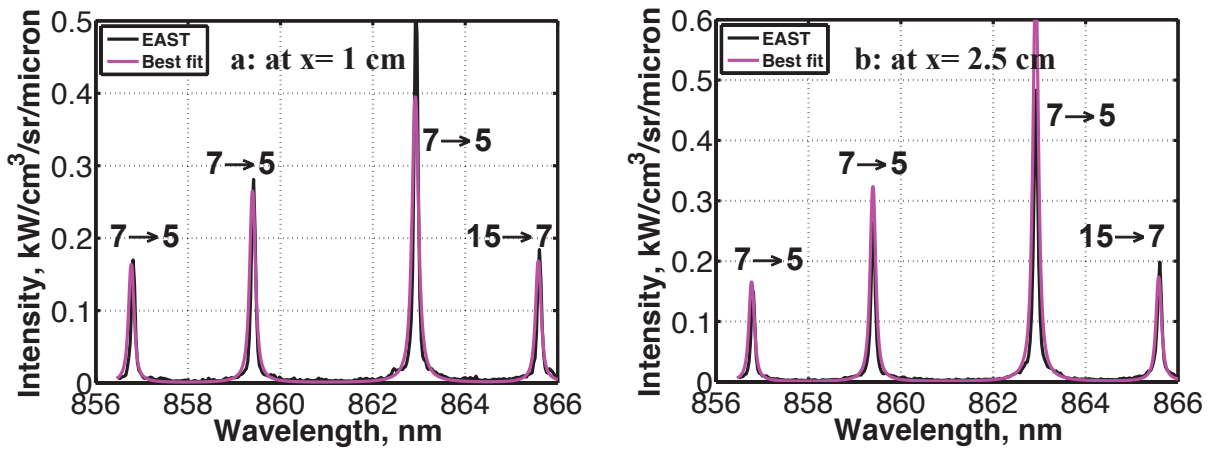


Figure 5.43: Fit of the experimental spectra for shot 119 ($V_\infty=11.17$ km/s, $p_\infty=13.3$ Pa) at a) $x=1$ cm and b) $x=2.5$ cm in the IR

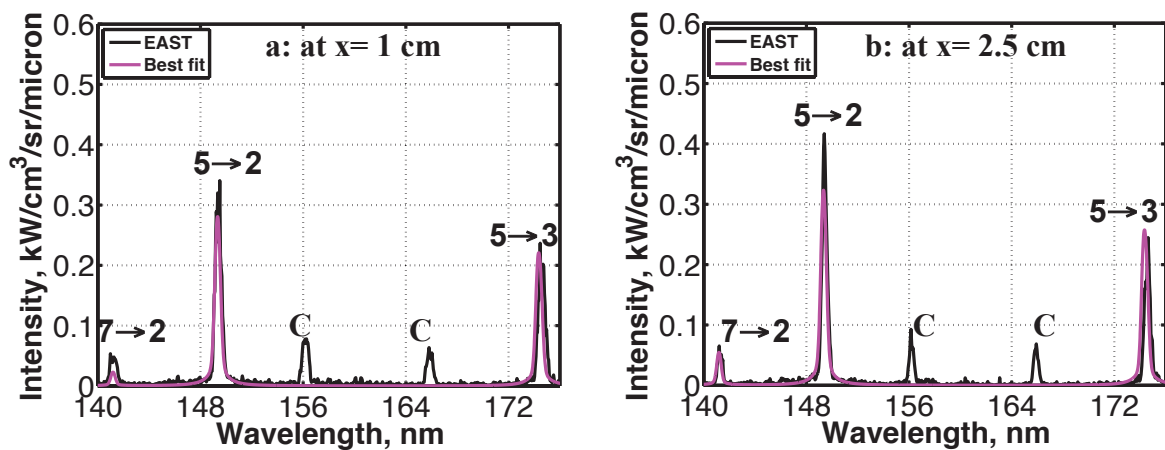


Figure 5.44: Fit of the experimental spectra for shot 116 ($V_\infty=10.54$ km/s, $p_\infty=13.3$ Pa) at a) $x=1$ cm and b) $x=2.5$ cm in the VUV

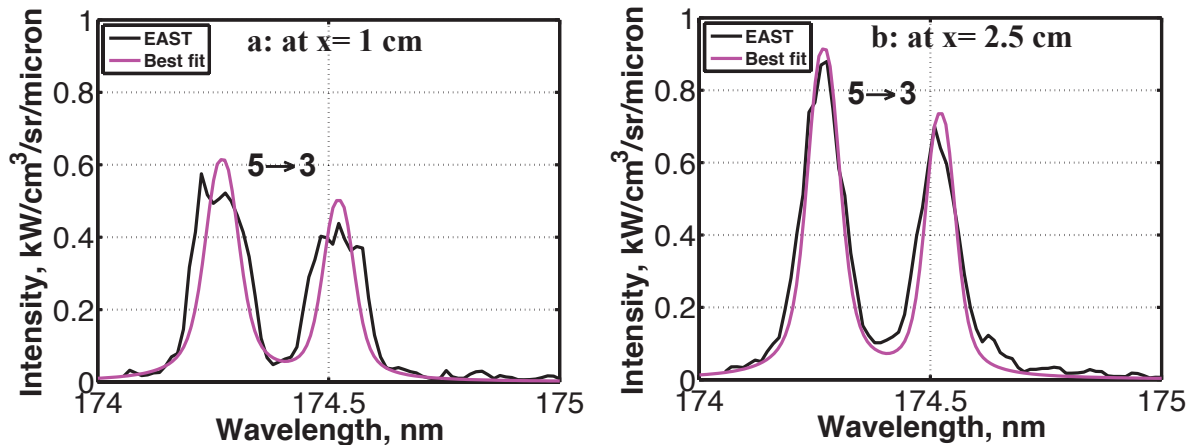


Figure 5.45: Fit of the experimental spectra for shot 119 ($V_\infty=11.17$ km/s, $p_\infty=13.3$ Pa) at a) $x=1$ cm and b) $x=2.5$ cm in the VUV

The populations of the excited states are tightly linked with each other and thus are subject to error propagation. The intensity ratio depends on the experimental and simulated intensities, which are subject to calibration uncertainty and transition line probability accuracy, respectively. The transition probabilities are well known (up to 30% uncertainty at most for the observed lines as presented in the NIST (2012) database), thus the intensity ratio mostly depends of the uncertainty of the calibration, which ranges from 10 to 40%. Therefore, the populations of the excited states are known within 60%.

V.3.1.2. Condition 117: $V_\infty=10.6$ km/s, $p_\infty=13.3$ Pa

Figure 5.46.a and b display the distribution of the considered nitrogen excited states at $x=1$ and 2.5 cm, respectively. In the nonequilibrium zone, it is shown that $N(2)$, $N(3)$, $N(5)$ excited states follow a Boltzmann distribution at T_{Ve} while $N(7)$ and $N(15)$ are slightly underpopulated with respect to this distribution. These distributions confirm the trends observed in post-shock intensity profiles in the VUV and IR spectral ranges, as discussed in section V.1.

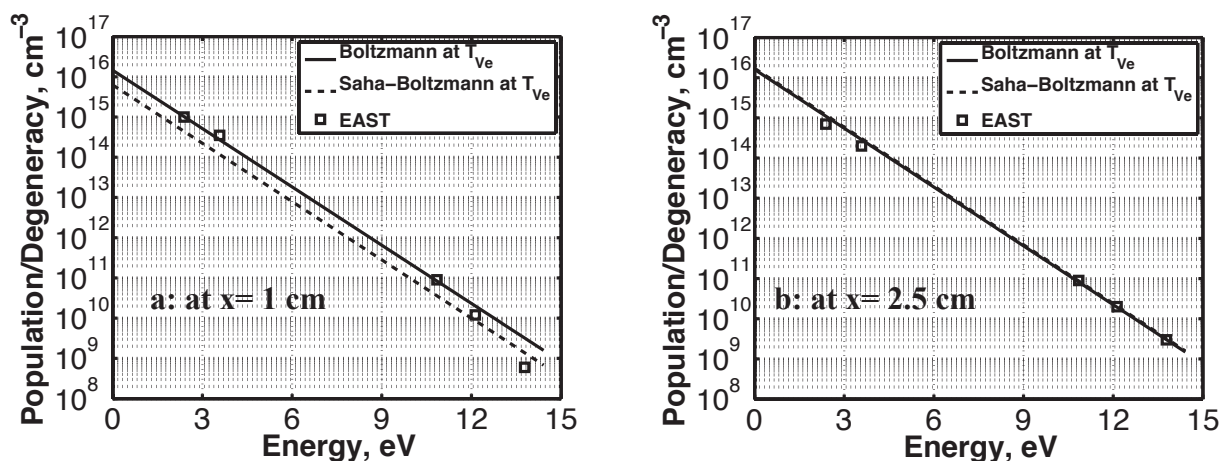


Figure 5.46: Experimental distribution of the excited states in N for shot 117 ($V_\infty=10.6$ km/s, $p_\infty=13.3$ Pa) at a) $x=1$ cm and b) $x=2.5$ cm

Figures 5.47.a-e display the experimental evolution of $N(2)$, $N(3)$, $N(5)$, $N(7)$ and $N(15)$ respectively. The $N(2)$, $N(3)$, $N(5)$ populations reach a peak due to strong collisions with

electrons and heavy-particle impact excitation processes while the populations of N(7) and N(15) rise towards equilibrium.

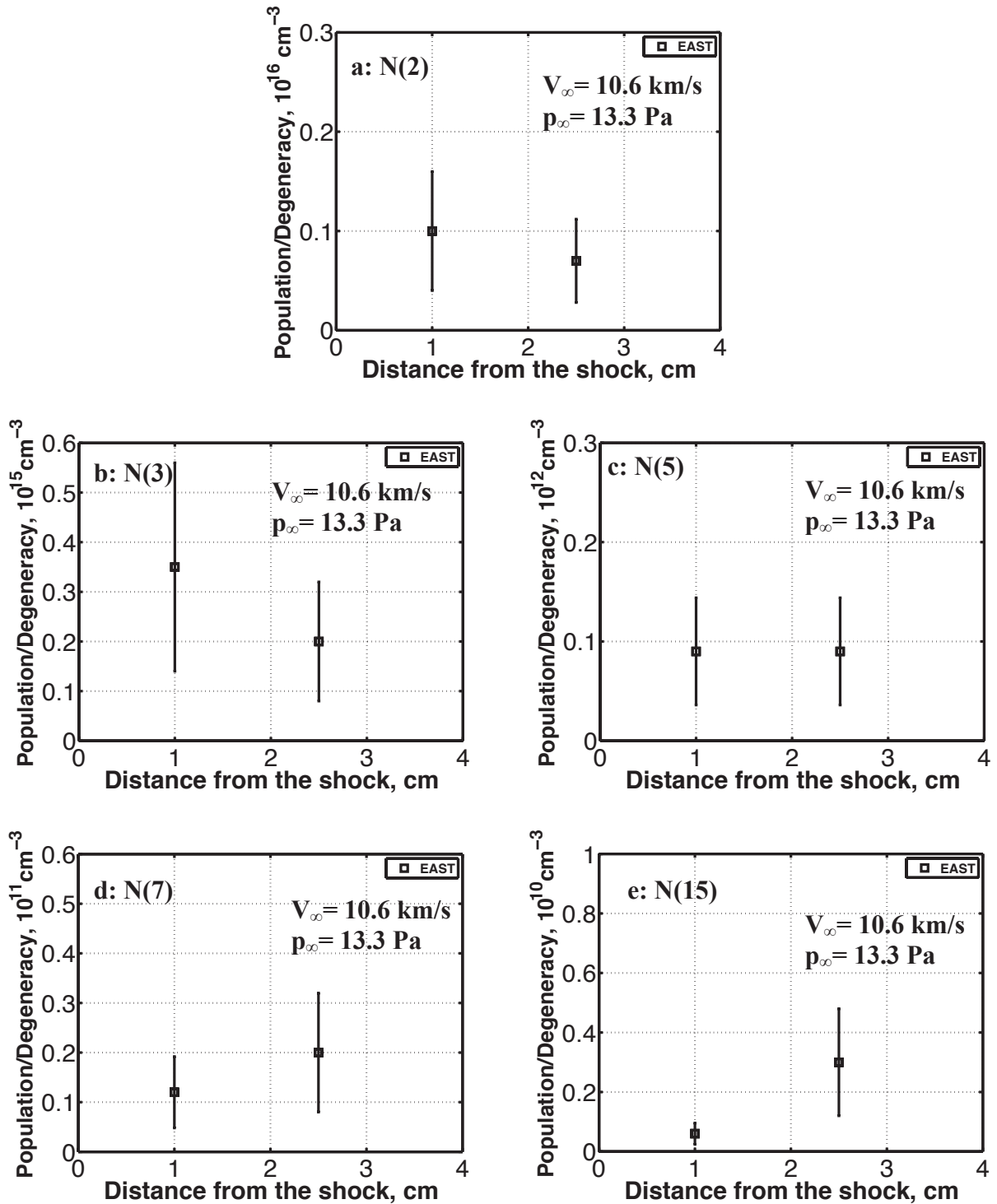


Figure 5.47: Post-shock experimental evolution of the 2nd, 3rd, 5th, 7th, 15th grouped level of nitrogen for shot 117 ($V_\infty = 10.6$ km/s, $p_\infty = 13.3$ Pa)

V.3.1.3. Condition 119: $V_\infty = 11.17$ km/s, $p_\infty = 13.3$ Pa

Figure 5.48.a-b display the distribution of the considered nitrogen excited states at $x = 1$ and 2.5 cm, respectively. In the nonequilibrium zone, it is shown that the N(3) and N(5) excited states follow a Boltzmann distribution at T_{Ve} while N(7) and N(15) are underpopulated with

respect to this distribution. These distributions confirm the trends observed in post-shock intensity profiles in the VUV, visible and IR spectral ranges, as discussed in section V.1.

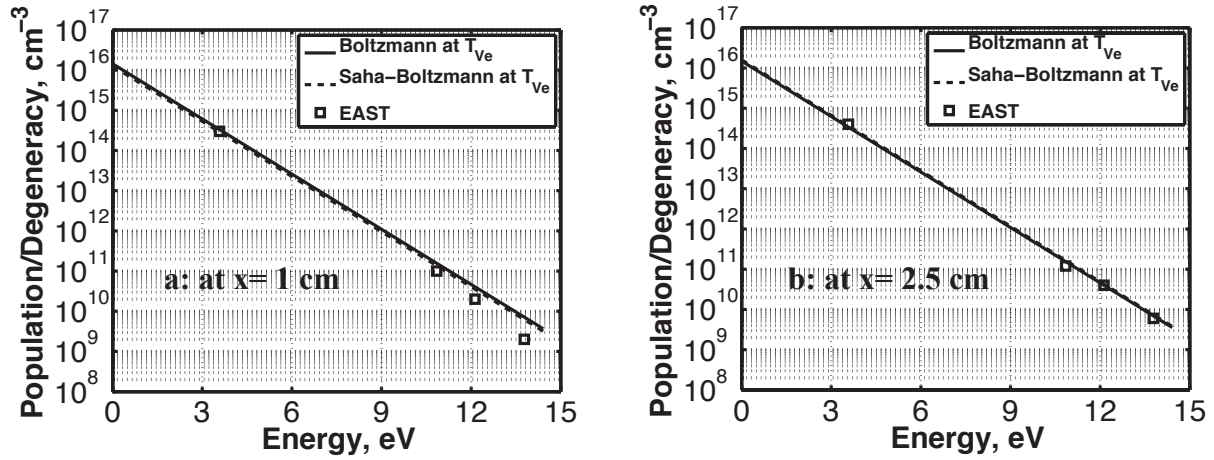


Figure 5.48: Experimental distribution of the excited states in N for shot 119 ($V_\infty=11.17$ km/s, $p_\infty=13.3$ Pa) Figures 5.49.a-d display the post-shock evolution of N(3), N(5), N(7) and N(15) respectively. The N(3), N(5) populations reach a peak due to strong collisions with electrons and heavy-particle impact excitation processes while the populations of N(7) and N(15) monotonically rise towards equilibrium.

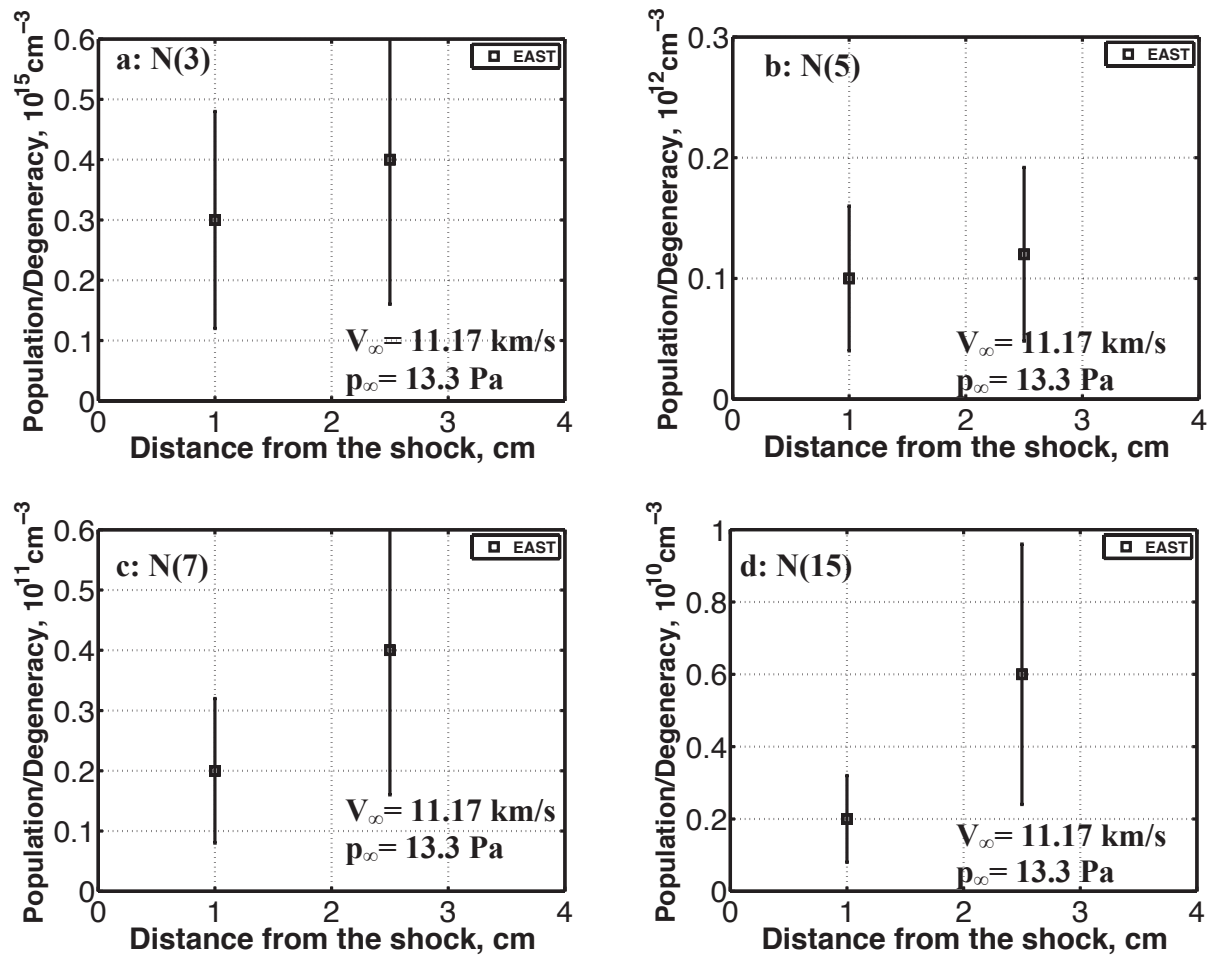


Figure 5.49: Post-shock experimental evolution of the 3rd, 5th, 7th, 15th grouped level of nitrogen for shot 119 ($V_\infty=11.17$ km/s, $p_\infty=13.3$ Pa)

V.3.2. Comparison with the CR and Boltzmann multi-temperature model predictions

In this subsection, the populations of the excited states inferred from the experimental profiles are compared with the populations predicted by the CR and the Boltzmann multi-temperature models to give further insight on predicted the post-shock intensity profiles presented in **chapter 4**. The reader is reminded that the simulated populations were smeared over the distance traveled by the shock wave (typically 0.5 cm).

V.3.2.1. Visible spectral range

In the visible spectral range, the observed lines were shown to be optically thin. Therefore, the analysis focuses on the upper state of the corresponding transition. Figure 5.50 compares the post-shock evolution of the N(15) excited state inferred from the experimental spectra with the post-shock evolution predicted by the Boltzmann multi-temperature model at electron temperature T_{Ve} and by the CR model. It is shown that the Boltzmann multi-temperature models strongly overpredicts the population of N(15) excited state in the nonequilibrium zone, while the latter is well predicted by the CR model.

V.3.2.2. Infrared spectral range

In the IR spectral range, the observed lines were shown to be slightly self-absorbed. Therefore, the analysis focuses on the upper state of the corresponding transitions. Figure 5.51 compares the post-shock evolution of the N(7) excited state inferred from the experimental spectra with the post-shock evolution predicted by the Boltzmann multi-temperature model at electron temperature T_{Ve} and by the CR model. It is shown that the Boltzmann multi-temperature models strongly overpredicts the population of N(7) excited state in the nonequilibrium zone, while the latter is well predicted by the CR model.

V.3.2.3. VUV spectral range

In the VUV spectral range, the observed lines were shown to be strongly self-absorbed. Therefore, the analysis focused on the lower and upper states of the corresponding transitions. Figure 5.52 and 5.53 compare the post-shock evolution of the N(5) and N(3) excited states inferred from the experimental spectra with the post-shock evolution predicted by the Boltzmann multi-temperature model at electron temperature T_{Ve} and by the CR model, respectively. It is shown that the Boltzmann multi-temperature model and the CR model agree very well with the experimental data.

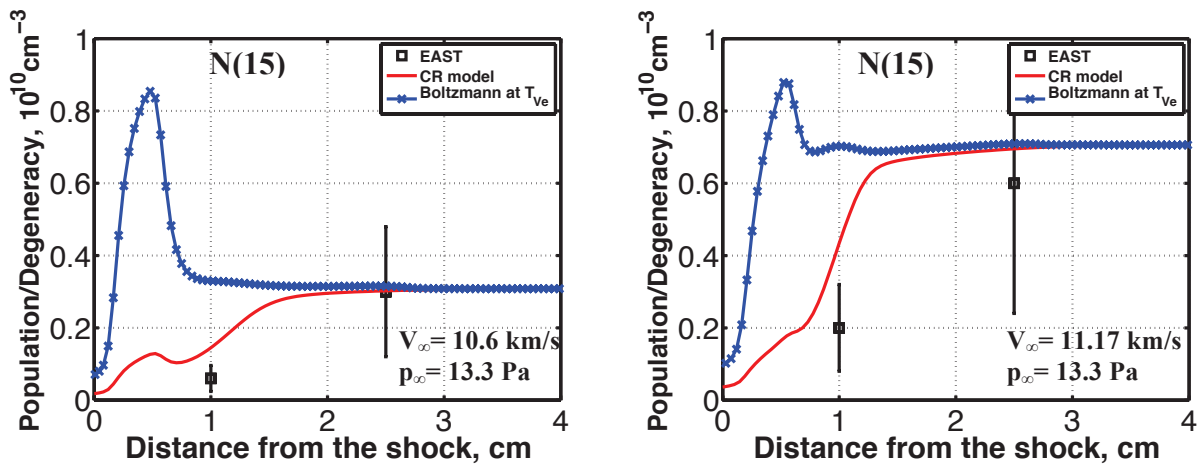


Figure 5.50: Comparison of the post-shock evolution of the 15th grouped level of N inferred from experiment with the predictions of the Boltzmann and CR models for shot 117 ($V_\infty=10.6$ km/s, $p_\infty=13.3$ Pa) and shot 119 ($V_\infty=11.17$ km/s, $p_\infty=13.3$ Pa)

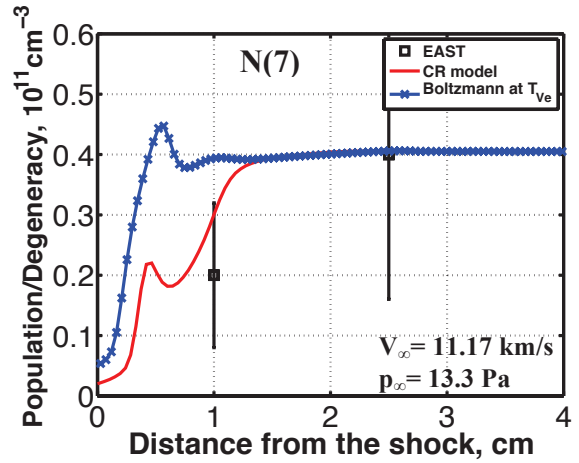
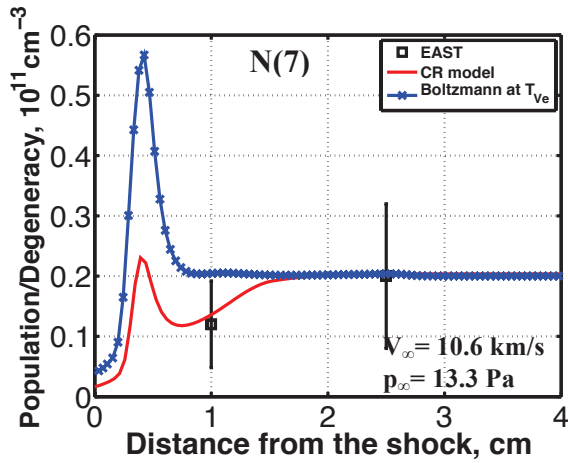


Figure 5.51: Comparison of the post-shock evolution of the 7th grouped level of N inferred from experiment with the predictions of the Boltzmann and CR models for shot 117 ($V_\infty=10.6$ km/s, $p_\infty=13.3$ Pa) and shot 119 ($V_\infty=11.17$ km/s, $p_\infty=13.3$ Pa)

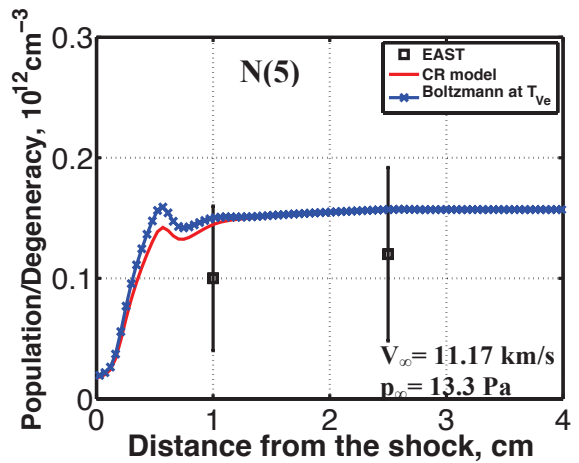
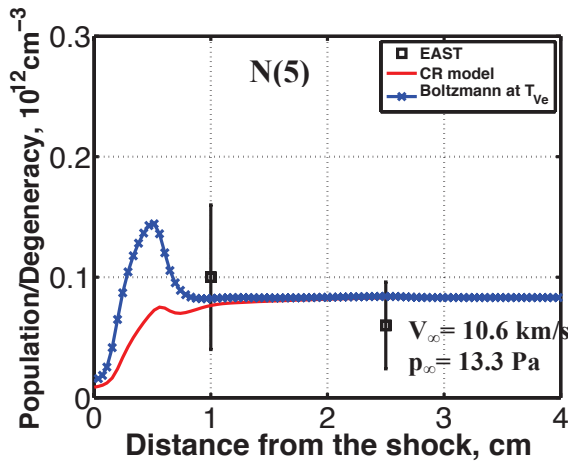


Figure 5.52: Comparison of the post-shock evolution of the 5th grouped level of N inferred from experiment with the predictions of the Boltzmann and CR models for shot 117 ($V_\infty=10.6$ km/s, $p_\infty=13.3$ Pa) and shot 119 ($V_\infty=11.17$ km/s, $p_\infty=13.3$ Pa)

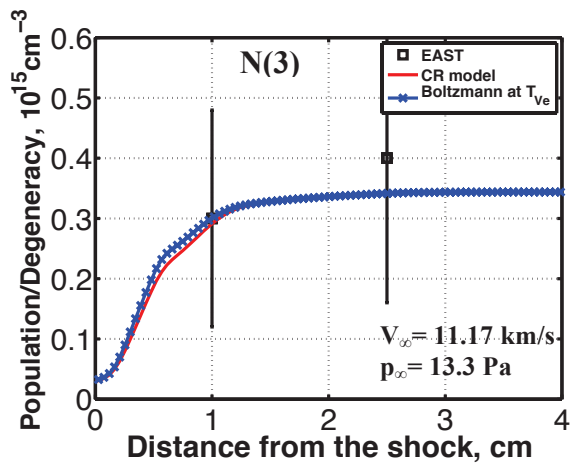
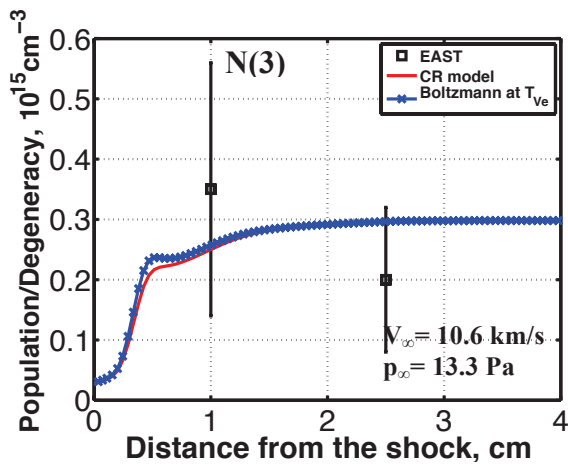


Figure 5.53: Comparison of the post-shock evolution of the 3rd grouped level of N inferred from experiment with the predictions of the Boltzmann and CR models for shot 117 ($V_\infty=10.6$ km/s, $p_\infty=13.3$ Pa) and shot 119 ($V_\infty=11.17$ km/s, $p_\infty=13.3$ Pa)

V.5. Summary

The assessment of the CR and spectral models developed in this work was performed by comparing the experimental and simulated post-shock intensity profiles as well as the experimental and simulated spectra. The nonequilibrium intensities observed in the VUV and IR spectral ranges were underpredicted by the CR model when only electron-impact excitation and ionization processes were taken into account.

Then, a sensitivity analysis on heavy-particle impact processes was conducted by starting from the baseline Park non-preferential dissociation rate constant model (1985) and by applying various dissociation rate constants and dissociation-vibration coupling models. The nonequilibrium post-shock intensities observed in the VUV and in the IR predicted with dissociation rate constant model of Park (1985) and Macheret and Rich (1993) were shown to be in good agreement with each other, but still to underpredict the experimental intensities. Moreover, the use of the preferential dissociation-vibration coupling models increase the equilibrium distance and still underpredict the experimental intensities. Subsequently, the various heavy-particle impact excitation processes were tested. Excellent agreement was obtained for both freestream conditions and for all the spectral ranges, when adjusting the heavy-particle impact excitation rate constants of Park (1985), demonstrating that the nonequilibrium peak intensities observed in the VUV and IR spectral ranges are controlled by heavy-particle impact processes.

The experimental post-shock intensity profiles were compared with the prediction of the Boltzmann model at electron temperature. For both conditions, the post-shock intensity profiles in the visible and IR spectral ranges were overpredicted by the Boltzmann model by a factor up to 5. In the VUV, the Boltzmann and CR predictions were shown to be very close with each other. The measured spectra were analyzed to infer the distribution of the excited states responsible for the observed lines. For both freestream conditions, the population of the excited states (i.e N(2), N(3), N(5)) emitting and absorbing in the VUV spectral range were shown to be well predicted by a Boltzmann distribution at electron temperature, T_{ve} , owing to strong collisions with electrons and heavy-particles. The excited state, N(15), radiating in the visible and infrared spectral ranges was shown to be strongly depleted from the Boltzmann distribution at electron temperature, T_{ve} , as a result of significant electron-impact ionization processes.

Chapter VI

Conclusions

VI.1. Contributions of this thesis

During reentry into Earth's atmosphere at hypervelocity ($V > 10$ km/s), a significant part of the heating experienced by the spacecraft is due to the radiation of the shock layer. The contribution of nonequilibrium radiation, currently not well known, can lead to significant TPS design margins, which jeopardize the safety, the scientific value and budget of the mission. The characterization of the nonequilibrium radiation remains a state-of-the-art challenge and has triggered the present work.

There were four main objectives:

1. Develop a nonequilibrium CR model accounting for electron- and heavy-particle-impact processes
2. Analyze the radiation measurements obtained in high enthalpy facilities ($V > 10$ km/s) to infer the thermodynamic properties of flowfield
3. Predict the spectral intensities and the post-shock intensity profiles and compare them with the experimental data
4. Implement the nonequilibrium CR model into EADS solvers to predict the radiative heat flux on a spacecraft reentering into Earth's atmosphere for future exploration missions.

The nonequilibrium radiation model developed in this work comprises a flowfield, a collisional-radiative (CR) and a spectral model. The CR model, which is the cornerstone of the present work, includes the electronic states of N and O atoms and the vibrational levels of N_2 and N_2^+ systems, which are the strongest radiators in Earth's reentry and are subject to nonequilibrium thermodynamic distributions. The collisional-radiative (CR) model encompasses the key processes responsible for the depletion/population of the emitting states such as electron-impact excitation, ionization, dissociation, heavy-particle impact excitation and dissociation, internal energy exchange processes such as vibration-vibration, vibration-translation, vibration-electron as well as bound-bound radiative mechanisms. A comprehensive review of the available experimental data and theoretical expressions was undertaken. The best dataset was selected to model the electron-impact and heavy-particle impact processes as accurately as possible. The bound-bound radiative mechanisms were treated using the escape factor concept, set to zero for VUV lines and set to one for visible and near-infrared lines, in accordance with literature results.

The CR model was interfaced either with the flowfield solver Poschax (Gollan, 2006; Potter, 2011) or the flowfield solver of EADS, and also with the line-by-line spectral radiation code SPECAIR (Laux *et al.*, 2003) under the QSS assumption. This CR model was used to predict the nonequilibrium radiation measured in the EAST facility at NASA Ames Research Center. Two shock-tube conditions ($V_\infty = 10.6$ km/s, $p_\infty = 13.3$ Pa; $V_\infty = 11.17$ km/s, $p_\infty = 13.3$ Pa) representative of the severe flight environment encountered by the spacecraft were investigated in the VUV, visible and IR spectral ranges. A detailed analysis of these measurements was performed to extract:

- the vibrational and rotational temperatures (from the N₂ Second positive and N₂⁺ First negative systems between 250 and 350 nm).
- the electron number density profiles (from the Stark-broadened H_α line at 656 nm and the N line at 410 nm)
- the post-shock intensity profiles in the VUV, visible and near IR spectral ranges
- the emission spectra throughout the post-shock region

The vibrational and rotational temperatures inferred from the experiments showed strong coupling within the vibrational and rotational modes of N₂ C and a similar behavior for N₂⁺ B. The rotational temperature of N₂⁺ B was close to the gas temperature predicted by the flowfield solver Poshax (Gollan, 2006; Potter, 2011), but the rotational temperature of N₂ C was about 8000 K cooler.

The electron number density profile inferred from experiments was compared with the prediction of the flowfield model. Excellent agreement was obtained for both freestream conditions, thus validating the ionization model and enabling the location of the shock front in the experimental intensity profile.

The experimental post-shock intensity profiles were compared with the predictions of the CR model. The nonequilibrium intensities observed in the VUV and IR spectral ranges were underpredicted by the CR model when only electron-impact excitation and ionization processes were taken into account.

Then, a sensitivity analysis on heavy-particle impact processes was conducted by starting from the baseline Park non-preferential dissociation rate constant model (1985) and by applying various dissociation rate constants and dissociation-vibration coupling models. The nonequilibrium post-shock intensities observed in the VUV and in the IR predicted with dissociation rate constant model of Park (1985) and Macheret and Rich (1993) were shown to be in good agreement with each other, but still to underpredict the experimental intensities. Moreover, the use of the preferential dissociation-vibration coupling models increased the equilibrium distance and still underpredicted the experimental intensities.

Subsequently, the various heavy-particle impact excitation processes were tested. Excellent agreement was obtained for both freestream conditions and for all the spectral ranges, with heavy-particle rate constants of the order of 10⁻¹⁵ to 10⁻¹³ cm³/s, which is consistent with Kelley (2012) analysis, suggesting that the nonequilibrium peak intensities are controlled by heavy-particle impact processes.

Then, the CR model predictions and the experimental intensity profiles were compared with the predictions of a Boltzmann model at electron temperature. For both conditions, the measured post-shock intensity profiles in the visible and IR spectral ranges were overpredicted by the Boltzmann model by a factor up to 5, while the Boltzmann and CR predictions were shown to be very close to each other, in the VUV.

The measured spectra were analyzed to infer the population distribution of the excited states responsible for the observed lines and to account for the comparison between the experimental post-shock intensity profiles and the simulations with the CR and Boltzmann multitemperature models. For both conditions, the population distribution of the excited states were shown to be fairly well reproduced by the CR model. Specifically, the populations of the low-lying excited states (E<11eV) were shown to be well predicted by a Boltzmann

distribution at the electron temperature, owing to strong collisions with electrons and heavy-particles. The higher excited states ($E > 11\text{eV}$) were shown to be strongly depleted from the Boltzmann distribution at the electron temperature, as a result of significant electron-impact ionization and radiative processes.

This work was the first quantitative comparison between VUV shock-tube radiation data and simulations at conditions representative of hypervelocity Earth reentry. The CR model developed in this work showed that the heavy-particle impact excitation processes are highly influential on the atomic excited states with energy less than 11eV , whereas the states above 11eV are mostly controlled by electron-impact processes. Because the low lying states are responsible for the bulk of radiation in the VUV, which can represent up to 60% of the radiation emitted by the post-shock region during Earth hypervelocity reentry, heavy-particle impact excitation processes appear to be essential to correctly predict the radiative heat flux encountered by a spacecraft during its reentry into Earth's atmosphere.

VI.2. Recommendations for future work

In this thesis, various physico-chemical processes were investigated. Further work in the following area will be useful:

First, the analysis of the radiation measurements showed that the nonequilibrium peak intensity observed in the VUV and in the IR is governed by heavy-particle impact excitation processes. Good agreement was obtained with the experimental data when the rate constants from the approximate formula of Park (1985) were divided by 8000; showing these critical rate constants must be verified through *ab initio* computations.

In this work, we investigated the shock-tube radiation measurements carried out in the EAST facility at NASA Ames Research Centre for conditions of hypervelocity reentry ($10.5 < V < 11.2$ km/s). The analysis showed that the shocked air mixture spectra were dominated by atomic lines in the VUV, visible and IR spectral ranges. These measurements showed the influence of the heavy-particle impact processes is more important at $V = 10.5$ km/s than at $V = 11.2$ km/s. It could be interesting to extend the present simulations to higher and lower velocities to determine the range of importance of these heavy-particle impact processes.

In addition, shock-tube radiation measurements overlapping and extending the range of velocities of the shot considered in this work would be useful to further test the CR model.

Then, the analysis of the radiation measurements showed the vibrational and rotational temperatures of N_2 C were close to each other. A similar observation was made for $\text{N}_2^+ \text{B}$. Although these states do not emit significant radiation at hypervelocity reentry, the knowledge of their internal distribution would give valuable insight on key processes such as dissociation and associative ionization. Therefore, advanced chemistry models are desirable.

Then, radiation was assumed to be fully uncoupled from the flowfield and the excited states evolution. However, radiation may have a strong influence on the state of the gas in case of high speed reentry at lower pressure. Accurate coupling of the flowfield solver and the CR model is desirable, particularly for the states absorbing and emitting in the IR spectral range. The coupling with radiation would allow us to accurately define and assess more precisely the values of the escape factors in the master equations and the source term Q_{Rad} in the energy

conservation equation, which will enable us to account for the radiative cooling effects. The radiative transport equation could be solved fully coupled with the master equation and for the species, momentum and energy conservation equations or loosely coupled, owing to the large computational resources needed to estimate the radiative properties of the medium such as its emission and absorption.

Finally, the present work focused on the modeling on the nonequilibrium radiation emitted by a shocked high temperature air mixture. Short-term and long-term objectives should investigate the modeling of TPS surface phenomena such as ablation and catalysis and transition to turbulence.

APPENDICES

Appendix A

Poshax flowfield solver

Overview

*The prediction of the nonequilibrium radiation encountered by the spacecraft relies upon an accurate description of the bulk thermodynamic variables, the distribution of the excited states responsible for the intense radiation as well as the radiative transitions probabilities. The radiative transitions were underscored in **chapter 2**. The computation of the populations of the excited states was performed with the CR model described in **chapter 3**. In this appendix, we briefly describe the flowfield model (Gollan, 2006; Potter, 2011). In section 1, we recall the compressible Euler equations governing the flow in a post-shock relaxation zone. In section 2, we present the chemical processes and their coupling with the internal energy modes. Finally, in section 3, we compare Poshax and EADS' flowfield solutions as well as intensity profile predictions for the conditions investigated in **chapter 4**.*

A.1. Assumptions and governing equations

We make use of the following assumptions:

- (H1): the flow is one-dimensional characterized by a flow speed u and steady,
- (H2): the flow is assumed continuous and laminar,
- (H3): gravity and electromagnetic forces are neglected,
- (H4): the gas mixture is assumed inviscid. Transport coefficients such as diffusion, viscosity and conductivity are neglected,
- (H5): the mixture is a plasma, ie, electrically neutral at macroscopic scale,
- (H6): the mixture is neutral as local scale as well, (the Debye length is negligible with respect to the spacecraft nose radius)
- (H7): the mixture is composed of species considered as perfect gases,
- (H8): the thermal nonequilibrium is represented by a two-temperature model
 $T_T = T_R = T_g, T_V = T_e,$
- (H9): the radiative energy is negligible with respect to the translational energy.

Let us denote the density of the flow by ρ , the species s number density by ρ_s , the flow speed by u , the pressure by p , the energy by E and the sources term by S .

Under the aforementioned assumptions, the species mass conservation equation reads:

$$\frac{\partial}{\partial x}(\rho_s u) = \dot{\omega}_s \quad (\text{A.1})$$

where $\dot{\omega}_s$ is the mass production term of species s .

The momentum conservation equation reads:

$$\frac{\partial}{\partial x}(\rho u^2 + p) = 0 \quad (\text{A.2})$$

The electron-vibration energy conservation equation reads:

$$\frac{\partial}{\partial x} \left(u(\rho E_{ve} + p_e) \right) = S_{VT} + S_{eT} + S_{VChm} + S_{eChm} \quad (\text{A.3})$$

The total energy equation reads:

$$\frac{\partial}{\partial x} \left(u(\rho E + p) \right) = 0 \quad (\text{A.4})$$

The electroneutrality of the flow reads:

$$\sum_{i \neq e} \frac{\rho_i}{W_i} = \frac{\rho_e}{W_e} \quad (\text{A.5})$$

The total pressure reads:

$$p = \sum_{i \neq e} \frac{\rho_i RT_g}{W_i} + \frac{\rho_e RT_e}{W_e} \quad (\text{A.6})$$

where W is the species mole weight.

The governing equations demonstrate the need for appropriate sources terms such as species production term and energy exchange source terms. The former are the subject of the following sections.

A.2. Nonequilibrium chemical kinetics

A simple reversible chemical reaction can be represented as (Vincenti and Kruger, 1965):



Through the Law of Mass action, the species production term for species due to all chemical reactions (r) is calculated by:

$$\dot{\omega}_s = \frac{1}{W_s} \sum_i^{N_r} (\beta_i - \alpha_i) \left\{ K_f \prod_i [X_i]^{\alpha_i} - K_b \prod_i [X_i]^{\beta_i} \right\} \quad (\text{A.8})$$

A.2.1. Forward and backward rate constants

The chemical reaction model of Park (1993) considered in the present work involves 11 species and provides forward rate constants in the generalized and semi-empirical Arrhenius form:

$$K_f = aT^b e^{-\frac{c}{T}} \quad (\text{A.9})$$

The backward rate constant is related to the forward rate constant by:

$$K_b = \frac{K_f}{K_{eq}} \quad (\text{A.10})$$

where K_{eq} is the equilibrium constant given by:

$$\ln(K_{eq}) = -\frac{\Delta G}{RT} \quad (\text{A.11})$$

where ΔG is the free energy given by:

$$\Delta G = \sum_i^{N_s} (\beta_i - \alpha_i)(h_i - Ts_i) \quad (\text{A.11})$$

where h, s are the specific enthalpy and entropy of species s given by a polynomial expansion, taken from Gordon and Mac Bride (1994).

A.2.2. Nonequilibrium dissociation rate constants

Under nonequilibrium condition, the rate constants must take into account which thermal mode is contributing to the reaction energy, thus which temperature governs the corresponding process. Ideally this would be achieved by considering reactions of individual rovibronic states, likewise in **chapter 3**. In the case of the computation of shock-tube flow radiation, this approach is computationally prohibitive. Thus, the calculation of nonequilibrium rate constants is achieved by correcting the forward rate constant K_f of the reaction by a factor Z , which models the nonequilibrium between the energy modes. We focus here on the dissociation of N_2 , which is the most influential reaction in air reentry flows (Brandis, 2009).

There exist several models to compute the correction factor Z , chief among them Park (1990), Marrone and Treanor (1963) and Macheret and Rich (1993). The reader is referred to the works of William (2000) and Lino da Silva *et al.* (2007) for a comprehensive review of the dissociation rate constant models.

Let us denote by Θ_V the vibrational characteristic temperature and by Θ_D the dissociation characteristic temperature.

The correction factor given by Park (1990) non-preferential model reads:

$$Z(T_T, T_V) = T_T^{s-1} T_V^{s-1} e^{-\frac{\sqrt{T_T T_V}}{T_T^s T_V^{1-s}} + \frac{\Theta_D}{T_T}} \quad (\text{A.12})$$

where s is the parameter controlling the dissociation of N_2 .

The correction factor given by Marrone and Treanor (1963) semi-empirical preferential model reads:

$$Z(T_T, T_V) = \frac{Q_V^{\Theta_D}(T_T) Q_V^{\Theta_D}(\Gamma)}{Q_V(T_V) Q_V(U)} \quad (\text{A.13.a})$$

where Γ is given by:

$$\frac{1}{\Gamma} = \frac{1}{T_V} - \frac{1}{T_T} - \frac{1}{U} \quad (\text{A.13.b})$$

where $Q_V, Q_V^{\Theta_D}$ are the vibrational partition functions for an harmonic oscillator with infinite vibrational levels and with the vibrational levels up to the dissociation limit $k \cdot \Theta_D$ respectively. U is a numerical parameter taken as $U = \Theta_D/3$ in the present work.

The correction factor given by Macheret and Rich (1993) preferential model reads:

$$Z(T_T, T_V) = (1-L) \frac{1 - e^{-\frac{\Theta_V}{T_V}}}{1 - e^{-\frac{\Theta_V}{T_T}}} e^{-\Theta_D \left(\frac{1}{T_V} - \frac{1}{T_T} \right)} + L e^{-\Theta_D \left(\frac{1}{T_a} - \frac{1}{T_T} \right)} \quad (\text{A.14.a})$$

where $T_a = \frac{T_V + 3T_T}{4}$ for the dissociation of homonuclear molecules

L is a paramater, which for dissociation by atom, is given by:

$$L = \frac{9\sqrt{3\pi}}{128} \left(1 + \frac{15T_T}{8\Theta_D} \right) \left(\frac{T_T}{\Theta_D} \right)^{1-b} \quad (\text{A.14.b})$$

and for dissociation by molecules by:

$$L = \frac{17}{4\pi^2} \left(1 + \frac{63T_T}{16\Theta_D} \right) \left(\frac{T_T}{\Theta_D} \right)^{\frac{3}{2}-b} \quad (\text{A.14.c})$$

where b is the temperature exposant in the Arrhenius law for the dissociation reaction in Park's (1993) chemistry model.

A.2.3. Energy exchanges between internal modes

A.2.3.1. V-T energy exchange source term S_{VT}

The VT energy exchange source term S_{VT} is modeled by the formula given by Landau and Teller (1966):

$$S_{VT} = \sum_{p=1}^M \rho_p \frac{E_V^p(T) - E_V^p(T_V)}{\tau_{VT}^p} \quad (\text{A.15.a})$$

where M is the number of molecules, ρ is the density of the molecule, τ is the VT relation time given by:

$$\tau_{VT}^p = \left[\sum_{c=1}^S \frac{x_c}{\tau_{VT}^{p-c}} \right]^{-1} \quad (\text{A.15.b})$$

where S is the number of species, x is the mass fraction and τ_{VT}^{p-c} is given by:

$$\tau_{VT}^{p-c} = \tau_{MW}^{p-c} + \left[N \sigma_V \sqrt{\frac{8kT}{\pi m}} \right]^{-1} \quad (\text{A.15.c})$$

Where N and m are the average total number density and mass of the mixture, respectively. The relaxation time τ_{MW}^{p-c} is given by Millikan and White (1963):

$$p \tau_{MW}^{p-c} [\text{atm.s}] = e^{a \left(T^{-\frac{1}{3}-b} \right) - 18.42} \quad (\text{A.15.d})$$

The coefficients a and b are listed in Potter (2011). The cross-section σ_V is taken from Park (1993): $\sigma_V = 3.0 \cdot 10^{-17} (5/T[10^4 \text{ K}])^2 \text{ cm}^2$.

A.2.3.2. e-T energy exchange source term S_{eT}

The e-T energy exchange source term S_{eT} is given by Appleton and Bray (1964):

$$S_{eT} = 3 \rho_e R (T - T_e) \sum_{s \neq e} \frac{\nu_{e-s}}{W_s} \quad (\text{A.16.a})$$

where the effective collision frequency ν_{e-s} is given for Coulomb collisions between electrons and ions by:

$$\nu_{e-s} = \frac{8}{3} \sqrt{\frac{\pi}{m_e}} n_s q_e^4 (2\pi k T_e)^{-\frac{3}{2}} \ln \left(\frac{k^3 T_e^3}{\pi n_e q_e^6} \right) \quad (\text{A.16.b})$$

and for collisions between neutral and electrons by:

$$\nu_{e-s} = n_s \sigma_{e-s} \sqrt{\frac{8kT_e}{\pi m_e}} \quad (\text{A.16.c})$$

where the cross-section σ_{e-s} is given by Gnoffo *et al.* (1989).

A.2.3.3. Nonequilibrium dissociation-vibration coupling S_{VChm}

Chemistry-vibration coupling represents the loss or gain of vibrational energy due to molecules being created or destroyed.

The chemistry-vibration energy exchange S_{VChm} for the dissociation of N_2 can be written as:

$$S_{VChm} = -G^f \dot{\omega}^f + G^b \dot{\omega}^b \quad (\text{A.17.a})$$

where G^f is the modal energy change per unit mass associated with the consumption of N_2 occurring at the rate $\dot{\omega}^f$ and G^b is the modal energy change per unit mass associated with the production of N_2 occurring at the rate $\dot{\omega}^b$.

The most basic model that can be applied is to assume all molecules are created or destroyed at the current average vibrational energy. Therefore the vanishing and appearing components

G^b and G^f may both be calculated at the vibrational energy of species i evaluated at T_V :

$$G^b = G^f = E_v(T_V) \quad (\text{A.17.b})$$

When applied to dissociation reactions, this model is referred to as a non-preferential dissociation-vibration model.

However, due to vibrational excitation reducing the energy required for molecular reactions to take place, the vibrational energy associated with molecular consumption and production may be greater than the average vibrational energy. In the present work, we refer to this phenomena as preferential chemistry-vibration coupling. The appearing component for all preferential chemistry-vibration coupling models is the vanishing component evaluated at the backwards rate controlling temperature, which is the translational temperature T_T .

$$G^b = G^f(T_T) \quad (\text{A.17.c})$$

The chemistry-vibration energy exchange S_{VChm} was thoroughly investigated in the last decades. We list hereafter the most common models used in the aerospace community.

There exist several models to compute chemistry-vibration energy exchange S_{VChm} (Park, 1990; Treanor and Marrone, 1962; Macheret and Rich, 1993).

The dissociation component G^f given by the Park (1990) non-preferential model reads:

$$G^f = (1-s) \left[b \frac{RT_V}{W} + D \left(\frac{T_V}{T_T} \right)^s \right] + E_v(T_V) \quad (\text{A.16})$$

where s is the parameter controlling the dissociation of N_2 and b is the temperature exposant in Park (1993) chemistry set.

The dissociation component G^f given by the Treanor and Marrone (1962) preferential model reads:

$$G^f = E_v(\Gamma) \quad (\text{A.17})$$

where Γ is defined in equation A.13.b.

The dissociation component G^f given by Macheret and Rich (1993) preferential model reads:

$$G^f = R\Theta_D \frac{\left(\frac{T_T}{T_a} \right)^2 \Psi_1(T_T, T_V) + \Psi_2(T_T, T_V)}{Z(T_T, T_V) K_f(T_T)} \quad (\text{A.18.a})$$

where T_a and Z are defined in equations A.14.a, and:

$$\Psi_1(T_T, T_V) = \frac{1-L}{4} AT_T^b e^{-\frac{\Theta_D}{\sqrt{T_T T_V}}}$$

$$\Psi_2(T_T, T_V) = LAT_T^b e^{-\frac{\Theta_D}{T_V}} \frac{1 - e^{-\frac{\Theta_V}{T_V}}}{1 - e^{-\frac{\Theta_V}{T_T}}}$$
(A.18.b)

where A and b are the preexponential factor and the temperature exponent in the Park (1993) chemistry set.

A.2.3.4. Nonequilibrium electron-chemistry coupling S_{eChm}

Chemistry-electron-electronic coupling accounts for the change in free electron and bound electronic energy due to chemical reactions.

The electron-chemistry energy exchange S_{eChm} for the dissociation of N_2 can be written as:

$$S_{eChm} = -G^f \dot{\omega}^f + G^b \dot{\omega}^b$$
(A.19.a)

where G^f is the modal energy change per unit mass associated with the consumption of electrons occurring at the rate $\dot{\omega}^f$ and G^b is the modal energy change per unit mass associated with the production of electrons occurring at the rate $\dot{\omega}^b$.

The recombination component G^f from electron-impact ionization and dissociative recombination is given by:

$$G^f = E_{Elec}(T_e) - \alpha E_{Ion} + E_{Elec}(T_e) + \beta [E_{Elec}(T) - E_{Elec}(T_e)]$$
(A.19.b)

where α and β were two coefficients set to 0.3 and 0.1 by Potter (2011), respectively.

Appendix B

NIST and grouped levels

Table B.1: NIST and grouped levels of N

NIST levels				Grouped levels		
Configuration	Term	g_i	E_i (cm ⁻¹)	I	g_I	E_I (cm ⁻¹)
2s2.2p3	4S*	4	0.000	1	4	0
2s2.2p3	2D*	6	19224.464	2	10	19228
		4	19233.177			
2s2.2p3	2P*	2	28838.920	3	6	28840
		4	28839.306			
2s2.2p2.(3P).3s	4P	2	83284.070	4	12	83337
		4	83317.830			
		6	83364.620			
2s2.2p2.(3P).3s	2P	2	86137.350	5	18	87488
		4	86220.510			
2s.2p4	4P	6	88107.260	7	18	96793
		4	88151.170			
2s2.2p2.(3P).3p	2S*	2	93581.550	6	36	95276
		4	94770.880			
2s2.2p2.(3P).3p	4D*	4	94793.490	7	18	96793
		6	94830.890			
		8	94881.820			
		2	95475.310			
2s2.2p2.(3P).3p	4P*	4	95493.690	8	18	103862
		6	95532.150			
2s2.2p2.(3P).3p	4S*	4	96750.840	9	60	104857
2s2.2p2.(3P).3p	2D*	4	96787.680			
2s2.2p2.(3P).3p	2P*	6	96864.050	10	30	104902
		2	97770.180			
2s2.2p2.(3P).3p	2P*	4	97805.840	9	60	104857
		6	99663.427			
2s2.2p2.(1D).3s	2D	4	99663.912	10	30	104902
		2	103622.510			
2s2.2p2.(3P).4s	4P	4	103667.160	8	18	103862
		6	103735.480			
2s2.2p2.(3P).4s	2P	2	104144.820	10	30	104902
		4	104221.630			
2s2.2p2.(3P).3d	2P	4	104615.470	9	60	104857
		2	104654.030			
2s2.2p2.(3P).3d	4F	4	104664.130	10	30	104902
		6	104683.060			
		8	104716.950			
		10	104765.770			
2s2.2p2.(3P).3d	2F	6	104810.360	9	60	104857
		8	104881.350			
2s2.2p2.(3P).3d	4P	6	104825.110	9	60	104857
		4	104859.730			
		2	104886.100			
2s2.2p2.(3P).3d	4D	2	104984.370	10	30	104902
		4	104996.270			
2s2.2p2.(3P).3d	2D	6	105008.550	10	30	104902
		8	105017.600			
2s2.2p2.(3P).3d	2D	4	105119.880	10	30	104902
		6	105143.710			
2s2.2p2.(3P).4p	2S*	2	106477.800	11	54	107082
2s2.2p2.(3P).4p	4D*	2	106758.731			
2s2.2p2.(3P).4p	4D*	4	106778.337	10	30	104902
		6	106814.459			
		8	106868.635			
2s2.2p2.(3P).4p	4P*	2	106980.480	11	54	107082
		4	106996.032			
2s2.2p2.(3P).4p	2D*	6	107037.069	10	30	104902
		4	107182.788			
2s2.2p2.(3P).4p	4S*	4	107253.106	11	54	107082
2s2.2p2.(3P).4p	2P*	2	107445.622			
2s2.2p2.(3P).4p	2P*	2	107588.469	11	54	107082
2s2.2p2.(3P).4p	2P*	2	107588.469			

		4	107628.283			
		2	109812.233			
2s2.2p2.(3P).5s	4P	4	109856.520	12	18	110021
		6	109926.661			
		2	110035.720			
2s2.2p2.(3P).5s	2P	4	110103.834			
		4	110194.654			
		6	110212.396			
2s2.2p2.(3P).4d	4F	8	110247.288			
		10	110303.233			
		4	110220.107	13	90	110315
2s2.2p2.(3P).4d	2P	2	110245.183			
		6	110286.305			
2s2.2p2.(3P).4d	2F	8	110362.462			
		6	110299.974			
2s2.2p2.(3P).4d	4P	4	110322.721			
		2	110350.014			
		6	110349.090			
2s2.2p2.(3P).4f D	2[3]*	8	110349.170	14	126	110486
		6	110385.290			
2s2.2p2.(3P).4f G	2[3]*	8	110385.360			
		2	110385.795			
		4	110395.463	13	90	110315
2s2.2p2.(3P).4d	4D	6	110401.356			
		8	110403.220			
		10	110402.090			
2s2.2p2.(3P).4f G	2[4]*	8	110402.180	14	126	110486
		4	110404.500			
2s2.2p2.(3P).4f D	2[2]*	6	110404.550			
		4	110447.032	13	90	110315
2s2.2p2.(3P).4d	2D	6	110470.244			
		4	110459.790			
2s2.2p2.(3P).4f D	2[1]*	2	110459.790			
		12	110473.090			
2s2.2p2.(3P).4f G	2[5]*	10	110473.240			
		4	110485.960	14	126	110486
2s2.2p2.(3P).4f F	2[2]*	6	110486.040			
		8	110498.420			
2s2.2p2.(3P).4f F	2[3]*	6	110498.430			
		10	110501.680			
2s2.2p2.(3P).4f F	2[4]*	8	110501.830			
		4	110521.050			
2s2.2p2.(1D).3p	2D*	6	110544.850			
		6	110710.739			
2s2.2p2.(1D).3p	2F*	8	110715.152			
		2	111060.905			
2s2.2p2.(3P).5p	2S*	2	111143.567			
		4	111165.158			
2s2.2p2.(3P).5p	4D*	6	111204.016	15	78	111140
		8	111260.873			
		2	111198.848			
2s2.2p2.(3P).5p	2P*	4	111213.271			
		2	111271.596			
2s2.2p2.(3P).5p	4P*	4	111285.644			
		6	111326.798			
2s2.2p2.(3P).5p	4S*	4	111501.368			
		4	111853.061			
2s2.2p2.(3P).5p	2D*	6	111905.609			
		2	112294.007	16	90	112851
2s2.2p2.(1D).3p	2P*	4	112319.805			
		2	112565.470			
2s2.2p2.(3P).6s	4P	4	112609.612	18	648	114298
		6	112681.389			
		2	112691.960			
2s2.2p2.(3P).6s	2P	4	112736.961			
		4	112759.966			
		6	112760.325			
2s2.2p2.(3P).5d	4F	8	112797.725			
		10	112861.348	16	90	112851
		4	112801.031			
2s2.2p2.(3P).5d	2P	2	112807.567			
		6	112812.518			
2s2.2p2.(3P).5d	2F	6	112812.518			

Table B.2: NIST and grouped levels of O

NIST levels				Grouped levels		
Configuration	Term	g_i	E_i (cm ⁻¹)	I	g_i	E_i (cm ⁻¹)
2s2.2p4	3P	2	0.000	1	9	78
		1	158.265			
		0	226.977			
2s2.2p4	1D	2	15867.862	2	5	15868
2s2.2p4	1S	0	33792.583	3	1	33792
2s2.2p3.(4S*).3s	5S*	2	73768.200	4	5	73768
2s2.2p3.(4S*).3s	3S*	1	76794.978	5	3	76794
		1	86625.757			
		2	86627.778			
2s2.2p3.(4S*).3p	5P	3	86631.454	6	15	86629
		2	88631.146			
		1	88630.587			
2s2.2p3.(4S*).3p	3P	0	88631.303	7	9	88631
		2	95476.728			
		1	96225.049			
2s2.2p3.(4S*).4s	5S*	2	95476.728	8	8	95757
2s2.2p3.(4S*).4s	3S*	1	96225.049			
2s2.2p3.(4S*).3d	5D*	4	97420.630	9	40	97745
		3	97420.716			
		2	97420.839			
		1	97420.942			
		0	97420.991			
2s2.2p3.(4S*).3d	3D*	1	97488.378			
		2	97488.448			
		3	97488.538			
2s2.2p3.(4S*).4p	5P	1	99092.968			
		2	99093.641			
		3	99094.837			
2s2.2p3.(4S*).4p	3P	1	99680.968	10	24	99313
		2	99681.049			
		0	99681.309			
2s2.2p3.(2D*).3s	3D*	3	101135.407			
		2	101147.526			
		1	101155.422			
2s2.2p3.(4S*).5s	5S*	2	102116.698	11	8	102227
2s2.2p3.(4S*).5s	3S*	1	102411.995			
2s2.2p3.(2D*).3s	1D*	2	102662.026			
2s2.2p3.(4S*).4d	5D*	4	102865.506	12	96	102881
		3	102865.547			
		2	102865.606			
		1	102865.655			
		0	102865.679			
2s2.2p3.(4S*).4d	3D*	3	102908.374			
		2	102908.443			
		1	102908.489			
2s2.2p3.(4S*).4f	5F	3	102968.249	13	24	103869
		2	102968.249			
		1	102968.249			
		5	102968.249			
		4	102968.249			
2s2.2p3.(4S*).4f	3F	3	102968.343			
		2	102968.343			
		4	102968.343			
2s2.2p3.(4S*).5p	5P	1	103625.754	13	24	103869
		2	103626.111			
		3	103626.611			
2s2.2p3.(4S*).5p	3P	2	103869.968			
		1	103870.028			
		0	103870.252			
2s2.2p3.(4S*).6s	5S*	2	105019.307	15	288	106639
2s2.2p3.(4S*).6s	3S*	1	105165.232			
2s2.2p3.(4S*).5d	5D*	4	105385.354	14	168	105694
		3	105385.377			
		2	105385.409			
		1	105385.436			
		0	105385.449			
2s2.2p3.(4S*).5d	3D*	1	105409.008			
		3	105409.008			
		2	105409.008			
2s2.2p3.(4S*).5f	5F	3	105441.645			
		2	105441.645			
		5	105441.645			

2s2.2p3.(4S*).5f	5F	4	105441.645	14	168	105694
		1	105441.645			
		4	105441.724			
2s2.2p3.(4S*).5f	3F	3	105441.724			
		2	105441.724			
2s2.2p3.(4S*).6p	5P	1	105788.431	15	288	106639
		2	105788.595			
		3	105788.856			
2s2.2p3.(4S*).6p	3P	0	105912.031			
		2	105912.031			
2s2.2p3.(4S*).7s	5S*	2	106545.354	16	392	107583
2s2.2p3.(4S*).7s	3S*	1	106627.934			
2s2.2p3.(4S*).6d	5D*	4	106751.447	15	288	106639
		3	106751.458			
		2	106751.474			
		1	106751.487			
		0	106751.494			
2s2.2p3.(4S*).6d	3D*	3	106765.803			
		2	106765.803			
		1	106765.803			
2s2.2p3.(4S*).6f	5F	1	106785.160			
		5	106785.160			
		2	106785.160			
		3	106785.160			
		4	106785.160			
2s2.2p3.(4S*).6f	3F	4	106785.201			
		3	106785.201			
		2	106785.201			
2s2.2p3.(4S*).6g	3G*	3	106787.903			
		4	106787.903			
		5	106787.903			
2s2.2p3.(4S*).6g	5G*	3	106787.903			
		2	106787.903			
		5	106787.903			
		4	106787.903			
		6	106787.903			
2s2.2p3.(4S*).8s	5S*	2	107446.036	17	512	108117
2s2.2p3.(4S*).8s	3S*	1	107497.224			
2s2.2p3.(4S*).7d	5D*	4	107573.476	16	392	107583
		3	107573.484			
		2	107573.495			
		1	107573.504			
		0	107573.508			
2s2.2p3.(4S*).7d	3D*	1	107582.777			
		2	107582.777			
		3	107582.777			
		2	107595.140			
2s2.2p3.(4S*).7f	5F	1	107595.140			
		4	107595.140			
		3	107595.140			
		5	107595.140			
2s2.2p3.(4S*).7f	3F	4	107595.147			
		3	107595.147			
		2	107595.147			
2s2.2p3.(4S*).9s	5S*	2	108021.400	18	648	108478
2s2.2p3.(4S*).9s	3S*	1	108056.000			
2s2.2p3.(4S*).8d	5D*	4	108106.072	17	512	108117
		3	108106.077			
		2	108106.085			
		1	108106.091			
		0	108106.094			
2s2.2p3.(4S*).8d	3D*	3	108114.000			
		2	108114.000			
		1	108114.000			
2s2.2p3.(4S*).10s	5S*	2	108412.000	19	800	108734
2s2.2p3.(4S*).10s	3S*	1	108436.300			
2s2.2p3.(4S*).9d	5D*	4	108470.230	18	648	108478
		3	108470.230			
		2	108470.230			
		1	108470.230			
		0	108470.230			
2s2.2p3.(4S*).9d	3D*	2	108476.700			
		3	108476.700			

Appendix C

Strongest atomic lines

Table C.1: Strongest nitrogen lines in the VUV

Line position (nm)	A_{ul} (s ⁻¹)	E_l (cm ⁻¹)	E_u (cm ⁻¹)	L	U
90.9697	2.93E+07	0.000	109926.661	1	12
91.0278	2.92E+07	0.000	109856.520	1	12
91.0645	2.92E+07	0.000	109812.233	1	12
95.3415	1.90E+08	0.000	104886.100	1	9
95.3655	1.81E+08	0.000	104859.730	1	9
95.3970	1.62E+08	0.000	104825.110	1	9
96.3990	5.94E+07	0.000	103735.480	1	8
96.4626	5.66E+07	0.000	103667.160	1	8
96.5041	5.52E+07	0.000	103622.510	1	8
106.7614	3.53E+07	19224.464	112891.238	2	16
106.8612	3.28E+07	19233.177	112812.518	2	16
109.7237	6.35E+07	19224.464	110362.462	2	13
109.8260	5.91E+07	19233.177	110286.305	2	13
110.0360	3.60E+07	19224.464	110103.834	2	12
110.1291	3.99E+07	19233.177	110035.720	1	12
113.4165	1.51E+08	0.000	88170.570	1	5
113.4415	1.49E+08	0.000	88151.170	1	5
113.4980	1.44E+08	0.000	88107.260	1	5
116.3884	3.25E+07	19224.464	105143.710	2	10
116.4325	2.82E+07	19233.177	105119.880	2	10
116.7448	1.10E+08	19224.464	104881.350	2	9
116.8334	1.24E+07	19233.177	104825.110	2	9
116.8536	9.32E+07	19233.177	104810.360	2	10
117.6510	8.52E+07	19224.464	104221.630	2	8
117.7695	1.03E+08	19233.177	104144.820	2	8
119.9550	4.07E+08	0.000	83364.620	1	4
120.0223	4.03E+08	0.000	83317.830	1	4
120.0710	4.00E+08	0.000	83284.070	1	4
122.5026	4.41E+07	28839.306	110470.244	3	13
122.5368	3.67E+07	28838.920	110447.032	3	13
122.8407	2.70E+07	28838.920	110245.183	3	13
122.8791	3.38E+07	28839.306	110220.107	3	13
124.3179	3.22E+08	19224.464	99663.427	2	7
124.3306	3.10E+08	19233.177	99663.912	2	7
131.0540	7.68E+07	28839.306	105143.710	3	10
131.0950	1.75E+07	28839.306	105119.880	3	10
131.8998	4.59E+07	28838.920	104654.030	3	10
131.9676	5.76E+07	28839.306	104615.470	3	10
141.1939	1.01E+07	28839.306	99663.912	3	7
149.2625	3.11E+08	19224.464	86220.510	2	5
149.2820	3.26E+07	19233.177	86220.510	2	5
149.4675	3.46E+08	19233.177	86137.350	2	5
174.2731	1.05E+08	28839.306	86220.510	3	5
174.5249	8.35E+07	28838.920	86137.350	3	5

Table C.2: Nitrogen lines in the visible

Line position (nm)	A_{ul} (s ⁻¹)	E_l (cm ⁻¹)	E_u (cm ⁻¹)	L	U
409.9943	3.48E+06	86137.350	110521.050	5	15
410.9949	3.90E+06	86220.510	110544.850	5	15

Table C.3: Strongest nitrogen lines in the IR

Line position (nm)	A_{ul} (s^{-1})	E_l (cm^{-1})	E_u (cm^{-1})	L	U
856.7735	4.86E+06	86137.350	97805.840	5	7
859.4000	2.09E+07	86137.350	97770.180	5	7
862.9235	2.67E+07	86220.510	97805.840	5	7
865.5748	5.46E+06	99663.427	111213.271	7	15
865.5878	1.07E+07	86220.510	97770.180	5	7
868.0282	2.53E+07	83364.620	94881.820	4	6
868.3403	1.88E+07	83317.830	94830.890	4	6
868.6149	1.15E+07	83284.070	94793.490	4	6
870.3247	2.16E+07	83284.070	94770.880	4	6
871.1703	1.29E+07	83317.830	94793.490	4	6
871.8837	6.54E+06	83364.620	94830.890	4	6
872.8901	3.75E+06	83317.830	94770.880	4	6
938.6805	2.13E+07	86137.350	96787.680	5	7
939.2793	2.51E+07	86220.510	96864.050	5	7
986.3330	1.03E+07	94881.820	105017.600	6	9
1010.5132	2.81E+07	94770.880	104664.130	6	9
1010.8892	3.02E+07	94793.490	104683.060	6	9
1011.2481	3.41E+07	94830.890	104716.950	6	9
1011.4640	3.90E+07	94881.820	104765.770	6	9
1053.9570	2.54E+07	95532.150	105017.600	6	9
1228.8810	1.41E+07	96750.840	104886.100	6	9
1232.8770	1.30E+07	96750.840	104859.730	6	9
1238.1633	1.09E+07	96750.840	104825.110	6	9
1246.1253	1.82E+07	96787.680	104810.360	7	10
1246.9615	2.18E+07	96864.050	104881.350	7	9
1360.2278	1.07E+07	97770.180	105119.880	7	10
1362.4208	1.33E+07	97805.840	105143.710	7	10

Table C.4: Strongest oxygen lines

Line position (nm)	A_{ul} (s^{-1})	E_l (cm^{-1})	E_u (cm^{-1})	L	U
97.6448	3.86E+07	0.000	102411.995	1	11
98.8773	2.26E+08	0.000	101135.407	1	11
99.0204	1.68E+08	158.265	101147.526	1	11
102.5762	7.66E+07	0.000	97488.538	1	9
102.5763	1.91E+07	0.000	97488.448	1	9
102.7431	5.71E+07	158.265	97488.448	1	9
103.9230	9.43E+07	0.000	96225.049	1	8
104.0943	5.64E+07	158.265	96225.049	1	8
115.2151	5.28E+08	15867.862	102662.026	2	11
130.2168	3.41E+08	0.000	76794.978	1	5
130.4858	2.03E+08	158.265	76794.978	1	5
130.6029	6.76E+07	226.977	76794.978	1	5
777.1944	3.69E+07	73768.200	86631.454	4	6
777.4166	3.69E+07	73768.200	86627.778	4	6
777.5388	3.69E+07	73768.200	86625.757	4	6
844.6247	3.22E+07	76794.978	88631.303	5	7
844.6359	3.22E+07	76794.978	88631.146	5	7
844.6758	3.22E+07	76794.978	88630.587	5	7
926.0806	1.56E+07	86625.757	97420.839	6	9
926.2582	1.11E+07	86627.778	97420.942	6	9
926.2670	2.60E+07	86627.778	97420.839	6	9
926.2776	2.97E+07	86627.778	97420.716	6	9
926.5932	1.48E+07	86631.454	97420.716	6	9
926.6006	4.45E+07	86631.454	97420.630	6	9

Appendix D: Spatial smearing

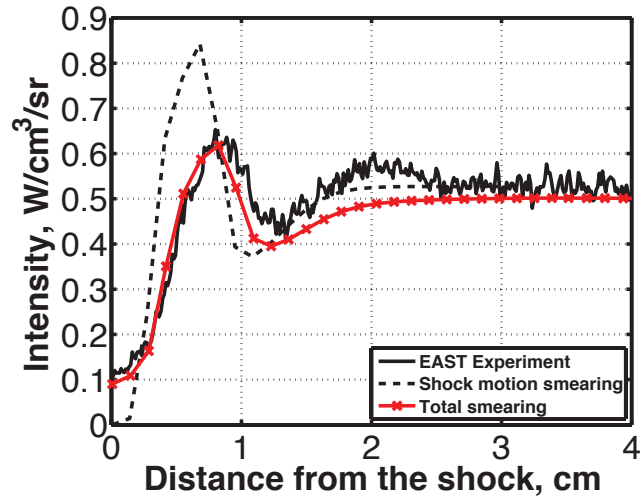


Figure D.1: Simulated post-shock intensity profile for shot 116 ($V_{\infty}=10.54$ km/s, $p_{\infty}=13.3$ Pa) in the VUV ($\Delta\lambda=140-176$ nm) with shock motion and total spatial smearing

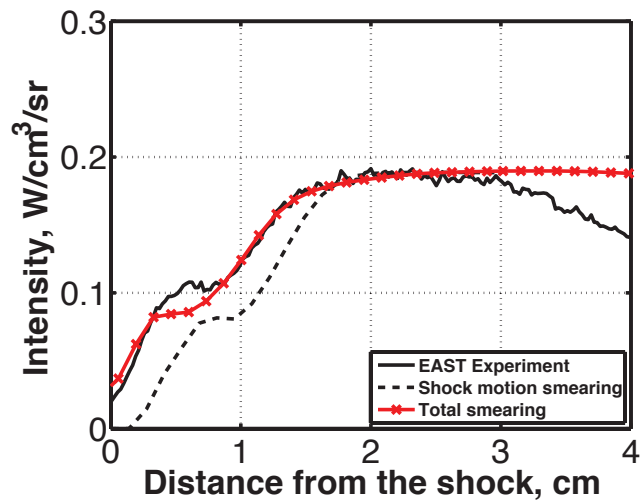


Figure D.2: Simulated post-shock intensity profile for shot 117 ($V_{\infty}=10.6$ km/s, $p_{\infty}=13.3$ Pa) in the IR ($\Delta\lambda=852-872$ nm) with shock motion and total spatial smearing

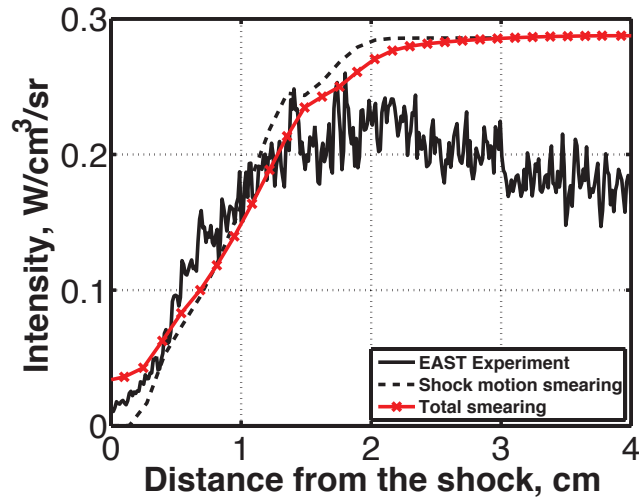


Figure D.3: Simulated post-shock intensity profile for shot 119 ($V_\infty=11.17$ km/s, $p_\infty=13.3$ Pa) in the VUV ($\Delta\lambda=175-176$ nm) with shock motion and total spatial smearing

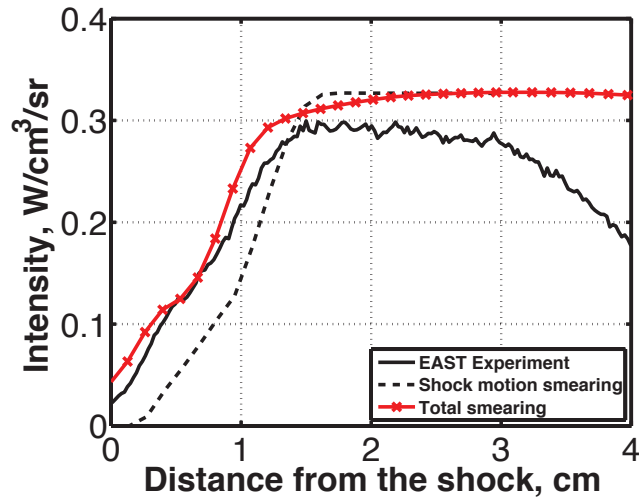


Figure D.4: Simulated post-shock intensity profile for shot 119 ($V_\infty=11.17$ km/s, $p_\infty=13.3$ Pa) in the IR ($\Delta\lambda=852-872$ nm), electron and heavy-particle impact processes

References

- M. Abramowitz and I. Stegun. Handbook of mathematical functions. Dover Publications, 1972.
- J. M. Ajello, G. K. James, B. O. Franklin, and D. E. Shemanski. Medium resolution studies of extreme ultraviolet emission from N_2 by electron-impact: vibrational perturbations and cross-sections of the $c'_4 \ ^1\Sigma_u^+$ and $b' \ ^1\Sigma_u^+$ states. *Physical Review A*, 40(7), 1989.
- R. A. Allen, Nonequilibrium and equilibrium radiation at super-orbital velocities. Technical report, 156, AVCO, 1962.
- J. D. Anderson. Hypersonic and high temperature gas dynamics. AIAA, 2006.
- J. Appleton and K. Bray. The conservation equations for a nonequilibrium plasma. *Journal of Fluid Mechanics* 20(4), 1964.
- S. V. Avakyan, R. N. Il'in, V. M. Lavrov, and G. N. Ogurtsov. Collision processes and excitation of UV emission from planetary atmospheric gases. Gordon and Breach Science Publishers, 1998.
- I. Armenise, M. Capitelli, E. V. Kustova, and E. A. Nagnibeda. Influence of nonequilibrium kinetics on heat transfer and diffusion near reentering body. *Journal of Thermophysics and Heat Transfer*, 13(2), 1999.
- I. Armenise and M. Capitelli. State to state vibrational kinetics in the boundary layer of an entering body in Earth atmosphere: particle distributions and chemical kinetics. *Plasma Source Science and Technology*, 14(2), 2005.
- J. Bacri, M. Lagreca, and A. Medani. Composition of a quasi-homogeneous stationary nitrogen plasma at atmospheric pressure. *Physica*, 113(3), 1982.
- J. Bacri and A. Medani. Electron diatomic molecule weighted total cross-section calculation. I. Principles for calculation. *Physica*, 101(3), 1980.
- J. Bacri and A. Medani. Electron diatomic molecule weighted total cross-section calculation. II. Application to the nitrogen molecule. *Physica*, 101(3), 1980.
- J. Bacri and A. Medani. Electron diatomic molecule weighted total cross-section calculation. III. Main inelastic processes for N_2 and N_2^+ . *Physica*, 112(1), 1982.
- G.D. Billing and E.R. Fisher. VT and VV Rate Coefficients in N_2 by a Quantum-Classical Model. *Chemical Physics*, 43, 1979.
- D. Bose, E. Mac Corkle, C. Thompson, D. W. Bogdanoff, D. Prabhu, G. A. Allen, and J. H. Grinstead. Analysis and model validation of shock layer radiation in air. AIAA paper 2008-1246, 2008.
- D. W. Bogdanoff. Shock-tube experiments for Earth and Mars entry conditions. Technical report RTO-EN-AVT-162, NATO, 2007.
- A. Bourdon and P. Vervisch. Three body recombination rate of atomic nitrogen in low pressure plasma flows. *Physical Review E*, 54(2), 1996.
- A. Bourdon, Y. Térésia, and P. Vervisch. Ionization and recombination rates of atomic oxygen in high temperature air plasma flows. *Physical Review E*, 57(4), 1998.
- A. M. Brandis, B. A. Cruden, D. Prabhu, D. Bose, M. Mac Gilvray, and R. G. Morgan. Analysis of air radiation measurements obtained in the EAST and the X2 shock-tube facilities. AIAA paper 2010-4510, 2010.

- A. M. Brandis. Private communication, January 2012.
- A. M. Brandis, C.O. Johnston, B. A. Cruden, D. K. Prabhu. Investigation of nonequilibrium radiation in Mars entry, AIAA paper 2013-1055, 2013.
- A. Broc. *Prise en compte du rayonnement dans les écoulements hyperenthalpiques*. Ph.D thesis, Université de Paris 11, France, 1998.
- A. Broc, V. Joly, J. P. Lafon, and C. Marmignon. Nonequilibrium radiative hypersonic flows: aerospace applications. *Astrophysics and Space Science*, 260(1-2), 1998.
- A. Bultel, B. Chéron, A. Bourdon, O. Motapon, and I. Schneider. Collisional radiative model in air for Earth reentry problems. *Physics of plasmas*, 13(4), 2006.
- J. L. Cambier and S. Moreau. Simulations of a molecular plasma in collisional radiative nonequilibrium. AIAA paper 1993-3196, 1993.
- M. Capitelli, C. M. Ferreira, B. F. Gordiets and A. I. Osipov. *Kinetics in atmospheric gases*, Springer, 2000.
- M. Capitelli, G. Colonna, and F. Esposito. On the coupling of vibrational relaxation with the dissociation-recombination kinetics: from dynamics to aerospace applications. *Journal of Physical Chemistry*, 110(17), 2006.
- D. C. Cartwright, S. Trajmar, A. Chutjan, and W. Williams. Electron-impact excitation of the electronic states of N_2 . II. Integral cross-sections at incident energies from 10 to 50 eV. *Physical Review A*, 16(3), 1977.
- D. L. Cauchon. Radiative heating results from the FIRE 2 flight experiment at a reentry velocity of 11.4 km/s. Technical report TM X-1402, NASA, 1967.
- S. M. Chauveau, C.O. Laux, J. D. Kelley, and C. H. Kruger. Vibrationally specific collisional radiative model for nonequilibrium air plasmas. AIAA paper 2002-2229, 2002.
- G. G. Chernyi and S. A. Losev. Development of thermal protection systems for interplanetary flight. ISTC Report, Research Institute of Mechanics, 1999.
- G. Colonna and M. Capitelli. The influence of atomic and metastable states in high enthalpy nozzle expansion nitrogen flows. *Journal of Physics D: Applied Physics*, 34(4), 2001.
- D. H. Crandall, W. E. Kaupilla, R. A. Phaneuf, P. O. Taylor, and G. H. Dunn. Absolute cross-sections for electron-impact excitation of N_2^+ . *Physical Review A*, 9(6), 1974.
- B. A. Cruden, R. Martinez, J. H. Grinstead, and J. Olejniczak. Simultaneous vacuum ultraviolet through near infrared absolute radiation measurements with spatio-temporal resolution in an electric arc shock-tube. AIAA paper 2009-4240, 2009.
- B. A. Cruden, H. Le, and R. Martinez. Electron density measurement in reentry shocks for lunar return. AIAA paper 2011-3628, 2011.
- B.A. Cruden. Recent progress in entry radiation measurements in the NASA Ames electric arc shock-tube facility. In the proceedings of the Fifth International Workshop of Radiation of High Temperature Gases in Atmospheric Entry, Barcelona, Spain, 2013.
- H. W. Drawin. Collision and transport cross-sections. Technical Report EUR-CEA-FC-383, 1966.

- P. J. Erbland. Current and near term RLV / hypersonic vehicle programs. Technical Report RTO-EN-AVT-116, NATO, 2005.
- M. R. Flannery. Semi-quantal theory of heavy-particle collisions with neutral atoms. I. Slow and intermediate energy collisions. Technical Report 322, Smithsonian Astrophysical Observatory, 1970.
- J. Fournier, O. Chazot, Review of high enthalpy facilities, RASTAS SPEAR deliverable D2.1, 2011.
- R. M. Frost, P. Awakowicz, H. P. Summers, and N. R. Badnell. Calculated cross-sections and measured rate coefficients for electron-impact excitation of neutral and singly ionized nitrogen. *Journal of Applied Physics*, 84(6), 1998.
- R. J. Gessman. An experimental investigation of the effects of chemical and ionizational nonequilibrium in recombining atmospheric pressure air plasmas. PhD thesis, The University of Stanford, USA, 2000.
- R. J. Gessman, C.O. Laux, and C. H. Kruger. Experimental study of kinetic mechanisms of recombining atmospheric pressure air plasmas. AIAA paper 1997-2364, 1997.
- H. Geisen, D. Neuschäfer, and C. Ottinger. State-specific predissociation of N_2 ($B^3\Pi_g$) measured by laser-induced fluorescence on a molecular Beam. *Journal of Chemical Physics*, 92(1), 1990.
- M. A. Gigoso and V. Cardeñoso. New plasma diagnosis tables of hydrogen Stark broadening including ion dynamics. *Journal of Physics B: Atomic Molecular and Optical Physics*, 29(20), 1996.
- F. R. Gilmore. Potential energy curves for N_2 , NO, O_2 and corresponding ions. RAND Corporation memorandum R-4034-PR, 1964.
- P. A. Gnoffo, R. N. Gupta, and J. L. Shinn. Conservation equations and physical models for hypersonic air flows in thermal and chemical nonequilibrium. Technical Paper 2867, NASA, United States, 1989.
- R. G. Gollan, The computational modelling of high-temperature gas effects with application to hypersonic Flows. Ph.D thesis, The University of Queensland, Australia, 2008.
- A. M. Gomes, A. Essoltani, and J. Bacri. Collisional-radiative modelling of a nonequilibrium stationary oxygen plasma at atmospheric pressure, $3000 < \Theta_e, K < 18000$. *Journal of Quantitative Spectroscopy and Radiative transfer*, 43(6), 1990.
- S. Gordon and B. Mac Bride. Computer program for calculation of complex chemical equilibrium compositions and applications. Part 1: Analysis. NASA Reference Publication 1311, 1994.
- F. J. Gordillo-Vazquez and J. A. Kunc. Diagnostics of plasmas with substantial concentrations of atomic oxygen. *Physical Review E*, 51, 1995.
- H. R. Griem. *Plasma Spectroscopy*, Mac Graw Hill Book Company, New York, 1964.
- J. H. Grinstead, M. C. Wilder, D. C. Reda, C. J. Cornelison, B. A. Cruden, and D. W. Bogdanoff. Shock-tube and ballistic range facilities at NASA Ames research center. Technical Report RTO-EN-AVT-186, NATO, 2010.

- J. H. Grinstead, M. C. Wilder, D. C. Reda, B. A. Cruden, and D. W. Bogdanoff. Advanced spectroscopic and thermal imaging instrumentation for shock-tube and ballistic range facilities. Technical Report RTO-EN-AVT-186, NATO, 2010.
- M. Gryzinski. Classical theory of electronic and ionic inelastic collisions. *Physical Review*, 138(2A), 1958.
- D. Hash, J. Olejniczak, M. J. Wright, D. Prabhu, M. Pulsonetti, B. Hollis, P. Gnoffo, M. Barhardt, I. Nompelis, and G. Candler. FIREII calculations for hypersonic nonequilibrium aerothermodynamics code verification: DPLR, LAURA and US3D. AIAA paper 2007-605, 2007.
- E. H. Hirshel. Historical perspective on programs, vehicles and technologies issues. Technical Report RTO-EN-AVT-116, NATO, 2005.
- W. Huo. Electron-impact excitation and ionisation of air. Technical Report RTO-EN-AVT-162, NATO, 2008.
- W. Huo. Electron recombination and collisional excitation in air. AIAA paper 2009-1593, 2009.
- W. Huo. Stark line shapes in a weakly ionized plasma. AIAA paper 2012-2740, 2012.
- W. Hwang, Y.-K. Kim, and M. E. Rudd. New model for electron-impact ionization cross-section of molecules. *Journal of Chemical Physics*, 104(8), 1996.
- S. Y. Hyun. Radiation code SPRADIAN07 and its applications. Ph.D thesis, KAIST, South Korea, 2009.
- Y. Itikawa. Cross-sections for electron collisions with nitrogen molecules. *Journal of Physical and Chemical Reference Data*, 35(1), 2006.
- C. M. Jacobs, Radiation in low density hypervelocity flows, Ph.D thesis (co-tutelle), The University of Queensland, Australia, Ecole Centrale Paris, 2012.
- G. K. James, J. M. Ajello, B. O. Franklin, and D. E. Shemanski. Medium resolution studies of extreme ultraviolet emission from N_2 by electron-impact: the effect of predissociation on the emission cross-section of the $b\ ^1\Pi_u$ state. *Journal of Physics B: Atomic Molecular and Optical Physics*, 23(12), 1990.
- P. V. Johnson, I. Kanik, D. E. Shemansky, and X. Liu. Electron-impact cross-sections of atomic oxygen. *Journal of Physics B: Atomic Molecular and Optical Physics*, 36(15), 2003.
- P. V. Johnson, I. Kanik, M. A. Khakoo, J. W. Mac Conkey, and S. Tayal. Low energy differential and integral electron-impact cross-sections for the $2s^22p^4\ ^3P - 2p^33s\ ^3S$ excitation in atomic oxygen. *Journal of Physics D: Applied Physics*, 36(21), 2003.
- P. V. Johnson, C. P. Malone, I. Kanik, K. Tran, and M. A. Khakoo. Integral cross-sections for the direct excitation of the $A\ ^3\Sigma_u^+$, $W\ ^3\Delta_u$, $B'\ ^3\Sigma_u^-$, $a'\ ^1\Sigma_u^+$, $a\ ^1\Pi_g$, $w\ ^1\Delta_u$ and $C\ ^3\Pi_u$ in N_2 by electron-impact. *Journal of Geophysical Research*, 110(8), 2005.
- C. O. Johnston. Nonequilibrium shock-layer radiative heating for Earth and Titan entry. Ph.D thesis, Virginia Polytechnic Institute and State University, USA, 2006.
- C. O. Johnston. A comparison of EAST shock-tube radiation measurements with a new air radiation model. AIAA paper 2008-1245, 2008.

- C. O. Johnston, B. Hollis, and K. Sutton. Non-Boltzmann modeling for air shock-layer radiation at lunar-return conditions. *Journal of Spacecrafts and Rockets*, 45(5), 2008.
- C. O. Johnston, R. B. Hollis, and K. Sutton. Nonequilibrium stagnation line radiative heating for FIRE 2. *Journal of Spacecrafts and Rockets*, 45(6), 2008.
- C. O. Johnston. Improved exponential integral approximation for tangent-slab radiation transport. *Journal of Thermophysics and Heat Transfer*, 24(3), 2010.
- I. Kanik, P. V. Johnson, M. B. Das, M. A. Khakoo, and S. Tayal. Electron-impact studies of atomic oxygen: differential and integral cross-sections, experiment and theory. *Journal of Physics B: Atomic Molecular and Optical Physics*, 34(26), 2003.
- T. Kato. Electron-impact excitation of nitrogen and nitrogen-like ions: a review of available data and recommendations. *Atomic data and nuclear tables*, 57(1-2), 1994.
- H. Katsurayama, K. Fujita, T. Abe, S. Y. Hyun, C. Park, and K. S. Chang. Structured package for radiation analysis 2007 (SPARDIAN07) program: user's manual, 2007.
- D. J. Kelley. Private communication, February 2013.
- M. A. Khakoo, C. P. Malone, P. V. Johnson, B. R. Lewis, R. Laher, S. Wang, V. Swaminathan, D. Nuyujukian, and I. Kanik. Electron-impact excitation of $X \ ^1\Sigma_g^+ (v''=0)$ to the $a'' \ ^1\Sigma_g^+$, $b \ ^1\Pi_u$, $c_3 \ ^1\Pi_u$, $c_3 \ ^1\Pi_u$, $b' \ ^1\Sigma_u^+$, $c'_4 \ ^1\Sigma_u^+$, $G \ ^3\Pi_u$ and $F \ ^3\Pi_u$ states of molecular nitrogen. *Physical Review A*, 77(1), 2008.
- A. K. Kazansky and I. S. Yelets. Quasiclassical calculation of the cross-sections for resonant vibrational excitation of the molecules N_2 and CO . *Zhurnal Eksperimental Teoretikal Fizik*, 82,1982. English translation.
- Y.-K. Kim and M. E. Rudd. Binary encounter dipole model for electron-impact ionization. *Physical Review A*, 50(5), 1994.
- Y.-K. Kim. Scaling of plane-wave Born cross-sections for electron-impact excitation of neutral atoms. *Physical Review A*, 64(3), 2001.
- Y.-K. Kim and J.-P. Desclaux. Ionization of carbon, nitrogen and oxygen by electron-impact. *Physical Review A*, 66(1), 2002.
- J. A. Kunc and W. H. Soon. Collisional-radiative nonequilibrium in partially ionized atomic nitrogen. *Physical Review A*, 40(10), 1989.
- J. M. Lamet. Transferts radiatifs dans les écoulements hypersoniques de rentrée atmosphérique terrestre. Ph.D thesis, Ecole Centrale Paris, France, 2009.
- L. Landau and E. Teller, Theory of sound dispersion, *Physikalische Zeitschrift der Sowjetunion*, 10,1936.
- A. Larichiutta. Aerothermochemistry models for reentry applications. I. Missing data evaluation and generation of advanced models. Technical report, ESA-ESTEC, 2010.
- A. Larichiutta. Aerothermochemistry models for reentry applications. II. Advanced models, data review and generation: *ab initio* data development. Technical report, ESA-ESTEC, 2010.

- C.O. Laux and C.H. Kruger. Arrays of radiative transition probabilities for the N₂ first and second positive, NO β and γ, N₂⁺ first negative, and O₂ Schumann-Runge band systems, *Journal of Quantitative Spectroscopy and Radiative Transfer*, 48(1), 1992.
- C.O. Laux, R. J. Gessman, and C. H. Kruger. Modelling the UV and VUV radiative emission of high temperature air. AIAA paper 1993-2802, 1993.
- C.O. Laux, R. J. Gessman, and C. H. Kruger. Mechanisms of ionizational nonequilibrium in air and nitrogen plasmas. AIAA paper 1995-1989, 1995
- C.O. Laux, T. G. Spence, C. H. Kruger, and R. N. Zare. Optical diagnostics of atmospheric pressure air plasmas. *Plasma Source Science and Technology*, 12, 2003.
- C.O. Laux, M. Winter, J. Merrifield, A. Smith, and P. Tran. Influence of ablation products on the radiation at the surface of a blunt hypersonic vehicle at 10 km/s. AIAA paper 2009-3925, 2009.
- C.O. Laux, L. Pierrot, R. J. Gessman. State-to-state modeling of a recombining nitrogen plasma experiment. *Journal of Chemical Physics*, 398, 2012.
- C.O. Laux and A. Lemal, Radiative transition probabilities and electron-impact excitation cross-sections for the VUV systems of N₂. 21th ESCAMPIG conference. Viana do Castelo, Portugal, July 10-14, 2012.
- Z. Li, T. Osawa, I. Sohn and D. A. Levin. Modeling of electronic excitation and radiation in non-continuum hypersonic reentry flows. *Physics of Fluids*, 23, 2011.
- Z. Li, I. Sohn and D. A. Levin. Effects of non-Maxwellian distribution on shock layer radiation from hypersonic reentry flows. *Journal of Thermophysics and Heat Transfer*, 27(1), 2013.
- H. Liebhart, G. Herdrich, H.-P. Röser, and M. Fertig. Contribution of VUV transitions of molecular nitrogen to radiation during atmospheric reentry. AIAA paper 2010-4774, 2010.
- Y. Liu, F. Shakib, and M. Vinokur. A comparison of internal energy calculation methods for diatomic molecules. *Physics of Fluids A*, 2(10), 1990.
- Y. Liu, W. Huo, A. Wray, D. Carbon. Electron Stark broadening database for atomic N, O and C lines. AIAA paper 2012-2739, 2012.
- M. Lino Da Silva, V. Guerra, and J. Loureiro. Two-temperature models for nitrogen dissociation. *Journal of Chemical Physics*, 342(7), 2007.
- B. Lopez, M.-Y. Perrin, P. Rivière, A. Soufiani. Coupled nonequilibrium flowfield radiative transfer calculation behind a shock wave. Accepted for publication in the *Journal of Thermophysics and Heat Transfer*, 2013.
- A. Louzet, A. Lemal, C.O. Laux, Instrumentation and optical diagnostics in world wide high enthalpy ground-test facilities, RASTAS SPEAR deliverable D2.2, 2011.
- S. Macheret and W. Rich. Nonequilibrium dissociation rates behind strong shock waves: classical model. *Journal of Chemical Physics*, 174, 1993.
- T.E. Magin, L. Caillaud, A. Bourdon, and C. Laux. Nonequilibrium radiative heat flux modelling for the Huygens entry probe. *Journal of Geophysical Research*, 111(8), 2006.

- T. Majeed and D. J. Strickland. New survey of electron-impact cross-sections for photoelectron and auroral electron energy cross-sections. *Journal of Physical and Chemical Reference Data*, 26(2), 1997.
- C. P. Malone, P. V. Johnson, X. Liu, B. Adjari, I. Kanik, and M. A. Khakoo. Integral cross-sections for the electron-impact excitation of the $b\ ^1\Pi_u$, $c_3\ ^1\Pi_u$, $b'\ ^1\Sigma_u^+$, $c'_4\ ^1\Sigma_u^+$, $G\ ^3\Pi_u$ and $F\ ^3\Pi_u$ states of N_2 . *Physical review A*, 85(6), 2011.
- P. Marrone and C. Treanor. Chemical relaxation with preferential dissociation from excited vibrational levels. *Physics of Fluids* 6(9), 1963.
- R. Millikan and D. White. Systematics of vibrational relaxation. *Journal of Chemical Physics*, 9(12), 1963.
- M. Mitchner and C. H. Kruger. *Partially ionized gases*. John Wiley and Sons, Inc, 1972.
- O. Nagy. Excitation cross-sections of N_2^+ molecular ion by electron-impact and the vibrational energy levels of the three target states. *Journal of Chemical Physics*, 286, 2003.
- NIST database (2012) available at: <http://physics.nist.gov/PhysRefData/ASD/>.
- J. J. Olivero and R. L. Longbothom, Empirical fits to the Voigt line width: a brief review, *Journal of Quantitative Spectroscopy and Radiative Transfer*, 17(2), 1977.
- M. Panesi. Physical models for nonequilibrium plasma flow simulations at high speed re-entry conditions. Ph.D thesis, VKI-Aerospace Department, Belgium, 2009.
- M. Panesi, T. E. Magin, A. Bourdon, A. Bultel, and O. Chazot. Analysis of the FIRE 2 flight experiment by means of a collisional radiative model. *AIAA paper 2008-1205*, 2009.
- M. Panesi, T. E. Magin, A. Bourdon, A. Bultel, and O. Chazot. FIRE 2 flight experiment analysis by means of a collisional-radiative model. *Journal of Thermophysics and Heat Transfer*, 23(2), 2009.
- M. Panesi, T. E. Magin, A. Bourdon, A. Bultel, O. Chazot, and Y. Babou. Collisional radiative modelling in flow simulations. *Technical Report RTO-EN-AVT-162*, NATO, 2009.
- M. Panesi, Y. Babou, and O. Chazot. Predictions of nonequilibrium radiation: analysis and comparison with EAST experiments. *AIAA paper 2008-3812*, 2010.
- M. Panesi and W. Huo. Nonequilibrium ionization phenomena behind shock waves. *AIAA paper 2011-3629*, 2011.
- M. Panesi, T. E. Magin, A. Bourdon, A. Bultel, and O. Chazot. Electronic excitation of atoms and molecules for the FIRE 2 flight experiment. *Journal of Thermophysics and Heat Transfer*, 25(3), 2011.
- C. Park. *Nonequilibrium Air Radiation (NEQAIR) program: user's manual*, 1985.
- C. Park. *Nonequilibrium hypersonic aerothermodynamics*. John Wiley and Sons, 1990.
- C. Park. Review of chemical-kinetic problems for future NASA missions. II. Earth entries. *Journal of Thermophysics and Heat Transfer*, 7(3), 1993.

- C. Park. Rate parameters for electronic excitation of diatomic molecules. I. Electron-impact processes. AIAA paper 2008-1206, 2008.
- C. Park. Rate parameters for electronic excitation of diatomic molecules. II. Heavy-particle impact processes. AIAA paper 2008-1446, 2008.
- G. Peach. Continuous absorption coefficient for non-hydrogenic atoms. *Memoirs of the Royal Astronomical Society*, 73, 1970
- L. Pierrot, L. Yu, R. J. Gessman, C. Laux, and C. H. Kruger. Collisional-radiative modelling of nonequilibrium effects in nitrogen plasmas. AIAA paper 1999-3478, 1999.
- Y. A. Plastinin, G. F. Karabadzhak, B. A. Khmelinin, B. A. Zemlianski, A. V. Gorshkov, and G. N. Zalogin. Measurements of the UV radiation generated by the Soyouz spacecraft transport capsule during reentry. AIAA paper 2007-815, 2007.
- D. Potter. Modelling of radiating shock layers for atmospheric entry in Mars and Earth. Ph.D thesis, The University of Queensland, Australia, 2011.
- E. Raynaud, P. Tran, J. Soler, and M. Baillon. Huygens aerothermal environment: radiative heating. In the proceedings of the Third International Planetary Probe Workshop, Anavyssos, Greece, 2005.
- RASTAS SPEAR (2010) project available at: <http://www.rastas-spear.eu/>.
- J. P. Sarrette, A. M. Gomes, and J. Bacri. Collisional-radiative modelling of quasi-thermal air plasmas with electronic temperatures between 2000 and 13000 K. II. $2000 \text{ K} < \Theta_e < 4000 \text{ K}$. *Journal of Quantitative Spectroscopy and Radiative Transfer*, 53(2), 1995.
- J. P. Sarrette, A. M. Gomes, and J. Bacri. Collisional-radiative modelling of quasi-thermal air plasmas with electronic temperatures between 2000 and 13000 K. II. $\Theta_e > 4000 \text{ K}$. *Journal of Quantitative Spectroscopy and Radiative Transfer*, 53(2), 1995.
- D. E. Shemansky, J. M. Ajello, and D. T. Hall. Electron-impact excitation of H_2 : Rydberg band systems and the benchmark dissociative cross-sections for H Lyman-alpha. *The Astrophysical Journal*, 296(2), 1985.
- M. J. Seaton. The theory of excitation and ionization by electron-impact. Academic Press, New York, 1962.
- M. Smart, R. Stalker, R. G. Morgan, and A. Paull. Hypersonics research in Australia. Technical Report RTO-EN-AVT-150, NATO, 1990.
- I. Sohn, Z. Li, and D. A. Levin. Effect of excape factor to a hypersonic nonequilibrium flow implemented in DSMC photon Monte Carlo radiation. AIAA paper 2011-533, 2011.
- W. H. Soon and J. A. Kunc. Thermal nonequilibrium in partially ionized atomic oxygen. *Physical Review A*, 41(2), 1990.
- T. Soubri . Prise en compte de l'ionisation et du rayonnement dans les rentr es terrestres et martiennes. Ph.D thesis, ISAE-ENSAE, France, 2006.
- D. Spence and P. D. Burrow. Cross-sections for excitation of the $2s^2 2p^2 3s \ ^4P$ and $2s^2 p^4 \ ^4P$ states of atomic nitrogen by near-threshold electron-impact. *Journal of Physics B: Atomic Molecular and Optical Physics*, 13(14), 1980.

- D. Stahel, M. Leoni, and K. Dressler. Nonadiabatic representations of the $^1\Sigma_u^+$ and $^1\Pi_u$ states of the N_2 molecule. *The Journal of Chemical Physics*, 79(6), 1983.
- E. J. Stone and E. C. Zipf. Excitation of atomic nitrogen by electron-impact. *Journal of Chemical Physics*, 58(10), 1973.
- S. T. Surzhikov. Electronic excitation in air and carbon dioxide gas. Technical Report RTO-EN-AVT-162, NATO, 2009.
- P. Teulet, J. P. Sarrette, and A. M. Gomes. Calculation of electron-impact inelastic cross-sections and rate coefficients for diatomic molecules. Application to air molecules. *Journal of Quantitative Spectroscopy and Radiative Transfer*, 62(5), 1999.
- P. Teulet, J. P. Sarrette, and A. M. Gomes. Collisional-radiative Modeling of one- and two-temperature air and air-sodium plasmas at atmospheric pressure with temperatures of 2000-12000 K. *Journal of Quantitative Spectroscopy and Radiative transfer*, 70(2), 2000.
- C. Treanor and P. Marrone. Effect of dissociation on rate of vibrational relaxation. *Physics of Fluids*, 5(9), 1962.
- P. Tran, J. C. Paulat, and P. Boukhobza. Reentry flight experiments lessons learned: the atmospheric reentry demonstrator ARD. Technical Report RTO-EN-AVT-130, NATO, 2007.
- G. Tumino, S. Mancuso, T. Walloschek, S. Langlois and C. Philippe, The IXV project : the European approach to in-flight experimentation for future space transportation systems and technologies. 58th International Astronautical Congress. Hyderabad, India, September 24 - 28, 2007.
- H. Van Regemorter. Rate of collisional excitation in stellar atmospheres. *The Astrophysical Journal*, 136(27), 1962.
- W. G. Vincenti and C. H. Kruger. Introduction to physical gas dynamics. Robert E. Krieger Publishing Company, 1965.
- E. E. Whiting, An Empirical Approximation to the Voigt Profile, *Journal of Quantitative Spectroscopy and Radiative Transfer*, 8(6), 1968.
- E. E. Whiting, C. Park, Y. Liu, J. Arnold, and J. A. Paterson. NEQAIR96, nonequilibrium and equilibrium radiative transport and spectra program: user's manual, 1996.
- W. L. Wiese, J. R. Fuhr, and T. M. Deters. Atomic transition probabilities of carbon, nitrogen, and oxygen, *Journal of Physical Chemistry Reference Data*, Monograph 7, 1996.
- J. William. Etude des processus physico-chimiques dans les écoulements détendus à haute enthalpie: application à la soufflerie F4. Ph.D thesis, Université de Provence, France, 2000.
- M. J. Wright, F. S. Milos, and P. Tran. Afterbody aeroheating flight data for planetary probe thermal protection system design. *Journal of Spacecrafts and Rockets*, 43(5), 2006.
- J. Yang and J. P. Doering, Absolute differential and integral electron excitation cross-sections for atomic nitrogen. 3. The $^4S^0 \rightarrow 2D$ ($\lambda=5200 \text{ \AA}$) transition from 5 to 30 eV, *Journal of Geophysical Research*, 101(A10), 1996.
- O. Zatsarinny and S. Tayal. Electron collisional excitation rates for O using the BSRM approach. *The Astrophysical Journal*, 148(2), 2003.

Y. B. Zel'dovich and Y. P. Raizer. Physics of shock waves and high temperature hydrodynamic phenomena. Dover Publications, 2002.

E. C. Zipf and M. R. Gorman. Electron-impact excitation of the singlet states of N_2 . The Birge-Hopfield system. *Journal of Chemical Physics*, 73(2), 1980.